Discovery and characterization of $P2Y_2$ receptor antagonists supported by site-directed mutagenesis studies

Dissertation

zur

Erlangung des Doktorgrades (Dr. rer. nat.)

der

Mathematisch-Naturwissenschaftlichen Fakultät

der

Rheinischen Friedrich-Wilhelms-Universität Bonn

vorgelegt von

Isaac Yaw Attah

aus

Accra, Ghana

Bonn 2018

Angefertigt mit Genehmigung der Mathematisch-Naturwissenschaftlichen Fakultät

der Rheinischen Friedrich-Wilhelms-Universität Bonn

1. Gutachter: Prof. Dr. Christa E. Müller

2. Gutachter: PD Dr. Anke C. Schiedel

Tag der Promotion: 21/02/2019

Erscheinungsjahr: 2019

Die vorliegende Arbeit wurde in der Zeit von Oktober 2014 bis November 2018 am Pharmazeutischen Institut, Pharmazeutische Chemie I, Bonn unter der Leitung von Frau Prof. Dr. Christa E. Müller und von Frau PD Dr. Anke C. Schiedel durchgeführt.

Printed with the support of the German Academic Exchange Service (DAAD).

To my family and friends…

Table of contents

1 Introduction

The most important drug targets are the cell surface receptors which belong to the superfamily of the G protein-coupled receptor (GPCR). These 7-transmembrane (7TM) receptors are activated by diverse stimuli including amino acids, peptides, steroids, neurotransmitters and light, to mediate several biological responses such as cell differentiation and death, cardiovascular changes, sensory perceptions, hormonal signaling, cancer progression and blood glucose modulation.[1,2]

1.1 Classification of GPCRs

All GPCRs share a common framework of an extracellular N-terminus linked to an intracellular C-terminus by seven hydrophobic transmembrane domains, three extracellular loops and three intracellular loops.[3,4] However, based on their sequence homology analysis, GPCRs have been classified by various systems. Prominent among such systems is the A-F system which stipulates six main classes: class A (rhodopsin-like), class B (secretin receptor family), class C (metabotropic glutamate), class D (fungal mating pheromone receptors), class E (cyclic AMP receptors) and class F (frizzled/smoothened).[5] The largest receptor family, the class A rhodopsin-like receptors, are further classified into α, β, γ and δ subgroups.

The α-branch of class A GPCRs include the muscarinic, adrenergic, dopaminergic and histaminic receptors among many others. Receptors activated by peptides (e.g., cholecystokinin, neuropeptide Y and oxytocin) as endogenous ligands constitute the β-subgroup. The γ-family includes the chemokine, angiotensin, somatostatin and opioid receptors. The δ-branch are the largest and most diverse of the class A family and includes the MAS-related receptors (MRGXs), nucleotide P2Y receptors (P2YR), formyl peptide receptors (FPRs), and many orphan receptors.[5] Altogether, approximately 800 GPCRs have been annotated from the human genome, half of which mediate sensory activity and are generally not considered as appropriate drug targets. About 34 % (475) of all FDA-approved drugs on the market target about 27 % (108) of the non-sensory GPCRs. Also, there are about 66 novel GPCR drug targets in clinical trials, summing up to about 40 % of GPCR drug targets (Figure 1). The remaining unexplored GPCR targets present an enormous potential for novel targets for treating diseases.[6–8]

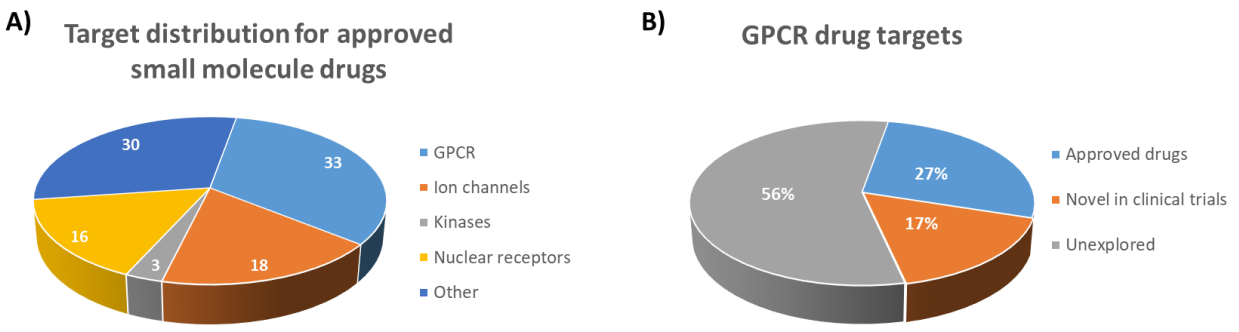

Figure 1: Pie charts showing: **A)** target distribution of FDA-approved small molecule drugs; GPCRs are the major target family and **B)** proportion of druggable GPCR targets that have been approved drugs, clinical candidates or have not been explored so far. [6,7]

1.2 GPCR signaling

GPCRs are so named because they are coupled to guanine-binding proteins (G-proteins) which mediate their cellular signaling (Figure 2). These G-proteins are heterotrimeric in structure, consisting of α- , β- and γ- subunits. Based on their structural and functional uniqueness of the Gα subunit, the G-proteins are further classified into four major subfamilies: G_s, G_i, $G_{q/11}$ and $G_{12/13}$. In its inactive state, the G-protein is GDP-bound. Upon receptor activation, GDP is exchanged for GTP leading to conformational changes that uncouple the monomeric α subunit from the dimeric βγ proteins. The separated units then transduce secondary messengers through effector systems such as enzymes. G_s activates the enzyme adenylate cyclase to convert ATP to cyclic adenosine monophosphate (cAMP) whilst G_i inhibits the production of cAMP.[9] cAMP further modulates physiological process such as the immune system by interaction with protein kinase A (PKA) or with exchange proteins directly activated by cAMP (Epac). Intracellular cAMP is degraded by phosphodiesterases (PDEs).[10] The G_q protein catalyzes, through phospholipase C (PLC), the breakdown of phosphatidylinositol-4,5-bisphosphate (PIP_2) into diacylglycerol (DAG) and inositol-1,4,5-trisphosphate (IP_3). The former activates protein kinase C (PKC) which catalyzes many other cellular responses while the latter activates the release of Ca^{2+} stored in the endoplasmic reticulum into the cytosol.

Through the RhoGTPase nucleotide exchange factors (RhoGEFs), the $G_{12/13}$ protein activates the small monomeric GTPase RhoA involved in cell actin cytoskeleton rearrangement, migration and

growth. [11,12] The previously "redundant" dimeric βγ subunit of the G-protein also directly recruits GPCR kinases (GRKs) to the receptor. βγ released from G_i-coupled GPCRs also activates PLC which induces the release of intracellular calcium by the classical pathway. Also, the βγ subunit couples to certain GPCRs and additionally, mediates unique signaling pathways, e.g., regulation of K^+ and calcium channels, through diverse protein-protein interactions.[13–15] Reassociation of the Gα and βγ subunits into the original inactive G-protein finally involves the hydrolysis of the bound GTP to GDP by the GTPase activity of the G-protein itself.

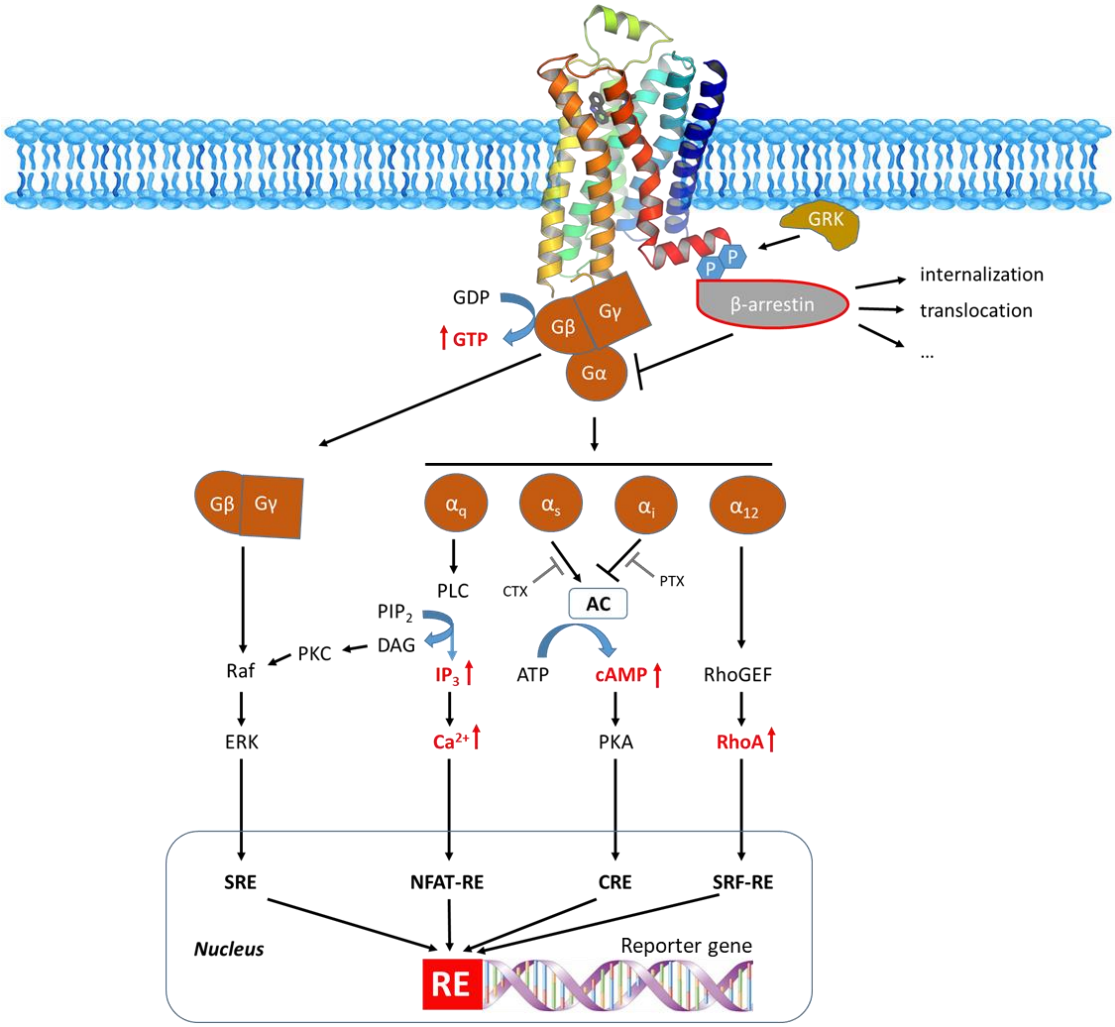

Figure 2: A brief illustration of known G-protein signaling pathways. Highlighted in red, including β-arrestin, are steps along the signaling cascade commonly utilized in assay development for GPCRs.

Moreover, additional regulation of the signaling cycle includes receptor desensitization and internalization. Persistent activation of the receptor by a ligand leads to phosphorylation of serine and threonine residues on the C-terminal end and the intracellular loops of the receptor by recruited GRKs. Phosphorylation by GRKs further recruits β-arrestins to the agonist-bound receptor. β-Arrestins lead to G-protein signal waning through three main process; receptor desensitization, ligand-receptor sequesterization and downregulation.[16] β-Arrestins might also act as signal transducers by interaction with several proteins such as Src family kinases and components of the ERK1/2 and JNK3 MAP kinase cascades.[9,16] There are four kinds of β-arrestins: those localized to the retina (arrestin 1 and 4) and those which are ubiquitously expressed, arrestin 2 and 3 (also known as β-arrestin 1 and 2, respectively). Oakley *et al.* classified GPCRs into Class A and B based on their affinity to the non-visual arrestins. Class A binds with higher affinity to β-arrestin 2 than β-arrestin 1 but the recruited arrestins are excluded from clarithrin-coated vesicles during receptor internalization. In contrast, both β-arrestin 1 and β-arrestin 2 are recruited by Class B GPCRs with equal affinity and are stably internalized together with the receptors in endocytic vesicles.[17]

1.3 **The drug discovery process**

There are two types of drug discovery processes: phenotypic and target-based. The phenotypic drug discovery focuses on developing compounds that modulate a disease-linked phenotype irrespective of the causal protein or system. In contrast, the widely used target-based drug discovery (TBDD) focuses on modulating the direct link between specific protein actions and a given disease.[18] The TBDD method is cheaper and faster. Target-based drugs approved so far span from small molecules through peptides to even nucleic acid-based therapeutics.

For TBDD, the first step is to establish and validate a direct connection of the target protein to the disease state based on an understanding of the biological and molecular processes involved. Pharmacological assays are then developed to quantify this target-disease relationship. Next, ligands are screened at the said target for active moieties called hits.[19] Compounds can be screened by *in vitro* high-throughput screening (HTS) and/or computer-based drug design (CBDD). There are two forms of CBDD: structure based drug design (SBDD) and ligand based drug design (LBDD). SBDD uses structural information such as a 3D X-ray crystallography structure of the target protein or where absent, a homology model of the target, based on a related 3D template to design and optimize hits. Homology models are relevant to in silico or virtual screening of compound libraries for hits. On the other hand, LBDD takes advantage of known interactions

between the target protein and other molecules. LBDD is also used in the absence of a 3D structure of the target protein. Ultimately, hits from in silico screens have to be validated by in vitro assays along the development pipeline.[20] Hits are then developed into lead compounds based on their selectivity, pharmacology and ease of chemical synthesis. Lead compounds are further optimized into drug candidates by improving efficacy and pharmacokinetics. Drug candidates then enter pre-clinical and subsequently clinical trials before being approved as drugs.

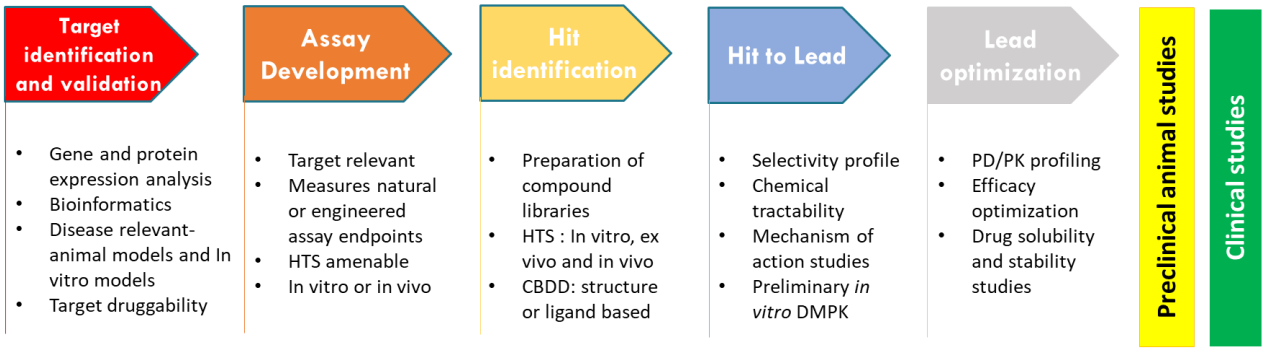

Figure 3: Simplified illustration of the drug discovery process from target identification to clinical trials.

HTS has become the mainstay of ligand discovery for GPCRs in both the pharmaceutical industry and academia. Assays developed for HTS have to be designed into miniaturized plate formats, and automation allows fast and efficient screening of large numbers of compounds without the waste of resources. The emergence of both commercial and in-house compound libraries provides a wide chemical space for discovery of novel scaffolds as active hits. Combinatorial chemistry also allows rapid development of structure-activity relationships (SAR) to fast-track the drug development process. Due to the high turnout of screening data, various metrics including the Z' factor have been introduced as means of validating HTS robustness and qualifying screening results. The hit discovery process has now become a multifaceted discipline with various laboratories combining both in vitro screening and CADD to successfully discover hit compounds, understand ligand-receptor interaction and design better drugs.[21]

1.4 **Functional Assays for drug discovery**

Functional assays are used to study the intracellular modulatory effects of ligand-receptor complexes. They are the preferred assays for primary screening of compound libraries in HTS and for the de-orphanization of orphan GPCRs.[22] Functional assays also allow mechanistic distinction of ligands into agonists (full, partial or inverse), antagonists and allosteric modulators, All GPCR functional assays are designed using insights into receptor signaling pathways and are classified accordingly into G protein-dependent, G protein-independent and universal functional assays. G protein-dependent assays, as the name suggests, commonly rely on signaling pathways that involve the selective activity of $G_{i/o}$, G_s, G_q, or G_{12} proteins.[12,23] G protein-independent assays employ β-arrestin recruitment and receptor internalization and desensitization mechanisms. Finally, universal functional assays measure whole cell phenotypic responses to activation irrespective of the downstream effector systems coupled to the receptor. Assays here include reporter gene assays, label-free assays, high content imaging, and even use of $G_{15/16}$ or β-arrestin in attenuated G protein-dependent or independent systems.[24–26] Readouts for functional assays are made possible by coupling them to various biophysical detection techniques such as fluorescent polarization (FP), fluorescence anitrosopy (FA), time-resolved fluorescence (TRF) and fluorescence and bioluminescence resonance energy transfer (FRET or BRET).[27] A few functional assays relevant to this work are described below.

1.4.1 **Calcium mobilization assay**

Activation of G_q- and G_i-coupled GPCR, leads to G_q- and G_i-βγ-mediated PLC hydrolysis of PIP_2 to IP_3 and DAG. Consequently, IP_3 then acts on calcium (Ca^{2+}) channels on the endoplasmic reticulum to release intracellular calcium $[Ca^{2+}]_i$ which is detected and quantified.

Fluorometric imaging plate readers (FLIPR®) from Molecular Devices and the use of cell-permeable synthetic Ca^{2+} sensitive fluorescent dyes have advanced calcium assays as one of the most commonly used assays for HTS. Fluorescent Ca^{2+}-chelating dyes allow monitoring of real time changes in cytosolic Ca^{2+} to about 10-fold above the baseline.[28] Single-wavelength non-ratiometric fluorescent indicators including Oregon green, BAPTA-2, Fluo-3, Fluo-4, Calcium 5 and FLUOFORTE® (from Enzo Life Sciences) employed as their lipophilic cell membrane-permeable ester derivatives are best for quantifying fluorescent intensity modulated by ligands. Fluorescent imaging is also possible with dual wavelength ratiometric dyes such as Fura-2 and

indo-1. [15,29] FLIPR® instruments have internal pipetting systems that enable complete automation of HTS for ligands. Also, non-Gq-coupled GPCRs have been studied with FLIPR and fluorescent dye-based calcium assays by transfecting cell-lines with the ubiquitous $G_{15/16}$ proteins.[30] Furthermore, FLIPR® calcium kits which are homogenous, have high signal-to-noise ratio and high sensitivity and assays miniaturized to the 1536-well format are available commercially. Further advancements such as multiplex FLIPR® assays allow for ligand discovery, counter-screening and selectivity studies to be carried out in the same plate with different GPCRs expressed either on the same or different cell-lines thus saving time and resources.[31,32] However, assays using sensitive fluorescent indicators can be affected by photobleaching, compartmentalization into intracellular vesicles, rapid Ca^{2+} kinetics and dye efflux.

Consequently, calcium assays employing Ca^{2+}-sensitive biosensors have been developed, that generate luminescence with coelenterazine as a substrate. Aequorin, a 21 kDa Ca^{2+}-sensitive photoprotein, isolated from jellyfish *Aequorea victoria*, is the most used bioluminescence protein for $[Ca^{2+}]_i$ mobilization assays. It selectively binds to $[Ca^{2+}]_i$ with a high and wide range of sensitivity, low background, zero interference from fluorescent compounds and no bio-toxicity to most cell-lines.[33]

Another engineered photoprotein, Photina® from PerkinElmer, can be stably transfected and localized to the mitochondrial compartment for efficient and sustained Ca^{2+}-induced bioluminescence assays. Photina®- and aequorin-based methods coupled to flash luminescence plate readers including CyBi®-Lumax flash HT (CyBio, Jena, Germany) enabled HTS studies for ligands at the serotonin 5-HT_{2B}, MCH_1, orexin Ox_2 and CX3CR1 receptors in miniaturized formats.[34,35] Stable cell-lines co-expressing ChemiBrite, a unique variant of the photoprotein clytin, alongside various GPCR are also available from Millipore (Billerica, MA, USA). Photoprotein-based calcium assays can be performed universally for any GPCR by co-expressing the ubiquitous Gα proteins such as $G_{15/16}$ or chimeric G_q. The assays have been used to study orphan receptors.[36]

Although not often used in HTS, genetically encoded calcium indicator (GECI)-based Ca^{2+} mobilization assays are worth mentioning. GECI involves the use of one or more variants of fluorescent proteins used alone or fused to bioluminescent aequorin to detect cytosolic Ca^{2+} through FRET or BRET technologies. The GECI systems has been used for measuring calcium influx, real time cellular imaging and studying cellular communication in tissues. [15] Notable among GECIs is the Premo Cameleon Calcium Sensor from Invitrogen (now ThermoFischer). This

ratiometric FRET-based platform utilizes the YC3.60 version of GFP variants (cameleon). The donor cyan fluorescent protein (CFP) is linked to the acceptor yellow fluorescent protein (YFP) by calmodulin and its binding peptide M13. Upon binding to Ca^{2+}, the calmodulin-M13 complex undergoes conformational changes and folds in a way that bring CFP and YFP in proximity for FRET to occur. Although this assay is wash-free, dye-free, sensitive and suitable for studying endogenous receptors, its high background signal precludes it from use in HTS.[37] An improved GECI-based Ca^{2+} mobilization assay with higher signal to noise ratio has recently been reported. It uses nanoluciferase (NanoLuc) as a bioluminescent Ca^{2+} indicator in a BRET based system. [38]

Calcium assays are versatile and sensitive to screen for all types of GPCR ligands in a single assay. They are used to study both endogenously and recombinantly expressed GPCRs. However, as a secondary messenger assay dependent on signal amplification, they are subject to a lot of false positives, particularly the fluorescent-based assays. This assay cannot be used to screen for inverse agonists as the basal activity of constitutively active GPCRs cannot be detected. Generally, assay protocols does not allow enough time for ligand-receptor equilibrium hence some slow equilibrating compounds may be missed whilst pharmacology of others may be overestimated.

1.4.2 **cAMP assay**

Activation of adenylyl cyclase by G_s-coupled GPCRs increases cellular cAMP levels whilst inhibition of the same enzyme by G_i-coupled receptors reduces cAMP concentrations. cAMP assays can be broadly classified into immuno- and non-immuno based assays.

Generally, cAMP immunoassays measure cAMP by competition between produced cytosolic cAMP and an exogenenously labelled form of cAMP for binding to an anti-cAMP antibody. The resulting changes in intracellular cAMP levels detected in this immunoassay measured by various detection technologies underline many different cAMP assays that are commercially available. G_s- or G_i-cAMP assays routinely require preincubation of cells with IBMX (3-isobutyl-1-methylxanthine), a phosphodiesterase (PDE) inhibitor, to prevent degradation of cAMP to AMP. Ligand screening by cAMP assays at G_s-coupled receptors are easier as the signal measured is directly proportional to agonist-induced cAMP levels. At G_i-coupled receptors, forskolin, a direct adenylyl cyclase activator, is used to pre-stimulate cytosolic cAMP which is then reduced by GPCR agonists. This detection of cAMP reduction by G_i-coupled GPCRs makes screening more

cumbersome particularly for antagonists.[39] Traditional radio-isotopic assays performed with ^{125}I- or ^{3}H-labelled cAMP continue to be a mainstay for many academic laboratories. PerkinElmer and GE Healthcare have introduced homogenous and convenient radio-labelled cAMP assays using Flashplate and scintillation proximity assay (SPA) technologies, respectively, used for HTS.[40–42]

Non-isotopic cAMP assays taking advantage of fluorescently labelled-cAMP have also been established. Assays kits directly detecting cAMP by fluorescent polarization (FP) assays such as [FP^{2}]-cAMP, CatchPoint^{TM} and Biotrak EIA^{TM} have been introduced by PerkinElmer, Molecular Devices, and GE Healthcare respectively. These homogenous FP-based assays used for HTS screening on both whole and lysed cells are however subject to interference from fluorescent compounds, a problem partly resolved by labelling cAMP with red-shifting fluorophores.[43,44]

Subsequently, ratiometric TR-FRET detection-based assays utilizing HTRF technology were established by PerkinElmer (LANCE_ Ultra cAMP assay kits) and Cisbio (HTRF cAMP dynamic kits) where the donor is a fluorescent-tagged cAMP bound to a labelled cAMP-antibody. The fluorescent donor is usually europium-labelled. Endogenous cAMP displaces the labeled cAMP from the antibody thereby reducing the FRET signal measured in a dose-dependent manner.[27,45] Similarly, AlphaScreen® and AlphaLISA cAMP® kits, marketed by PerkinElmer, are highly sensitive proximity assays measuring decreasing cellular chemiluminescence. Here, native cAMP competes with biotinylated cAMP for streptavidin-coated donor beads in proximity to a cAMP-antibody-acceptor bead complex. The AlphaScreen and HTRF cAMP kits are preferred for studying native or low-expressing receptors due to their higher sensitivities, moderate cost and HTS-compartibilies. [46]

Meso Scale Discovery (Gaithersburg, Maryland) have established an electrochemiluminescence-based cAMP assay which requires competitive displacement of ruthenium-labeled cAMP from an anti-cAMP antibody sequestered on the surface of a novel multi-array plate. Again, the basal signal generated upon addition of a chemical substrate and electric stimulation, is quenched in a titrated manner during cAMP competition. The multi-array cAMP assay is fast, easy-to-run, accurate and require low amounts of samples. However, the high cost of the sophisticated carbon-electrode based plates which cannot be re-used make this assay relatively expensive compared to AlphaScreen.[39]

Other non-fluorescent-based cAMP immunoassay kits are available commercially. cAMP-Screen Direct® system (ThermoFisher) is also a highly sensitive immunoassay wherein alkaline phosphatase-cAMP conjugate (cAMP-AP) competes with endogenous cAMP for an anti-cAMP antibody. The assay measures a very stable chemiluminescence signal generated by CSPD® Substrate with the Sapphire-II™ Enhancer and is very convenient for ligand screening.[47,48] The Screen Quest™ Colorimetric ELISA cAMP assay kit from AAT Bioquest is an immunoassay which uses horseradish peroxidase (HRP)-labeled cAMP as a competitor to native cAMP and Amplite™ Red as a fluorogenic HRP substrate to quantify displaced HRP activity. This assay is cheaper than the AlphaScreen®, simple, accurate, HTS-compatible and measures absorbance hence avoiding sophisticated instrumentation.[49,50]

Furthermore, BD Act*One* cAMP assays utilizing the cyclic nucleotide-gated (CNG) Ca^{2+} channel which is opened by intracellular cAMP has been reported by BD Biosciences. The assay enables real-time kinetic and endpoint monitoring of cellular cAMP and has been validated for HTS. This assay coupled to Flashplate and FLIPR technology enables simultaneous characterization of G_s-, G_i- and G_q-coupled native and exogenous receptors.[51,52]

Enzyme Fragment complementation (EFC) cAMP assay systems from DiscoveRx/Eurofins (HitHunter ™) involve two fragments of the β-galactosidase enzyme, an enzyme donor (ED) fused to cAMP (ED-cAMP) and an acceptor (EA). Competition between EA-cAMP and cellular cAMP for the anti-cAMP antibody makes ED-cAMP available to complement fully with EA, generating the active β-galactosidase enzyme that hydrolyzes a substrate to generate chemiluminescence. The assay is fast, reproducible and has been validated for use in HTS. [53].

Promega (Madison, WI, USA) also introduced the GloSensor™ cAMP assay, a bioluminescence assay using a proprietary engineered construct of the *Photinus pyralis* luciferase. When bound to intracellular cAMP, a change in conformation of luciferase leads to bioluminescence. This assay enables a live-cell, non-lytic assay format wherein real-time cAMP kinetics can be measured.[54–56] The assay allows for detection of G_i-coupled GPCR ligands without pre-incubation with forskolin since it is very sensitive.[57]

Barak et al developed a BRET-based cAMP assay using an Epac-biosenser to screening ligands at the human Trace Amine-Associated Receptor 1 (TAAR1) and the dopaminergic D2 receptor (D2R). The substrate-dependent humanized *Renilla reniformis luciferase* Rluc and the acceptor

citrine (a yellow fluorescent protein variant) are fused to the Epac protein at the N- and C- termini respectively. When cAMP binds to Epac there is a conformational change that seperates donor from acceptor and yields a low BRET ratio compared to the basal. The BRET response is reversible, enabling both real-time cell imaging and kinetic measurements with high sensitivity even on low expressed native receptors.[58] This method is a modification of a previous FRET-based cAMP biosensor assays.[59,60]

1.4.3 **β-arrestin assays**

β-Arrestin activity is independent of which G-protein is coupled to the receptor making them a "universal" platform for ligand discovery. β-Arrestin assays have extensively been used to discover endogenous or surrogate ligands for orphan GPCRs (oGPCR) particularly when their second messengers are unknown.[61] The assays are of enormous importance to screen drugs at G_i-coupled GPCRs, which usually have narrow assay windows in functional assays.[9] Certain ligands are reported to selectively and independently modulate either β-arrestin or G-protein signaling pathways. β-Arrestin assays have therefore become relevant to screen for so-called functionally "biased ligands", potential drug candidates that efficiently treat diseases by interacting with desired pathways whilst avoiding unwanted side effects associated with other pathways.[16]

The Transfluor™ assay from Molecular Devices was the first β-arrestin based assay to be reported. This is a fluorescent-based imaging assay wherein a GFP-labelled β-arrestin is sequestered to the agonist-receptor complex. Monitoring and quantifying the redistribution of the β-arrestin-GFP and receptor complexes under high content imaging set-ups such as INCell Analyzer System (INCAS) allow HTS for small molecules.[62,63] The Transfluor assay is robust, sensitive and requires no extra dyes or substrates. Additionally, the assay allows real-time visualization and reveals different pharmacological profiles of compounds being devoid of masking by signal amplification. The Ligand Independent Translocation (LITe™) system is another proprietary assay from Molecular Devices used to complement the Transfluor technology particularly for screening at orphan GPCRs. The LITe™ assay is used before screening with Transfluor.™ The LITe™ assay uses a modified GRK2 isoform to verify the translocation of β-arrestin-GFP to receptors in the absence of agonist, which is observed with most orphan GPCRs, and to select cellular clones with homogenous response to β-arrestin-GFP translocation.[64]

The use of the BRET technology for β-arrestin assays demands tagging of β-arresin with an Rluc, and of the GPCR C-terminus with a fluorescent protein such as GFP or vice versa. Receptor activation recruits β-arrestin generating a BRET signal. This assay has a high background signal as circulating cytosolic β-arrestin can lead to signals in the absence of agonist activity hence limiting its use in HTS. Consequently, novel luciferase constructs (Rluc2 and Rluc8) were developed and the better BRET partners Rluc8/YPet and Rluc8/RGFP were discovered and validated in HTS.[65,66] BRET-based β-arrestin assays have been used to screen for novel GPCR ligands in HTS at chemokine receptor CCR5, β-adrenergic, neurokinin type 1 (NK-1), neuropeptide Y type 2 (NPY2) and TG1019 receptors.[67,68]

The β-arrestin protease-based reporter assay, Tango™ from Thermofischer/Invitrogen was validated and used in HTS to screen for ligands at various GPCRs.[69,70] β-arrestin is tagged with a tobacco etch virus (TEV) protease whilst the targeted GPCR is fused at its C-terminus with a GAl4-Vp16 chimeric protein. Upon agonist activation, the β-arrestin-TEV fusion protein is recruited to the GPCR. The Gal4 DNA-binding domain is cleaved off the GAl4-Vp16 complex by TEV protease inducing transcription of the β-lactamase reporter gene (*bla*) from the nucleus. Consequently, the β-lactamase cleaves the LiveBlAzer™ FRET substrates, modifying their FRET signals, which are then quantified. The assay could be multiplexed with other secondary messenger assays to measure ligand selectivity simultaneously. However, false hits from this assay result from compounds which interfere with TEV activity. The assay is time-consuming and also demands very expensive instrumentation and substrates.[69,71] To address such challenges, an easy, novel, improved and universal β-arrestin reporter assay was developed. It involves self-splicing activity of DnaE intein from *Nostoc punctiforme* upon binding of β-arrestin to the activated GPCR. Subsequently, the split reporter *Renilla* luciferase (Rluc) is reconstituted and generates bioluminescence. The assay is sensitive and allows non-invasive live imaging and automation for HTS.[72–74] The Trio, a novel fluorogenic GPCR reporter assay based on a tripartite GFP activation system has been developed. The tripartite complementation system involves the β-sheets β1-9, β10 and β11 of GFP. β11 is fused to the C-terminus of GPCR and β10 to the N-terminus of β-arrestin. Trio emits fluorescence only after β10 and β11 of activated GPCR/β-arrestin complements with β1-9 of GFP. This assay has little to no background signal compared to the Tango™ system. The assay was used to study β-arrestin recruitment, receptor internalization and other protein-protein

interactions. Although not yet demonstrated, the functional readout of Trio could be of immense usefulness in HTS.[75]

Arguably, the PathHunter™ enzyme fragment complementation (EFC) assay from DiscoveRx is the most used β-arrestin recruitment assay. In this assay, β-galactosidase (β-gal) is split into two inactive fragments. β-arrestin is tethered to the N-terminal deletion mutant of the larger β-gal fragment known as the enzyme acceptor (EA) and the GPCR tagged at the C-terminus with the smaller β-gal fragment (ProLink™ tag). Agonist-mediated β-arrestin recruitment to the GPCR enables complementation of EA and ProLink™ to form the active β-gal enzyme which produces substrate–dependent chemiluminescence. The measured chemiluminescence directly reflects ligand modulation of GPCR-β-arrestin activity. The PathHunter™ assay also allows multiplexing with other assays on the same cell-line.[47] This is a very convenient, fast, homogeneous and well validated HTS assay used for ligand discovery at more than a dozen receptors including orphan GPCRs such as GPR84 and GPR18.[76,77]

1.5 **The purinergic receptors**

The purinergic P2Y receptors (P2YRs) phylogenetically belong to the δ branch of the class A GPCRs (Figure 4) and are potential therapeutic targets for various human disorders such as cancer, inflammation and neuro-degenerative diseases.[78,79] They are widely distributed in the body and are subdivided into two groups, $P2Y_1$-like and $P2Y_{12}$-like receptor subtypes.[80,81]

The $P2Y_{12}$-like receptor family are G_i-coupled and comprises of $P2Y_{12}$, $P2Y_{13}$ and $P2Y_{14}$R. $P2Y_{12}$R and $P2Y_{13}$R are activated by ADP (**3**) and its chemically stable derivatives (but also ATP, **2**) whilst $P2Y_{14}$R is activated by UDP (**3**) and UDP-glucose (Figure 5). The $P2Y_{13}$R is a potential drug target for atherosclerosis, diabetes and pain management whilst the $P2Y_{14}$R may be relevant to treating neuropathic pain and diabetes. Very few ligands have been described for the $P2Y_{13}$R and the $P2Y_{14}$R.[82–84] The $P2Y_{12}$R is the most investigated P2YR subtypes. Its role in platelet aggregation and allodynia is well characterized. $P2Y_{12}$R antagonists such as ticagrelor, cangrelor, clopidrogel and prasugrel are approved drugs used as anti-coagulants. Tool compounds such as AZD1283 (**7**), PSB-0739 (**8**) and the radioligand [^{3}H]PSB-0413 are also available for further receptor studies. Moreover, recent co-crystallization of human $P2Y_{12}$R with the agonist 2MeSADP (**5**) and the

antagonist AZD1283 (**7**) at 2.6 Å and 2.5 Å resolutions respectively, has provided more insights into P2YR binding mechanisms.[84,85].

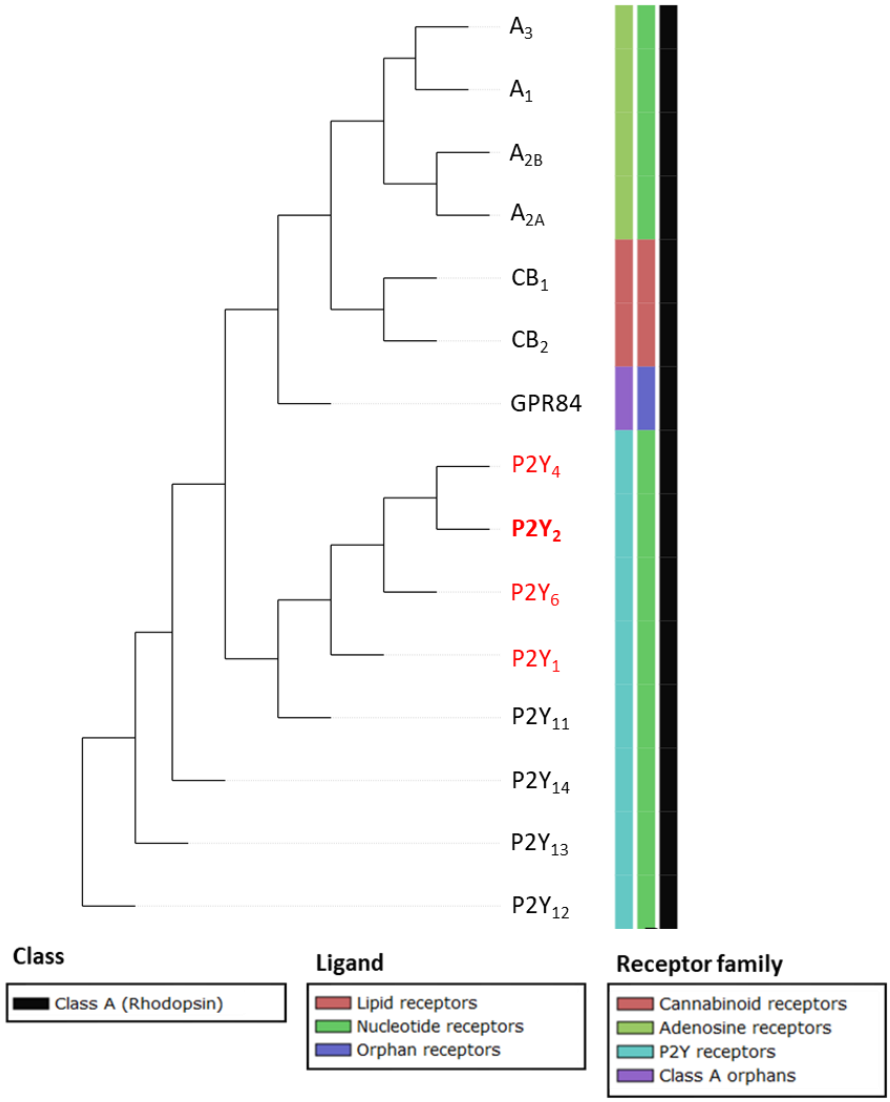

Figure 4: Phylogenetic tree of the human orthologs of some Class A GPCRs. Target receptors investigated are highlighted in red particularly $P2Y_2$ (in bold). Receptors highlighted in black are closely related P2Y receptors and P1 adenosine (A_1, A_{2A}, A_{2B} and A_3) receptors. Others such cannabinoid CB_1 and CB_2, and the orphan receptor GPR84 were utilized in ligand selectivity testing for this dissertation. The phylogenetic tree was designed with GPCRdb.org. [86,87]

The $P2Y_1$-like family consists of the $P2Y_1R$ activated by ADP (**3**), the $P2Y_2R$ activated by ATP (**2**) and UTP (**1**), the $P2Y_4R$ activated by UTP (**1**), the $P2Y_6R$ activated by UDP (**4**), and the $P2Y_{11}R$ by ATP (**2**). They are primarily G_q-coupled although some interact with other secondary tranducers

such G_i and G_s. Their therapeutic potential is summarized below (Table 1). As a focus of this dissertation, $P2Y_1R$, $P2Y_2R$, $P2Y_4R$ and $P2Y_6R$, together with a few of their important ligands will be briefly described here. Excellent reviews have recently been published on the uracil nucleotide-activated P2YR.[84,88] However, the $P2Y_2R$ will particularly be further elaborated since it is the main topic of this thesis.

Table 1: Overview and some therapeutic indications for ligands of the $P2Y_1$-like receptors.

Target	$P2Y_1R$	$P2Y_2R$	$P2Y_4R$	$P2Y_6R$
Transducer	$G_{q/11}$; $G_{i/o}$	$G_{q/11}$; $G_{i/o}$	$G_{q/11}$	$G_{q/11}$; $G_{12/13}$
Potential indications for agonists	Diabetes[89], Cancer[90], Osteoarthritis[91]	Cystic fibrosis[92], Dry eye disease[93], Chronic bronchitis[94], Antiviral agents[95], Alzheimer's[96], Myocardial infarction[97]	Cystic fibrosis[98], Alzheimer's disease[99]	Cystic fibrosis[100], Cancer[101], Hypertension[102], Glaucoma[103], Diabetes[104]
Potential indications for antagonists	Alzheimer's[105], Addiction[106], Atherosclerosis[107], Thrombosis[108], Inflammatory bowel syndrome[109]	Asthma[110], Cancer[111], Pain[112], Psoriasis[113], Inflammation[114], Atherosclerosis[115], Osteoporosis[116]	Gastrointestinal tract (GIT) disorders[117], Cancer[118]	Atherosclerosis[119], Cancer[120], Obesity[121], Pain[122], Osteoporosis[123]

1.5.1 **$P2Y_1$ receptor**

The $P2Y_1R$ is a potential therapeutic target for treating thrombosis, atherosclerosis and cancer. It is expressed in bodily tissues including pituitary, placenta, lung, macrophages, pancreas, liver, and kidney. Activation of $P2Y_1R$ with analogues of ADP and ATP (partial agonist) lead to increase in intracellular Ca^{2+} and decrease cAMP as it is both G_q- and G_i-coupled.[124] In 2015, the first $P2Y_1R$

X-ray crystal structure was reported. It was co-crystallized with two different antagonists: the nucleotide antagonist (1'*R*,2'*S*,4'*S*,5'*S*)-4-(2-Iodo-6-methylaminopurin-9-yl)-1-[(phosphato)methyl]-2-(phosphato)bicyclo[3.1.0]-hexane (MRS2500; **6**) and the non-nucleotide allosteric modulator 1-(2-(2-(*tert*-butyl)phenoxy)pyridin-3-yl)-3-(4-(trifuoromethoxy)phenyl)urea (BPTU, **9**) at 2.7 Å and 2.2 Å resolutions, respectively (Figure 5).[125]

1.5.2 **$P2Y_6$ receptor**

This receptor is both $G_{q/11}$- and $G_{12/13}$-coupled and found in various tissues.[126]–Agonists of interest include MRS2957 (**10**), PSB-0474 (**11**), and recently the glyceryl ester of prostaglandin E_2 (PGE_2-G, **12**) was reported to be the most specific and potent $P2Y_6R$ agonist so far (EC_{50} = 1 pM vs. 50 nM of the endogenous agonist UDP).[127–129] The antagonist MRS2578 (**13**) is a useful pharmacological tool for studying the $P2Y_6R$ (Figure 5).[130] Agonists of $P2Y_6R$ may be useful for treating cystic fibrosis as it induces bronchial epithelial chloride (Cl^-) exchange dependent on the cystic fibrosis transmembrane conductance regulator (CFTR)[131,132] $P2Y_6R$ is also a potential target for treating atherosclerosis, cardiac hypertrophy, asthma, obesity and breast cancer metastasis.[120,133,134]

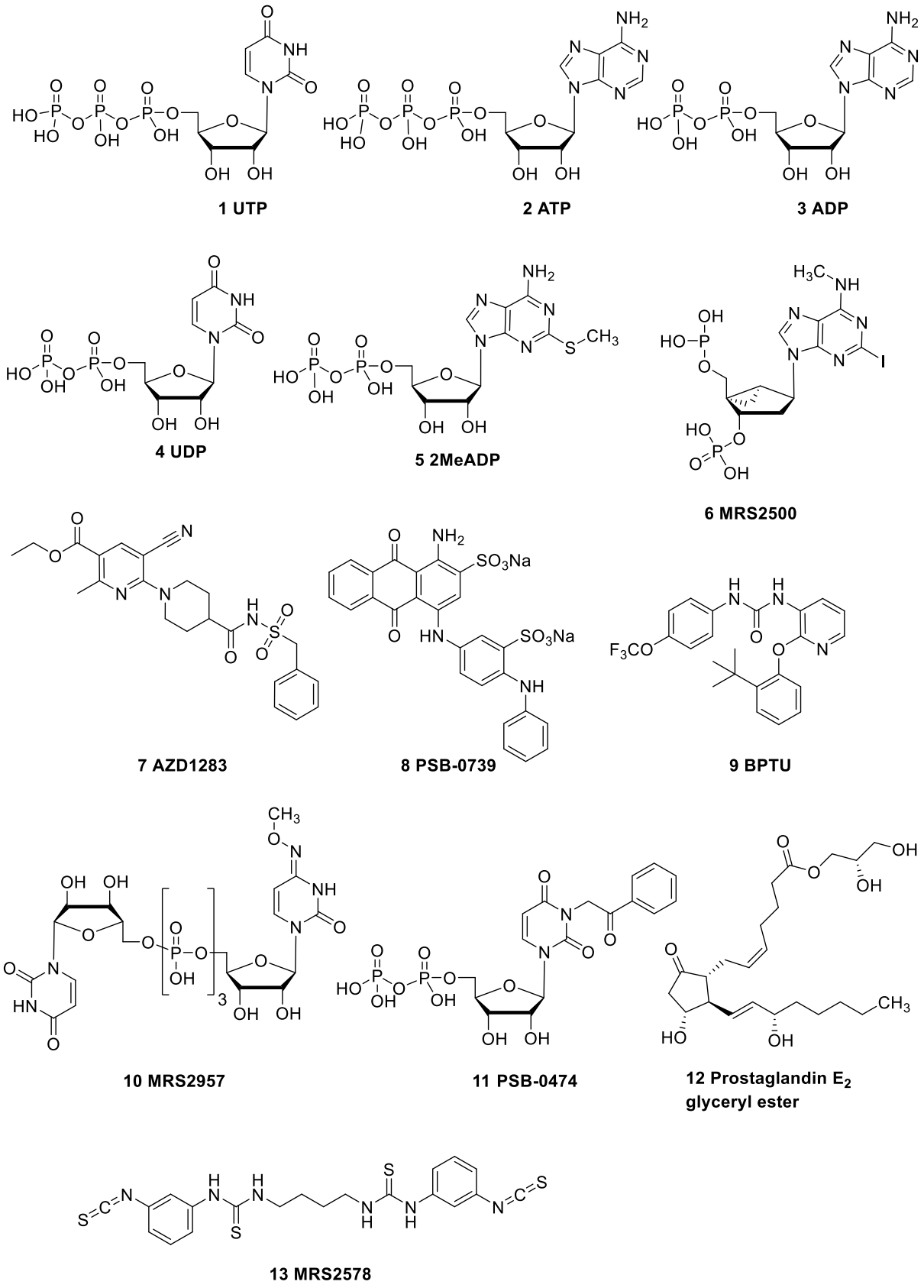

Figure 5: Selected P2YR ligands used as pharmacological tools.

1.5.3 **P2Y$_4$ receptor**

The G_q-coupled P2Y$_4$R can be found in the jejenum where it regulates chloride ion secretion, in colon, retina, adipose tissues and in the brain, where it mediates production and secretion of amyloid precursor proteins.[98,135–137] It is of primary interest as a target for the treatment of diseases such as diarrhea, cystic fibrosis and Alzheimer's disease.[84] The human P2Y$_4$ receptor is activated by UTP (**1**) and antagonized by ATP (**2**). ATP is however a full agonist in the rat P2Y$_4$ receptor. MRS4062, an N^4-phenylpropoxy-substituted of cytidine-5'-triphosphate, was reported to be a selective agonist (EC_{50} = 0.023μM) for the human P2Y$_4$ receptor with 28-fold and 38-fold selectivity, respectively, over the P2Y$_2$ and P2Y$_6$ receptors.[138] Recently, PSB-1633 (**15**), PSB-1635 (**16**) and PSB-1699 (**17**) have been described as potent anthraquinone-based antagonists. Compound **15** was the most selective one for the P2Y$_4$R compared to **16** and **17** (Figure 6). These antagonists were confirmed by functional data and docking studies on a new P2Y$_4$ homology model to be non-competitive inhibitors.[139]

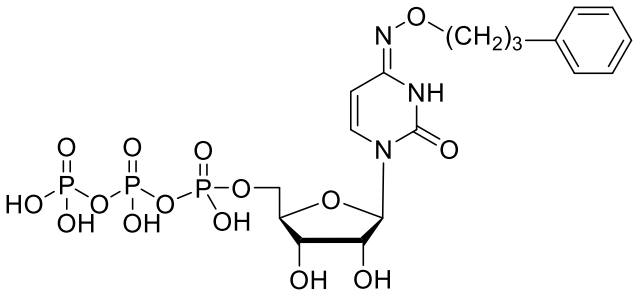

14 MRS4062

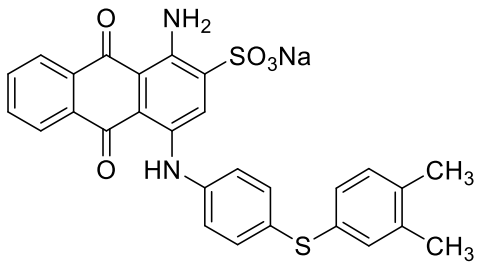

15 PSB-16133

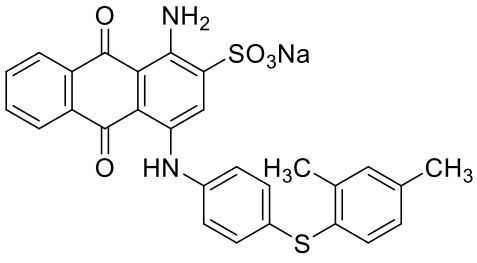

16 PSB-16135

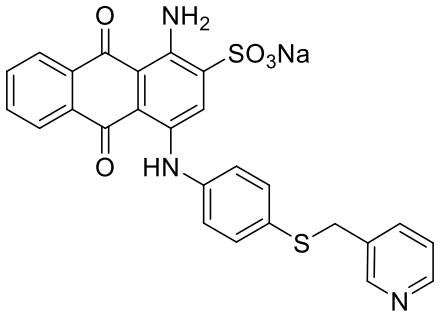

17 PSB-1699

Figure 6: Structures of selected ligands of the human P2Y$_4$R.

1.5.4 **$P2Y_2$ receptor**

This receptor bridges the pyrimidine ($P2Y_{2,4,6,14}$) and the purine ($P2Y_{1,\ 2,11\text{-}13}$) receptor subtypes since it is activated by both UTP (**1**) and ATP (**2**) (Figure 5) in equipotent amounts.[80,140] It is mainly G_q-coupled but there are also some reports of $G_{i/o}$ and $G_{12/13}$ coupling.[141,142] The $P2Y_2R$ is widely expressed on cells of the liver, skeletal muscle, heart, bone marrow, brain, spleen, lung and stomach. It is also expressed on the endothelium and on immune cells including macrophages, lymphocytes, T-cells, neutrophils and eosinophils, indicating its role in immuno-inflammatory processes.[126]

1.6 **Pathophysiological role and therapeutic potential of the $P2Y_2R$**

1.6.1 **Cancer**

A study on the highly metastatic breast cancer cell lines, MDA-MB-231 and SK-BR-3, indicates that compared to the wide-type, $P2Y_2$ knockdown abolished their invasiveness. This corresponds to a significant down-regulation in extracellular signal-regulated kinases (ERK) and protein kinase C (PKC) phosphorylation levels compared to controls. Hence it was postulated that $P2Y_2$ receptor mediated invasion of cancerous breast cells may involve over-activated ERK and PKC pathways.[143] Another knockdown study on the human prostate cancer cell lines 1E8, 2B4 and DU-145 reveals an association between loss of $P2Y_2R$ expression and significant suppression of EGFR and ERK1/2 phosphorylation. Furthermore, inactivation of EGFR and ERK1/2 prevented ATP-receptor-induced cancerous cell invasion. The nucleotide receptor $P2Y_2$ therefore functions together with EGFR through the ERK1/2 pathways to induce prostate cancer cell metastasis and invasion.[144] Further works by Xie *et al.* (2014) on cancerous human hepatocytes buttress the significant role of the $P2Y_2R$ in enhancing cancer metastasis.[145] The $P2Y_2R$ knockout mice also showed reduced ATP-dependent tumor cell metastastis from endothelial cells.[111] Antagonists of the $P2Y_2R$ are therefore needed as therapeutic agents to mitigate cancer.

1.6.2 **Dementia**

Alzheimer's disease (AD), a form of dementia, has been predicted to double by the year 2040. Different risk factors - age, lifestyle, genetics and environmental – are associated with the disease. A key feature of progression is the formation of β-amyloid (Aβ) plaques in the brain and subsequent localized neuronal death. Purinergic receptors investigated in AD disease models include $P2Y_{1,\ 2,}$

[4, 6, 14]. Primary microglial $P2Y_2$ receptor activation mediates phagocytosis and degradation of insoluble fibrillar β-amyloid ($fA\beta_{1-42}$) and oligomeric β-amyloid ($oA\beta_{1-42}$) aggregates.[146] Activation of the $P2Y_2$ receptor also mediates increased α-secretase-dependent non-amyloidogenic processing of APP and thus prevents formation of $A\beta$.[147] Immunoreactivity studies on post-mortem human AD brains associated reduced $P2Y_2$ receptor expression with increased neuropathology in AD.[148] Further knockout studies In the TgCRND8 mouse model expressing APP mutations correlates loss of the neuroprotective role of the $P2Y_2$ receptors with early progression of AD.[96] Potent and selective $P2Y_2$ agonists and antagonists are needed both as pharmacological tools for the studies of AD and subsequently as therapeutic agents.

1.6.3 **HIV and viral infections**

Upon interaction of $CD4^+$ T-cell and CXCR+ receptors on the HIV-1 target cell surface, the mechanosensitive pannexin channels on the HIV-1 target cells cause ATP to be released into the extracellular space. The released ATP through autocrine signaling acts on the $P2Y_2$ receptor to activate the proline-rich tyrosine kinase and causes a cell membrane depolarization. This subsequently leads to fusion of plasma membranes between the Env-expressing cell and the target cell and hence to cellular HIV infection and propagation.[149] $P2Y_2R$ antagonists may therefore be used as immunoprotective agents against HIV infection. Contrarily, agonists of the $P2Y_2R$ are proposed as antiviral agents to treat viral lung infection by regulating Th1 response. Additionally, it was observed that there were high morbidity and mortality rates and persistently high viral load in $P2Y_2$ knockout mice compared to control groups.[95]

1.6.4 **Mechanotransduction and cross-talk**

The $P2Y_2R$ is involved in a unidirectional cross-talk with the formyl peptide receptors (FPRs) on neutrophils. ATP activation of $P2Y_2$ receptors reactivates NADPH-oxidase in FPR subtype-1-desensitized neutrophils ($FPR1_{des}$neutrophils) to produce superoxide. This cross-talk is ATP dose-dependent and was blocked by the $P2Y_2$-selective antagonist AR-C118925 as well as the FPR1-specific antagonist cyclosporine H. The cross-talk does not trigger a transient rise in cytosolic Ca^{2+} concentration.[150] Gabl et al. (2015) performed functional selectivity studies on neutrophils and proposed a new signaling pathway for the ATP-bound $P2Y_2R$ in the presence of latrunculin A, a cytosolic actin-disrupting agent. The cytoskeleton inhibits access of activated $P2Y_2R$ to NADPH-

oxidase and when disrupted by latrunculin A, this results in $P2Y_2R$ mediated superoxide production similar to that by agonist-bound FPR1. This signaling pathway occurred parallel to the G-protein mediated $[Ca^{2+}]_i$ increase. The superoxide production is rapidly turned off through non-cytoskeleton dependent desensitization of $P2Y_2R$ and is not reactivated.[151]

Wang et al. also report that the $P2Y_2R$ and G_q/G_{11} proteins mediate fluid shear stress-induced endothelial responses in human and bovine endothelial cells. This *in vitro* response includes transient increase in cytosolic $[Ca^{2+}]_i$ in endothelial cells, activation of Ca^{2+}/calmodulin-dependent endothelial nitric oxide synthase (eNOS), and tyrosinse phosphorylation of SRC kinases PECAM-1 and VEGFR-2. Physiological investigations on pre-contracted mesenteric arteries from the endothelium-specific $P2Y_2$-deficient mice let to the conclusions that $P2Y_2$ controls both vascular tone, blood pressure and eNOS activity.[152]

A recent study associates the role of the $P2Y_2R$ with another G_q-coupled receptor, the B2 bradykinin (BK) receptor (B2R). Measuring $[Ca^{2+}]_i$, the response of $P2Y_2R$ to ATP, in CHO-K1 cells transiently expressing B2R, was significantly reduced after desensitization of the B2R with BK or B2R internalization-inducing glycans. Further fluorescence resonance energy transfer (FRET) analysis on AcGFP-fused $P2Y_2R$ and B2R-DsRed co-transfected in live HEK293 cells, detected a close relationship of the two receptors. Furthermore, from β-galactosidase complementation assays, the B2R and $P2Y_2R$ were each shown to cross-talk, bein co-activated, co-desensitized and co-internalized, by BK and ATP.[153]

Altogether, these reports underpin the role of the $P2Y_2R$ in the release of nitric oxide, regulation of vascular tone and control of hypertension. $P2Y_2$ receptor agonists have also been reported to yield cardio-protective effects against hypoxia and myocardial infarction, respectively, in cultured rat cardiomyocytes and, in mice *in vivo*.[97,154]

1.6.5 **Cystic Fibrosis, chronic bronchitis and asthma**

The $P2Y_2R$ mediates over 85-95 % of nucleotide stimulated chloride secretion in the trachea.[155] In cystic fibrosis (CF), where there is an impaired bronchial chloride transport, stimulation of $P2Y_2$ receptor by agonists can activate alternate chloride channels to improve mucociliary clearance and treat symptoms. Novel drugs are being developed in this direction for treating CF, chronic bronchitis and chronic obstructive pulmonary disease (COPD). [92,94] Studies using knockout mice,

real-time PCR and migration assays reveal asthmatic conditions could also be treated with $P2Y_2R$ antagonists, which decreased the recruitment of human monocyte-derived dendritic cells, eosinophils and other inflammatory cells in allergic lung inflammation.[95,110]

1.7 $P2Y_2R$ agonists

UTP (**1**) and ATP (**2**) are the endogenous agonists for the $P2Y_2R$. They are equipotent at activating the receptor except at the human subtype where UTP is slightly more potent.[140] The disparity might be due to faster hydrolysis of ATP by ectonucleotidases, compared to UTP. The receptors are more selective for the nucleoside triphosphates over the diphosphates while the monophosphates show no activity. However, a derivative of uridine monophosphate (UMP) with 2-phenethylthio substitution, **18**, (EC_{50} = 1.32 μM, Figure 7) was potent and had >100-fold selectivity at the $hP2Y_2R$ relative to $P2Y_4$ and $P2Y_6$ receptors. A derivative of uridine diphosphate (UDP), 2-amino-UDP (**21**) also yielded >100 selectivity at the $hP2Y_2R$ (EC_{50} = 0.604 μM) versus $P2Y_4$ and $P2Y_6$ (Figure 7).[156]

Reviewing various derivatives or analogues of UTP and ATP synthesized as $P2Y_2$ agonists, modifications of the phosphate chain at the α,β- and the β,γ- oxygen bridge with groups such as NH, CF_2 and CH_2 generally yielded products that are far less potent than ATP and UTP.[80] Derivatives from modifications to both the base and the ribose moiety were relatively more potent. 4-Thio-β,γ-difluoromethylene-UTP (**19**), with an EC_{50} of 0.134 μM and >60-fold selectivity over $P2Y_4$ and $P2Y_6$, was the most potent among a series of UTP analogues studied at the $P2Y_2R$.[156] UTPγS (**22**) with an EC_{50} value of 0.240 μM, was equipotent as UTP at the $hP2Y_2R$ albeit more stable.[80,157] Other nucleotide agonists tested at the $P2Y_2R$ include MRS2768 (**24**) and MRS2698 (**28**) with EC_{50} values of 1.90 and 0.008 μM respectively (Figure 7). MRS2768 though less potent is relatively selective for the receptor and also chemically more stable than MRS2698.[79,158] MRS2768 protected the heart from ischemic damage both in in vitro and in vivo experiments.[154] MRS2698 is by far the most potent UTP analogues reported till date as $hP2Y_2R$ agonist and highly selective over $hP2Y_4R$. The phosphonate analogue of 5-aryl-UMP, SVP333 (**23**), has been reported as an allosteric agonist with 43 % E_{max} compared to UTP and with selectivity for $P2Y_2$.[159] The C-linked benzothiazole derivative **20** is twice as potent as UTP at the $P2Y_2R$ and relatively selective against $P2Y_{1,4,6}$ receptors (Figure 7).[79,160]

The tetraanionic forms of the nucleotide agonists including dinucleotides seems preferred at the $P2Y_2R$. Several dinucleotides have been synthesized with varying potency and stability. The dinucleotide diadenosine tetraphosphate (Ap_4A, **27**) contributes to carbachol-induced tear secretion through activation of retinal $P2Y_2Rs$.[161,162] Up_4U, known as diquafosol (EC_{50} = 0.100 µM, **25**) has been approved for the treatment of dry eye syndrome in Japan and South Korea [162,163] whilst 2'-desoxycytidine-5'-tetraphospho-5'-uridine (Ip_4U, denufosol, INS37217, **26**) failed in clinical trials as novel drug for cystic fibrosis. [164–167] Sakuma et al. published a weakly potent, selective non-nucleotide $P2Y_2R$ allosteric agonist (**29**) that attenuated cardiac hypertrophy in a dose-dependent manner.[168]

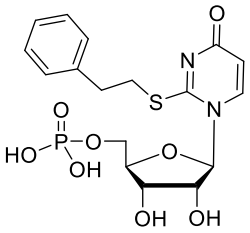

18 2-Phenethylthio-UMP

$hP2Y_2R$ EC_{50} = 1.32 μM[156]
$hP2Y_4R$ EC_{50} > 100 μM
$hP2Y_6R$ EC_{50} > 100 μM

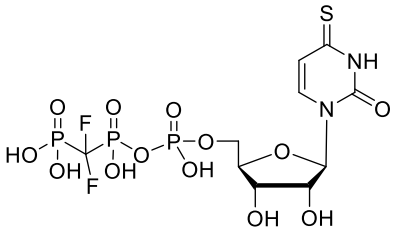

19 4-Thio-*ß,y*-difluoromethylene-UTP

$hP2Y_2R$ EC_{50} = 0.134 μM[156]
$hP2Y_4R$ EC_{50} = 9.30 μM
$hP2Y_6R$ EC_{50} = 7.00 μM

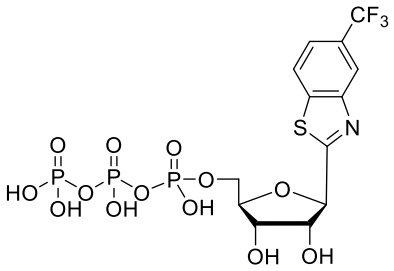

20 C-linked benzothiazole derivative of UTP

$hP2Y_2R$ EC_{50} = 0.003 μM[160]
[2x potent as UTP; (EC_{50} = 0.007 μM)]
$hP2Y_4R$ EC_{50} > 20.0 μM
$hP2Y_6R$ EC_{50} > 20.0 μM

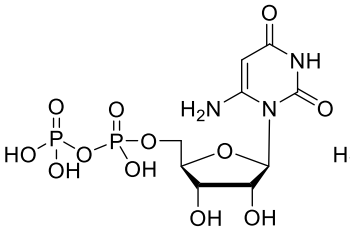

21 2-amino-UDP

$hP2Y_2R$ EC_{50} = 0.604 μM[156]
$hP2Y_4R$ EC_{50} > 100 μM
$hP2Y_6R$ EC_{50} > 100 μM

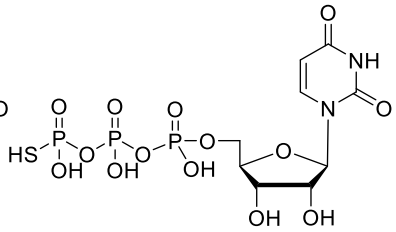

22 UTP*y*S

$hP2Y_2R$ EC_{50} = 0.240 μM[80,157]
[UTP EC_{50} = 0.0179 μM]
$hP2Y_4R$ EC_{50} = 1.60 μM
$hP2Y_6R$ EC_{50} = n.d.

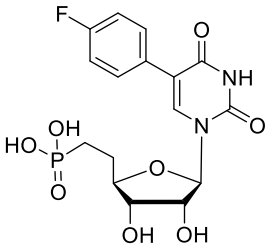

23 SVP333

$hP2Y_2R$ EC_{50} = 0.400 μM[159]
[UTP EC_{50} = 0.020 μM]
$hP2Y_4R$ EC_{50} > 100 μM
$hP2Y_6R$ EC_{50} > 100 μM

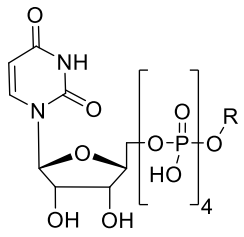

24 - 26

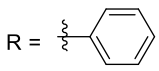

24 MRS 2768

$hP2Y_2R$ EC_{50} = 1.89 μM[158]
[UTP EC_{50} = 0.060 μM]
$hP2Y_4R$ EC_{50} > 10.0 μM
$hP2Y_6R$ EC_{50} > 10.0 μM

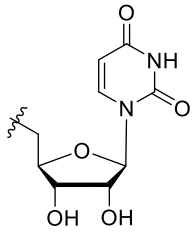

25 Up_4U

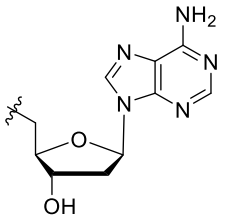

26 Ip_4U

$hP2Y_2R$ EC_{50} = 0.220 μM[162,164]
$hP2Y_4R$ EC_{50} = 0.800 μM
$hP2Y_6R$ EC_{50} > 100 μM

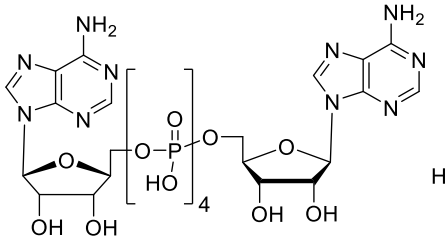

27 Ap_4A

$hP2Y_2R$ EC_{50} = 0.0540 μM[162]
$hP2Y_4R$ EC_{50} > 100.0 μM
$hP2Y_6R$ EC_{50} > 100.0 μM

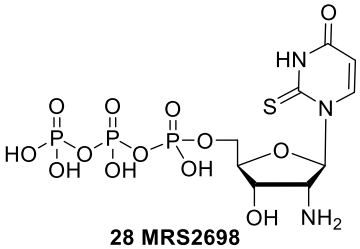

28 MRS2698

$hP2Y_2R$ EC_{50} = 0.008 μM[158]
[UTP EC_{50} = 0.049 μM]
$hP2Y_4R$ EC_{50} = 2.40 μM
$hP2Y_6R$ EC_{50} > 10.0 μM

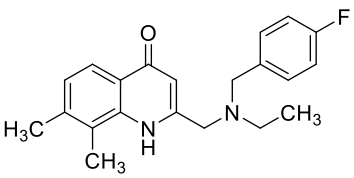

29 Sakuma et al. (2017)

$hP2Y_2R$ EC_{50} = 10.5 μM Emax = 66 %[168]
$hP2Y_4R$ EC_{50} > 30.0 μM
$hP2Y_6R$ EC_{50} > 30.0 μM

Figure 7: Structures of selected $P2Y_2$ receptor agonists.

1.8 **P2Y$_2$R antagonists**

The classical P2 antagonists, reactive blue 2 (RB-2, **30**) and suramin (**31**) are only moderately potent at the hP2Y$_2$R (Figure 8). Their promiscuity extends to interactions with other P2Y and P2X receptors, ectonucleotidases and kinases, limiting their therapeutic and pharmacological usefulness. [80,169,170] Analogues of uracil nucleotides with the ribose moiety replaced by acyclic groups, represented by compound **39**, were moderately potent at inhibiting P2Y$_2$R stimulation by UTP.[171]

β-Oxo-aurentiacin (**32**) and flavonoids such as heptamethoxyflavone (**33**), tangeretin (**34**) and kaempferol (**35**) have been investigated for their antagonism at the P2Y$_2$ receptor. These non-nucleotide antagonists showed varied potencies (IC_{50} values between 6 – 19 μM) at the mouse P2Y$_2$R analog but did not show selectivity.[80,172] They were found to be allosteric possessing higher potency than suramin and comparable to RB-2. Also, the potency of β-oxo-aurentiacin reveals that for flavonoid derivatives, the bicyclic benzopyranone ring system may not be necessary for P2Y$_2$ antagonism.[172]

Of a series of anthraquinone derivatives synthesized by copper(0)-catalyzed Ullmann coupling of bromaminic acid with anilines, PSB-716 (**36**) and PSB-09114 (**37**) were found to be of low micromolar potency, comparable to RB-2.[173–175]

AR-C-118925 (**38**), a thiouracil derivative, is relatively selective and potent as a competitive P2Y$_2$R antagonist with a better pharmacokinetic profile than the classical P2 antagonists.[176] Initial pre-clinical trials for treating psoriasis failed since it was less efficacious compared to the positive controls with no additional benefit over the placebo.[177] It was potent at the human P2Y$_2$ receptor but inactive at 37 other receptors at 10 μM. [176,178].

Most of the developed agonists and antagonists of the P2Y$_2$ receptor have low selectivity, potency and specificity. The nucleotide derivatives as agonists are metabolically unstable while the few antagonists are either weakly potent, have high molecular weights, display polyanionic structures or are unstable. These characteristics undermine that their use as research tools and their therapeutic properties are far from being ideal. Hence there is a great need for better hP2Y$_2$R modulators.

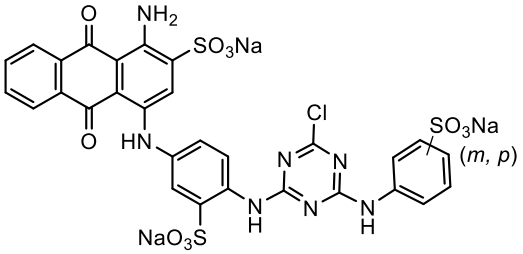

30 Reactive blue 2 (RB-2)

$hP2Y_2R$ IC_{50} = 1.85 µM[80,175]
$hP2Y_4R$ IC_{50} = 1.14 µM
$hP2Y_6R$ IC_{50} > 30.0 µM

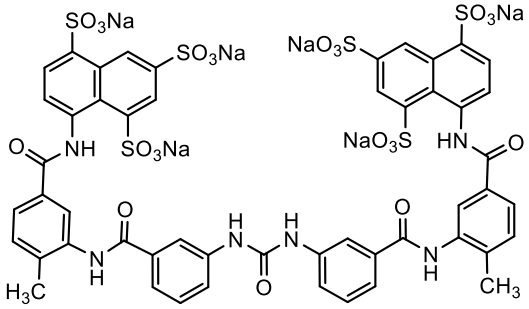

31 Suramin

$hP2Y_2R$ IC_{50} = 48.0 µM[169,170]
$hP2Y_4R$ IC_{50} > 300 µM
$hP2Y_6R$ IC_{50} > 100 µM

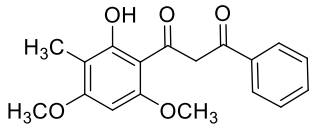

32 ß-Oxo-Aurentiacin

$mP2Y_2R$ IC_{50} = 19.0 µM[172]

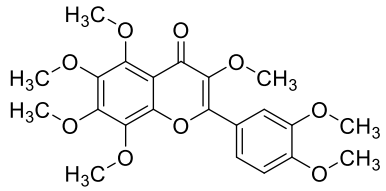

33 3,5,6,7,8,3',4'-Heptamethoxyflavone

$mP2Y_2R$ IC_{50} = 13.0 µM[172]

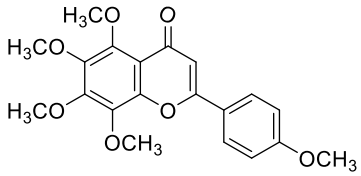

34 Tangeretin

$mP2Y_2R$ IC_{50} = 12.0 µM[172]

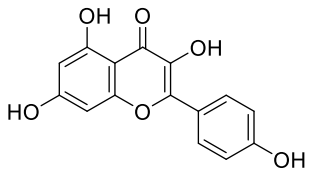

35 Kaempferol

$mP2Y_2R$ IC_{50} = 19.0 µM[172]

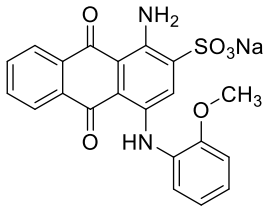

36 PSB-716

$hP2Y_2R$ IC_{50} = 9.82 µM[175]
$hP2Y_4R$ IC_{50} = n.d.
$hP2Y_6R$ IC_{50} = n.d.

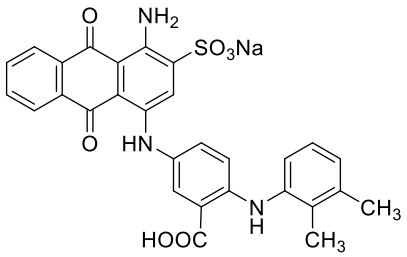

37 PSB-09114

$hP2Y_2R$ IC_{50} = 5.10 µM[175,183]
$hP2Y_4R$ IC_{50} = n.d.
$hP2Y_6R$ IC_{50} = n.d.

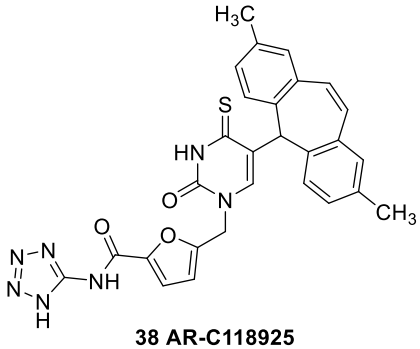

38 AR-C118925

$hP2Y_2R$ IC_{50} = 0.0574 µM[176,178]
$hP2Y_4R$ IC_{50} = 37.1 µM
$hP2Y_6R$ IC_{50} = 30.4 µM

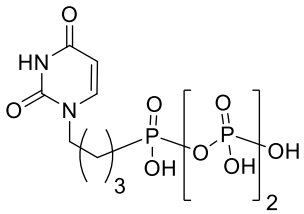

39 Uracil nucleotide with acyclic ribose

$hP2Y_2R$ IC_{50} = 92.0 µM[171]

Figure 8: Structures of selected $P2Y_2$ receptor antagonists

2 Aim of study

The P2Y receptors possess an enormous potential for treating a plethora of diseases. However only a handful of approved drugs on the market target such receptors. Efforts to develop drugs for these important GPCRs are hampered by the lack of well characterized ligands as either lead structures or pharmacological tools. This is partly due to their low potency and partly because most of the available P2Y ligands are derivatives of nucleotides and hence heavily charged and unstable.

In this study we focused on hit discovery and lead optimization. We sought to discover and develop novel non-nucleotide scaffolds as antagonists of the human $P2Y_1$-like receptor family, mainly focusing on the elusive $P2Y_2R$ subtype. It can be observed that some of the $P2Y_1$-like receptors share common therapeutic indications (see Table 1), although the intervening ligand functionality might be different. This indicates the need for developing specific and selective receptor ligands with drug-like properties. However, a second implication is the need to design multitarget (or multifunctional) ligands that combat a disease through more than one pathway. The advent and importance of such multitarget ligands or polypharmacology in the field of medicinal chemistry and pharmacology has long been proposed for diseases such as Alzheimer's and cancer.[179–182] Therefore it is also our ultimate goal to develop very potent selective or multifunctional ligands with suitable pharmacokinetic profile for the $P2Y_1$-like receptors.

To achieve our desired aims, we established and validated calcium and β-arrestin recruitment assays for in vitro high-throughput screening (HTS) of target-focused compound libraries from the Pharma-Zentrum Bonn. We plan to select and completely characterize promising hits and their mechanism of action. Hits found favorable would further be explored. Synthetic analogs of these hits would then be assessed by dose-response curves to ascertain their potencies by which a comprehensive structure-activity relationship study would be performed and a pharmacophore proposed.

The availability of X-ray crystallography structures of the $P2Y_1R$ and $P2Y_{12}R$ open up opportunities to study the P2Y receptor-ligand interactions. To this regard, homology models of other closely related P2Y could be constructed using the said crystal structures as templates. Such a homology model has been reported for the human $P2Y_2R$ and $P2Y_4Rs$.[183] Using the human $P2Y_2R$ homology model, we intend to carry-out computer aided in-silico (or virtual) screening of compound libraries available on-line thereby exploring a broader chemical space for potential

ligands. The hits from virtual screening would be tested in vitro at the $P2Y_2R$ vs. other $P2Y_1$-like receptors for potency, selectivity (or multifunctionality) and SAR analysis.

A homology model of the human $P2Y_4R$ that gives us insights of the binding pocket has also been published.[139] However, there has been no comparative analysis between the ligand binding sites of the $P2Y_2R$ and $P2Y_4Rs$ so far. Such a study would aid the rational design of selective lead compounds for each of these closely related P2Y receptors. Moreover, homology models need to be continually validated and updated for structural integrity. Accordingly, we sought to undertake site-directed mutagenesis studies based on insights from the $P2Y_2R$ and $P2Y_4R$ homology models. We will then investigated the functional impact of such mutated amino acids on some well-characterized agonists and antagonists of both receptors. It is expected that the results will enable further validation of the homology models, detailed description of the binding sites of the $P2Y_2$ and $P2Y_4Rs$, and their interactive differences with the selected ligands, and highlight factors to be considered in designing discriminative ligands.

3 Development of novel $P2Y_2$ receptor antagonists

3.1 Introduction

The $P2Y_2$ receptor ($P2Y_2R$) has become of immense importance due to its role in several physiopathological conditions such as cancer, Alzheimer's disease and inflammation. However, the available antagonists lack drug-like properties or are only moderately potent. Hence, there is an urgent need for novel scaffolds. To this end, we undertook high-throughput screening using functional assays and further developed the hit compounds.

3.2 Development of functional assays for screening

The use of functional assays instead of radioligand binding assays in high-throughput screening (HTS) for novel scaffolds has become commonplace in many laboratories. Radioligand binding assays have limitations such as high cost of the radioligand, safety concerns, challenges with radioactive waste disposal and bureaucratic regulations. Additionally, whereas radioligand binding assays could be used to identify and characterize agonists and antagonists as hit molecules, functional assays enable the detection and characterization of such hits into full, partial or inverse agonists and antagonists. Functional assays allow true ligand discrimination into positive, negative or silent allosteric receptor modulators. Moreover, a suitable radioligand for the $P2Y_2R$ is not available.

For the detection of antagonist hits and the development of lead compounds through HTS for the $P2Y_2R$, two different assays were established and validated. The first one was intracellular calcium mobilization using 1321N1 astrocytoma cells transfected with $P2Y_2R$. Briefly, the $P2Y_2R$ and the fluorescent mCherry protein cDNAs separated by an internal ribosome entry site (IRES) were transfected into the 1321N1 astrocytoma cells. Cells successfully expressing both proteins independently were selected by fluorescent-activated cell sorting (FACS) utilizing the fluorescence from the mCherry protein. Monoclonal cells with high receptor activity were then selected and cultured for the in vitro calcium assay.

The second functional assay, β-arrestin recruitment assay, was developed based on galactosidase enzyme complementation technology from DiscoverX®. This method involves two inactive fragments of the β-galactosidase (β-gal) enzyme. The larger fragment (enzyme acceptor; EA) with an N-terminal deletion is fused to β-arrestin while the smaller (deletion) fragment (Prolink; PK) is

fused to the GPCR. Upon receptor activation and recruitment of β-arrestin, there is complementation of both fragments resulting in an active β-galactosidase enzyme that cleaves an appropriate substrate to generate a chemiluminescent signal measured as the readout. The human $P2Y_2R$ cDNA was cloned into the pCMV-ProLink 1 (PK1) vector and transfected into a recombinant Chinese hamster ovary (CHO) cell line to perform $P2Y_2R$-induced β-arrestin recruitment assays.

3.3 **Validation of functional assay**

Both calcium and β-arrestin functional assays were validated with the agonists UTP (**1**), ATP (**2**) and Ap_4A (**27**), and the highly selective antagonist AR-C118925 (**38**). In calcium assays, compounds **1**, **2** and **27** yielded EC_{50} values of 0.0683 µM, 0.0845 µM and 0.0773 µM respectively (Table 2, Figure 9A), whilst by β-arrestin recruitment assays the EC_{50} values were 0.496 µM, 1.91 µM and 0.878 µM respectively (Figure 9B). Compared to calcium assay, β-arrestin yielded about 10-fold decrease in potency of **1** and **27** whilst **2** was 20-fold less potent. Ap_4A (**27**) was found to be a partial agonist relative to UTP and ATP in both assay systems. The high potency of agonists in the calcium assay over the β-arrestin assay after receptor activation may be attributed to non-equilibrium binding of ligands. Due to its potency in both assays and relative selectivity over the other agonists, UTP was selected as the endogenous agonist for screening antagonists at the $P2Y_2R$. Next, the assays were validated using the potent and selective $P2Y_2R$ antagonist AR-C118925 (**38)** as the gold standard. Antagonist **38** inhibited UTP activation of $P2Y_2R$ with an IC_{50} value of 0.0862 µM and 0.744 µM by calcium assay and β-arrestin assay respectively - correspondingly, there was approximately a 10-fold difference (Figure 9C and 9D). The ligand potencies obtained from the established assays were consistent with those from literature thus pharmacological validation was successful.[80,88] The dip of the inhibition curve for antagonist **38** below the baseline in Figure 9D may be due to blockade of intrinsic-receptor activity hence basal cellular β-arrestin activity. AR-C118925 (**38**) may therefore be an inverse agonist.

Table 2: Potencies of $P2Y_2R$ standard ligands during assay validation

Assay type	EC_{50}/IC_{50} values ± SEM (μM)			
	UTP (**1**)	ATP (**2**)[a]	Ap4A (**27**)[a]	AR-C118925 (**38**) [vs UTP as its EC_{80} value]
Calcium mobilization	0.0683 ± 0.0089	0.0845 ± 0.0165	0.0773 ± 0.0033	0.0862 ± 0.0116
β-arrestin recruitment	0.496 ± 0.025	1.91 ± 0.17	0.878 ± 0.061	0.744 ± 0.044 (K_B = 0.0452 μM)

[a] Efficacy of ligands were normalized to 100 μM UTP (**1**) concentration. [b] Final concentrations of 500 μM for calcium assay and 3 μM for β-arrestin assay.

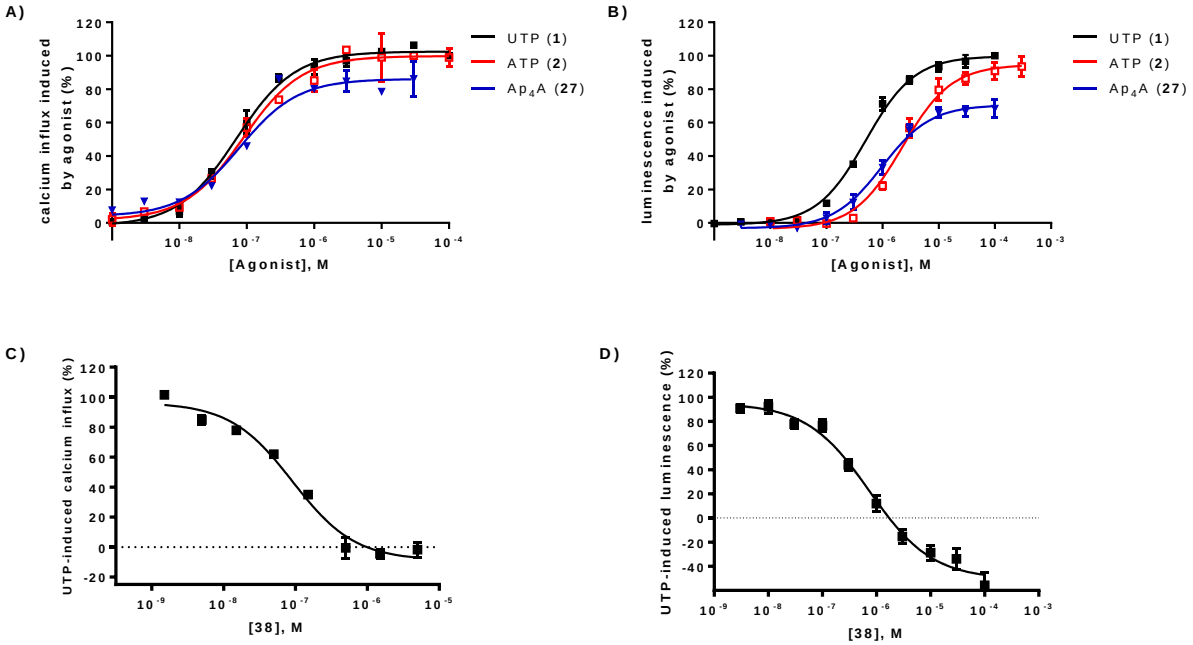

Figure 9: Dose-response curves from pharmacological assessment of $P2Y_2R$ agonists **1**, **2** and **27** and antagonist **38** by calcium mobilization assay (**A** and **C**) and β-arrestin recruitment assay (**B** and **D**) respectively. Each data point represents mean ± SEM of 3 – 4 independent experiments each in duplicate. Potencies (EC_{50} and IC_{50} values) are reported in Table 2.

AR-C118925 (**38**) was further validated as a competitive antagonist at the $P2Y_2R$ by β-arrestin assay using Schild curve analysis and plots (see Figure 10). Schild plot for AR-C118925 against UTP yielded a Schild slope of 0.897 with an R^2 value of 0.9631, $p > 0.05$. The Schild slope was not significantly different from unity. This implies AR-C118925 antagonizes β-arrestin recruitment to the $hP2Y_2R$ competitively. The affinity of AR-C118925, pA_2 was 7.345 and the dissociation constant at equilibrium with the receptor, K_B, was 0.0452 µM (see Table 2). Again, we observed inhibition of basal β-arrrestin activity at higher concentrations of the antagonist **38** (Figure 10A).

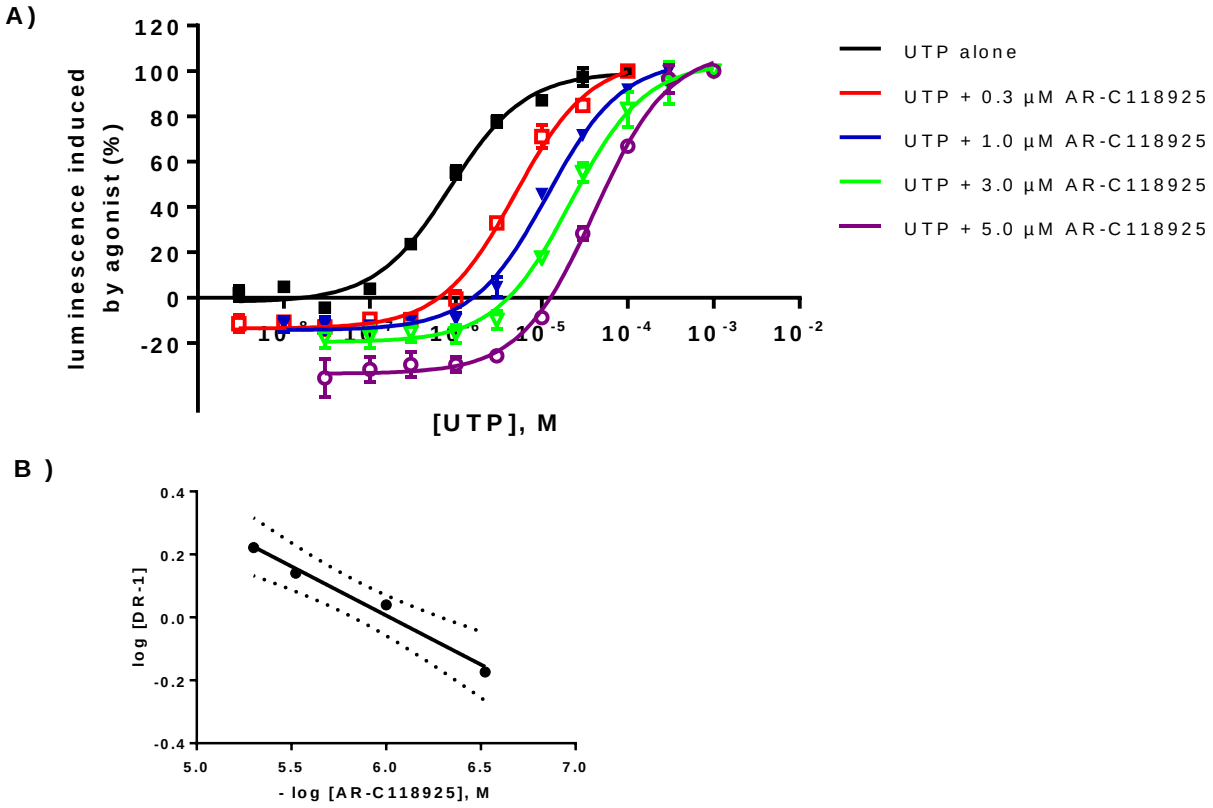

Figure 10: A) Schild analysis of UTP in the presence of various concentrations of the antagonist AR-C118925 at the $hP2Y_2$ as determined by β-arrestin asssays. **B)** Schild plot to determine the pA_2 of AR-C118925 at the $hP2Y_2$ receptor.

As the supposed test compounds for screening are dissolved in dimethyl sulfoxide (DMSO), we performed a DMSO compatibility test at the $P2Y_2R$ to detect the minimum concentration of DMSO that interferes with the assay response. For functional assays, it is recommended that the DMSO final concentration in assays should not exceed 1 % of total assay volume.[184] However, we observed

that at the $P2Y_2R$ expressed in 1321N21 astrocytoma cells, 1 % DMSO already elicits a significant response in calcium assays (Figure 11) but was well tolerated in β-arrestin recruitment assays (data not shown). Concentrations of test compound plates were therefore prepared such that the final screening concentration would yield a final DMSO concentration not exceeding 0.5 % in both assay systems.

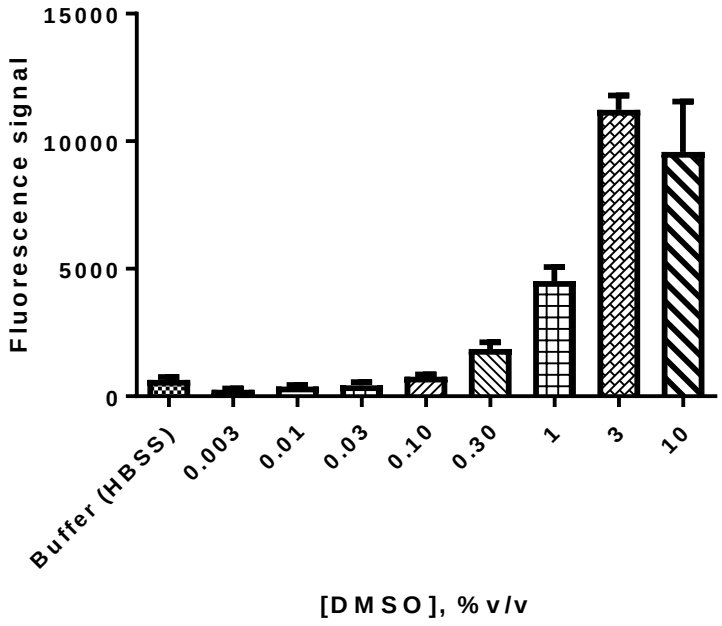

Figure 11: Bar graph showing increase in fluorescence signal in 1321N1 asstrocytoma cells transfected with the $P2Y_2R$ by DMSO. Final DMSO concentration in subsequent calcium assays for screening compound libraries was set at 0.5 % v/v.

3.4 **Quality control of HTS protocol**

The validated assays were used for screening compound libraries at the Pharma Zentrum Bonn for potential antagonist hits. Using a 96-well format, each plate from a compound library was screened twice. To assess the quality and robustness of the HTS system, we measured the signal window (or Z' factor) for each plate. As values for positive and negative controls for an assay vary from plate to plate, the Z'factor assesses the suitability of an assay window per plate for HTS using the following equation:

$$Z' = 1 - \left|\frac{3.\sigma_+ + 3.\sigma_-}{\mu_+ - \mu_-}\right| \qquad \textbf{Equation 1}$$

where μ_+ and μ_-, and σ_+ and σ_- represent the mean and standard deviation of both the positive (+) and the negative (-) assay controls.[185]

The average Z'- factors determined for all screening plates in calcium assay and β-arrestin assays were 0.531 and 0.614 respectively as represented below (Figure 12). Assays with Z'-factors between 0.5 and 1.0 are excellent, reliable and robust with sufficiently wide assay windows whilst values between 0 and 0.5 are considered relatively good.[185] β-arrestin assays had a better window than calcium assays due to a very stable signal and a low background noise.

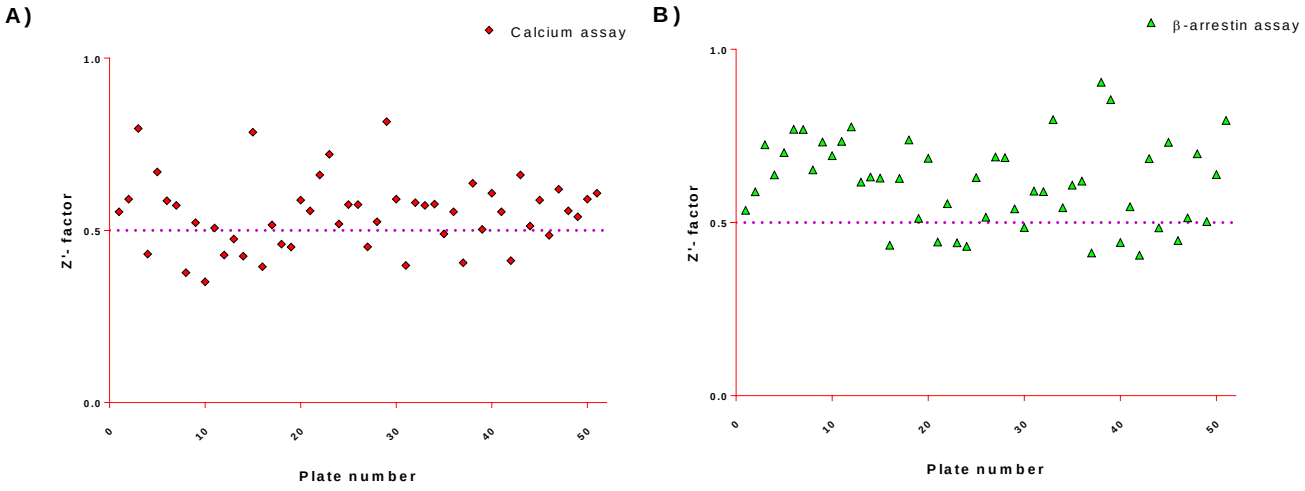

Figure 12: Representative scatter plot of Z'-factors for selected compound plates as determined by **A)** calcium assay (red squares) and **B)** β-arrestin recruitment assay (green triangles). Plates were selected from the nucleoside library.

Another metric used to check HTS robustness was to determine the degree of correlation between replicates for each well. Here, we found out that the correlation coefficient (r) was ≥ 0.9000 for all the plates measured indicating a high degree of reproducibility between plates and a high quality of the assays (represented in Figure 13).

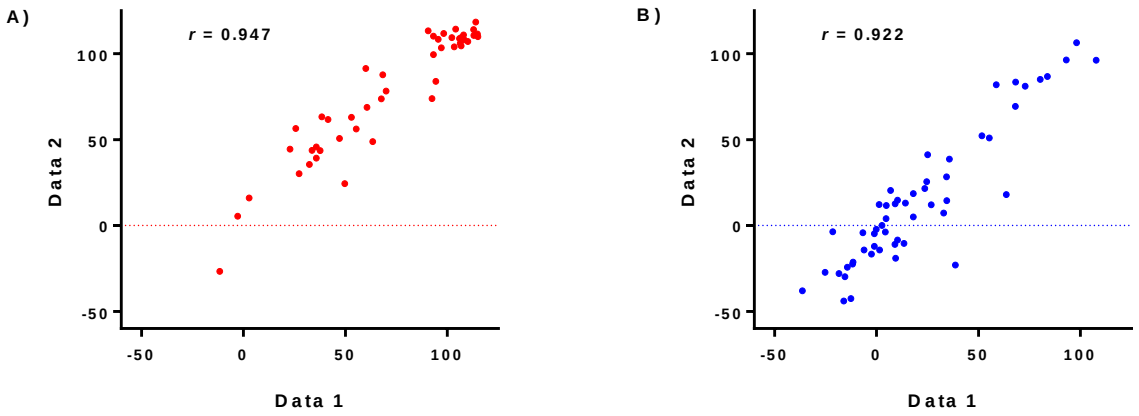

Figure 13: Representative data: correlation plots between replicates of the lipid-like compound library as determined by **A**) calcium assay and **B**) β-arrestin assay. Correlation coefficients, r, are 0.947 and 0.922 respectively in both assays.

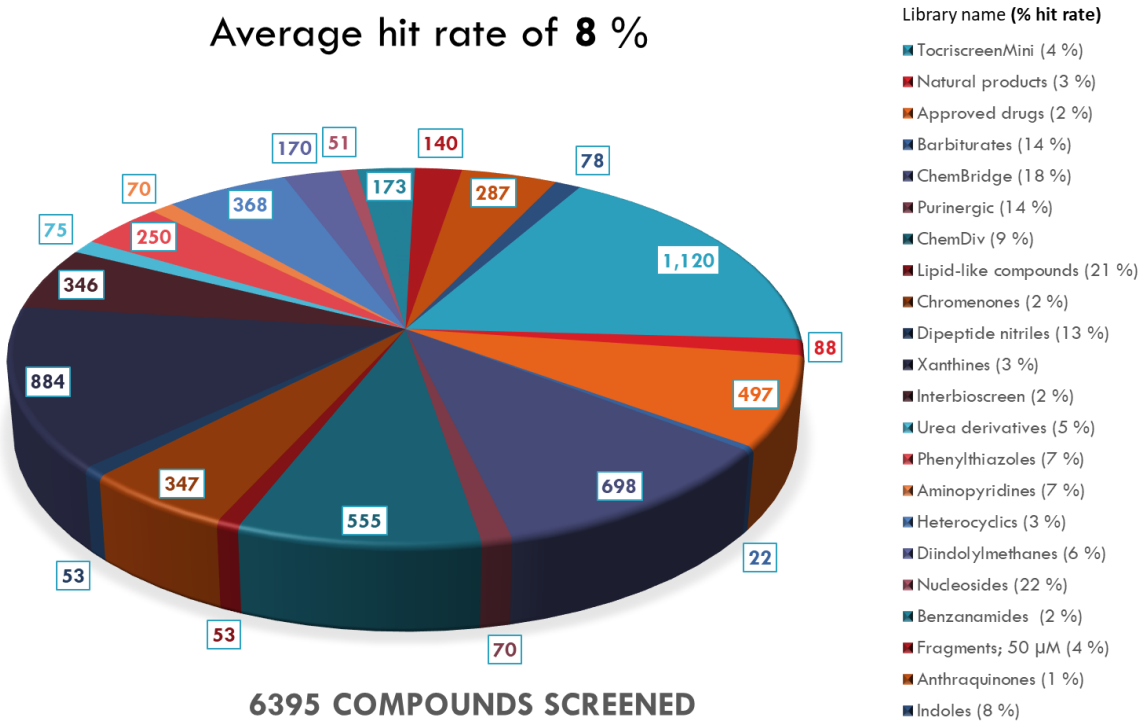

Figure 14: Summary of compound libraries screened as antagonists at the $P2Y_2R$ including their % hit rates from primary screening using the calcium assay. All compound libraries, except the fragment library, were screened at ≤ 10 µM.

In all, about 6400 compounds from 22 different sub-libraries were screened (Figure 14). Each compound library, except the fragment library, was screened at ≤ 10 µM for potential antagonistic activity. The fragment library was screened at 50 µM. The signal of the assay buffer in the absence of the agonist was normalized to 100 % whilst the UTP EC_{80} effect was normalized to 0 %. Compounds with ≥ 50 % inhibition were considered as hits (see Figure 15, approved drugs library). The average hit rate from primary screening using the calcium assay was 8 %.

From screening, we also observed that a lot of compounds showed < 0 % inhibition values (as shown with dashed red rectangle in Figure 15). These may be activators or positive allosteric modulators of the receptor or systemic artifacts of the assay used.

The use of a secondary assay to confirm activities of hit compounds from high throughput screening (HTS) has become very important primarily for eliminating artifacts. Additionally, it also facilitates detection of potential functional bias.[9] In the current work, β-arrestin recruitment assay was used to confirm (or otherwise) the activity of selected compounds in modulating the $hP2Y_2$ receptor-mediated release of intracellular calcium. Dose-response curves were plotted for the cherry-picked hits and their IC_{50} values were estimated. The most potent hits, with IC_{50} values of ≤ 10 µM among a cohort from each library were further characterized.

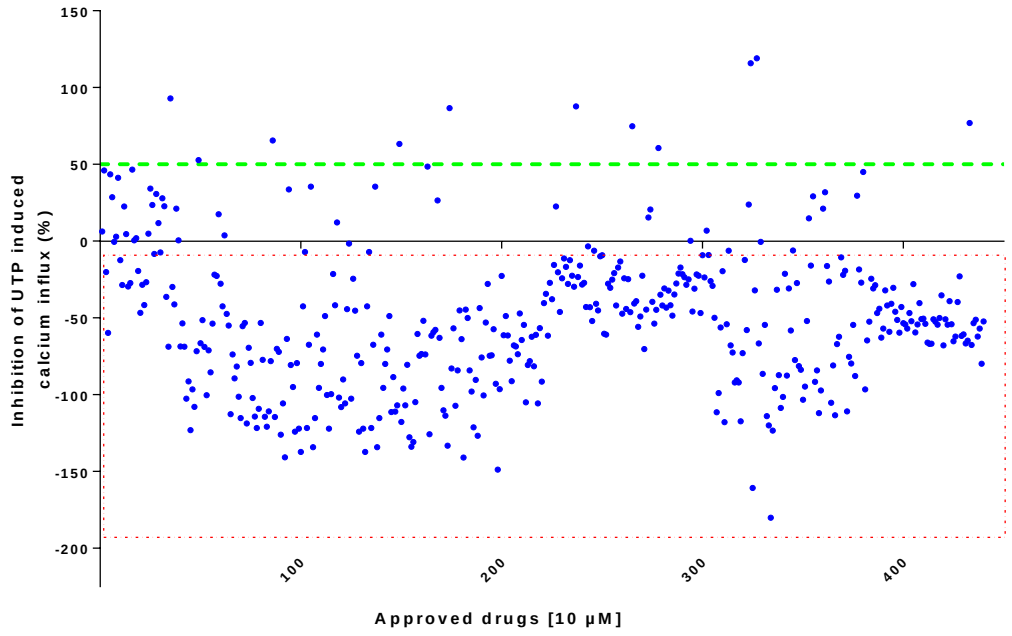

Figure 15: Representative graph: scatter plot of primary screening results from the Approved drugs library as determined by calcium assay. Each blue dot represents a compound. Hit compounds are above the 50 % inhibition threshold (broken green line). Percentage hit rate was 2 %. Compounds within dashed red rectangle may be receptor activators or positive allosteric modulators.

A cardinal step in screening for hit compounds is the elimination of false negatives and particularly false positives. This prevents the waste of resources and time in the drug development process. False positives may arise due to interference of the compounds with the assay or readout models, poor solubility (precipitation), aggregation of small molecules, nonspecific protein/hydrophobic binding, reactive functional groups, experimental errors or presence of impurities. The less troublesome false negatives could also arise in cases of lower compound concentration than expected, compound instability or experimental errors.[186] Triangulating visual inspection of compounds, their activities at other targets from literature (especially for commercial libraries as data for activity at other targets may be available), stability, ease of synthesis and the current activity from screening constitute efficient cherry-picking of hits for further characterization. Also, compounds which showed high background fluorescence during screening were also eliminated. Cherry-picking drastically increases the attrition rate of primary hits in the chain of development.

Diverse scaffolds were found as hits from different compound libraries showing antagonistic activity at the human $P2Y_2R$. These include urea derivatives, diindolylmethanes, xanthine derivatives and chromenones (see Figure 16). These scaffolds, some of which were further developed, are supposed to be either orthosteric or allosteric antagonists at the $P2Y_2R$.

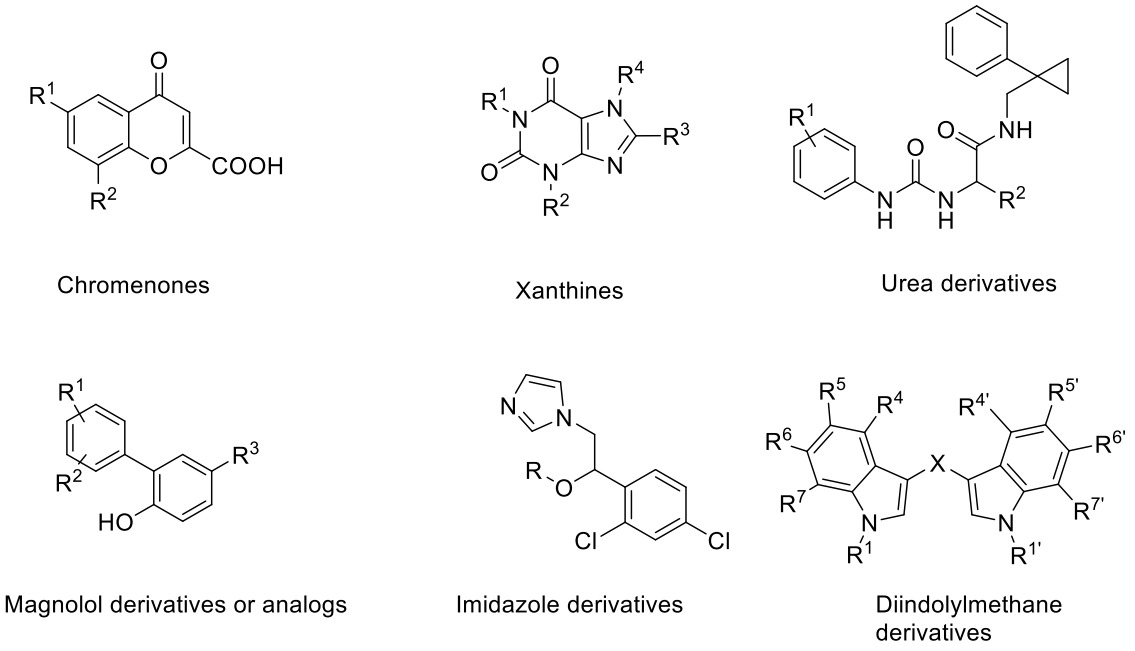

Figure 16: Structures of some interesting scaffolds identified as hits from screening compound libraries at the human $P2Y_2$ receptor.

3.5 **Hits from the approved drugs library**

The hit rate from this library was 2 %, the majority of which were imidazole antifungals (Table 3). The imidazoles were generally inactive in β-arrestin assays but moderately potent in calcium assays. Imidazole derivatives with substituted single aromatic rings (**40**, **41**, **42** and **43**) showed better potency compared to those with bicyclic rings (**44** and **45**). The derivatives **40** and **41**, with dihalophenyl substitutions were more potent than **42** which has a halophenyl moiety. Comparatively, it appears that the phenyl ring (**42**) is preferred for potency over a thiophenyl ring (**43**). There was also no difference in activity between miconazole (**40**) with *ortho,para*- and isoconazole (**41**) with *ortho,meta*- dichloro-substitution. Other derivatives such as ketoconazole (**46**), oxiconazole (**47**) and clotrimazole (**48**), without an ethoxy linkage between substituents and the imidazole moiety, were inactive in both assay. This indicates that the ethoxy group is important for activity and also, elongation of side chains as with **44**, **45** and **46** diminishes activity. Although these small molecules appear to have a definite initial structure-activity relationship (SAR) and could be suitable for further development into lead compound, they face some limitations. The imidazoles are broad spectrum antifungals known to inhibit the ergosterol synthesis in fungal cell membrane and to also inhibit human cytochrome P450.[187] It is no surprise then that most of them are used as topical agents.[188] These compounds have been generally found to be promiscuous showing interaction with β-lactamases, chymotrypsin and malate dehydrogenase. They have been found to be active inhibitors of various receptor targets in our group with about similar potencies (data not shown). Their false positivity has been attributed to aggregation mechanisms in assays.[189] Their non-selectivity makes them non-ideal candidates for further development into $P2Y_2R$ antagonists. Interestingly, none of the triazole antifungal derivatives such as fluconazole and itraconazole were found to be active in the screening.

Table 3: Potencies of hits from the Approved drugs library as antagonists of the human $P2Y_2R$.[a]

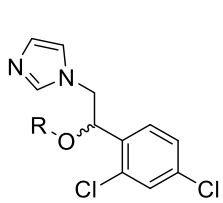

Imidazole derivatives (**40 - 44**)

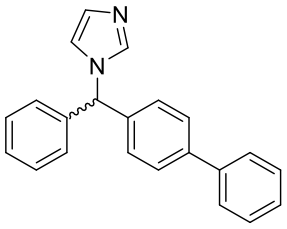

45 Bifonazole

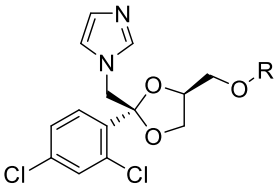

46 (±) Ketoconazole

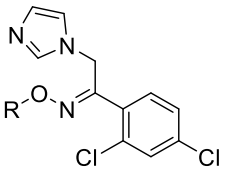

47 Oxiconazole

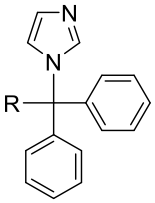

48 Clotrimazole

No.	Cpd name	R	IC_{50} ± S.E.M (µM), n = 3-4 (% inhibition at 10 µM)	
			β-arrestin assay	Calcium assay
40	Miconazole	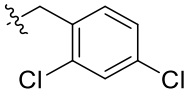	>10 (- 7 %)	**5.37** ± 0.70
41	Isoconazole	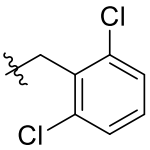	>10 (- 21 %)	**5.85** ± 0.89
42	Econazole	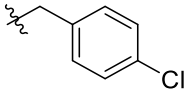	>10 (25 %)	**6.11** ± 1.11
43	Tioconazole	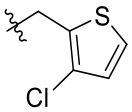	>10 (21 %)	**9.53** ± 0.69
44	Sertaconazole	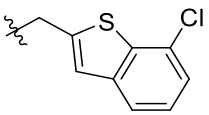	>10 (- 15 %)	**26.7** ± 17.1
45	Bifonazole	See structure above	>10 (- 11 %)	**13.1** ± 3.5
46	(±) Ketoconazole	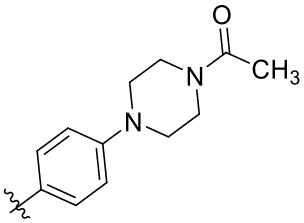	>10 (3 %)	>10 (- 80 %)

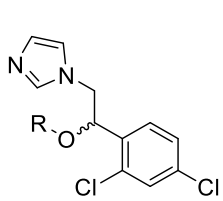

Imidazole derivatives (**40 - 44**)

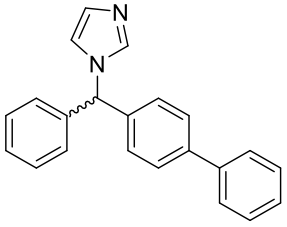

45 Bifonazole

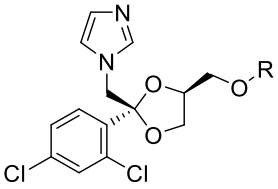

46 (±) Ketoconazole

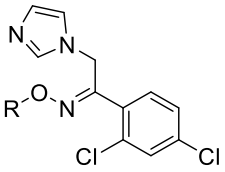

47 Oxiconazole

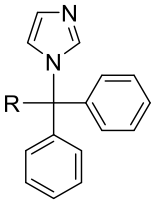

48 Clotrimazole

No.	Cpd name	R	IC_{50} ± S.E.M (μM), n = 3-4 (% inhibition at 10 μM)	
			β-arrestin assay	Calcium assay
47	Oxiconazole	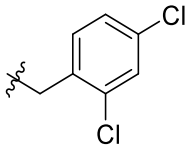	>10 (12 %)	>10 (-28 %)
48	Clotrimazole	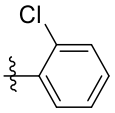	>10 (0 %)	>10 (24 %)

[a] All data values was normalized against UTP EC_{80} values; represents results from 3-4 independent dose-response experiments with each data point in duplicate.

Other hits from the approved drugs library were Digitonine (**49**), β-Escin (**50**) and Carvedilol (**51**) (see Figure 17). Digitonine (**49**) and β-Escin (**50**) are both saponins that act as detergents. The former is a glycosidic cholesterol-binding saponin, known to modify cell membrane permeability[190] whilst the latter is a triterpenoid known as a signal transducer and activator of transcription 3 (STAT3) inhibitor and as an antitumor agent.[191,192] Despite their significant potency (in the low micromolar range) in both calcium and β-arrestin assays, their varied biochemical and pharmacological effects rules them out as selective drug candidates. In contrast, Carvedilol (**51**), a non-selective β-adrenergic blocker used clinically for treating congestive heart failure and an inhibitor of multidrug resistance protein-1 (MDR1)[193] is a plausible candidate for developing $P2Y_2R$ receptor antagonists. Compound **51** was about 12-fold more potent in blocking the UTP-$P2Y_2R$ activation in calcium assays (IC_{50} = 10.4 μM) than in β-arrestin assays (IC_{50} = 129 μM). This is consistent with the fold-shift of the standard, AR-C118925 (**38)** in both assays. Compound

51 is also the only hit among the β-adrenergic receptor blockers of the approved drug library to antagonize UTP activity at the $P2Y_2R$.

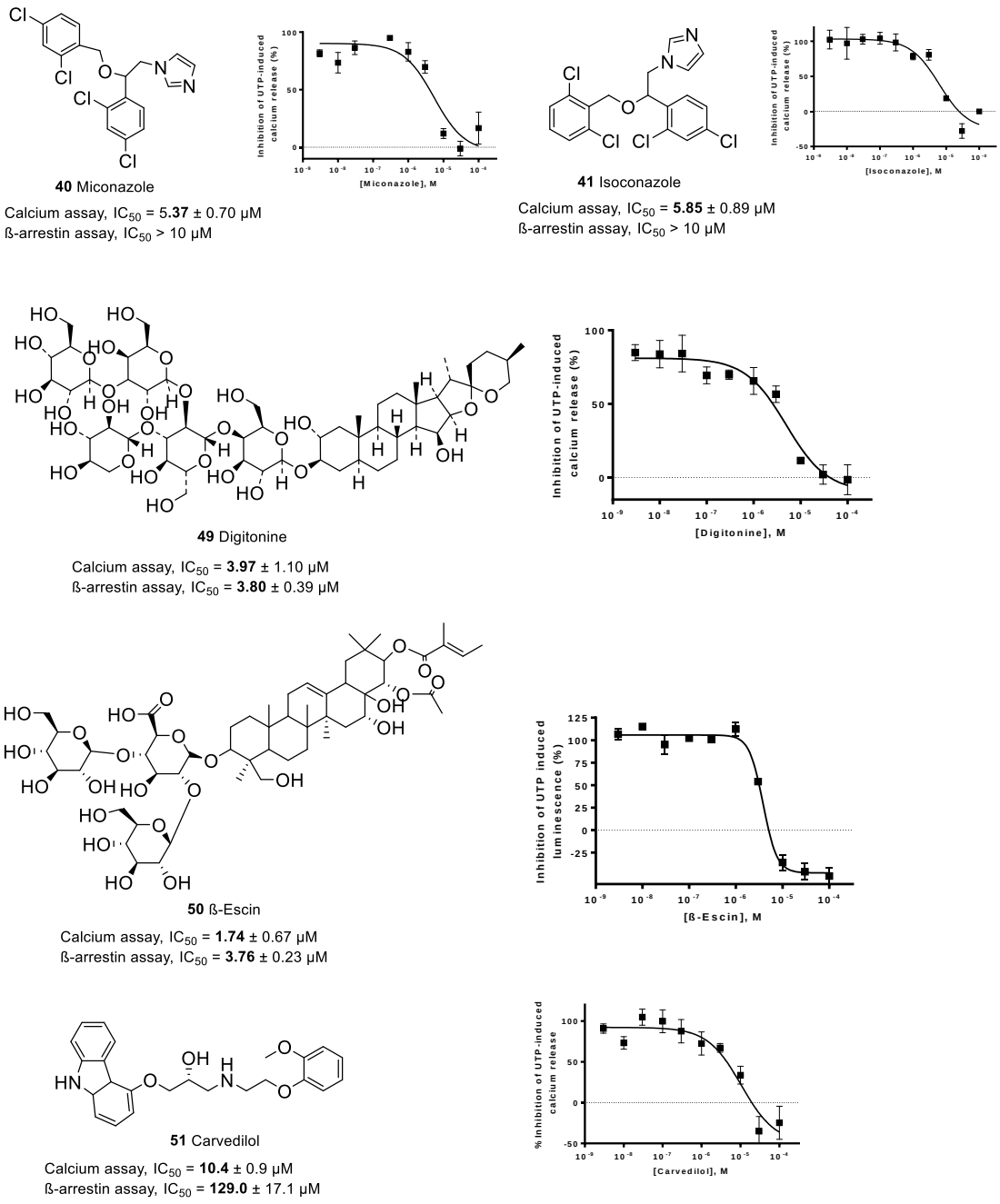

Figure 17: Structures and dose-response curves for some hits from the approved drug library at the $hP2Y_2R$. Logarithmic dose-response curves represent an average of 3-4 independent experiments with each data point in duplicates.

3.6 **Urea derivatives**

The compounds in this library are chiral and were synthesized by the group of Prof. Marcello Leopoldo. These compounds have previously been reported as *N*-formyl peptide receptor 2 (FPR2) agonists which displayed microsomal stability, neuroprotective effects and in vitro blood-brain barrier permeability.[194] They were screened in β-arrestin assays at 5 µM for potential antagonistic and agonistic activity at the $P2Y_2R$. Compounds which were hits in the antagonist screen were expected to yield little to no activation in agonist screening and vice versa. The test compounds were mostly inactive as agonists. Compound **93** yielded the highest activation (16 %) and correspondingly, no inhibition validating the fore-mentioned assertion (see Table 4).

In contrast, the urea library was active as potential antagonists of the human $P2Y_2R$ with a hit rate of 5 %. Dose-response curves were performed for the hit compounds **76**, **84**, **85** and **90**. Compound **84**, the *R*-enantiomer was the most potent (IC_{50} = 1.31 µM) among the current series. The *S*-enantiomer of **84** was unavailable hence not tested. Compounds **90**, **76** and **85** followed closely with IC_{50} values of 2.15 µM, 9.17 µM and 24.1 µM respectively. The results are summarized in Table 4.

Table 4: Antagonistic or agonistic activity of the urea derivatives screened at the human $P2Y_2R$ by β-arrestin assay.[a]

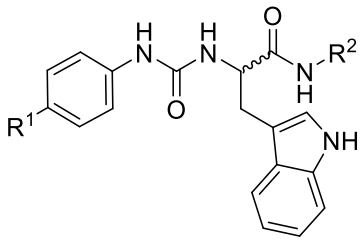

Scaffold A
(52 - 60)

No.	Name	R^1	R^2	**Antagonistic activity** IC_{50} ± SEM (% inhibition at 5 µM)	**Agonistic activity** EC_{50} ± SEM (% activation at 5 µM)
52	CLP-13 R-enantiomer	NO_2	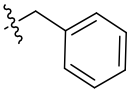	>10 (24 %)	>10 (-15 %)
53	CLP14 R-enantiomer	NO_2	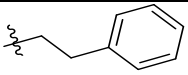	>10 (13 %)	>10 (2 %)

54	CLP-17 R-enantiomer	NO_2		>10 (7 %)	>10 (-28 %)
55	EMY-124 S-enantiomer	NO_2	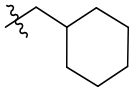	>10 (32 %)	>10 (-13 %)
56	CLP-15 R-enantiomer	NO_2	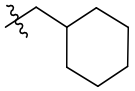	≈ 10 (49 %)	>10 (-11 %)
57	CLP-16 R-enantiomer	NO_2	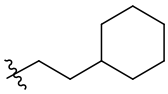	>10 (26 %)	>10 (-15 %)
58	CLP-18 R-enantiomer	NO_2	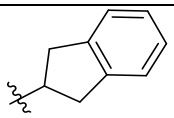	>10 (43 %)	>10 (-20 %)
59	EMY-87 R-enantiomer	NO_2	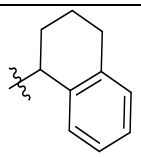	≈ 10 (48 %)	>10 (-29 %)
60	ML-8 S-enantiomer	NO_2	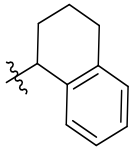	≥ 10 (41 %)	>10 (-20 %)
			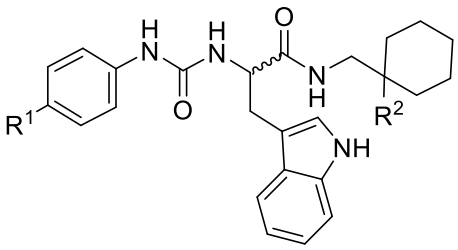 **Scaffold B (61 - 78)**		
61	AM-25 R-enantiomer	OCH_3	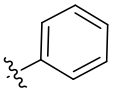	>10 (17 %)	>10 (-9 %)
62	AM-26 S-enantiomer	OCH_3	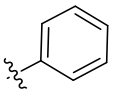	>10 (29 %)	>10 (-3 %)
63	ST-11 S-enantiomer	NO_2	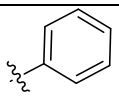	>10 (31 %)	>10 (-8 %)
64	AM-13 R-enantiomer	OCH_3	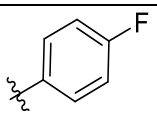	>10 (33 %)	>10 (-19 %)
65	AM-14 S-enantiomer	OCH_3	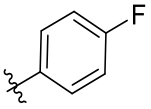	>10 (34 %)	>10 (-18 %)

66	ML-18 S-enantiomer	NO_2	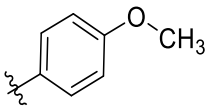	>10 (37 %)	>10 (-20 %)
67	EMY-98 R-enantiomer	NO_2	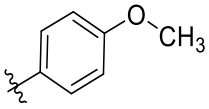	≥10 (45 %)	>10 (-24 %)
68	ML-16 S-enantiomer	NO_2	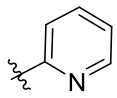	≥10 (47 %)	>10 (-9 %)
69	AM-29 R-enantiomer	OCH_3	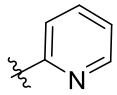	>10 (12 %)	>10 (10 %)
70	AM-34 S-enantiomer	OCH_3	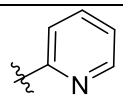	>10 (17 %)	>10 (-24 %)
71	AM-37 R-enantiomer	OCH_3	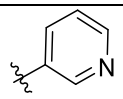	>10 (23 %)	>10 (12 %)
72	ST36 S-enantiomer	OCH_3	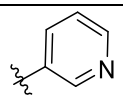	>10 (-6 %)	>10 (-5 %)
73	ST-13 S-enantiomer	CF_3	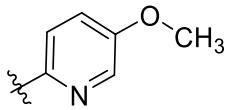	>10 (35 %)	>10 (-7 %)
74	ST-15 S-enantiomer	Br	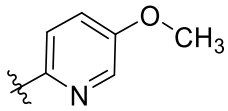	>10 (30 %)	>10 (12 %)
75	ST-16 S-enantiomer	CH_3	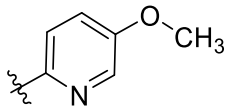	>10 (32 %)	>10 (-4 %)
76	ST-6 R-enantiomer	NO_2	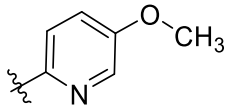	**9.17** ± 0.95	>10 (-30 %)
77	ST-20 R-enantiomer	OCH_3	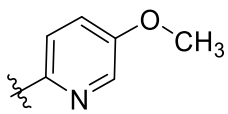	>10 (26 %)	>10 (-19 %)
78	AM-20 S-enantiomer	OCH_3	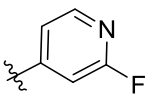	>10 (27 %)	>10 (-15 %)

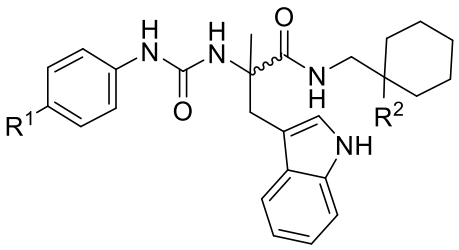

Scaffold C
(79 - 82)

79	PD-176252 S-enantiomer	NO_2	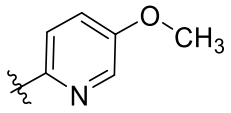	>10 (31 %)	>10 (-10 %)
80	PD-408 S-enantiomer	NO_2	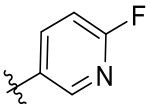	>10 (44 %)	>10 (-16 %)
81	EL-411 S-enantiomer	NO_2	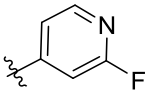	>10 (30 %)	>10 (-25 %)
82	PD-412 S-enantiomer	NO_2	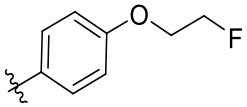	>10 (27 %)	>10 (-32 %)

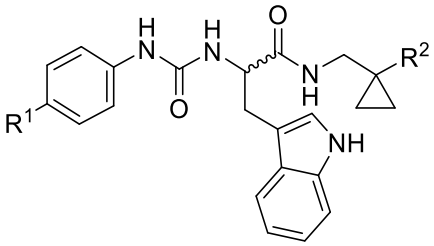

Scaffold D
(83 - 90)

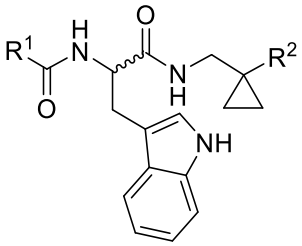

Scaffold E
(91 - 92)

83	CLP-25 R-enantiomer	H	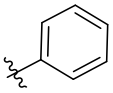	>10 (33 %)	>10 (-15 %)
84	PQ30 R-enantiomer	H	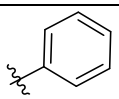	**1.31** ± 0.19	>10 (-42 %)
85	ML-11 S-enantiomer	NO_2	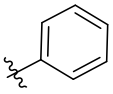	**24.1** ± 3.5	>10 (-16 %)
86	EMY-89 R-enantiomer	NO_2	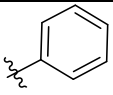	>10 (35 %)	>10 (-16 %)
87	PQ-28 S-enantiomer	OCH_3	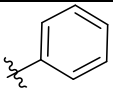	>10 (10 %)	>10 (-3 %)
88	CLP-23 R-enantiomer	OCH_3	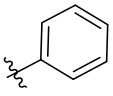	>10 (20 %)	>10 (-14 %)

89	CLP-24 R-enantiomer	F	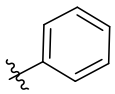	>10 (28 %)	>10 (-21 %)
90	PQ-29 S-enantiomer	F	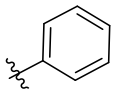	**2.15** ± 0.27	>10 (-36 %)
91	CLP-26 R-enantiomer	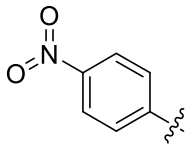	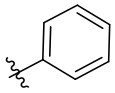	>10 (23 %)	>10 (-28 %)
92	CLP-31 R-enantiomer	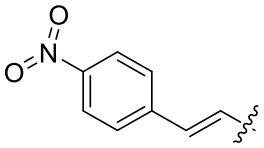	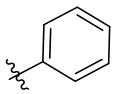	>10 (23 %)	>10 (-12 %)
		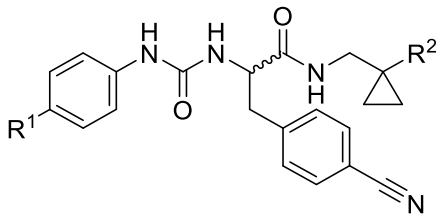 **Scaffold F (93 - 106)**			
93	DB-14 R-enantiomer	OH	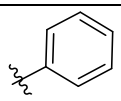	>10 (-10 %)	>10 (16 %)
94	DB-12 S-enantiomer	OH	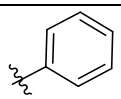	>10 (-26 %)	>10 (5 %)
95	CLP-32 R-enantiomer	NO_2	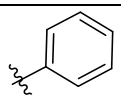	>10 (47 %)	>10 (-19 %)
96	CLP-33 S-enantiomer	NO_2	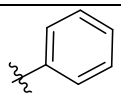	>10 (39 %)	>10 (-1 %)
97	MR-26 S-enantiomer	F	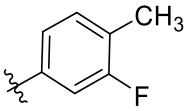	>10 (41 %)	>10 (-19 %)
98	MR-25 R-enantiomer	OCH_3	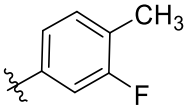	>10 (-1 %)	>10 (-1 %)
99	MR-31 S-enantiomer	OCH_3	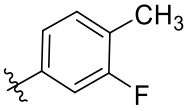	>10 (-1 %)	>10 (-5 %)v
100	MR-36 R-enantiomer	OCH_3	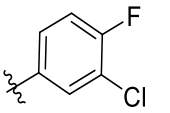	>10 (19 %)	>10 (-27 %)

101	MR-38 S-enantiomer	OCH_3	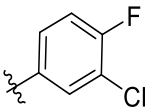	>10 (41 %)	>10 (-17 %)
102	MR-39 S-enantiomer	F	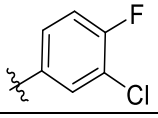	>10 (39 %)	>10 (-8 %)
103	MR-18 R-enantiomer	F	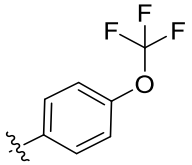	>10 (46 %)	>10 (-17 %)
104	MR-20 S-enantiomer	F	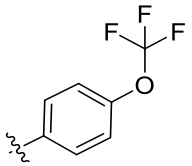	>10 (20 %)	>10 (-1 %)
105	MR-10 R-enantiomer	OCH_3	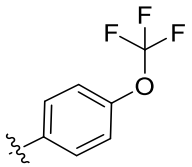	>10 (15 %)	>10 (4 %)
106	MR-14 S-enantiomer	OCH_3	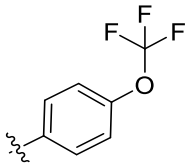	>10 (-5 %)	>10 (9 %)
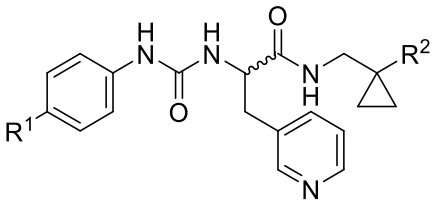 **Scaffold G (107 - 108)**			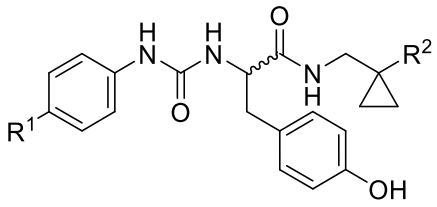 **Scaffold H (109)**		
107	CLP-39 R-enantiomer	NO_2	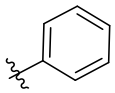	>10 (2 %)	>10 (-12 %)
108	CLP-37 S-enantiomer	NO_2	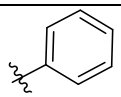	>10 (1 %)	>10 (-16 %)
109	DB-10 R-enantiomer	OCH_3	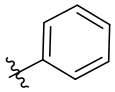	>10 (-15 %)	>10 (-4 %)

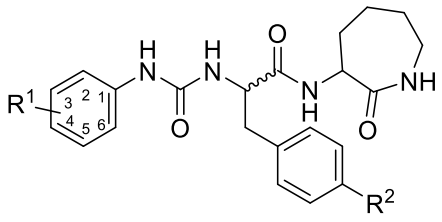

Scaffold I (110 - 114)

110	DB-30 S-enantiomer	4-OH	H	>10 (-12 %)	>10 (6 %)
111	ST140 S-enantiomer	4-OH	H	>10 (-36 %)	>10 (-10 %)
112	ST141 R-enantiomer	3-OH	H	>10 (-10 %)	>10 (-5 %)
113	ST142 R-enantiomer	4-Br	OH	>10 (11 %)	>10 (-21 %)
114	DB49 S-enantiomer	4-Br	OH	>10 (-13 %)	>10 (-1 %)

To better understand the SAR of this urea derivatives, we grouped all test compounds based on their different scaffolds and analyzed the inhibitory activities of both hits and non-hits. Among the series with core structure A, compound **54** showed the least inhibition (7 %) as an antagonist. Exchanging the small cyclopropyl ring at R^2 for a cyclohexyl ring (**56**) increased inhibitory activity to 49 % at 10 µM. Compound **55**, the *S*-enantiomer of **56** was less active. Extending the cyclohexyl ring with a propyl linker as with **57** reduced inhibition by about 2-fold. The bicyclic derivatives such as **59** and **60** (with tetrahydronaphthalene), and **58** (with dihydroindene) were as active as **56** in inhibiting UTP-induced $P2Y_2R$ activation. Aromatic substituents (**61** and **62**) resulted in less inhibitions

Compounds with scaffold B are derivatives of **55** or **56** where various extensions over the cyclohexyl group were investigated. Whereas at R^2 phenyl (**62** and **63**) and 4-fluorophenyl (**64** and **65**) substitutions did not improve inhibitory activity compared to **55**, the *R*-enantiomer of **67** with 4-methoxyphenyl increased $P2Y_2R$ inhibition. Furthermore, antagonistic activity also improved at **68** with 2-pyridinyl groups. Additionally, at position R^1, the substituents rank as NO_2 > Br (or other halogens) > CF_3 > OCH_3. The most potent compound with scaffold B was **76** (IC_{50} = 9.17 µM) combining 4-methoxy-2-pyridinyl substitution at position R^2 with NO_2 at R^1. With scaffold B, it was observed that the *R*-enantiomers of the test compounds were generally more active. In principle, compound **76** did exhibit better antagonism than **56**. Therefore we proceeded to explore other scaffolds. The most interesting compound with scaffold C was **80** (44 % inhibition) with NO_2 and 2-fluoropyridin-3-yl substitutions at R^1 and R^2 respectively.

Scaffold D yielded the most potent compounds from this library. Here, analogs explore the spatial effect on potency by exchanging the bulky cyclohexyl group for cyclopropane. Interestingly, there was improved inhibitory activity with phenyl groups for **85** (52 %) and **86** (35 %) over the parent structure **54** (7 %). Among the two, the *S*-enantiomer **85** yielded an IC_{50} of 24.1 µM upon further investigation. Replacing the NO_2 of **85** with a fluoro at R^1 resulted in compound **90** with a significant 10-fold increase in potency (IC_{50} = 2.15 µM). The potency further improves to 1.31 µM (**84**) when NO_2 was replaced with a hydrogen. Compound **84** is by far the most potent analog in the entire urea library screened. Again, the R-enantiomers of scaffold D derivatives exhibited better inhibitory activity. The improved antagonistic activity of scaffold D derivatives over **54** juxtaposed to the moderate activity of scaffold B derivatives over **56** indicates there is a critical spatial requirement to fulfill before potency could further be improved. Analogs of scaffold E are amides that exhibited reduced inhibitory activity at the $P2Y_2R$ compared to analogs with scaffold D (urea analogs). This supposes the urea functional group is very important for antagonism.

Next, the importance of the indolyl group was investigated by replacing it in scaffolds F, G and H. All derivatives of scaffolds G and H were inactive as potential $P2Y_2R$ antagonists. Pyridinyl and 4-hydroxyphenyl groups may therefore not be tolerated. Among the series with scaffold F, compound **95** showed the highest inhibition (47 %) comparable to that of **85**. Also, other active compounds from this series are **101** (41 %) and **103** (46 %) with 3-chloro-4-fluorophenyl and 4-(trifluoromethoxy)phenyl substituents respectively. Generally, the inhibitory activity of series with scaffold F analogs were comparable to those with scaffold D. The 4-cyanophenyl group may be well tolerated as an isostere for replacing the indole moiety when further developing the urea derivatives. The last set of compounds based on scaffold I (**110** - **114**) was also inactive as antagonists in screening. The bulky 2-oxazepan-3-yl group may not be well tolerated in the $P2Y_2R$ binding pocket. The SARs of the urea derivatives at the $P2Y_2R$ are summarized in Figure 18 below.

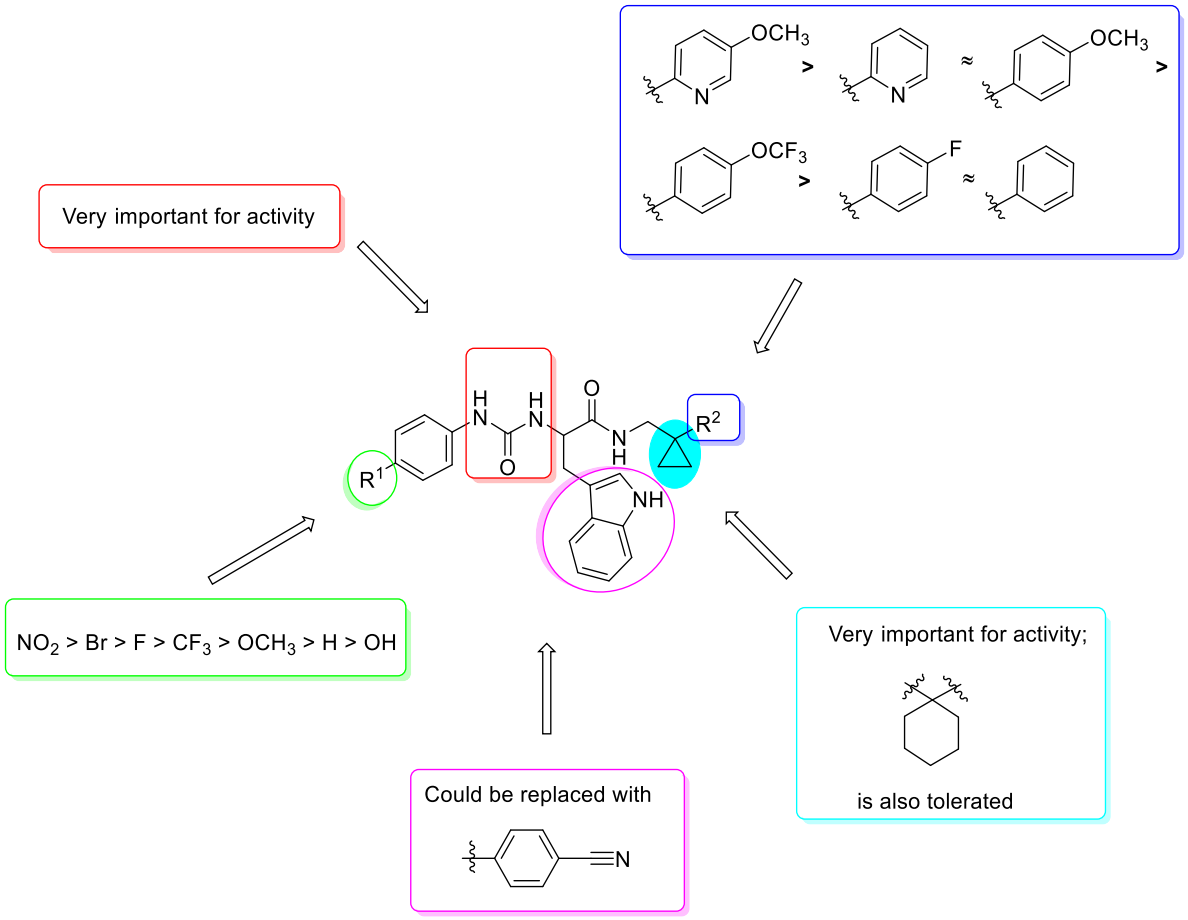

Figure 18: Structure-activity relationships of the urea derivatives showing functional groups that are important for activity.

The potencies of the four hits **76**, **84**, **85** and **90**, from the urea series were determined by β-arrestin assay. However, when screened in a calcium assay at 5 µM (same concentration as in β-arrestin assay), they were completely inactive in blocking $P2Y_2$-UTP induced intracellular calcium influx (Table 5). The urea derivatives may be biased toward the β-arrestin pathway. Furthermore, the compounds were tested at other non-related targets such as GPR18 and cannabinoid receptors for selectivity. At GPR18, we used a β-arrestin assay to confirm that compound activity was not due to a systematic error associated with the assay system. As presented in Table 5, all the compounds, except **85**, were relatively selective for the $P2Y_2R$ over the cannabinoid receptors and GPR18. Compound **85** was 2.5-fold more active as an antagonist at GPR18 than at the human $P2Y_2R$ (IC_{50}: 9.50 µM vs 24.1 µM).

Table 5: Selectivity of urea derivatives as $P2Y_2R$ antagonists

		hP2Y$_2$ IC$_{50}$ ± S.E.M (μM, n = 3 or 4) (% inhibition at 5 μM)[a]		**Radioligand binding** versus **[^{3}H]CP55,940 (μM,** n = 3 or 4) (% inhibition at 10 μM)		**Human GPR18**	
No.	**Cpd name**	**β-arrestin assay**	**Calcium assay**	**Human CB$_1$ K$_i$ (μM)**	**Human CB$_2$ K$_i$ (μM)**	**Antagonistic activity, IC$_{50}$ ± S.E.M (μM) (% inhibition of 0.1 μM MZ1415)**	**Agonistic activity, EC$_{50}$ ± S.E.M (μM) (% activation compared to 0.1 μM MZ1415)**
76	ST-6 R	**9.17** ± 0.95	(11 %)	>10 (33 %)	>10 (12 %)	>10 (46 %)	>10 (11 %)
84	PQ30 R	**1.31** ± 0.19	(24 %)	(51 %)	(67%)	>10 (30 %)	>10 (18 %)
85	ML-11 S	**24.1** ± 3.5	(28 %)	>10 (43 %)	(56 %)	**9.50** ± 3.07	>10 (5 %)
90	PQ-29 S	**2.15** ± 0.27	(27 %)	>10 (49 %)	(63%)	>10 (46 %)	>10 (18 %)

[a] Antagonism was determined using the agonist (UTP) EC_{80} concentration in the respective assays. All data are presented as means from 3-5 independent assays.

The structure of the urea derivatives are similar to that of BPTU (**9**), a known allosteric antagonist selective for the human $P2Y_1R$.[125] We therefore investigated the mechanism of action of compound **84** at the $P2Y_2R$ using Schild analysis and Schild plot (Figure 19). Whilst there was a rightward shift in UTP dose-response curves in the presence of increasing concentrations of **84**, maximum UTP response decreased accordingly. From the Schild plot, the slope of the regression line was determined to be -0.7246. Considering the non-parallel nature of the UTP shift curves with a Schild

slope less than unity, a non-competitive allosteric mechanism of action is assumed. The affinity (pA_2) of **84** was determined to be 5.48. Interestingly, compound **9** (BPTU) was also reported to bind in a hydrophobic allosteric pocket at the lipidic interface of the $P2Y_1R$ transmembrane domain. The urea group of BPTU (**9**) anchors the ligand firmly in the hydrophobic pocket through hydrogen bonding.[125] This underscores the importance of the urea functionality for antagonism of **84** and its analogs as there is a possibility that **84** may bind in a similar pocket. BPTU is currently used only as a pharmacological tool at the $P2Y_1$ receptor. Similarly, **84** and its analogs may be used as pharmacological tools for the $P2Y_2R$. However, based on insights from the SARs above (Figure 19), urea derivatives with improved potency and more drug-like properties could be developed as $P2Y_2R$ therapeutics.

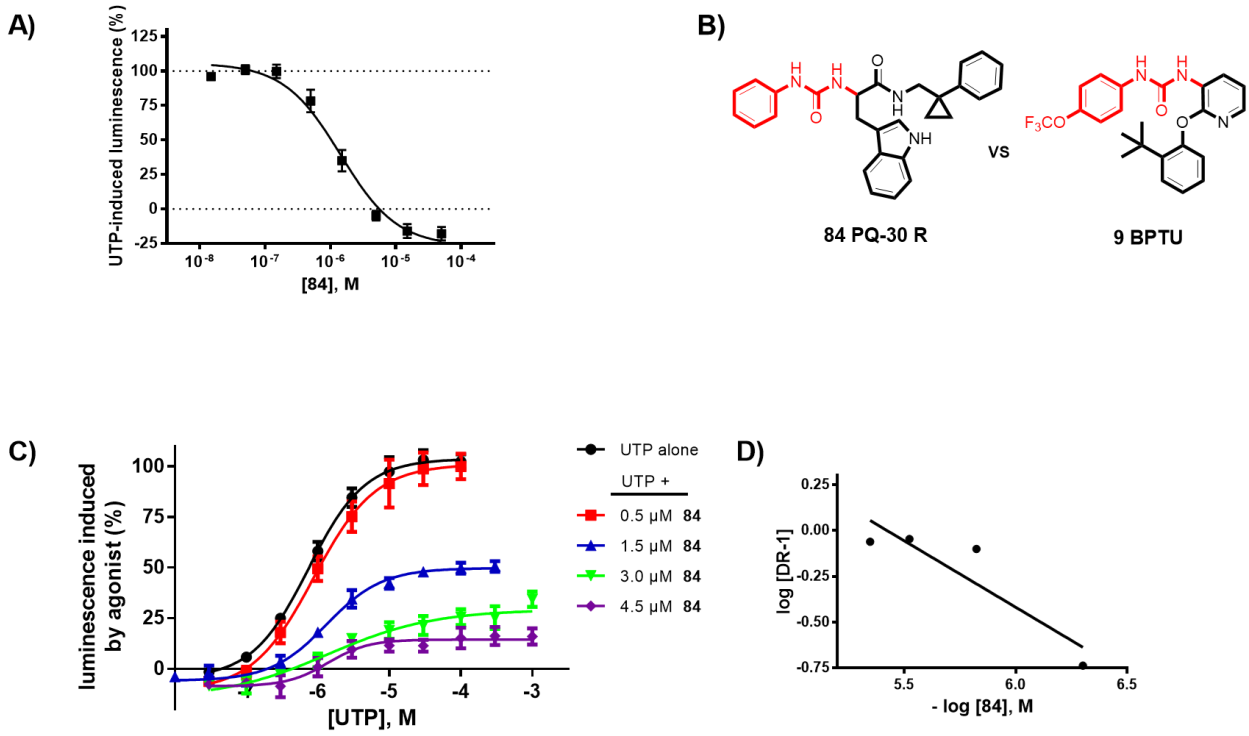

Figure 19: **A)** Logarithm dose-response curve of **84** at inhibiting $P2Y_2R$-UTP mediated recruitment of β-arrestin. **B)** Structures of compound **84** and **9** (BPTU); common substructures are highlighted in red. **C)** Schild analysis of UTP curve shifts in the presence of varying concentration of compound **84**. **D)** Schild plot of UTP dose-ratios versus various concentrations of **84** to determine the schild slope and pA_2.

3.7 **Diindolylmethane (DIM) derivatives**

There was a hit rate of 6 % from screening the diindolylmethane (DIM) library as potential antagonists of the human $P2Y_2R$ library. The lead compound, 3,3'-diindolylmethane (DIM, **115**, see Table 6), is a dimeric metabolite of indole-3-carbinol (I3C) found in members of the family of Cruciferae such as broccoli, cabbages, cauliflower and radishes. It is a privileged scaffold formed from indole-3-carbinol by acid-catalyzed self-condensation both in vivo and in vitro.[195]

The role of **115** in inhibiting cancer growth has been extensively reported in literature. For instance, binding of **115** to the aryl hydrocarbon receptor (AhR) in T47D human breast cancer cells significantly reduced Cytochrome P4501A1 (CYPlAl)-dependent ethoxyresorufin O-deethylase (EROD) activity.[196] The DIMs have been shown in an orthotopic pancreatic cancer model to potentiate the apoptosis-inducing effect of the kinase inhibitor erlotinib both *in vitro* and *in vivo* but only in tumors in which the epidermal growth factor receptor (EGFR) and the nuclear factor-$_K$B (NF-$_K$B) are activated.[197] They have also been shown to have anti-carcinogenic activity in colon cancer through the activation of Krüppel-like factor 4 (KLF4) dependent cyclin-dependent kinase inhibitor p21.[198] Furthermore, they were reported to activate peroxisome proliferator-activated receptor γ (PPARγ) and the orphan receptor N77 to induce apoptosis of cancerous colon cells through an endoplasmic reticulum (ER)-independent c-jun N-terminal kinase (JNK) pathway.[199]

DIM was also reported as a potential antidiabetic agent as it increases adipocytes differentiation and expression of glucose transporter 4 (GLUT4) in adipocytes hence increasing insulin sensitivity and glucose uptake.[200] Derivatives of DIM have also shown anti-tubercular effects.[201] Also, 3,3'-diindolylmethane has anti-inflammatory[202] and immuno-modulatory effects against viral infection.[203] DIM was discovered to be a partial agonist at the cannabinoid CB_2 receptor with a binding affinity of about 1.0 μM, mediating the anti-inflammatory effects of CB_2 in murine monocyte/macrophage RAW264.7 cells.[204] Recently, **115** and its derivatives were reported as agonists of the orphan receptor GPR84, a potential target for the immunotherapy of cancer.[76,205]

The preliminary hits from screening were validated by both calcium mobilization and β-arrestin translocation assays. Based on their activities, new derivatives were further synthesized and tested. The synthesis was performed by Dr. Pillaiyar Thanigaimalai of our group. We also investigated these compounds for selectivity against different GPCRs (see Table 6).

Table 6: Potencies of diindolylmethane derivatives as antagonists of the $P2Y_2R$ compared to their activity at selected receptors.

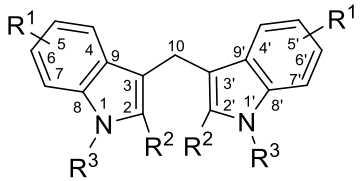

Scaffold A
(115-145)

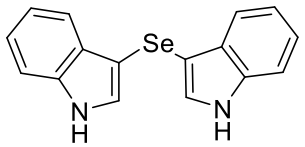

Yazh-622
(146)

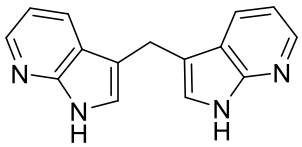

Yazh-186
(147)

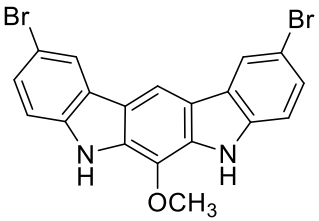

Yazh-107
(148)

No.	Cpd name	R^1	R^2	R^3	Human $P2Y_2R$ β-arrestin assay[a] IC_{50} ± SEM (μM, n = 3 or 4) (% inhibition at 5 μM)	Human $P2Y_2R$ Calcium assay[a] IC_{50} ± SEM (μM, n = 3 or 4) (% inhibition at 5 μM)	Human P2X4R Calcium assay[b] IC_{50} ± SEM (μM, n = 3 or 4)	Cannabinoid receptors versus [^{3}H]CP55,940 Human CB_1 K_i ± SEM (μM) (or percent receptor activation at 5 μM)	Cannabinoid receptors versus [^{3}H]CP55,940 Human CB_2 K_i ± SEM (μM) (or percent receptor activation at 5 μM)	Human GPR84 cAMP assay[c] EC_{50} ± SEM (μM) (or percent receptor activation at 10 μM)	Human GPR84 β-arrestin assay[d] EC_{50} ± SEM (μM) (or percent receptor activation at 10 μM)	Human GPR84 Radioligand Binding K_i ± SEM [μM] (% activation of 2 nM [^{3}H]PSB-1584 at 10 μM (n=3)
Structure A: Symmetrical diindolylmethane derivatives with no substitution at position 10												
115	Yazh-25 (DIM)	H	H	H	>5 (9 %)	**19.4** ± 1.2	>5 (-8 %)	**5.42** ± 1.00	**0.690** ± 0.15	**0.252** ± 0.088	**1.64** ± 0.81	**0.335** ± 0.033
116	Yazh-456	4-CH_3	H	H	n.d.	>5 (20 %)	n.d.	>5 (4%)	**0.845** ± 0.086	**0.987** ± 0.235	> 10 (24 %)	**0.938** ± 0.142 [47 %]
117	Yazh-176	4-OCH_3	H	H	>5 (4 %)	**6.52** ±0.85	>5 (4 %)	**5.03** ± 2.29 (extrapolated)	**0.579** ± 0.157	≥ 10 (47%)	n.d.	n.d.
118	Yazh-357	4-F	H	H	**33.4** ± 1.0	**13.6** ± 2.1	n.d.	>5 (28%)	**0.279** ± 0.056	**0.328** ± 0.005	**1.23** ± 0.03	**1.52** ± 0.19 [56 %]

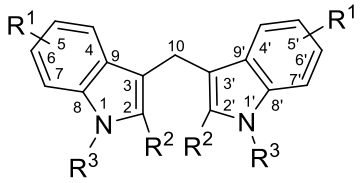

Scaffold A
(115-145)

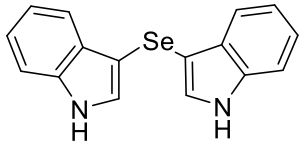

Yazh-622
(146)

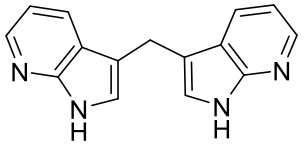

Yazh-186
(147)

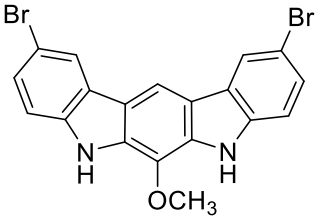

Yazh-107
(148)

No.	Cpd name	R^1	R^2	R^3	**Human $P2Y_2R$**		**Human P2X4R**	**Cannabinoid receptors versus** [^{3}H]CP55,940		**Human GPR84**		
					β-arrestin assay[a]	Calcium assay[a]	Calcium assay[b]	**Human CB_1**	**Human CB_2**	cAMP assay[c]	β-arrestin assay[d]	Radioligand Binding
					IC_{50} ± SEM (µM, n = 3 or 4) (% inhibition at 5 µM)	**IC_{50}** ± SEM (µM, n = 3 or 4) (% inhibition at 5 µM)	**IC_{50}** ± SEM (µM, n = 3 or 4)	**K_i** ± SEM (µM) (or percent receptor activation at 5 µM)	**K_i** ± SEM (µM) (or percent receptor activation at 5 µM)	**EC_{50}** ± SEM (µM) (or percent receptor activation at 10 µM)	**EC_{50}** ± SEM (µM) (or percent receptor activation at 10 µM)	**K_i** ± SEM [µM] (% activation of 2 nM [^{3}H]PSB-1584 at 10 µM (n=3)
119	Yazh-457	4-Cl	H	H	n.d.	>5 (38 %)	n.d.	**0.753** ± 0.048 (maximum inhibition: 60%)	**0.332** ± 0.230	**1.14** ± 0.06	> 10 (25%)	**0.175** ± 0.016 [*94 %*]
120	Yazh-417	4-NO_2	H	H	n.d.	>5 (1 %)	n.d.	>5 (6%)	>5 (29%)	n.d.	n.d.	n.d.
121	Yazh-131	5-CH_3	H	H	>5 (5 %)	**14.7** ± 2.1	n.d.	>5 (26%)	**2.78 ±** 1.36	≥ 10 (4 %)	≥ 10 (49%)	n.d.
122	Yazh-105	5-OCH_3	H	H	>5 (4 %)	**16.8** ± 1.7	n.d.	**5.89** ± 1.28 (extrapolated)	**2.84** ± 1.51	**0.369** ± 0.025	**1.20** ± 0.80	**0.103** ± 0.063 [46 %]
123	Yazh-160	5-F	H	H	**63.0** ± 0.1	**6.55** ± 1.17	n.d.	**4.08** ± 0.22	**1.17** ± 0.33	**0.0800** ± 0.0212	**4.33** ± 2.12	**0.199** ± 0.049 [125 %][b]

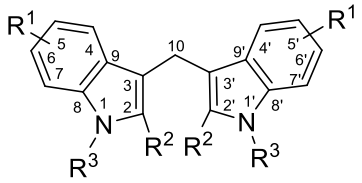

Scaffold A
(115-145)

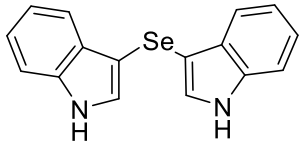

Yazh-622
(146)

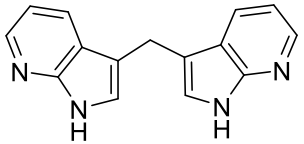

Yazh-186
(147)

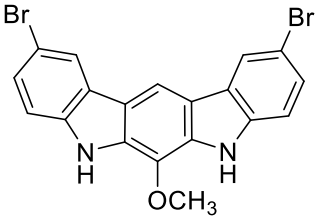

Yazh-107
(148)

No.	Cpd name	R^1	R^2	R^3	Human $P2Y_2R$		Human P2X4R	Cannabinoid receptors versus [^{3}H]CP55,940		Human GPR84		
					β-arrestin assay[a]	Calcium assay[a]	Calcium assay[b]	**Human CB_1**	**Human CB_2**	cAMP assay[c]	β-arrestin assay[d]	Radioligand Binding
					IC_{50} ± SEM (µM, n = 3 or 4) (% inhibition at 5 µM)	**IC_{50}** ± SEM (µM, n = 3 or 4) (% inhibition at 5 µM)	**IC_{50}** ± SEM (µM, n = 3 or 4)	**K_i** ± SEM (µM) (or percent receptor activation at 5 µM)	**K_i** ± SEM (µM) (or percent receptor activation at 5 µM)	**EC_{50}** ± SEM (µM) (or percent receptor activation at 10 µM)	**EC_{50}** ± SEM (µM) (or percent receptor activation at 10 µM)	**K_i** ± SEM [µM] (% activation of 2 nM [^{3}H]PSB-1584 at 10 µM (n=3)
124	Yazh-130	5-Cl	H	H	**28.7** ± 5.7	**15.0** ± 1.0 (19 %)	< 5 (80 %)	>5 (6%)	**0.747 ±** 0.067	**4.96** ± 3.08	n.d.	**0.250** ± 0.080 [90 %]
125	Yazh-116	5-Br	H	H	**54.8** ± 3.5	**9.41** ± 0.22	< 5 (90 %)	>5 (34%)	**1.27** ± 0.226	**3.44** ± 0.29	n.d.	**0.0591** ± 0.0145 [69 %]
126	Yazh-185	5-CN	H	H	>5 (11 %)	**9.50** ± 0.93	n.d.	>5 (35%)	>5 (30%)	≥ 10 (49%)	n.d.	n.d.
127	Yazh-297	5-NO_2	H	H	n.d.	≈5 (51 %)	n.d.	>5 (19%)	>5 (45%)	> 10 (31%)	n.d.	n.d.
128	Yazh-151	5-COOCH_3	H	H	>5 (3 %)	**15.0 ±** 1.9	n.d.	>5 (31%)	**2.99** ± 0.029	> 10 (11%)	n.d.	n.d.
129	Yazh-232	5-CHO	H	H	n.d.	>5 (40 %)	n.d.	>5 (23%)	**7.25** ± 1.39	> 10 (-4%)	n.d.	n.d.

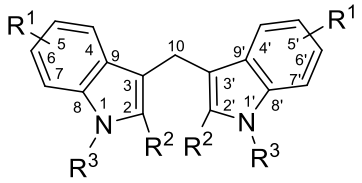

Scaffold A
(115-145)

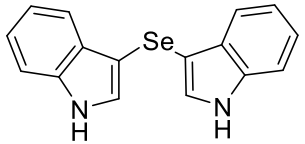

Yazh-622
(146)

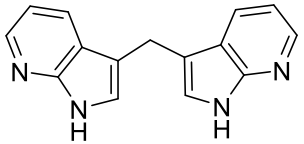

Yazh-186
(147)

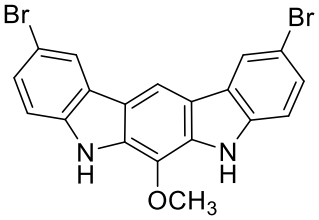

Yazh-107
(148)

No.	Cpd name	R^1	R^2	R^3	Human $P2Y_2R$ β-arrestin assay[a] IC_{50} ± SEM (μM, n = 3 or 4) (% inhibition at 5 μM)	Human $P2Y_2R$ Calcium assay[a] IC_{50} ± SEM (μM, n = 3 or 4) (% inhibition at 5 μM)	Human P2X4R Calcium assay[b] IC_{50} ± SEM (μM, n = 3 or 4)	Cannabinoid receptors versus [^{3}H]CP55,940 Human CB_1 K_i ± SEM (μM) (or percent receptor activation at 5 μM)	Cannabinoid receptors versus [^{3}H]CP55,940 Human CB_2 K_i ± SEM (μM) (or percent receptor activation at 5 μM)	Human GPR84 cAMP assay[c] EC_{50} ± SEM (μM) (or percent receptor activation at 10 μM)	Human GPR84 β-arrestin assay[d] EC_{50} ± SEM (μM) (or percent receptor activation at 10 μM)	Human GPR84 Radioligand Binding K_i ± SEM [μM] (% activation of 2 nM [^{3}H]PSB-1584 at 10 μM (n=3)
130	Yazh-159	5-COOH	H	H	n.d.	>5 (1 %)	n.d.	>5 (-7%)	>5 (34%)	≥ 10 (28%)	>> 10 (-5%)	n.d.
131	Yazh-117	5-OCH_2Ph	H	H	n.d.	>5 (34 %)	n.d.	**2.95** ± 0.749	**0.628** ± 0.181 (maximum inhibition: 50%)	> 10 (36%)	n.d.	n.d.
132	Yazh-106	6-CH_3	H	H	>5 (1 %)	**15.0** ± 1.3	n.d.	>5 (30%)	**0.504** ± 0.252	> 10 (-22%)	n.d.	n.d.
133	Yazh-165	6-OCH_3	H	H	n.d.	>5 (28 %).	n.d.	>5 (26%)	>5 (32%)	> 10 (31%)	n.d.	n.d.
134	Yazh-358	6-F	H	H	n.d.	>5 (29 %)	n.d.	>5 (27%)	**0.985** ± 0.094	**0.625** ± 0.070	**7.53** ± 2.30	**0.302** ± 0.059 [57 %]

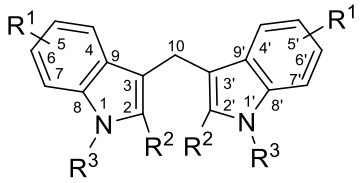

Scaffold A
(115-145)

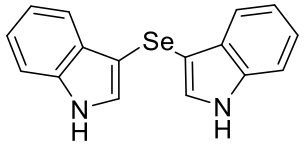

Yazh-622
(146)

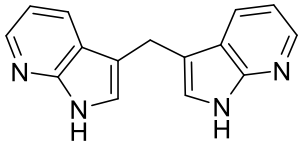

Yazh-186
(147)

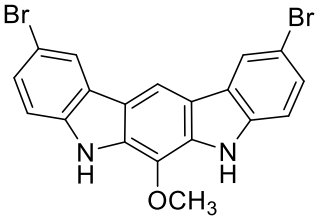

Yazh-107
(148)

No.	Cpd name	R^1	R^2	R^3	Human $P2Y_2R$ β-arrestin assay[a] IC_{50} ± SEM (μM, n = 3 or 4) (% inhibition at 5 μM)	Human $P2Y_2R$ Calcium assay[a] IC_{50} ± SEM (μM, n = 3 or 4) (% inhibition at 5 μM)	Human P2X4R Calcium assay[b] IC_{50} ± SEM (μM, n = 3 or 4)	Cannabinoid receptors versus [^{3}H]CP55,940 Human CB_1 K_i ± SEM (μM) (or percent receptor activation at 5 μM)	Cannabinoid receptors versus [^{3}H]CP55,940 Human CB_2 K_i ± SEM (μM) (or percent receptor activation at 5 μM)	Human GPR84 cAMP assay[c] EC_{50} ± SEM (μM) (or percent receptor activation at 10 μM)	Human GPR84 β-arrestin assay[d] EC_{50} ± SEM (μM) (or percent receptor activation at 10 μM)	Human GPR84 Radioligand Binding K_i ± SEM [μM] (% activation of 2 nM [^{3}H]PSB-1584 at 10 μM (n=3)
135	Yazh-428	6-Cl	H	H	n.d.	>5 (49 %)	n.d.	**0.820** ± 0.385 (maximal inhibition:53%)	**0.911** ± 0.105	> 10 (4 %)	**5.34** ± 1.84	**43.7** ± 9.6
136	Yazh-175	7-OCH_3	H	H	n.d.	>5 (45 %)	n.d.	>5 (30%)	≈ 5 (48%)	> 10 (18 %)	n.d.	n.d.
137	Yazh-381	7-F	H	H	n.d.	>5 (19 %)	n.d.	>5 (18%)	≈ 5 (49%)	**0.113** ± 0.047	**6.07** ± 3.37	**0.0618** ± 0.0136 [153 %]
138	Yazh-118	4-Cl,6-Cl	H	H	**8.54** ± 1.20	**6.90** ± 0.59	>5 (20 %)	**1.68** ± 0.32 (maximum inhibition: 68%)	**0.626** ± 0.22	≈ 10 (51 %)	n.d.	**6.79** ± 1.04
139	Yazh-582	4-F,5-F	H	H	n.d.	>5 (41 %)	n.d.	**5.34** ± 1.81	**3.04** ± 0.781	**0.377** ± 0.030	>> 10 (-2%)	**0.0836** ± 0.0167 [67 %]

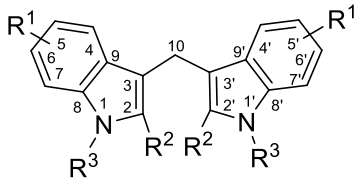

Scaffold A
(115-145)

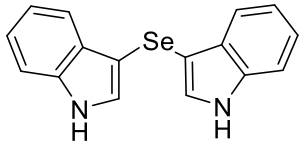

Yazh-622
(146)

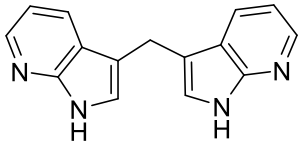

Yazh-186
(147)

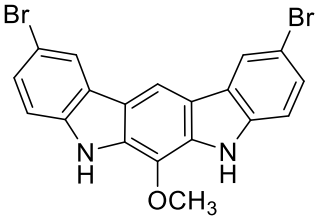

Yazh-107
(148)

No.	Cpd name	R^1	R^2	R^3	**Human $P2Y_2R$**		**Human P2X4R**	**Cannabinoid receptors versus** [^{3}H]CP55,940		**Human GPR84**		
					β-arrestin assay[a]	Calcium assay[a]	Calcium assay[b]	**Human CB_1**	**Human CB_2**	cAMP assay[c]	β-arrestin assay[d]	Radioligand Binding
					IC_{50} ± SEM (µM, n = 3 or 4) (% inhibition at 5 µM)	**IC_{50}** ± SEM (µM, n = 3 or 4) (% inhibition at 5 µM)	**IC_{50}** ± SEM (µM, n = 3 or 4)	**K_i** ± SEM (µM) (or percent receptor activation at 5 µM)	**K_i** ± SEM (µM) (or percent receptor activation at 5 µM)	**EC_{50}** ± SEM (µM) (or percent receptor activation at 10 µM)	**EC_{50}** ± SEM (µM) (or percent receptor activation at 10 µM)	**K_i** ± SEM [µM] (% activation of 2 nM [^{3}H]PSB-1584 at 10 µM (n=3)
140	Yazh-K-30	5-Cl, 7-Cl	H	H	**73.3** ± 6.1	**16.2** ± 4.8	n.d.	>5 (22%)	**10.7** ± 0.591	n.d.	n.d.	> 10 µM (30 ± 12 %)
141	Yazh-586	5-F,6-F	H	H	n.d.	>5 (40 %)	n.d.	>5 (39%)	< 5 (59%)	**0.187** ± 0.053	**10.3** ± 5.6	**0.0524** ± 0.0068 [55 %]
142	Yazh-383	5-F,6-Cl	H	H	n.d.	>5 (48 %)	n.d.	>5 (25%)	>5 (36%)	**10.8** ± 0.50	**3.98** ± 0.86	**0.129** ± 0.009 [36 %]
143	Yazh-671	5-F,7-F	H	H	**37.2** ± 4.4	**8.98** ± 1.02	**4.51** ± 0.65	**2.64** ± 0.28	**1.10** ± 0.19	**0.0413** ± 0.0098	**5.47** ± 0.13	**4.51** ± 0.65
144	Yazh-27	H	H	CH_3	>5 (15 %)	>5 (12 %)	< 5 (81 %)	>5 (35%)	**3.39** ± 1.14	> 10 (-37 %)	>> 10 (-3 %)	n.d.
145	Yazh-143	H	CH_3	H	n.d.	>5 (18 %)	n.d.	>5 (45%)	>5 (48%)	≥ 10 (42 %)	> 10 (23 %)	n.d.

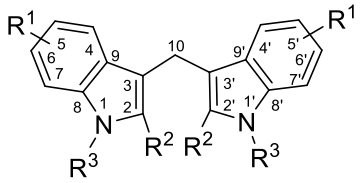

Scaffold A
(115-145)

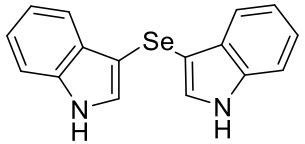

Yazh-622
(146)

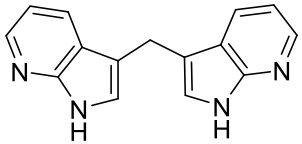

Yazh-186
(147)

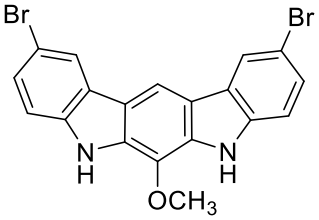

Yazh-107
(148)

No.	Cpd name	R^1	R^2	R^3	**Human $P2Y_2R$** β-arrestin assay[a] **IC_{50}** ± SEM (μM, n = 3 or 4) (% inhibition at 5 μM)	**Human $P2Y_2R$** Calcium assay[a] **IC_{50}** ± SEM (μM, n = 3 or 4) (% inhibition at 5 μM)	**Human P2X4R** Calcium assay[b] **IC_{50}** ± SEM (μM, n = 3 or 4)	**Cannabinoid receptors versus** [^{3}H]CP55,940 **Human CB_1** **K_i** ± SEM (μM) (or percent receptor activation at 5 μM)	**Cannabinoid receptors versus** [^{3}H]CP55,940 **Human CB_2** **K_i** ± SEM (μM) (or percent receptor activation at 5 μM)	**Human GPR84** cAMP assay[c] **EC_{50}** ± SEM (μM) (or percent receptor activation at 10 μM)	**Human GPR84** β-arrestin assay[d] **EC_{50}** ± SEM (μM) (or percent receptor activation at 10 μM)	**Human GPR84** Radioligand Binding **K_i** ± SEM [μM] (% activation of 2 nM [^{3}H]PSB-1584 at 10 μM (n=3)
146	Yazh-622	see structure above		-	>5 (48 %)	**4.29** ± 0.64	>5 (-19 %)	>5 (37%)	**1.53** ± 0.206	n.d.	n.d.	n.d.
147	Yazh-186	see structure above		-	>5 (1 %)	**65.9** ± 6.1	n.d.	>5 (20%)	>5 (3%)	**1.67** ± 0.26	>> 10	n.d
148	Yazh-107	see structure above		-	**59.6** ± 9.3	>5 (19 %)	n.d.	>5 (35%)	>5 (39%)	n.d.	>> 10	n.d

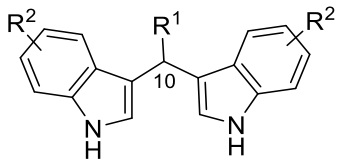

Scaffold B (149-216)

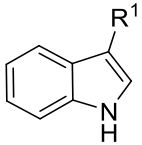

Scaffold C (217-253)

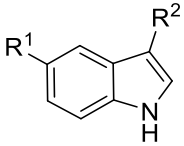

Scaffold D (254-269)

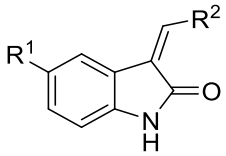

Scaffold E (270-277)

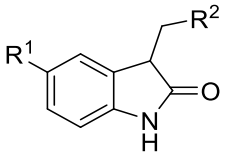

Scaffold F (278-281)

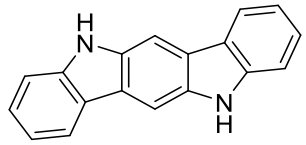

Indolo[3,2-b]carbazole (282)

No.	Cpd name	R^1	R^2	Human $P2Y_2R$ β-arrestin assay[a] IC_{50} ± SEM [µM, n = 3 or 4] (% inhibition at 5 µM)	Human $P2Y_2R$ Calcium assay[a] IC_{50} ± SEM [µM, n = 3 or 4] (% inhibition at 5 µM)	Human P2X4R Calcium assay[b] IC_{50} ± SEM [µM, n = 3 or 4]	Cannabinoid receptors versus [^{3}H]CP55,940 Human CB_1 K_i ± SEM [µM] (or % inhibition at 5 µM)	Cannabinoid receptors versus [^{3}H]CP55,940 Human CB_2 K_i ± SEM [µM] (or % inhibition at 5 µM)	Human GPR84 cAMP assay[c] EC_{50} ± SEM [µM] (% activation at 10 µM)	Human GPR84 β-arrestin assay[d] EC_{50} ± SEM [µM] (% activation at 10 µM)	Human GPR84 Radioligand Binding K_i ± SEM [µM] (% activation of 2 nM [^{3}H]PSB-1584 at 10 µM (n=3)
Structure B: Symmetrically diindolylmethane derivatives with alkyl substituents at position 10											
149	Yazh-653		–	>5 (10 %)	**7.38** ±0.78	n.d.	**8.15** ± 2.40 (extrapolated)	**5.74** ± 0.308 (extrapolated)	> 10 (-5%)	> 10 (3%)	n.d
150	Yazh-657		4-F	>5 (7 %)	**10.9** ± 1.6	>5 (10 %)	>5 (24%)	>5 (39%)	> 10 (5%)	> 10 (34%)	n.d.
151	Yazh-K-25		5-Cl	**60.3** ± 8.2	**8.89** ±1.39	< 5 (89 %)	n.d.	n.d.	n.d.	n.d.	n.d.
152	Yazh-650		7-F	>5 (24 %)	**12.2** ± 1.4	>5 (-8 %)	>5 (30%)	>5 (38%)	n.d.	n.d.	n.d.
153	Yazh-16	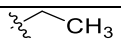	–	>5 (9 %)	**4.06** ±0.40	**5.03** ± 1.33	**2.70** ± 1.86	**0.804** ± 0.25	> 10 (-24 %)	**2.97** ± 1.03	**46.3** ± 14.9 inhibition of radioligand binding
154	Yazh-K-66A	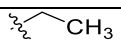	4-F	>5 (28 %)	**2.49** ± 0.42	n.d	**6.23** ± 2.71	**3.12** ± 0.577	n.d.	n.d.	> 10 µM (15%)
155	Yazh-K-61	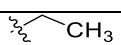	5-F	**34.2** ± 5.3 (15 %)	**6.52** ± 0.61	n.d.	**3.47** ± 0.358 (extrapolated)	**2.48** ± 0.333	n.d.	n.d.	> 10 µM (-20%)
156	Yazh-K-59	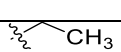	7-F	>5 (25 %)	**3.97** ± 0.30	n.d.	**>5** (44%)	**9.66** ± 2.71	n.d.	n.d.	> 10 µM (-18%)

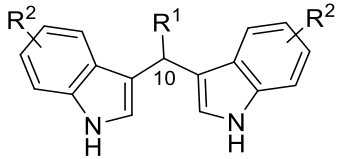

Scaffold B (149-216)

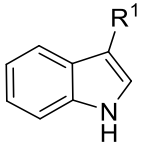

Scaffold C (217-253)

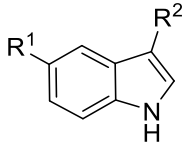

Scaffold D (254-269)

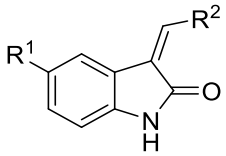

Scaffold E (270-277)

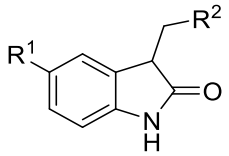

Scaffold F (278-281)

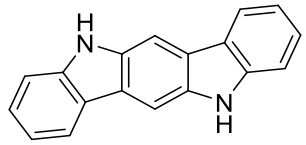

Indolo[3,2-b]carbazole (282)

No.	Cpd name	R^1	R^2	Human $P2Y_2R$ β-arrestin assay[a] IC_{50} ± SEM [µM, n = 3 or 4] (% inhibition at 5 µM)	Human $P2Y_2R$ Calcium assay[a] IC_{50} ± SEM [µM, n = 3 or 4] (% inhibition at 5 µM)	Human P2X4R Calcium assay[b] IC_{50} ± SEM [µM, n = 3 or 4]	Cannabinoid receptors versus [^{3}H]CP55,940 Human CB_1 K_i ± SEM [µM] (or % inhibition at 5 µM)	Cannabinoid receptors versus [^{3}H]CP55,940 Human CB_2 K_i ± SEM [µM] (or % inhibition at 5 µM)	Human GPR84 cAMP assay[c] EC_{50} ± SEM [µM] (% activation at 10 µM)	Human GPR84 β-arrestin assay[d] EC_{50} ± SEM [µM] (% activation at 10 µM)	Human GPR84 Radioligand Binding K_i ± SEM [µM] (% activation of 2 nM [^{3}H]PSB-1584 at 10 µM (n=3)
157	Yazh-4	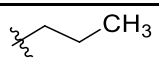	–	>5 (12 %)	**4.81** ±0.51	n.d.	**>5** (45%)	>5 (33%)	> 10 (-24%)	**6.07** ± 0.77	**22.4** ± 9.60 inhibition of radioligand binding
158	Yazh-2	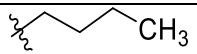	–	n.d.	>5 (48 %)	n.d.	>5 (-2%)	>5 (36%)	> 10 (-4%)	> 10 (-3%)	n.d.
159	Yazh-3	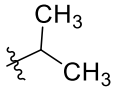	–	>5 (11 %)	**3.01** ±0.37	**8.48** ± 1.78	**8.61** ± 1.49	**4.19** ± 1.69	> 10 (16%)	**7.29** ± 0.19	n.d.
160	Yazh-K-186A	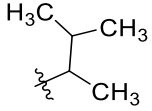	-	>5 (2 %)	**7.56** ±0.64	n.d.	n.d.	n.d.	n.d.	n.d.	n.d.
161	Yazh-K-42	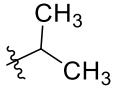	4-F	>5 (34 %)	**3.40** ±0.72	n.d.	≈ 5 (49%)	≈ 5 (48%)	n.d.	n.d.	> 10 µM (33%)
162	Yazh-K-45A	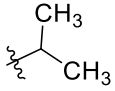	4-OCH_3	>5 (10 %)	**6.93** ±0.16	n.d.	**5.46** ± 0.287	>5 (42%)	n.d.	n.d.	≥ 10 µM (38 %)

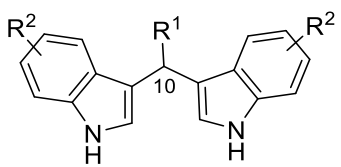

Scaffold B (149-216)

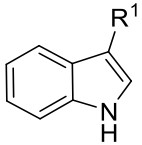

Scaffold C (217-253)

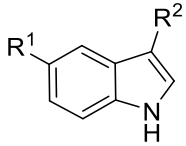

Scaffold D (254-269)

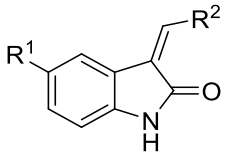

Scaffold E (270-277)

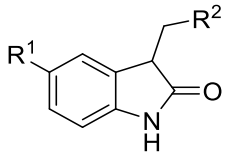

Scaffold F (278-281)

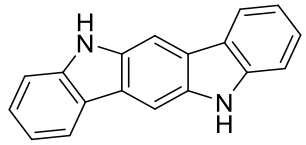

Indolo[3,2-b]carbazole (282)

No.	Cpd name	R^1	R^2	Human $P2Y_2R$ β-arrestin assay[a] IC_{50} ± SEM [µM, n = 3 or 4] (% inhibition at 5 µM)	Human $P2Y_2R$ Calcium assay[a] IC_{50} ± SEM [µM, n = 3 or 4] (% inhibition at 5 µM)	Human P2X4R Calcium assay[b] IC_{50} ± SEM [µM, n = 3 or 4]	Cannabinoid receptors versus [^{3}H]CP55,940 Human CB_1 K_i ± SEM [µM] (or % inhibition at 5 µM)	Cannabinoid receptors versus [^{3}H]CP55,940 Human CB_2 K_i ± SEM [µM] (or % inhibition at 5 µM)	Human GPR84 cAMP assay[c] EC_{50} ± SEM [µM] (% activation at 10 µM)	Human GPR84 β-arrestin assay[d] EC_{50} ± SEM [µM] (% activation at 10 µM)	Human GPR84 Radioligand Binding K_i ± SEM [µM] (% activation of 2 nM [^{3}H]PSB-1584 at 10 µM (n=3)
163	Yazh-K-65A	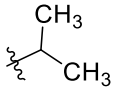	5-F	>5 (28 %)	**5.59** ±0.33	n.d.	**4.32** ± 0.736 (extrapolated)	**5.62** ± 0.673 (extrapolated)	n.d.	n.d.	> 10 µM (-2 %)
164	Yazh-K-67A	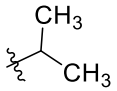	6-F	**51.0** ± 13.3 (9 %)	**3.41** ±0.77	n.d.	**4.62** ± 0.929	**7.71** ± 0.284	n.d.	n.d.	> 10 µM (34 %)
165	Yazh-K-64	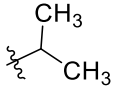	7-F	>5 (19 %)	**6.17** ±0.50	n.d.	**3.66** ± 0.692	**>5** (39%)	n.d.	n.d.	> 10 µM (-2 %)
166	Yazh-K-203A	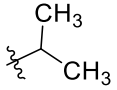	5-F, 6-F	**21.2** ± 0.9 (extrapolated)	**5.05** ±0.41	n.d.	n.d.	n.d.	n.d.	n.d.	n.d.
167	Yazh-K-204	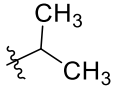	5-Br, 7-F	>5 (7 %)	**12.7** ± 2.5 (extrapolated)	n.d.	n.d.	n.d.	n.d.	n.d.	n.d.
168	Yazh-K-191	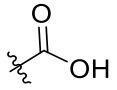	H	>5 (-8 %)	>5 (7 %)	n.d.	n.d.	n.d.	n.d.	n.d.	n.d.

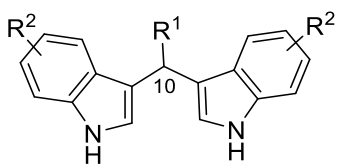

Scaffold B (149-216)

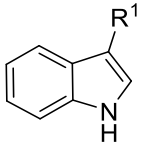

Scaffold C (217-253)

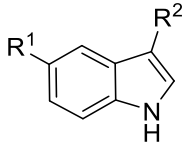

Scaffold D (254-269)

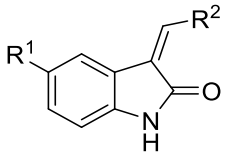

Scaffold E (270-277)

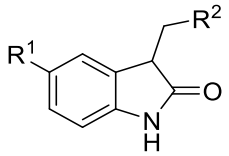

Scaffold F (278-281)

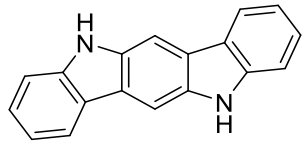

Indolo[3,2-b]carbazole (282)

No.	Cpd name	R^1	R^2	Human $P2Y_2R$ β-arrestin assay[a] IC_{50} ± SEM [µM, n = 3 or 4] (% inhibition at 5 µM)	Human $P2Y_2R$ Calcium assay[a] IC_{50} ± SEM [µM, n = 3 or 4] (% inhibition at 5 µM)	Human P2X4R Calcium assay[b] IC_{50} ± SEM [µM, n = 3 or 4]	Cannabinoid receptors versus [^{3}H]CP55,940 Human CB_1 K_i ± SEM [µM] (or % inhibition at 5 µM)	Cannabinoid receptors versus [^{3}H]CP55,940 Human CB_2 K_i ± SEM [µM] (or % inhibition at 5 µM)	Human GPR84 cAMP assay[c] EC_{50} ± SEM [µM] (% activation at 10 µM)	Human GPR84 β-arrestin assay[d] EC_{50} ± SEM [µM] (% activation at 10 µM)	Human GPR84 Radioligand Binding K_i ± SEM [µM] (% activation of 2 nM [^{3}H]PSB-1584 at 10 µM (n=3)
169	Yazh-K-193	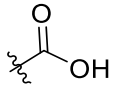	5-F	>5 (5 %)	>5 (1 %)	n.d.	n.d.	n.d.	n.d.	n.d.	n.d.
170	Yazh-K-195	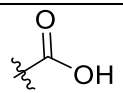	5-Cl	>5 (-1 %)	**13.0** ± 1.1 (extrapolated)	n.d	n.d.	n.d.	n.d.	n.d.	n.d.
171	Yazh-K-190	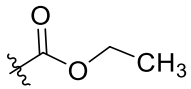	H	>5 (-1 %)	**8.17** ±0.66	n.d.	n.d.	n.d.	n.d.	n.d.	n.d.
172	Yazh-K-192	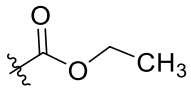	5-F	>5 (4 %)	**8.48** ±0.64	n.d.	n.d.	n.d.	n.d.	n.d.	n.d.
173	Yazh-194	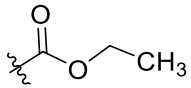	5-Cl	**40.8** ± 1.3 (4 %)	**9.14** ±0.86	n.d.	n.d.	n.d.	n.d.	n.d.	n.d.
174	Yazh-K-188	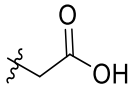	H	>5 (-9 %)	>5 (1 %)	n.d.	n.d.	n.d.	n.d.	n.d.	n.d.

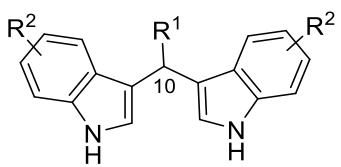

Scaffold B (149-216)

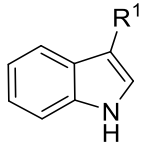

Scaffold C (217-253)

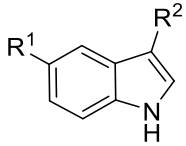

Scaffold D (254-269)

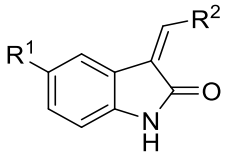

Scaffold E (270-277)

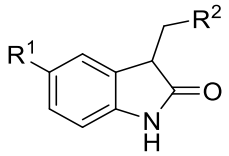

Scaffold F (278-281)

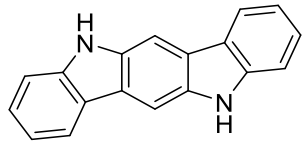

Indolo[3,2-b]carbazole (282)

No.	Cpd name	R^1	R^2	Human $P2Y_2R$ β-arrestin assay[a] IC_{50} ± SEM [µM, n = 3 or 4] (% inhibition at 5 µM)	Human $P2Y_2R$ Calcium assay[a] IC_{50} ± SEM [µM, n = 3 or 4] (% inhibition at 5 µM)	Human P2X4R Calcium assay[b] IC_{50} ± SEM [µM, n = 3 or 4]	Cannabinoid receptors versus [^{3}H]CP55,940 Human CB_1 K_i ± SEM [µM] (or % inhibition at 5 µM)	Cannabinoid receptors versus [^{3}H]CP55,940 Human CB_2 K_i ± SEM [µM] (or % inhibition at 5 µM)	Human GPR84 cAMP assay[c] EC_{50} ± SEM [µM] (% activation at 10 µM)	Human GPR84 β-arrestin assay[d] EC_{50} ± SEM [µM] (% activation at 10 µM)	Human GPR84 Radioligand Binding K_i ± SEM [µM] (% activation of 2 nM [^{3}H]PSB-1584 at 10 µM (n=3)
175	Yazh-K-187	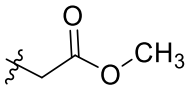	H	>5 (1 %)	**14.3** ± 0.8	n.d.	n.d.	n.d.	n.d.	n.d.	n.d.
176	Yazh-K-91	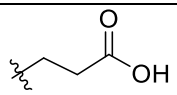	4-F	>5 (17 %)	**34.6** ± 6.1	n.d.	>5 (25%)	>5 (29%)	n.d.	n.d.	> 10 µM (17 %)
177	Yazh-K-88	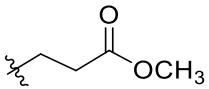	4-F	**56.5** ± 7.0 (17 %)	**6.76** ±0.48	n.d.	**3.17** ± 0.149	**1.75** ± 0.07	n.d.	n.d.	> 10 µM (-27 %)
178	Yazh-K-81		5-CH_3	**37.5** ± 6.2	**26.6** ± 9.5	n.d.	**4.87** ± 0.751	**3.39** ± 0.311	n.d.	n.d.	**5.25** ± 1.91 µM Max inhib: only 67 %
179	Yazh-K-72B	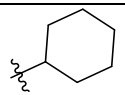	5-F	>5 (2 %)	**9.67** ±0.75	n.d.	>5 (47%)	**12.8** ± 0.37	n.d.	n.d.	> 10 µM (24 %)
180	Yazh-K296A		H	>5 (-3 %)	**6.62** ±0.39	n.d.	n.d.	n.d.	n.d.	n.d.	n.d.

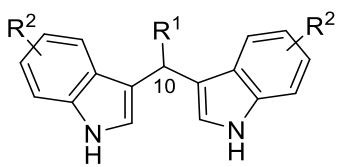

Scaffold B (149-216)

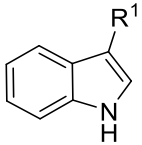

Scaffold C (217-253)

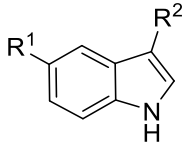

Scaffold D (254-269)

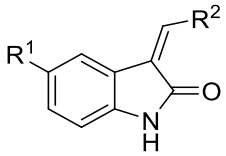

Scaffold E (270-277)

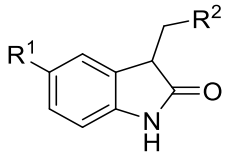

Scaffold F (278-281)

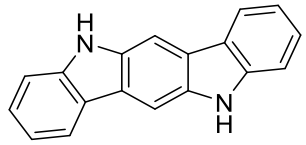

Indolo[3,2-b]carbazole (282)

No.	Cpd name	R^1	R^2	Human $P2Y_2R$ β-arrestin assay[a] IC_{50} ± SEM [µM, n = 3 or 4] (% inhibition at 5 µM)	Human $P2Y_2R$ Calcium assay[a] IC_{50} ± SEM [µM, n = 3 or 4] (% inhibition at 5 µM)	Human P2X4R Calcium assay[b] IC_{50} ± SEM [µM, n = 3 or 4]	Cannabinoid receptors versus [^{3}H]CP55,940 Human CB_1 K_i ± SEM [µM] (or % inhibition at 5 µM)	Cannabinoid receptors versus [^{3}H]CP55,940 Human CB_2 K_i ± SEM [µM] (or % inhibition at 5 µM)	Human GPR84 cAMP assay[c] EC_{50} ± SEM [µM] (% activation at 10 µM)	Human GPR84 β-arrestin assay[d] EC_{50} ± SEM [µM] (% activation at 10 µM)	Human GPR84 Radioligand Binding K_i ± SEM [µM] (% activation of 2 nM [^{3}H]PSB-1584 at 10 µM (n=3)
181	Yazh-K-172	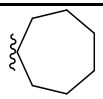	H	>5 (-4 %)	**16.3** ± 2.5	n.d.	n.d.	n.d.	n.d.	n.d.	n.d.

Structure B: Symmetrically diindolylmethane derivatives with aryl substituents at position 10

182	Yazh-K-80	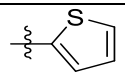	5-CH_3	**13.6** ± 1.6	**9.79** ± 0.91	n.d.	**3.10** ± 0.316	**4.40** ± 0.086	n.d.	n.d.	**5.55** ± 3.91 µM (n=2) Max inhib: only 51 %
183	Yazh-K-43	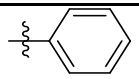	H	**13.4** ± 1.7 (Incomplete curve) (15 %)	**18.7** ± 1.1	>5 (5 %)	n.d.	n.d.	n.d.	n.d.	n.d.
184	Yazh-K-50	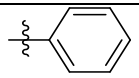	4-OCH_3	>5 (30 %)	**4.11** ± 0.74	n.d.	>5 (44%)	>5 (35%)	n.d.	n.d.	> 10 µM (30 ± 12 %)
185	Yazh-K-51	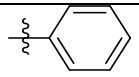	5-CH_3	>5 (22 %)	>5 (8 %)	n.d.	>5 (-31%)	>5 (-8%)	n.d.	n.d.	> 10 µM (6 %)

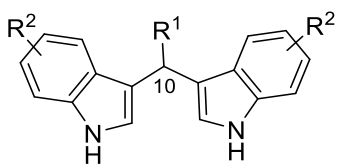

Scaffold B (149-216)

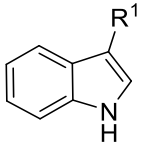

Scaffold C (217-253)

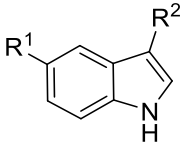

Scaffold D (254-269)

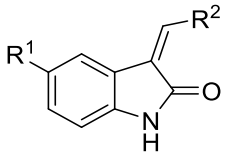

Scaffold E (270-277)

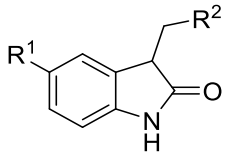

Scaffold F (278-281)

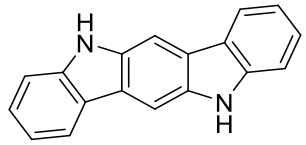

Indolo[3,2-b]carbazole (282)

No.	Cpd name	R^1	R^2	**Human $P2Y_2R$** β-arrestin assay[a] **IC_{50} ± SEM** [µM, n = 3 or 4] (% inhibition at 5 µM)	**Human $P2Y_2R$** Calcium assay[a] **IC_{50} ± SEM** [µM, n = 3 or 4] (% inhibition at 5 µM)	**Human P2X4R** Calcium assay[b] **IC_{50} ±** SEM [µM, n = 3 or 4]	**Cannabinoid receptors versus** [^{3}H]CP55,940 **Human CB_1** **K_i** ± SEM [µM] (or % inhibition at 5 µM)	**Cannabinoid receptors versus** [^{3}H]CP55,940 **Human CB_2** **K_i** ± SEM [µM] (or % inhibition at 5 µM)	**Human GPR84** cAMP assay[c] **EC_{50}** ± SEM [µM] (% activation at 10 µM)	**Human GPR84** β-arrestin assay[d] **EC_{50}** ± SEM [µM] (% activation at 10 µM)	**Human GPR84** Radioligand Binding K_i ± SEM [µM] (% activation of 2 nM [^{3}H]PSB-1584 at 10 µM (n=3)
186	Yazh-5	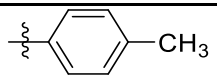	–	**11.5** ± 2.1	**15.2** ± 2.2	>5 (28 %)	**2.51** ± 0.40	**2.55** ± 0.28	> 10 (2%)	> 10 (10%)	n.d.
187	Yazh-103	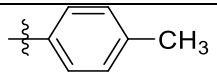	5-OCH_3	n.d.	≈ 5 (48 %)	n.d.	**0.414** ± 0.26 (maximal inhibition: 58%)	>5 (42%)	n.d.	n.d.	n.d.
188	Yazh-78	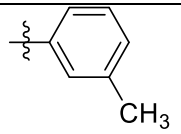	–	n.d.	>5 (41 %)	n.d.	**3.56** ± 1.47	**1.79** ± 0.361	n.d.	n.d.	n.d.
189	Yazh-79	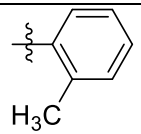	–	n.d.	≈ 5 (50 %)	n.d.	**2.98** ± 1.76 (maximal inhibition: 58%)	**4.55** ± 1.52 (maximal inhibition: 59%)	n.d.	n.d.	n.d.
190	Yazh-15	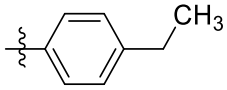	–	n.d.	≈ 5 (47 %)	n.d.	**4.44** ± 2.16	**1.35**± 0.56	n.d.	n.d.	n.d.

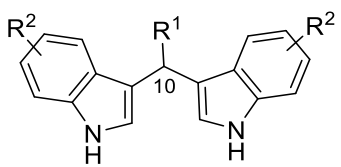

Scaffold B (149-216)

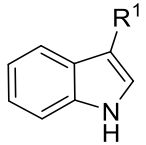

Scaffold C (217-253)

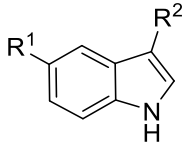

Scaffold D (254-269)

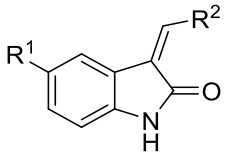

Scaffold E (270-277)

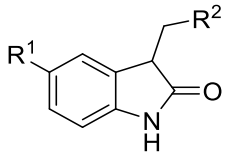

Scaffold F (278-281)

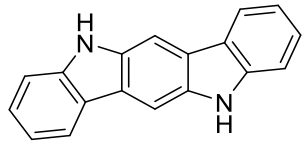

Indolo[3,2-b]carbazole (282)

No.	Cpd name	R^1	R^2	Human $P2Y_2R$ β-arrestin assay[a] IC_{50} ± SEM [µM, n = 3 or 4] (% inhibition at 5 µM)	Human $P2Y_2R$ Calcium assay[a] IC_{50} ± SEM [µM, n = 3 or 4] (% inhibition at 5 µM)	Human P2X4R Calcium assay[b] IC_{50} ± SEM [µM, n = 3 or 4]	Cannabinoid receptors versus [^{3}H]CP55,940 Human CB_1 K_i ± SEM [µM] (or % inhibition at 5 µM)	Cannabinoid receptors versus [^{3}H]CP55,940 Human CB_2 K_i ± SEM [µM] (or % inhibition at 5 µM)	Human GPR84 cAMP assay[c] EC_{50} ± SEM [µM] (% activation at 10 µM)	Human GPR84 β-arrestin assay[d] EC_{50} ± SEM [µM] (% activation at 10 µM)	Human GPR84 Radioligand Binding K_i ± SEM [µM] (% activation of 2 nM [^{3}H]PSB-1584 at 10 µM (n=3)
191	Yazh-32	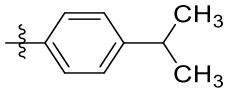	–	n.d.	≥5 (44 %)	n.d.	**0.832** ± 0.281	**1.55** ± 0.415	n.d.	n.d.	n.d.
192	Yazh-10	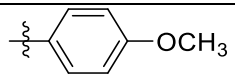	–	n.d.	≥ 5 (46 %)	n.d.	**0.774** ± 0.169	**2.41** ± 0.020	> 10 (-3 %)	n.d.	n.d.
193	Yazh-K-58	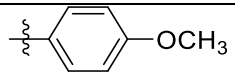	4-OCH_3	>5 (24 %)	>5 (25 %)	n.d.	**0.541** ± 0.173	>5 (26%)	n.d.	n.d.	> 10 µM (6 %)
194	Yazh-104	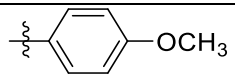	5-OCH_3	**15.8** ± 0.5	**10.4** ± 0.7	>5 (10 %)	**1.01** ± 0.649	**2.04** ± 0.377	n.d.	n.d.	n.d.
195	Yazh-K-57	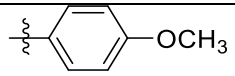	5-CH_3	>5 (19 %)	>5 (24 %)	n.d.	**2.34** ± 0.172	**1.30** ± 0.459 (maximum inhibition:64%)	n.d.	n.d.	> 10 µM (24 %)

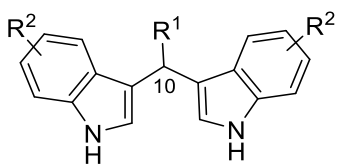

Scaffold B (149-216)

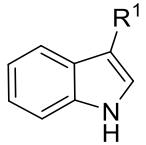

Scaffold C (217-253)

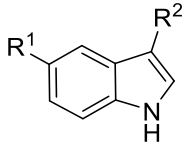

Scaffold D (254-269)

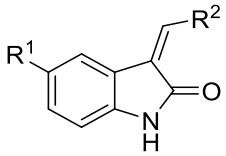

Scaffold E (270-277)

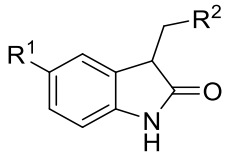

Scaffold F (278-281)

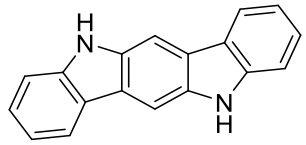

Indolo[3,2-b]carbazole (282)

No.	Cpd name	R^1	R^2	**Human $P2Y_2R$** β-arrestin assay[a] **IC_{50} ± SEM** [µM, n = 3 or 4] (% inhibition at 5 µM)	**Human $P2Y_2R$** Calcium assay[a] **IC_{50} ± SEM** [µM, n = 3 or 4] (% inhibition at 5 µM)	**Human P2X4R** Calcium assay[b] **IC_{50} ±** SEM [µM, n = 3 or 4]	**Cannabinoid receptors versus** [^{3}H]CP55,940 **Human CB_1** **K_i** ± SEM [µM] (or % inhibition at 5 µM)	**Cannabinoid receptors versus** [^{3}H]CP55,940 **Human CB_2** **K_i** ± SEM [µM] (or % inhibition at 5 µM)	**Human GPR84** cAMP assay[c] **EC_{50}** ± SEM [µM] (% activation at 10 µM)	**Human GPR84** β-arrestin assay[d] **EC_{50}** ± SEM [µM] (% activation at 10 µM)	**Human GPR84** Radioligand Binding K_i ± SEM [µM] (% activation of 2 nM [^{3}H]PSB-1584 at 10 µM (n=3)
196	Yazh-77	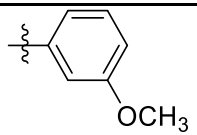	–	n.d.	>5 (45 %)	n.d.	**2.07** ± 0.753	**2.07** ± 0.753	n.d.	n.d.	n.d.
197	Yazh-76	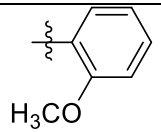	–	>5 (23 %)	>5 (31 %)	n.d.	**1.70** ± 0.41	**2.72** ± 2.02 (maximal inhibition: 84%)	n.d.	n.d.	n.d.
198	Yazh-20	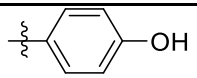	–	**63.3** ± 8.5	**14.9** ± 2.4	**8.06** ± 0.33	>5 (43%)	**7.13** ± 0.617 (extrapolated, maximal inhibition: 60%)	> 10 (7%)	> 10 (-5%)	n.d.
199	Yazh-1	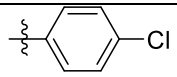	–	n.d.	>5 (38 %)	n.d.	**1.24** ± 0.398	**3.06** ± 0.901	> 10 (-4%)	n.d.	n.d.
200	Yazh-21	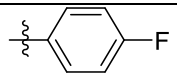	–	**16.5** ± 2.6	**5.26** ± 0.46	**7.85** ± 1.51	**3.54** ± 1.49	>5 (44%)	> 10 (8%)	n.d.	n.d.
201	Yazh-K-56	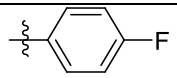	5-CH_3	**10.4** ± 0.5	>5 (13 %)	n.d.	**2.69** ± 0.601	**2.18** ± 0.293	n.d.	n.d.	≥ 10 µM (45 %)

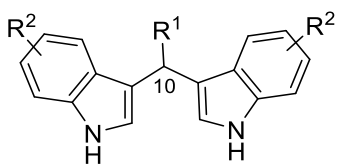

Scaffold B (149-216)

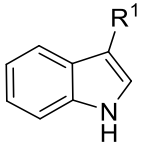

Scaffold C (217-253)

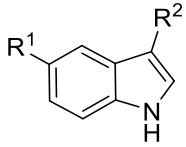

Scaffold D (254-269)

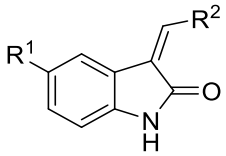

Scaffold E (270-277)

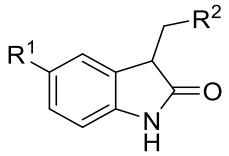

Scaffold F (278-281)

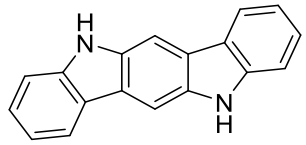

Indolo[3,2-b]carbazole (282)

No.	Cpd name	R^1	R^2	**Human $P2Y_2R$** β-arrestin assay[a] **IC_{50} ± SEM** [µM, n = 3 or 4] (% inhibition at 5 µM)	**Human $P2Y_2R$** Calcium assay[a] **IC_{50} ± SEM** [µM, n = 3 or 4] (% inhibition at 5 µM)	**Human P2X4R** Calcium assay[b] **IC_{50} ±** SEM [µM, n = 3 or 4]	**Cannabinoid receptors versus** [^{3}H]CP55,940 **Human CB_1** **K_i** ± SEM [µM] (or % inhibition at 5 µM)	**Cannabinoid receptors versus** [^{3}H]CP55,940 **Human CB_2** **K_i** ± SEM [µM] (or % inhibition at 5 µM)	**Human GPR84** cAMP assay[c] **EC_{50}** ± SEM [µM] (% activation at 10 µM)	**Human GPR84** β-arrestin assay[d] **EC_{50}** ± SEM [µM] (% activation at 10 µM)	**Human GPR84** Radioligand Binding K_i ± SEM [µM] (% activation of 2 nM [^{3}H]PSB-1584 at 10 µM (n=3)
202	Yazh-K-55	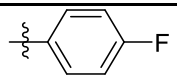	5-OCH_3	(29 %)	>5 (17 %)	n.d.	>5 (34%)	**>5** (18%)	n.d.	n.d.	> 10 µM (18 %)
203	Yazh-K-100	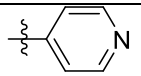	H	**39.4** ± 9.5 (extrapolated)	>5 (-4 %)	n.d.	n.d.	n.d.	n.d.	n.d.	n.d.
204	Yazh-K-76	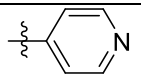	4-F	**36.2** ± 8.6	**8.72** ± 0.58	n.d.	**4.96** ± 0.17	**5.42** ± 0.225	n.d.	n.d.	> 10 µM (18 %)
205	Yazh-K-69	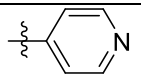	5-F	**54.0** ± 10.7	**8.55** ± 0.56	n.d.	>5 (47%)	>5 (28%)	n.d.	n.d.	**≥ 10** µM (47 %)
206	Yazh-K-79	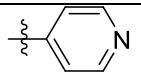	5-Cl	>5 (17 %)	>5 (-4 %)	n.d.	>5 (-7%)	>5 (9%)	n.d.	n.d.	> 10 µM (11 %) Solubility issues
207	Yazh-K-74	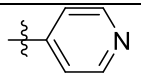	6-F	**37.4** ± 8.8	**13.8** ± 1.3	n.d.	**5.03** ± 1.40	**>5** (29%)	n.d.	n.d.	**≥ 10** µM (39 %)
208	Yazh-K-75	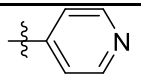	7-F	>5 (21 %)	**14.9** ± 0.9	n.d.	>5 (23%)	>5 (14%)	n.d.	n.d.	**≥ 10** µM (29 %)

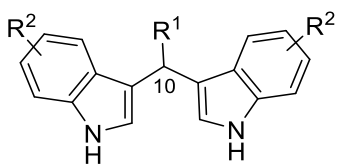

Scaffold B (149-216)

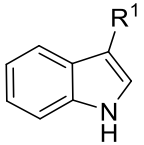

Scaffold C (217-253)

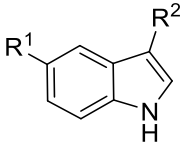

Scaffold D (254-269)

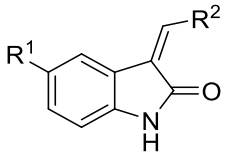

Scaffold E (270-277)

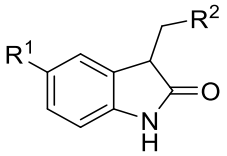

Scaffold F (278-281)

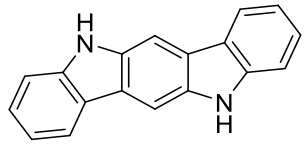

Indolo[3,2-b]carbazole (282)

No.	Cpd name	R^1	R^2	Human $P2Y_2R$ β-arrestin assay[a] IC_{50} ± SEM [µM, n = 3 or 4] (% inhibition at 5 µM)	Human $P2Y_2R$ Calcium assay[a] IC_{50} ± SEM [µM, n = 3 or 4] (% inhibition at 5 µM)	Human P2X4R Calcium assay[b] IC_{50} ± SEM [µM, n = 3 or 4]	Cannabinoid receptors versus [^{3}H]CP55,940 Human CB_1 K_i ± SEM [µM] (or % inhibition at 5 µM)	Cannabinoid receptors versus [^{3}H]CP55,940 Human CB_2 K_i ± SEM [µM] (or % inhibition at 5 µM)	Human GPR84 cAMP assay[c] EC_{50} ± SEM [µM] (% activation at 10 µM)	Human GPR84 β-arrestin assay[d] EC_{50} ± SEM [µM] (% activation at 10 µM)	Human GPR84 Radioligand Binding K_i ± SEM [µM] (% activation of 2 nM [^{3}H]PSB-1584 at 10 µM (n=3)
209	Yazh-12	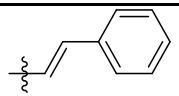	H	**61.6** ± 9.9 (14 %)	>5 (12 %)	n.d.	n.d.	n.d.	n.d.	n.d.	n.d.
210	Yazh-11	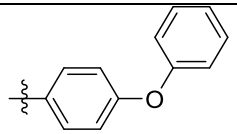	–	n.d.	>5 (39 %)	n.d.	**0.402** ± 0.306 (maximal inhibition: 50%)	**>5** (41%)	n.d.	n.d.	n.d.
211	Yazh-19	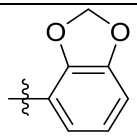	–	n.d.	≈5 (50 %)	n.d.	**1.19** ± 0.102	**3.04** ± 0.223	> 10 (1 %)	> 10 (7 %)	n.d.
212	Yazh-K-78	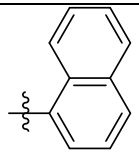	4-OCH_3	>5 (8 %)	>5 (3 %)	n.d.	>5 (7%)	>5 (9%)	n.d.	n.d.	> 10 µM (16 %)

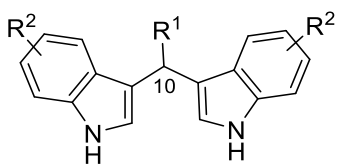

Scaffold B (149-216)

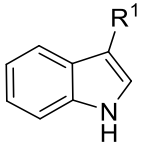

Scaffold C (217-253)

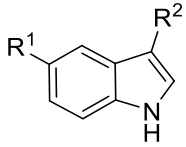

Scaffold D (254-269)

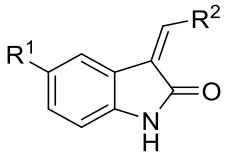

Scaffold E (270-277)

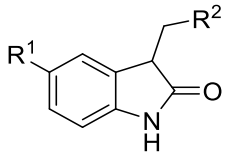

Scaffold F (278-281)

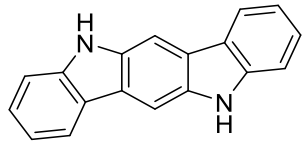

Indolo[3,2-b]carbazole (282)

No.	Cpd name	R^1	R^2	Human $P2Y_2R$ β-arrestin assay[a] **IC_{50} ± SEM** [µM, n = 3 or 4] (% inhibition at 5 µM)	Human $P2Y_2R$ Calcium assay[a] **IC_{50} ± SEM** [µM, n = 3 or 4] (% inhibition at 5 µM)	Human P2X4R Calcium assay[b] **IC_{50} ±** SEM [µM, n = 3 or 4]	Cannabinoid receptors versus [^{3}H]CP55,940 **Human CB_1** **K_i ± SEM** [µM] (or % inhibition at 5 µM)	Cannabinoid receptors versus [^{3}H]CP55,940 **Human CB_2** **K_i ± SEM** [µM] (or % inhibition at 5 µM)	Human GPR84 cAMP assay[c] **EC_{50} ±** SEM [µM] (% activation at 10 µM)	Human GPR84 β-arrestin assay[d] **EC_{50} ±** SEM [µM] (% activation at 10 µM)	Human GPR84 Radioligand Binding K_i ± SEM [µM] (% activation of 2 nM [^{3}H]PSB-1584 at 10 µM (n=3)
213	Yazh-K-82	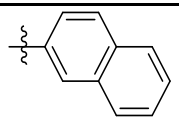	5-F	**14.8** ± 0.8	>5 (25 %)	n.d.	**2.79** ± 0.61	**2.35** ± 0.190	n.d.	n.d.	> 10 µM (-16 %)
214	Yazh-22	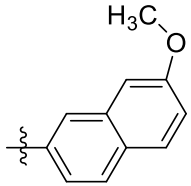	–	n.d.	>5 (23 %)	n.d.	**0.940** ± 0.65	>5 (36%)	n.d.	n.d.	n.d.
215	Yazh-9	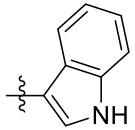	–	>5 (11 %)	**12.3** ± 1.1	>5 (24 %)	>5 (18%)	>5 (9%)	> 10 (-10%)	> 10 (10%)	n.d.
216	Yazh-6	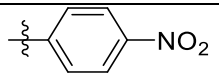	–	n.d.	>5 (48 %)	n.d.	**0.596** ± 0.240	**1.57** ± 0.042	> 10 (6%)	n.d.	n.d.

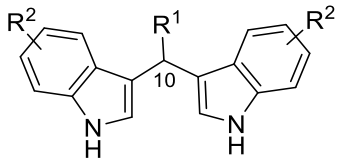

Scaffold B (149-216)

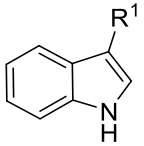

Scaffold C (217-253)

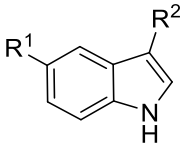

Scaffold D (254-269)

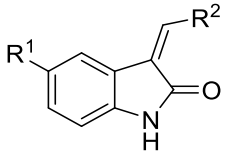

Scaffold E (270-277)

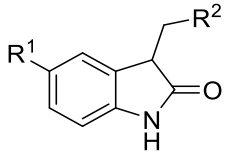

Scaffold F (278-281)

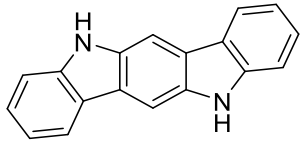

Indolo[3,2-b]carbazole (282)

No.	Cpd Name	R^1	R^2	Human $P2Y_2R$ β-arrestin assay[a] IC_{50} ± S.E.M [µM, n = 3 or 4] (% inhibition at 5 µM)	Human $P2Y_2R$ Calcium assay[a] IC_{50} ± S.E.M [µM, n = 3 or 4] (% inhibition at 5 µM)	Human P2X4R Calcium assay[b] IC_{50} ± S.E.M [µM, n = 3 or 4]	Cannabinoid receptors versus [^{3}H]CP55,940 **Human CB_1** K_i ± SEM [µM] (or % inhibition at 5 µM)	Cannabinoid receptors versus [^{3}H]CP55,940 **Human CB_2** K_i ± SEM [µM] (or % inhibition at 5 µM)	Human GPR84 cAMP assay[c] EC_{50} ± SEM [µM] (% activation at 10 µM)	Human GPR84 β-arrestin assay[d] EC_{50} ± SEM [µM] (% activation at 10 µM)	Human GPR84 Radioligand Binding K_i ± SEM [µM] (% activation of 2 nM [^{3}H]PSB-1584 at 10 µM (n=3)
Structure C: Diindolylmethanones and unsymmetrically substituted diindolylmethane derivatives											
217	Yazh-359	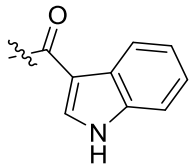	–	>5 (7 %)	>5 (9 %)	>5 (26 %)	>5 (9 %)	**1.81** ± 0.317	**0.553** ± 0.141	**17.9** ± 6.99	**1.93** ± 0.42
218	Yazh-K-277	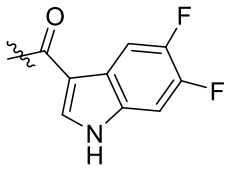	-	>5 (28%)	>5 (37%)	n.d.	n.d.	(188 %)	n.d.	< 5 (69 %)	n.d.

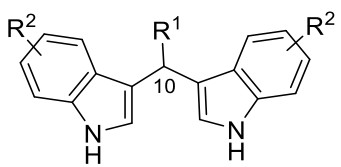

Scaffold B (149-216)

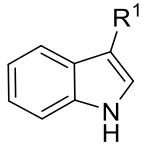

Scaffold C (217-253)

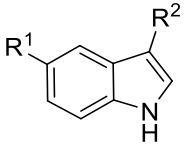

Scaffold D (254-269)

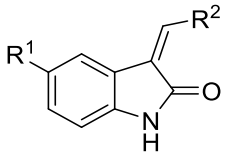

Scaffold E (270-277)

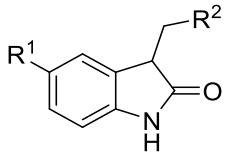

Scaffold F (278-281)

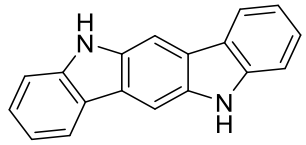

Indolo[3,2-b]carbazole (282)

No.	Cpd Name	R^1	R^2	**Human $P2Y_2R$** β-arrestin assay[a] **IC_{50}** ± S.E.M [µM, n = 3 or 4] (% inhibition at 5 µM)	**Human $P2Y_2R$** Calcium assay[a] **IC_{50}** ± S.E.M [µM, n = 3 or 4] (% inhibition at 5 µM)	**Human P2X4R** Calcium assay[b] **IC_{50}** ± S.E.M [µM, n = 3 or 4]	**Cannabinoid receptors versus** [^{3}H]CP55,940 **Human CB_1** **K_i** ± SEM [µM] (or % inhibition at 5 µM)	**Cannabinoid receptors versus** [^{3}H]CP55,940 **Human CB_2** **K_i** ± SEM [µM] (or % inhibition at 5 µM)	**Human GPR84** cAMP assay[c] **EC_{50}** ± SEM [µM] (% activation at 10 µM)	**Human GPR84** β-arrestin assay[d] **EC_{50}** ± SEM [µM] (% activation at 10 µM)	**Human GPR84** Radioligand Binding K_i ± SEM [µM] (% activation of 2 nM [^{3}H]PSB-1584 at 10 µM (n=3)
219	Yazh-K-279	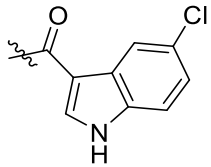	-	n.d.	>5 (27 %)	n.d.	>5 (38%)	n.d.	n.d.	n.d.	(145 %)
220	Yazh-K-280	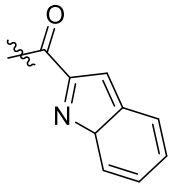	-	n.d.	>5 (35 %)	n.d.	>5 (26%)	>5 (47%)	n.d.	n.d.	**0.658** ± 0.157 (162 %)
221	Yazh-K-286	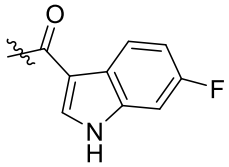	-	n.d.	>5 (19 %)	n.d.	>5 (48%)	n.d.	n.d.	n.d.	(165 %)

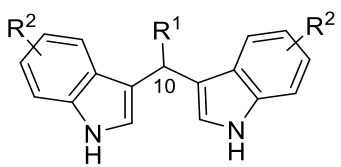

Scaffold B (149-216)

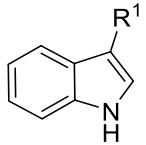

Scaffold C (217-253)

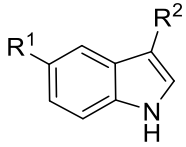

Scaffold D (254-269)

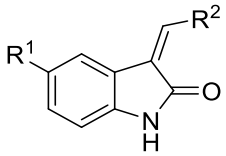

Scaffold E (270-277)

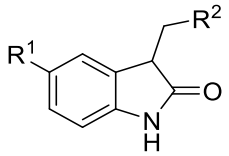

Scaffold F (278-281)

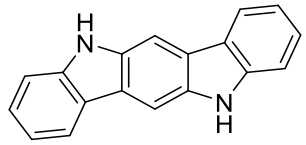

Indolo[3,2-b]carbazole (282)

No.	Cpd Name	R^1	R^2	**Human $P2Y_2R$** β-arrestin assay[a] **IC_{50}** ± S.E.M [µM, n = 3 or 4] (% inhibition at 5 µM)	**Human $P2Y_2R$** Calcium assay[a] **IC_{50}** ± S.E.M [µM, n = 3 or 4] (% inhibition at 5 µM)	**Human P2X4R** Calcium assay[b] **IC_{50}** ± S.E.M [µM, n = 3 or 4]	**Cannabinoid receptors versus** [^{3}H]CP55,940 **Human CB_1** **K_i** ± SEM [µM] (or % inhibition at 5 µM)	**Cannabinoid receptors versus** [^{3}H]CP55,940 **Human CB_2** **K_i** ± SEM [µM] (or % inhibition at 5 µM)	**Human GPR84** cAMP assay[c] **EC_{50}** ± SEM [µM] (% activation at 10 µM)	**Human GPR84** β-arrestin assay[d] **EC_{50}** ± SEM [µM] (% activation at 10 µM)	**Human GPR84** Radioligand Binding K_i ± SEM [µM] (% activation of 2 nM [^{3}H]PSB-1584 at 10 µM (n=3)
222	Yazh-K-296	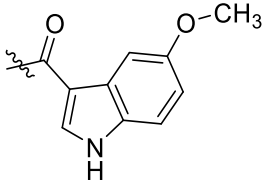	-	n.d.	>5 (27 %)	n.d.	>5 (38%)	n.d.	n.d.	n.d.	(145 %)
223	Yazh-K-313	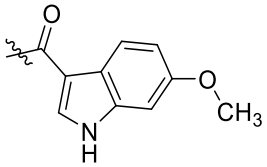	-	n.d.	>5 (35 %)	n.d.	>5 (26%)	>5 (47%)	n.d.	n.d.	**0.658** ± 0.157 (162 %)
224	Yazh-K-317	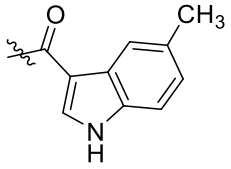	-	n.d.	>5 (19 %)	n.d.	>5 (48%)	n.d.	n.d.	n.d.	(165 %)

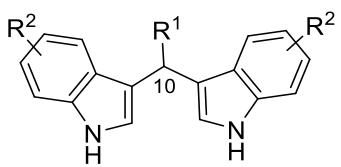

Scaffold B (149-216)

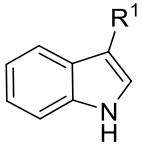

Scaffold C (217-253)

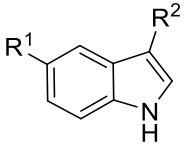

Scaffold D (254-269)

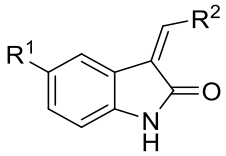

Scaffold E (270-277)

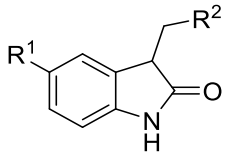

Scaffold F (278-281)

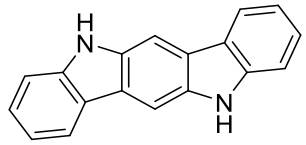

Indolo[3,2-b]carbazole (282)

No.	Cpd Name	R^1	R^2	Human $P2Y_2R$ β-arrestin assay[a] IC_{50} ± S.E.M [µM, n = 3 or 4] (% inhibition at 5 µM)	Human $P2Y_2R$ Calcium assay[a] IC_{50} ± S.E.M [µM, n = 3 or 4] (% inhibition at 5 µM)	Human P2X4R Calcium assay[b] IC_{50} ± S.E.M [µM, n = 3 or 4]	Cannabinoid receptors versus [^{3}H]CP55,940 Human CB_1 K_i ± SEM [µM] (or % inhibition at 5 µM)	Cannabinoid receptors versus [^{3}H]CP55,940 Human CB_2 K_i ± SEM [µM] (or % inhibition at 5 µM)	Human GPR84 cAMP assay[c] EC_{50} ± SEM [µM] (% activation at 10 µM)	Human GPR84 β-arrestin assay[d] EC_{50} ± SEM [µM] (% activation at 10 µM)	Human GPR84 Radioligand Binding K_i ± SEM [µM] (% activation of 2 nM [^{3}H]PSB-1584 at 10 µM (n=3)
225	Yazh-K-233	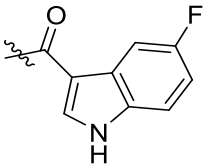	-	n.d.	>5 (-21 %)	n.d.	>5 (16%)	>5 (16%)	n.d.	n.d.	n.d.
226	Yazh-K-267	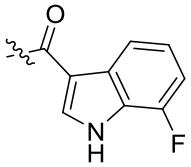	-	n.d.	>5 (1 %)	n.d.	>5 (30%)	>5 (20%)	n.d.	n.d.	>1 (101± 4)
227	Yazh-K-320	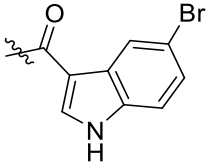	-	n.d.	>5 (29 %)	n.d.	>5 (40%)	n.d.	n.d.	n.d.	**0.120** ± 0.017 (198 %)

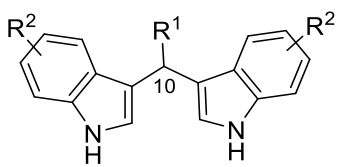

Scaffold B (149-216)

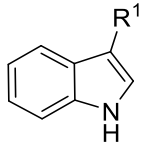

Scaffold C (217-253)

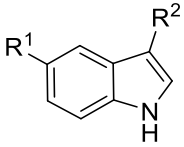

Scaffold D (254-269)

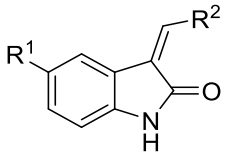

Scaffold E (270-277)

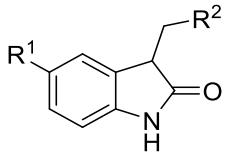

Scaffold F (278-281)

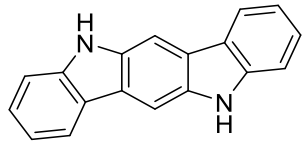

Indolo[3,2-b]carbazole (282)

No.	Cpd Name	R^1	R^2	**Human $P2Y_2R$** β-arrestin assay[a] **IC_{50}** ± S.E.M [µM, n = 3 or 4] (% inhibition at 5 µM)	**Human $P2Y_2R$** Calcium assay[a] **IC_{50}** ± S.E.M [µM, n = 3 or 4] (% inhibition at 5 µM)	**Human P2X4R** Calcium assay[b] **IC_{50}** ± S.E.M [µM, n = 3 or 4]	**Cannabinoid receptors versus** [^{3}H]CP55,940 **Human CB_1** **K_i** ± SEM [µM] (or % inhibition at 5 µM)	**Cannabinoid receptors versus** [^{3}H]CP55,940 **Human CB_2** **K_i** ± SEM [µM] (or % inhibition at 5 µM)	**Human GPR84** cAMP assay[c] **EC_{50}** ± SEM [µM] (% activation at 10 µM)	**Human GPR84** β-arrestin assay[d] **EC_{50}** ± SEM [µM] (% activation at 10 µM)	**Human GPR84** Radioligand Binding K_i ± SEM [µM] (% activation of 2 nM [^{3}H]PSB-1584 at 10 µM (n=3)
228	Yazh-K-321	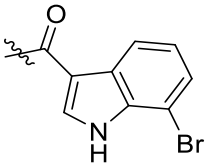	-	n.d.	>5 (45 %)	n.d.	>5 (41%)	n.d.	n.d.	n.d.	**0.404** ± 0.024 (156 %)
229	Yazh-K-329	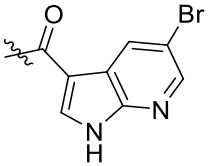	-	n.d.	>5 (36 %)	n.d.	>5 (40%)	>5 (38%)	n.d.	n.d.	**0.541** ± 0194 (146 %)
230	Yazh-K-337	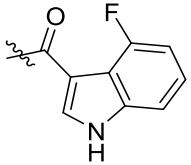	-	n.d.	>5 (6 %)	n.d.	>5 (32%)	n.d.	n.d.	n.d.	(138 %)

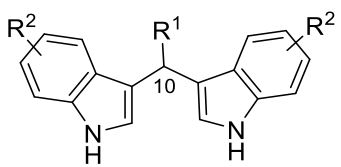

Scaffold B (149-216)

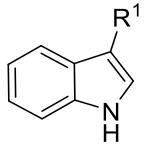

Scaffold C (217-253)

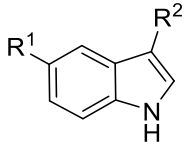

Scaffold D (254-269)

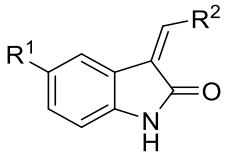

Scaffold E (270-277)

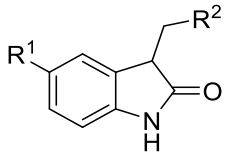

Scaffold F (278-281)

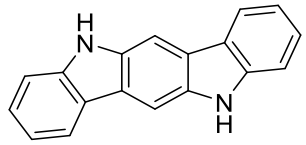

Indolo[3,2-b]carbazole (282)

No.	Cpd Name	R^1	R^2	Human $P2Y_2R$ β-arrestin assay[a] IC_{50} ± S.E.M [µM, n = 3 or 4] (% inhibition at 5 µM)	Human $P2Y_2R$ Calcium assay[a] IC_{50} ± S.E.M [µM, n = 3 or 4] (% inhibition at 5 µM)	Human P2X4R Calcium assay[b] IC_{50} ± S.E.M [µM, n = 3 or 4]	Cannabinoid receptors versus [^{3}H]CP55,940 Human CB_1 K_i ± SEM [µM] (or % inhibition at 5 µM)	Cannabinoid receptors versus [^{3}H]CP55,940 Human CB_2 K_i ± SEM [µM] (or % inhibition at 5 µM)	Human GPR84 cAMP assay[c] EC_{50} ± SEM [µM] (% activation at 10 µM)	Human GPR84 β-arrestin assay[d] EC_{50} ± SEM [µM] (% activation at 10 µM)	Human GPR84 Radioligand Binding K_i ± SEM [µM] (% activation of 2 nM [^{3}H]PSB-1584 at 10 µM (n=3)
231	Yazh-K-338	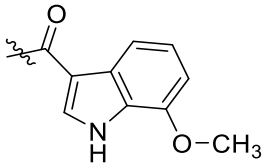	-	n.d.	>5 (8 %)	n.d.	n.d.	>5 (27%)	n.d.	n.d.	(97 %)
232	Yazh-K-346	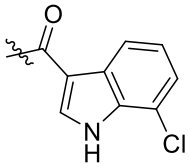	-	n.d.	≈5 (51 %)	n.d.	>5 (46%)	n.d.	n.d.	n.d.	(150 %)
233	Yazh-K-349	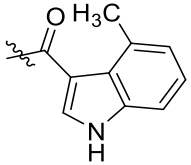	-	n.d.	>5 (24 %)	n.d.	n.d.	n.d.	n.d.	n.d.	(146 %)

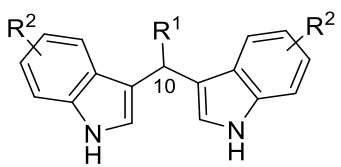

Scaffold B (149-216)

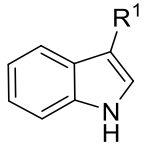

Scaffold C (217-253)

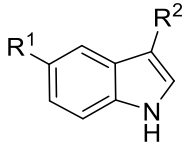

Scaffold D (254-269)

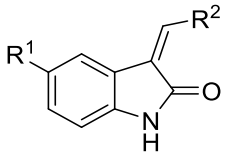

Scaffold E (270-277)

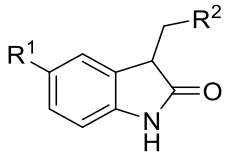

Scaffold F (278-281)

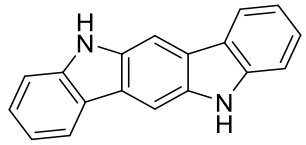

Indolo[3,2-b]carbazole (282)

No.	Cpd Name	R^1	R^2	Human $P2Y_2R$ β-arrestin assay[a] IC_{50} ± S.E.M [µM, n = 3 or 4] (% inhibition at 5 µM)	Human $P2Y_2R$ Calcium assay[a] IC_{50} ± S.E.M [µM, n = 3 or 4] (% inhibition at 5 µM)	Human P2X4R Calcium assay[b] IC_{50} ± S.E.M [µM, n = 3 or 4]	Cannabinoid receptors versus [^{3}H]CP55,940 Human CB_1 K_i ± SEM [µM] (or % inhibition at 5 µM)	Cannabinoid receptors versus [^{3}H]CP55,940 Human CB_2 K_i ± SEM [µM] (or % inhibition at 5 µM)	Human GPR84 cAMP assay[c] EC_{50} ± SEM [µM] (% activation at 10 µM)	Human GPR84 β-arrestin assay[d] EC_{50} ± SEM [µM] (% activation at 10 µM)	Human GPR84 Radioligand Binding K_i ± SEM [µM] (% activation of 2 nM [^{3}H]PSB-1584 at 10 µM (n=3)
234	Yazh-242	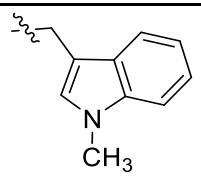	–	**22.6** ± 3.4	**5.84** ± 0.86	>5 (23 %)	>5 (16%)	>5 (30%)	≥ 10 (43%)	> 10 (8%)	n.d.
235	Yazh-184	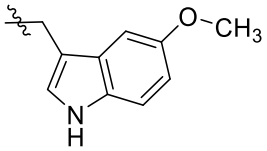	–	n.d.	>5 (29 %)	n.d.	>5 (33%)	**2.32** ± 0.716	**1.89** ± 0.19	**6.47** ± 3.20	**0.495** ± 0.096 [53 %]
236	Yazh-244	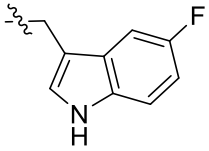	–	n.d.	>5 (47 %)	n.d.	>5 (20%)	**3.78** ± 0.303	**0.264** ± 0.075	**1.08** ± 0.58	**0.276** ± 0.065 [55 %]
237	Yazh-K-117A	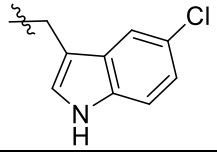	–	**19.4** ± 3.1	**6.23** ± 0.74	**n.d**	**4.40** ± 0.407	**1.21** ± 0.053	n.d.	n.d.	**0.322** ± 0.033 (230 %)

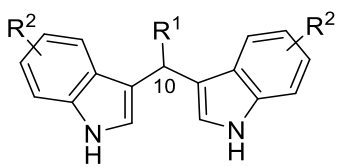

Scaffold B (149-216)

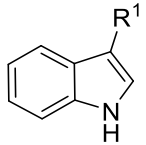

Scaffold C (217-253)

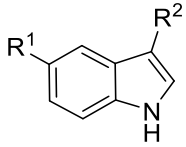

Scaffold D (254-269)

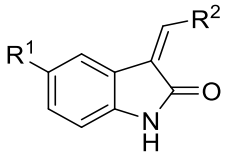

Scaffold E (270-277)

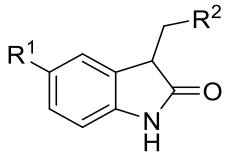

Scaffold F (278-281)

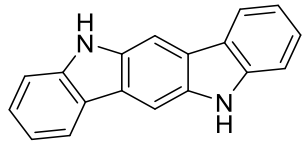

Indolo[3,2-b]carbazole (282)

No.	Cpd Name	R^1	R^2	Human $P2Y_2R$ β-arrestin assay[a] IC_{50} ± S.E.M [µM, n = 3 or 4] (% inhibition at 5 µM)	Human $P2Y_2R$ Calcium assay[a] IC_{50} ± S.E.M [µM, n = 3 or 4] (% inhibition at 5 µM)	Human P2X4R Calcium assay[b] IC_{50} ± S.E.M [µM, n = 3 or 4]	Cannabinoid receptors versus [^{3}H]CP55,940 Human CB_1 K_i ± SEM [µM] (or % inhibition at 5 µM)	Cannabinoid receptors versus [^{3}H]CP55,940 Human CB_2 K_i ± SEM [µM] (or % inhibition at 5 µM)	Human GPR84 cAMP assay[c] EC_{50} ± SEM [µM] (% activation at 10 µM)	Human GPR84 β-arrestin assay[d] EC_{50} ± SEM [µM] (% activation at 10 µM)	Human GPR84 Radioligand Binding K_i ± SEM [µM] (% activation of 2 nM [^{3}H]PSB-1584 at 10 µM (n=3)
238	Yazh-K-189B	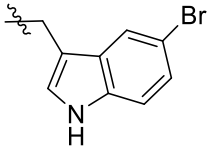	-	**49.1** ± 1.3 (4 %) (extrapolated)	**7.56** ± 0.43	n.d.	n.d.	n.d.	n.d.	n.d.	n.d.
239	Yazh-198	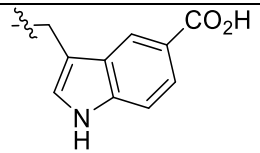	–	n.d.	>5 (1 %)	n.d.	>5 (-7%)	>5 (20%)	> 10 (5%)	n.d.	n.d.
240	Yazh-195	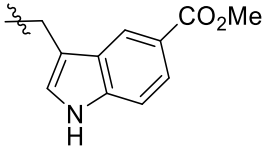	–	n.d.	>5 (39 %)	n.d.	>5 (41%)	< 5 (78%)	≈ 10 (57%)	n.d.	n.d.
241	Yazh-K-169	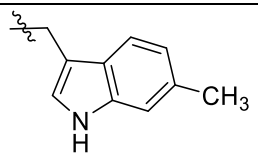	-	>5 (5 %)	**8.37** ± 0.86	n.d.	n.d.	n.d.	n.d.	n.d.	**0.247** ± 0.059 (222 %)

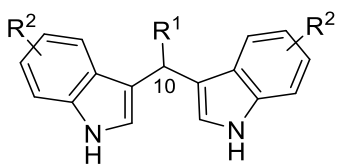

Scaffold B (149-216)

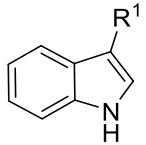

Scaffold C (217-253)

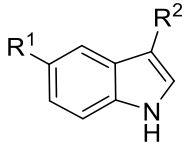

Scaffold D (254-269)

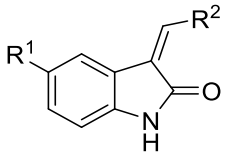

Scaffold E (270-277)

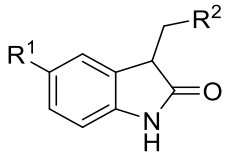

Scaffold F (278-281)

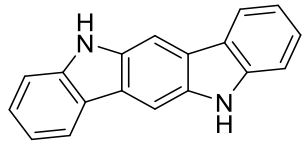

Indolo[3,2-b]carbazole (282)

No.	Cpd Name	R^1	R^2	Human $P2Y_2R$ β-arrestin assay[a] IC_{50} ± S.E.M [µM, n = 3 or 4] (% inhibition at 5 µM)	Human $P2Y_2R$ Calcium assay[a] IC_{50} ± S.E.M [µM, n = 3 or 4] (% inhibition at 5 µM)	Human P2X4R Calcium assay[b] IC_{50} ± S.E.M [µM, n = 3 or 4]	Cannabinoid receptors versus [^{3}H]CP55,940 Human CB_1 K_i ± SEM [µM] (or % inhibition at 5 µM)	Cannabinoid receptors versus [^{3}H]CP55,940 Human CB_2 K_i ± SEM [µM] (or % inhibition at 5 µM)	Human GPR84 cAMP assay[c] EC_{50} ± SEM [µM] (% activation at 10 µM)	Human GPR84 β-arrestin assay[d] EC_{50} ± SEM [µM] (% activation at 10 µM)	Human GPR84 Radioligand Binding K_i ± SEM [µM] (% activation of 2 nM [^{3}H]PSB-1584 at 10 µM (n=3)
242	Yazh-K141	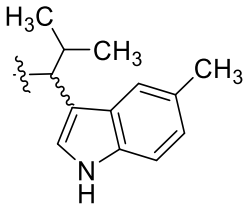	–	>5 (12 %)	**3.85** ± 1.00	n.d.	**4.48** ± 1.16	**6.85** ± 2.24	n.d.	n.d.	> 10 µM (38 %)
243	Yazh-K137A	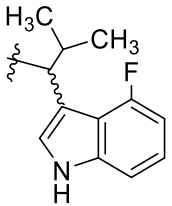	–	>5 (13 %)	**2.67** ± 0.58	n.d.	>5 (32%)	**14.4** ± 0.667	n.d.	n.d.	> 10 µM (30 %)
244	Yazh-K139	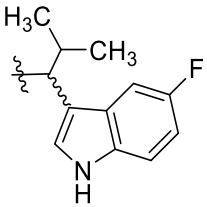	–	>5 (5 %)	**3.77** ± 0.84	n.d.	**3.55** ± 0.88	>5 (48%)	n.d.	n.d.	> 10 µM (-2 %)

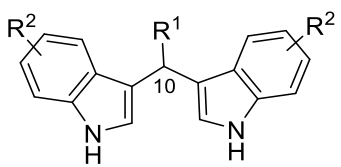

Scaffold B (149-216)

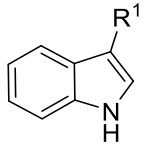

Scaffold C (217-253)

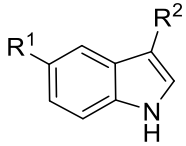

Scaffold D (254-269)

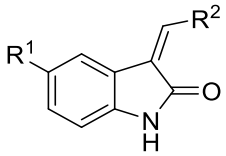

Scaffold E (270-277)

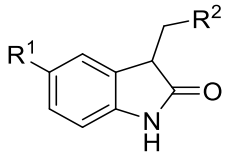

Scaffold F (278-281)

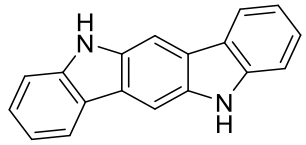

Indolo[3,2-b]carbazole (282)

No.	Cpd Name	R^1	R^2	Human $P2Y_2R$ β-arrestin assay[a] IC_{50} ± S.E.M [µM, n = 3 or 4] (% inhibition at 5 µM)	Human $P2Y_2R$ Calcium assay[a] IC_{50} ± S.E.M [µM, n = 3 or 4] (% inhibition at 5 µM)	Human P2X4R Calcium assay[b] IC_{50} ± S.E.M [µM, n = 3 or 4]	Cannabinoid receptors versus [^{3}H]CP55,940 Human CB_1 K_i ± SEM [µM] (or % inhibition at 5 µM)	Cannabinoid receptors versus [^{3}H]CP55,940 Human CB_2 K_i ± SEM [µM] (or % inhibition at 5 µM)	Human GPR84 cAMP assay[c] EC_{50} ± SEM [µM] (% activation at 10 µM)	Human GPR84 β-arrestin assay[d] EC_{50} ± SEM [µM] (% activation at 10 µM)	Human GPR84 Radioligand Binding K_i ± SEM [µM] (% activation of 2 nM [^{3}H]PSB-1584 at 10 µM (n=3)
245	Yazh-K138	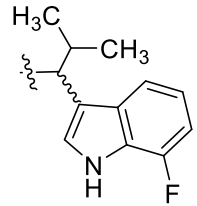	–	>5 (8 %)	**3.82** ± 0.81	n.d.	**8.06** ± 0.747	>5 (44%)	n.d.	n.d.	> 10 µM (6 %)
246	Yazh-K134	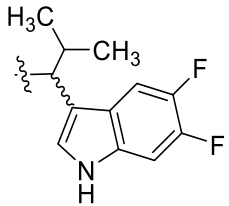	–	>5 (11 %)	**3.31** ± 0.76	n.d	>5 (38%)	≈ 5 (49 %)	n.d.	n.d.	> 10 µM (14 %)
247	Yazh-K135A	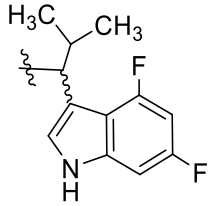	–	>5 (10 %)	**1.91** ± 0.22	**4.52** ± 1.06	**4.43** ± 0.546	**8.38** ± 0.404	n.d.	n.d.	> 10 µM (27 %)

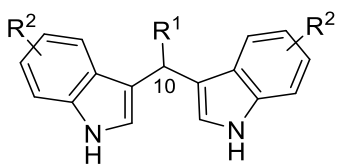

Scaffold B (149-216)

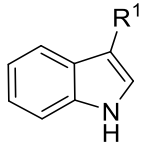

Scaffold C (217-253)

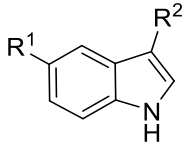

Scaffold D (254-269)

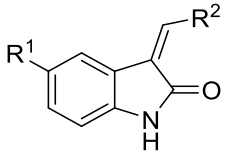

Scaffold E (270-277)

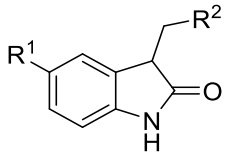

Scaffold F (278-281)

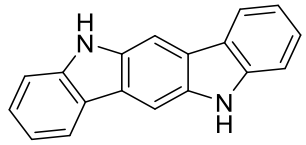

Indolo[3,2-b]carbazole (282)

No.	Cpd Name	R^1	R^2	Human $P2Y_2R$ β-arrestin assay[a] IC_{50} ± S.E.M [µM, n = 3 or 4] (% inhibition at 5 µM)	Human $P2Y_2R$ Calcium assay[a] IC_{50} ± S.E.M [µM, n = 3 or 4] (% inhibition at 5 µM)	Human P2X4R Calcium assay[b] IC_{50} ± S.E.M [µM, n = 3 or 4]	Cannabinoid receptors versus [^{3}H]CP55,940 Human CB_1 K_i ± SEM [µM] (or % inhibition at 5 µM)	Cannabinoid receptors versus [^{3}H]CP55,940 Human CB_2 K_i ± SEM [µM] (or % inhibition at 5 µM)	Human GPR84 cAMP assay[c] EC_{50} ± SEM [µM] (% activation at 10 µM)	Human GPR84 β-arrestin assay[d] EC_{50} ± SEM [µM] (% activation at 10 µM)	Human GPR84 Radioligand Binding K_i ± SEM [µM] (% activation of 2 nM [^{3}H]PSB-1584 at 10 µM (n=3)
248	Yazh-K136	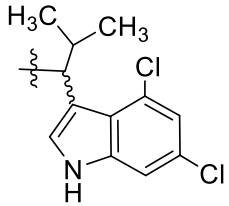	–	>5 (12 %)	**4.35** ± 1.08	n.d.	**3.81** ± 0.569	**6.68** ± 0.414	n.d.	n.d.	> 10 µM (22 %)
249	Yazh-86	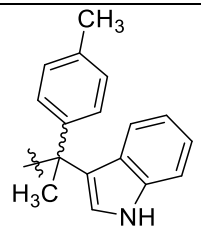	–	**25.1** ± 0.9	**12.7** ± 2.0*	n.d	>5 (44%)	**0.674** ± 0.529 (maximal inhibition: 53%)	n.d.	n.d.	n.d

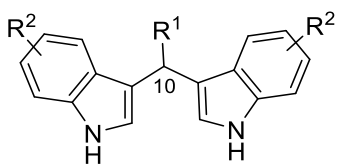

Scaffold B (149-216)

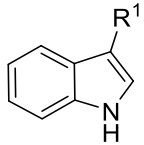

Scaffold C (217-253)

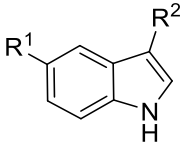

Scaffold D (254-269)

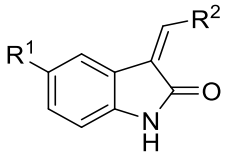

Scaffold E (270-277)

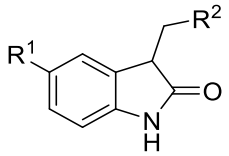

Scaffold F (278-281)

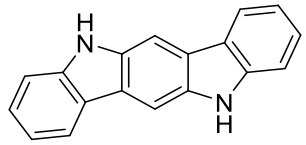

Indolo[3,2-b]carbazole (282)

No.	Cpd Name	R^1	R^2	Human $P2Y_2R$ β-arrestin assay[a] IC_{50} ± S.E.M [µM, n = 3 or 4] (% inhibition at 5 µM)	Human $P2Y_2R$ Calcium assay[a] IC_{50} ± S.E.M [µM, n = 3 or 4] (% inhibition at 5 µM)	Human P2X4R Calcium assay[b] IC_{50} ± S.E.M [µM, n = 3 or 4]	Cannabinoid receptors versus [^{3}H]CP55,940 Human CB_1 K_i ± SEM [µM] (or % inhibition at 5 µM)	Cannabinoid receptors versus [^{3}H]CP55,940 Human CB_2 K_i ± SEM [µM] (or % inhibition at 5 µM)	Human GPR84 cAMP assay[c] EC_{50} ± SEM [µM] (% activation at 10 µM)	Human GPR84 β-arrestin assay[d] EC_{50} ± SEM [µM] (% activation at 10 µM)	Human GPR84 Radioligand Binding K_i ± SEM [µM] (% activation of 2 nM [^{3}H]PSB-1584 at 10 µM (n=3)
250	Yazh-83	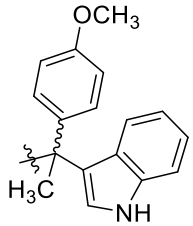	–	n.d.	>5 (43 %)	n.d.	**2.84** ± 0.171	>5 (35%)	n.d.	n.d.	n.d.
251	Yazh-80	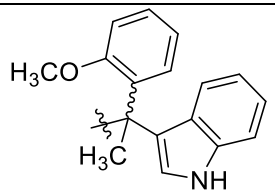	–	n.d.	>5 (47 %)	n.d.	**1.14** ± 0.245	>5 (39%)	n.d.	n.d.	n.d.
252	Yazh-K130A	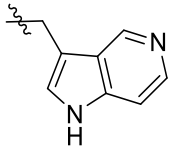	–	>5 (1 %)	>5 (-6 %)	n.d.	>5 (30%)	>5 (25%)	n.d.	n.d.	> 10 µM (-7 %)

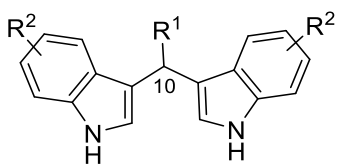

Scaffold B (149-216)

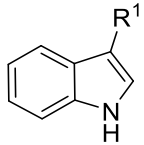

Scaffold C (217-253)

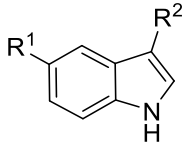

Scaffold D (254-269)

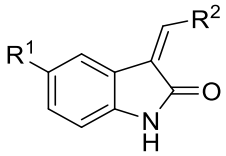

Scaffold E (270-277)

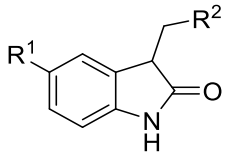

Scaffold F (278-281)

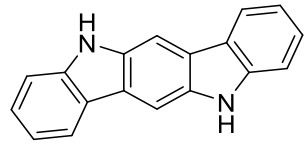

Indolo[3,2-b]carbazole (282)

No.	Cpd Name	R^1	R^2	Human $P2Y_2R$		Human P2X4R	Cannabinoid receptors versus [^{3}H]CP55,940		Human GPR84		
				β-arrestin assay[a]	Calcium assay[a]	Calcium assay[b]	**Human CB_1**	**Human CB_2**	cAMP assay[c]	β-arrestin assay[d]	Radioligand Binding
				IC_{50} ± S.E.M [µM, n = 3 or 4] (% inhibition at 5 µM)	**IC_{50}** ± S.E.M [µM, n = 3 or 4] (% inhibition at 5 µM)	**IC_{50}** ± S.E.M [µM, n = 3 or 4]	**K_i** ± SEM [µM] (or % inhibition at 5 µM)	**K_i** ± SEM [µM] (or % inhibition at 5 µM)	**EC_{50}** ± SEM [µM] (% activation at 10 µM)	**EC_{50}** ± SEM [µM] (% activation at 10 µM)	K_i ± SEM [µM] (% activation of 2 nM [^{3}H]PSB-1584 at 10 µM (n=3)
253	Yazh-K-131	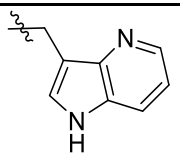	–	>5 (-7 %)	>5 (7 %)	n.d.	>5 (27%)	>5 (44%)	n.d.	n.d.	> 10 µM (21 %)

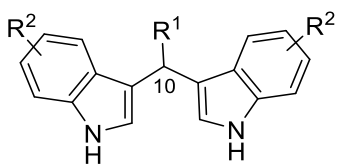

Scaffold B (149-216)

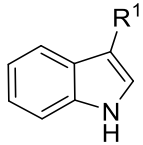

Scaffold C (217-253)

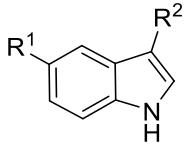

Scaffold D (254-269)

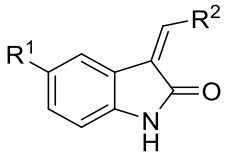

Scaffold E (270-277)

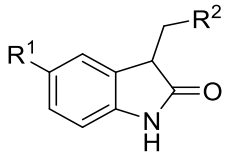

Scaffold F (278-281)

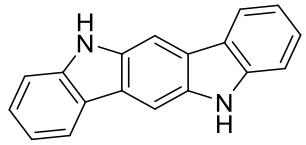

Indolo[3,2-b]carbazole (282)

No.	Cpd Name	R^1	R^2	Human $P2Y_2R$ β-arrestin assay[a] IC_{50} ± S.E.M [µM, n = 3 or 4] (% inhibition at 5 µM)	Human $P2Y_2R$ Calcium assay[a] IC_{50} ± S.E.M [µM, n = 3 or 4] (% inhibition at 5 µM)	Human P2X4R Calcium assay[b] IC_{50} ± S.E.M [µM, n = 3 or 4]	Cannabinoid receptors versus [^{3}H]CP55,940 Human CB_1[c] K_i ± SEM [µM] (or % inhibition at 5 µM)	Cannabinoid receptors versus [^{3}H]CP55,940 Human CB_2[c] K_i ± SEM [µM] (or % inhibition at 5 µM)	Human GPR84 cAMP assay[c] EC_{50} ± SEM [µM] (% activation at 10 µM)	Human GPR84 β-arrestin assay[d] EC_{50} ± SEM [µM] (% activation at 10 µM)	Human GPR84 Radioligand Binding K_i ± SEM [µM] (% activation of 2 nM [^{3}H]PSB-1584 at 10 µM (n=3)
Structure D: Unsymmetrically substituted diindolylmethanone and 5-indolylmethane derivatives											
254	Yazh-K-283	CH_3	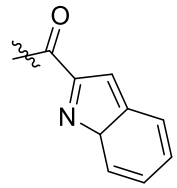	n.d.	>5 (12 %)	n.d.	n.d.	>5 (49%)	n.d.	n.d.	(123 %)
255	Yazh-K-330	F	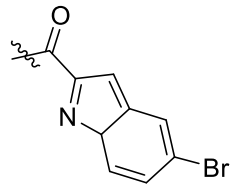	n.d.	>5 (19 %)	n.d.	>5 (37%)	>5 (32%)	n.d.	n.d.	(106 %)
256	Yazh-K-304	F	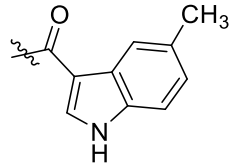	n.d.	>5 (34 %)	n.d.	>5 (38%)	n.d.	n.d.	n.d.	(164 %)

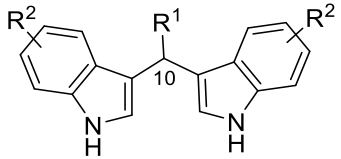

Scaffold B (149-216)

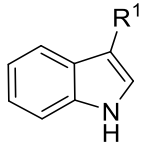

Scaffold C (217-253)

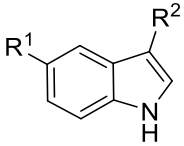

Scaffold D (254-269)

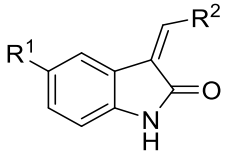

Scaffold E (270-277)

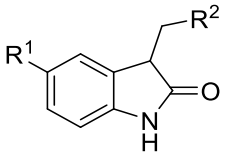

Scaffold F (278-281)

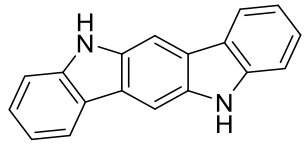

Indolo[3,2-b]carbazole (282)

No.	Cpd Name	R^1	R^2	Human $P2Y_2R$ β-arrestin assay[a] IC_{50} ± S.E.M [µM, n = 3 or 4] (% inhibition at 5 µM)	Human $P2Y_2R$ Calcium assay[a] IC_{50} ± S.E.M [µM, n = 3 or 4] (% inhibition at 5 µM)	Human P2X4R Calcium assay[b] IC_{50} ± S.E.M [µM, n = 3 or 4]	Cannabinoid receptors versus [^{3}H]CP55,940 Human CB_1[c] K_i ± SEM [µM] (or % inhibition at 5 µM)	Cannabinoid receptors versus [^{3}H]CP55,940 Human CB_2[c] K_i ± SEM [µM] (or % inhibition at 5 µM)	Human GPR84 cAMP assay[c] EC_{50} ± SEM [µM] (% activation at 10 µM)	Human GPR84 β-arrestin assay[d] EC_{50} ± SEM [µM] (% activation at 10 µM)	Human GPR84 Radioligand Binding K_i ± SEM [µM] (% activation of 2 nM [^{3}H]PSB-1584 at 10 µM (n=3)
257	Yazh-K-312		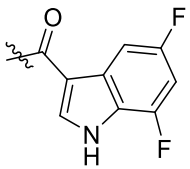	n.d.	>5 (29 %)	n.d.	>5 (19%)	>5 (42%)	n.d.	n.d.	**0.149** ± 0.027 (205 %)
258	Yazh-K-319		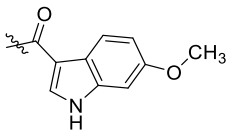	n.d.	≥5 (47 %)	n.d.	n.d.	>5 (37%)	n.d.	n.d.	**0.170** ± 0.027 (188 %)
259	Yazh-K-318	4-F, 6-F	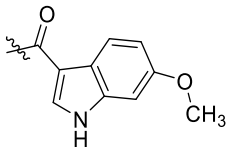	n.d.	< 5 (64 %)	n.d.	>5 (45%)	n.d.	n.d.	n.d.	**0.167** ± 0.053 (223 %)
260	Yazh-K-305		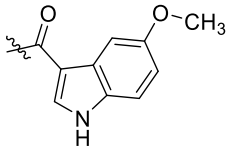	n.d.	>5 (17 %)	n.d.	>5 (38%)	>5 (38%)	n.d.	n.d.	(162 %)

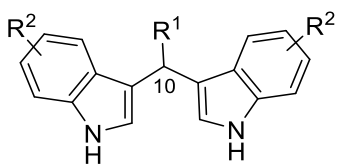

Scaffold B (149-216)

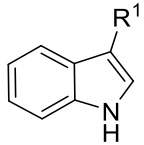

Scaffold C (217-253)

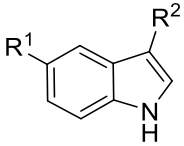

Scaffold D (254-269)

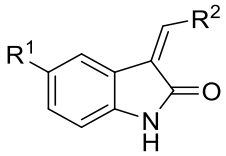

Scaffold E (270-277)

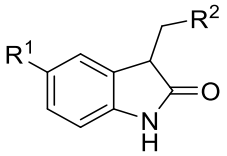

Scaffold F (278-281)

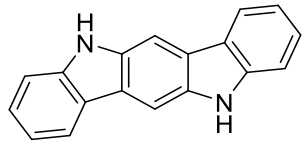

Indolo[3,2-b]carbazole (282)

No.	Cpd Name	R^1	R^2	Human $P2Y_2R$		Human P2X4R	Cannabinoid receptors versus [^{3}H]CP55,940		Human GPR84		
				β-arrestin assay[a]	Calcium assay[a]	Calcium assay[b]	Human CB_1[c]	Human CB_2[c]	cAMP assay[c]	β-arrestin assay[d]	Radioligand Binding
				IC_{50} ± S.E.M [µM, n = 3 or 4] (% inhibition at 5 µM)	**IC_{50}** ± S.E.M [µM, n = 3 or 4] (% inhibition at 5 µM)	**IC_{50}** ± S.E.M [µM, n = 3 or 4]	**K_i** ± SEM [µM] (or % inhibition at 5 µM)	**K_i** ± SEM [µM] (or % inhibition at 5 µM)	**EC_{50}** ± SEM [µM] (% activation at 10 µM)	**EC_{50}** ± SEM [µM] (% activation at 10 µM)	K_i ± SEM [µM] (% activation of 2 nM [^{3}H]PSB-1584 at 10 µM (n=3)
261	Yazh-K-379		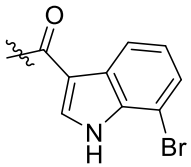	n.d.	>5 (47 %)	n.d.	>5 (40%)	n.d.	n.d.	n.d.	163 %)
262	Yazh-K-380		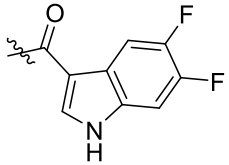	n.d.	<5 (76 %)	n.d.	>5 (29%)	>5 (38%)	n.d.	n.d.	(170 %)
263	Yazh-K-122B		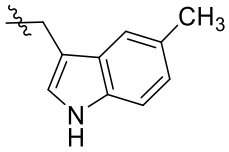	>5 (-6 %)	**8.65** ± 1.25	n.d	>5 (48%)	**1.20** ± 0.286	n.d.	n.d.	**0.711** ± 0.250 (192 %)

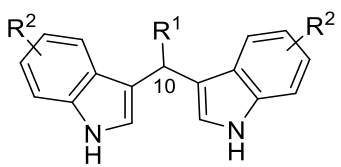

Scaffold B (149-216)

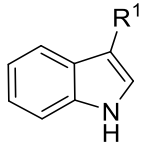

Scaffold C (217-253)

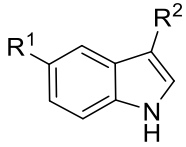

Scaffold D (254-269)

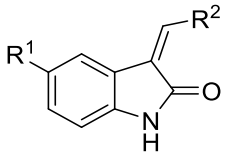

Scaffold E (270-277)

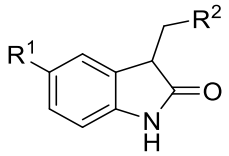

Scaffold F (278-281)

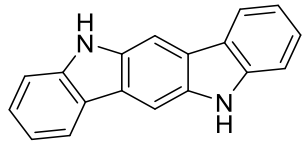

Indolo[3,2-b]carbazole (282)

No.	Cpd Name	R^1	R^2	Human $P2Y_2R$ β-arrestin assay[a] IC_{50} ± S.E.M [µM, n = 3 or 4] (% inhibition at 5 µM)	Human $P2Y_2R$ Calcium assay[a] IC_{50} ± S.E.M [µM, n = 3 or 4] (% inhibition at 5 µM)	Human P2X4R Calcium assay[b] IC_{50} ± S.E.M [µM, n = 3 or 4]	Cannabinoid receptors versus [^{3}H]CP55,940 Human CB_1[c] K_i ± SEM [µM] (or % inhibition at 5 µM)	Cannabinoid receptors versus [^{3}H]CP55,940 Human CB_2[c] K_i ± SEM [µM] (or % inhibition at 5 µM)	Human GPR84 cAMP assay[c] EC_{50} ± SEM [µM] (% activation at 10 µM)	Human GPR84 β-arrestin assay[d] EC_{50} ± SEM [µM] (% activation at 10 µM)	Human GPR84 Radioligand Binding K_i ± SEM [µM] (% activation of 2 nM [^{3}H]PSB-1584 at 10 µM (n=3)
264	Yazh-K-126		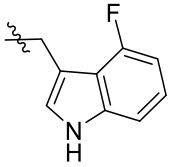	>5 (19 %)	**8.29** ± 1.06	n.d.	>5 (39%)	**1.17** ± 0.136	n.d.	n.d.	**0.568** ± 0.080 (261 %)
265	Yazh-K-118a		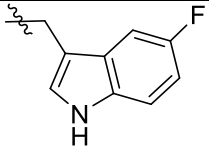	**49.8** ± 3.6	**8.74** ± 1.25	n.d.	>5 (49%)	**2.44** ± 0.267	n.d.	n.d.	**0.676** ± 0.170 (192 %)
266	Yazh-K-123A		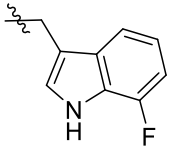	>5 (18 %)	**9.04** ± 1.07	n.d.	>5 (31%)	**2.82** ± 0.09	n.d.	n.d.	**0.241** ± 0.116 (230 %)

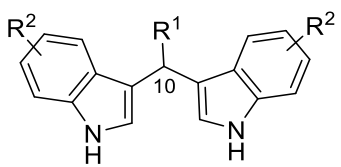

Scaffold B (149-216)

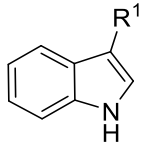

Scaffold C (217-253)

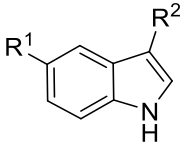

Scaffold D (254-269)

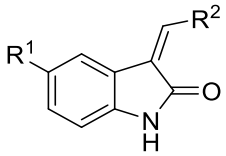

Scaffold E (270-277)

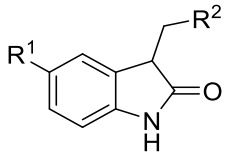

Scaffold F (278-281)

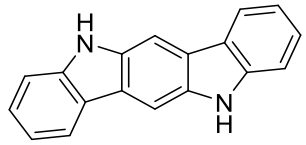

Indolo[3,2-b]carbazole (282)

No.	Cpd Name	R^1	R^2	Human $P2Y_2R$ β-arrestin assay[a] IC_{50} ± S.E.M [µM, n = 3 or 4] (% inhibition at 5 µM)	Human $P2Y_2R$ Calcium assay[a] IC_{50} ± S.E.M [µM, n = 3 or 4] (% inhibition at 5 µM)	Human P2X4R Calcium assay[b] IC_{50} ± S.E.M [µM, n = 3 or 4]	Cannabinoid receptors versus [^{3}H]CP55,940 Human CB_1[c] K_i ± SEM [µM] (or % inhibition at 5 µM)	Cannabinoid receptors versus [^{3}H]CP55,940 Human CB_2[c] K_i ± SEM [µM] (or % inhibition at 5 µM)	Human GPR84 cAMP assay[c] EC_{50} ± SEM [µM] (% activation at 10 µM)	Human GPR84 β-arrestin assay[d] EC_{50} ± SEM [µM] (% activation at 10 µM)	Human GPR84 Radioligand Binding K_i ± SEM [µM] (% activation of 2 nM [^{3}H]PSB-1584 at 10 µM (n=3)
267	Yazh-K-119		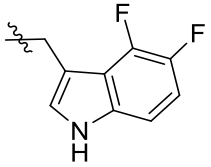	**29.3** ± 6.1	**7.13** ± 0.82	n.d	>5 (36%)	**3.74** ± 0.143	n.d.	n.d.	**0.286** ± 0.041 (222 %)
268	Yazh-K-125A		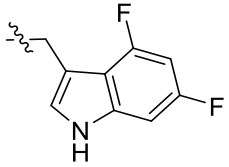	**33.0** ± 5.3	**6.17** ± 0.46	n.d.	>5 (44%)	**1.65** ± 0.155	n.d.	n.d.	**0.960** ± 0.420 (289 %)
269	Yazh-K-121D		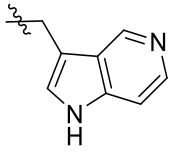	>5 (16 %)	>5 (5 %)	n.d	>5 (11%)	>5 (11%)	n.d.	n.d.	> 10 µM (-7 %)

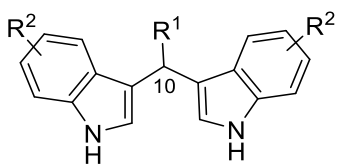

Scaffold B (149-216)

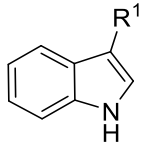

Scaffold C (217-253)

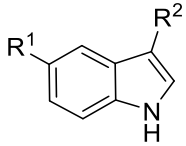

Scaffold D (254-269)

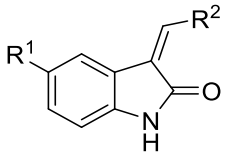

Scaffold E (270-277)

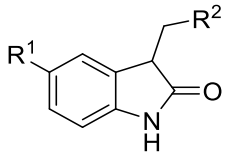

Scaffold F (278-281)

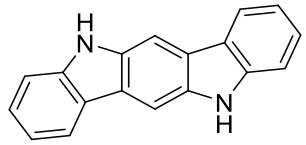

Indolo[3,2-b]carbazole (282)

No.	Cpd Name	R^1	R^2	Human $P2Y_2R$ β-arrestin assay[a] IC_{50} ± S.E.M [µM, n = 3 or 4] (% inhibition at 5 µM)	Human $P2Y_2R$ Calcium assay[a] IC_{50} ± S.E.M [µM, n = 3 or 4] (% inhibition at 5 µM)	Human P2X4R Calcium assay[b] IC_{50} ± S.E.M [µM, n = 3 or 4]	Cannabinoid receptors versus [^{3}H]CP55,940 Human CB_1 K_i ± SEM [µM] (or % inhibition at 5 µM)	Cannabinoid receptors versus [^{3}H]CP55,940 Human CB_2 K_i ± SEM [µM] (or % inhibition at 5 µM)	Human GPR84 cAMP assay[c] EC_{50} ± SEM [µM] (% activation at 10 µM)	Human GPR84 β-arrestin assay[d] EC_{50} ± SEM [µM] (% activation at 10 µM)	Human GPR84 Radioligand Binding K_i ± SEM [µM] (% activation of 2 nM [^{3}H]PSB-1584 at 10 µM (n=3)
Structure E: Unsymmetrically substituted 2-indolinone derivatives (with methene bridge)											
270	Yazh-260	H	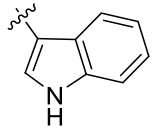	n.d.	≈5 (50 %)	>5 (4 %)	>5 (30%)	>5 (43%)	> 10 (-17%)	> 10 (-22 %)	n.d
271	Yazh-250	H	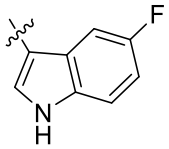	n.d.	≈5 (49 %)	n.d.	>5 (43%)	>5 (43%)	> 10 (-1%)	n.d.	n.d.
272	Yazh-236	H	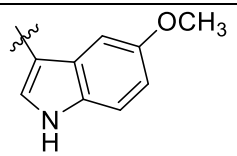	n.d.	≈5 (54 %)	n.d.	>5 (38%)	>5 (28%)	> 10 (-10%)	n.d.	n.d.

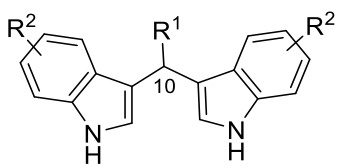

Scaffold B (149-216)

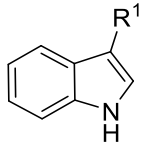

Scaffold C (217-253)

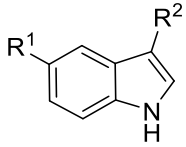

Scaffold D (254-269)

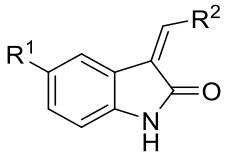

Scaffold E (270-277)

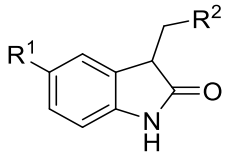

Scaffold F (278-281)

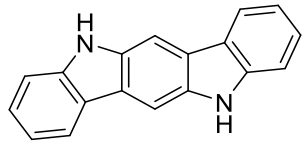

Indolo[3,2-b]carbazole (282)

No.	Cpd Name	R^1	R^2	Human $P2Y_2R$ β-arrestin assay[a] IC_{50} ± S.E.M [µM, n = 3 or 4] (% inhibition at 5 µM)	Human $P2Y_2R$ Calcium assay[a] IC_{50} ± S.E.M [µM, n = 3 or 4] (% inhibition at 5 µM)	Human P2X4R Calcium assay[b] IC_{50} ± S.E.M [µM, n = 3 or 4]	Cannabinoid receptors versus [^{3}H]CP55,940 Human CB_1 K_i ± SEM [µM] (or % inhibition at 5 µM)	Cannabinoid receptors versus [^{3}H]CP55,940 Human CB_2 K_i ± SEM [µM] (or % inhibition at 5 µM)	Human GPR84 cAMP assay[c] EC_{50} ± SEM [µM] (% activation at 10 µM)	Human GPR84 β-arrestin assay[d] EC_{50} ± SEM [µM] (% activation at 10 µM)	Human GPR84 Radioligand Binding K_i ± SEM [µM] (% activation of 2 nM [^{3}H]PSB-1584 at 10 µM (n=3)
273	Yazh-247	5-F	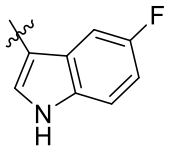	n.d.	>5 (7 %)	n.d.	**4.72** ± 0.143	**3.42** ± 0.226	> 10 (5%)	n.d.	n.d.
274	Yazh-246	5-F	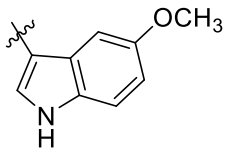	n.d.	>5 (40 %)	n.d.	**9.14** ± 0.87 (extrapolated)	>5 (39%)	> 10 (7%)	> 10 (-31%)	n.d.
275	Yazh-238	H	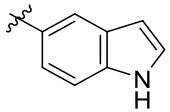	**32.7** ± 8.1	**10.5** ± 0.2	>5 (-12 %)	>5 (38%)	>5 (16%)	> 10 (-16%)	> 10 (-7%)	n.d.
276	Yazh-K-70	H	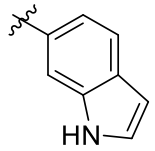	>5 (29 %)	**12.5** ± 1.7	n.d.	>5 (49%)	>5 (37%)	n.d.	n.d.	> 10 µM (30 %)

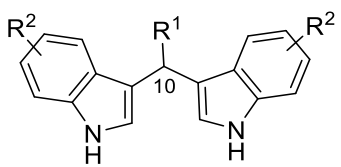

Scaffold B (149-216)

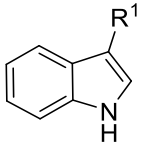

Scaffold C (217-253)

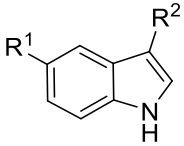

Scaffold D (254-269)

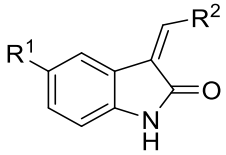

Scaffold E (270-277)

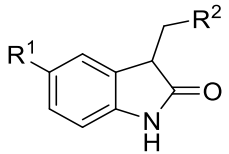

Scaffold F (278-281)

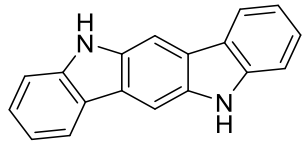

Indolo[3,2-b]carbazole (282)

No.	Cpd Name	R^1	R^2	**Human $P2Y_2R$** β-arrestin assay[a] **IC_{50} ± S.E.M [µM, n = 3 or 4] (% inhibition at 5 µM)**	**Human $P2Y_2R$** Calcium assay[a] **IC_{50} ± S.E.M [µM, n = 3 or 4] (% inhibition at 5 µM)**	**Human P2X4R** Calcium assay[b] **IC_{50} ± S.E.M [µM, n = 3 or 4]**	**Cannabinoid receptors versus [^{3}H]CP55,940** **Human CB_1** **K_i ± SEM [µM] (or % inhibition at 5 µM)**	**Cannabinoid receptors versus [^{3}H]CP55,940** **Human CB_2** **K_i ± SEM [µM] (or % inhibition at 5 µM)**	**Human GPR84** cAMP assay[c] **EC_{50} ± SEM [µM] (% activation at 10 µM)**	**Human GPR84** β-arrestin assay[d] **EC_{50} ± SEM [µM] (% activation at 10 µM)**	**Human GPR84** Radioligand Binding **K_i ± SEM [µM] (% activation of 2 nM [^{3}H]PSB-1584 at 10 µM (n=3)**
277	Yazh-261	5-F	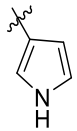	n.d.	>5 (1 %)	n.d.	>5 (29%)	>5 (2%)	n.d.	n.d.	n.d.

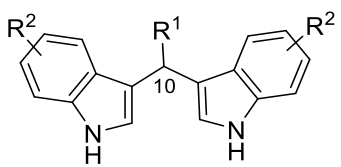

Scaffold B (149-216)

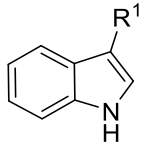

Scaffold C (217-253)

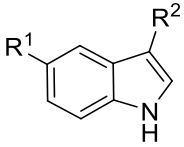

Scaffold D (254-269)

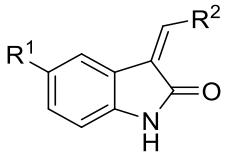

Scaffold E (270-277)

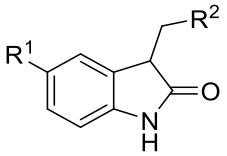

Scaffold F (278-281)

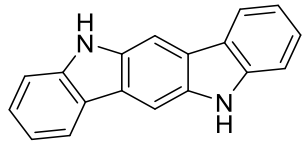

Indolo[3,2-b]carbazole (282)

No.	Cpd Name	R^1	R^2	Human $P2Y_2R$ β-arrestin assay[a] IC_{50} ± S.E.M [µM, n = 3 or 4] (% inhibition at 5 µM)	Human $P2Y_2R$ Calcium assay[a] IC_{50} ± S.E.M [µM, n = 3 or 4] (% inhibition at 5 µM)	Human P2X4R Calcium assay[b] IC_{50} ± S.E.M [µM, n = 3 or 4]	Cannabinoid receptors versus [^{3}H]CP55,940 Human CB_1 Ki ± SEM [µM] (or % inhibition at 5 µM)	Cannabinoid receptors versus [^{3}H]CP55,940 Human CB_2 Ki ± SEM [µM] (or % inhibition at 5 µM)	Human GPR84 cAMP assay[c] EC_{50} ± SEM [µM] (% activation at 10 µM)	Human GPR84 β-arrestin assay[d] EC_{50} ± SEM [µM] (% activation at 10 µM)	Human GPR84 Radioligand Binding K_i ± SEM [µM] (% activation of 2 nM [^{3}H]PSB-1584 at 10 µM (n=3)
Structure F: 2-Oxodihydroindolyl-indolylmethane derivatives											
278	Yazh-237	H	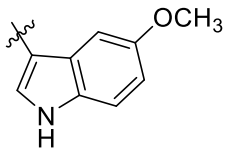	n.d.	>5 (26 %)	n.d.	>5 (33%)	>5 (33%)	> 10 (-21%)	n.d.	n.d.
279	Yazh-248	5-F	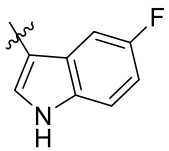	n.d.	>5 (1 %)	n.d.	>5 (33%)	>5 (20%)	> 10 (16%)	n.d.	n.d.
280	Yazh-249	5-F	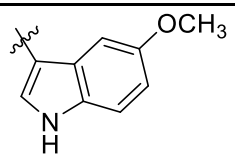	n.d.	>5 (29 %)	n.d.	>5 (16%)	>5 (41%)	> 10 (-10%)	n.d.	n.d.
281	Yazh-239	H	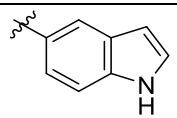	n.d.	>5 (26 %)	n.d.	>5 (9%)	>5 (15%)	> 10 (7%)	n.d.	n.d.

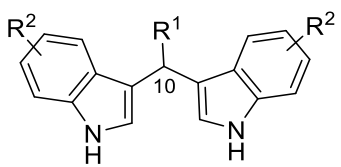

Scaffold B (149-216)

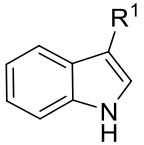

Scaffold C (217-253)

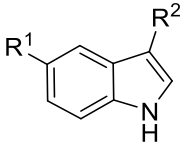

Scaffold D (254-269)

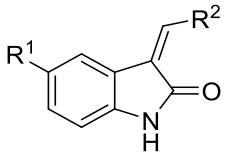

Scaffold E (270-277)

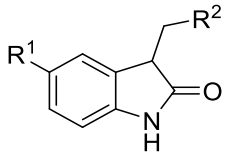

Scaffold F (278-281)

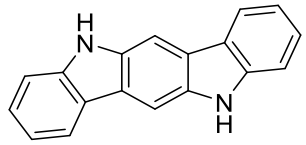

Indolo[3,2-b]carbazole (282)

No.	Cpd Name	R^1	R^2	Human $P2Y_2R$ β-arrestin assay[a] IC_{50} ± S.E.M [µM, n = 3 or 4] (% inhibition at 5 µM)	Human $P2Y_2R$ Calcium assay[a] IC_{50} ± S.E.M [µM, n = 3 or 4] (% inhibition at 5 µM)	Human P2X4R Calcium assay[b] IC_{50} ± S.E.M [µM, n = 3 or 4]	Cannabinoid receptors versus [^{3}H]CP55,940 Human CB_1 Ki ± SEM [µM] (or % inhibition at 5 µM)	Cannabinoid receptors versus [^{3}H]CP55,940 Human CB_2 Ki ± SEM [µM] (or % inhibition at 5 µM)	Human GPR84 cAMP assay[c] EC_{50} ± SEM [µM] (% activation at 10 µM)	Human GPR84 β-arrestin assay[d] EC_{50} ± SEM [µM] (% activation at 10 µM)	Human GPR84 Radioligand Binding K_i ± SEM [µM] (% activation of 2 nM [^{3}H]PSB-1584 at 10 µM (n=3)
282	DIM Carbazole (Indolo[3,2-b]carbazole)		See above	>5 (5 %)	>5 (17 %)	n.d.	n.d.	n.d.	n.d.	n.d.	n.d.

[a]Antagonism was determined using the agonist (UTP) EC_{80} concentration in the respective assays. [b]Inhibitory effect was determined against ATP EC_{80} concentration. [c]Inhibition of forskolin (10 µM) induced decrease in cAMP accumulation. [d]Agonistic activity of each compound was normalized to maxium efficacy of 10 µM of embelin. All data are presented as mean from 3-5 independent assays.

3.7.1 **Structure-activity relationship of the DIM derivatives in Ca^{2+} assays**

Generally, the diindolylmethanes and their analogs, including the lead compound (**115**) were more active in calcium assays than in β-arrestin assays over the same test concentration range. Therefore, the SAR analysis of these diindolylmethane derivatives were performed based on the different scaffolds presented in Table 6 with results from calcium assay.

Scaffold A

These are DIM derivatives with R,R'-disubstitutions on the indole rings resulting in symmetrical compounds. Scaffold A derivatives (**115 – 145**) are symmetrical with no substitution at the 3,3'-position, the C10 methylene bridge. We investigated the effects of substitutions at the 4,4'-positions. Here, OCH_3 substitution (**117**, IC_{50} = 6.52 µM) increased antagonistic activity over the lead compound (**115**, IC_{50} 19.4 µM) and was preferred to F (**118**, IC_{50} 13.6 µM) and CH_3 (**116**, inactive).

At the 5,5'-positions, difluoro substitutents (**123)** conferred a better potency (IC_{50} = 6.55 µM) over the lead compound (**115**) than dibromo (**121**, IC_{50} 9.41 µM) and 5,5'-dicyano (**121**, IC_{50} 9.50 µM). Derivatives with 5,5'-dimethyl (**121**, IC_{50} 14.7 µM), 5,5'-dimethoxy (**122**, IC_{50} 16.8 µM), 5,5'-dichloro (**124**, IC_{50} 15.0 µM) and 5,5'-dimethylcarboxylate (**128**, IC_{50} 15.0 µM) substituents were also moderately potent. Disubstitutions at the 5,5'-positions with NO_2 (**127**), CHO (**129**), COOH (**130**) and OCH_2Ph (**131**) yielded inactive diindolylmethane derivatives.

Further investigation of the 6,6'-positions reveal the dimethyl derivative **132** showed improved potency (IC_{50} = 15.0 µM) over the lead compound (**115**) whereas derivatives **133**, **134** and **135** with OCH_3, F and Cl disubstituents respectively, were inactive. Also, substitution with 7,7'-dimethoxy (**136**) and 7,7'-difluoro (**137**) abolished antagonism at the $P2Y_2R$.

Subsequently, we considered also multiple halo-substituents on the lead compound (**115**) yielding compounds **138-143**. At R^1 (also $R^{1'}$), disubstituted derivatives with 4-F,5-F (**139**) and 5-F,6-F (**141**) were inactive whilst that with 5-F,7-F (**143**) was moderately potent (IC_{50} = 8.98 µM). Compound **142** with 5-F and 6-Cl substitutions was also inactive. Also, compound **140** (5-Cl,7-Cl) was moderately active with IC_{50} 16.2 µM. Due to the similarity in potency between **143** and **123**, the activity of **143** may be due to the 5-F and not the 7-F substitution. The 7-F on **143** may be having a deleterious or no effect at all on antagonism at the $P2Y_2R$. Similarly, comparing the

potencies of **140** and **124** (IC_{50}s 16.2 µM vs. 15.0 µM), the 7-Cl substituent may not be well tolerated. Although **119** (4-Cl) and **135** (6-Cl) were inactive as $P2Y_2R$ antagonists, interestingly, compound **138** (4-Cl,6-Cl) showed a significant potency of 6.90 µM. This indicates that the right combination of substituents could sharply increase the potency of ligands as $P2Y_2R$ antagonists.

$P2Y_2R$ antagonism was abolished for **145** with CH_3 substitutions at R^2 (2,2'-positions). Similarly, replacement of the amino hydrogen of the lead compound **115** at R^2 (1,1'-positions) of the indole rings with CH_3 resulted in an inactive derivative **144**. Dimethyl substituents may not be tolerated at these positions. However, mono-substitution with CH_3 at position R^2 (position 1) may improve antagonistic activity of the lead compound (see compound **234** under scaffold C). The exchange of methylene group of **115** at position C10 for selenoether group (**146**, IC_{50} 4.29 µM) significantly resulted in a 4-fold increase in potency. The selenoether bridge is preferred to the methylene group at the C10 position. In contrast, the weak activity of **147** (IC_{50} 65.9 µM) compared to **115** (IC_{50} 19.4 µM) indicates the indole rings are important for $P2Y_2R$ antagonism.

In summary, for the symmetrical scaffold A of the DIM derivatives 4-OCH_3, 5-F and 6-CH_3 are preferred as substituents at R^1 for improved potency. Methylene group at C10 may be exchanged for a selenoether group whilst substitutions at R^2 and R^3 may not be tolerated. The SARs for scaffold A is juxtaposed with that of scaffold B in Figure 20 below.

Scaffold B: (Cyclo)alkyl substituents

These DIM derivatives are also symmetrical and categorized into those with (cyclo)alkyl and carbonyl substituents (**149-181**) and with aryl (**182-216**) substituents at the C10 position. Their potencies were assessed and structure-activity relationships performed on each group.

Most of the C10 alkyl-substituted DIM derivatives (**149-167**) showed enhanced potencies over the lead compound (**115**) as antagonists at the $P2Y_2R$. Compounds **149** (methyl), **153** (n-ethyl) and **157** (n-propyl) were moderately potent with IC_{50} values of 7.38 µM, 4.06 µM and 4.81 µM. The derivative with an n-butyl substituent (**158**) was inactive whilst that with a 2,3-dimethylbutyl residue (**160**) yielded a moderate potency of 7.56 µM. However, the best alkyl substituent at C10 was isopropyl (**159**) with a potency of 3.01 µM. The maximum tolerated length of the alkyl group at C10 appears to be four (4) carbons with branched isomers showing better potencies than their corresponding straight chains.

Next, we investigated the effects of combining indolyl ring substitutions with alkyl substitutions on the 3,3' methylene bridge. Additions to compound **149** at R^2 with various halogens such 4-F (**150**), 5-Cl (**151**) and 7-F (**152**) did not improve its potency. Among the derivatives with an n-ethyl group at C10, **154** with 4-F at R^2 exhibited an about 2-fold increase in potency over **153**, whilst **155** (5-F) and **156** (7-F) showed no improvement.

Various substituted derivatives (**161-167**) of compound **159**, expected to have better potencies were also synthesized and tested. Contrarily, none of these derivatives showed enhanced potency. With the exception of compounds **161** (4,4'-difluoro) and **164** (6,6'-difluoro) which had similar IC_{50} values (3.40 µM) to 159 (3.01 µM), others including **162** (4,4'-dimethoxy), **163** (5,5'-difluoro) and **165** (7,7'-difluoro) showed reduced potencies. The tetrahalo-substituted derivatives **166** (5,5',6,6'-tetrafluoro) and **167** (5,5'-dibromo-7,7'-difluoro) also displayed reduced potencies.

A series of C10-carboxyl derivatives of the lead compound **115** and their corresponding ester derivatives were also investigated. Interestingly, derivatives substituted at C10 with carboxylic acid (**168-170**) were inactive whilst those with ethylcarboxylate derivatives (**171-173**) were moderately potent antagonists of the $P2Y_2R$. Similarly, at C10, n-ethanoic acid (**174**) and n-propanoic acid (**176**) led to loss of activity whilst their methyl esters (**175** and **177**) were moderately potent with IC_{50} values of 14.3 µM and 6.76 µM respectively.

Also, we explored the effect of cycloalkyl groups at C10. Cycloalkyl groups were also well tolerated at the 3,3'-methylene bridge. The smallest ring investigated was cyclopropane (**178**) with the least potency (IC_{50} 26.6 µM) and the largest was cycloheptane (**181**, IC_{50} 16.3 µM). However, cyclopentane (**180**, IC_{50} 6.62 µM) and cyclohexane (**179**, IC_{50} 9.67 µM) yielded more potent $P2Y_2R$ antagonists. The structure-activity relation of scaffold A and scaffold B derivatives with cyclo(alkyl) substituents are presented below (Figure 20).

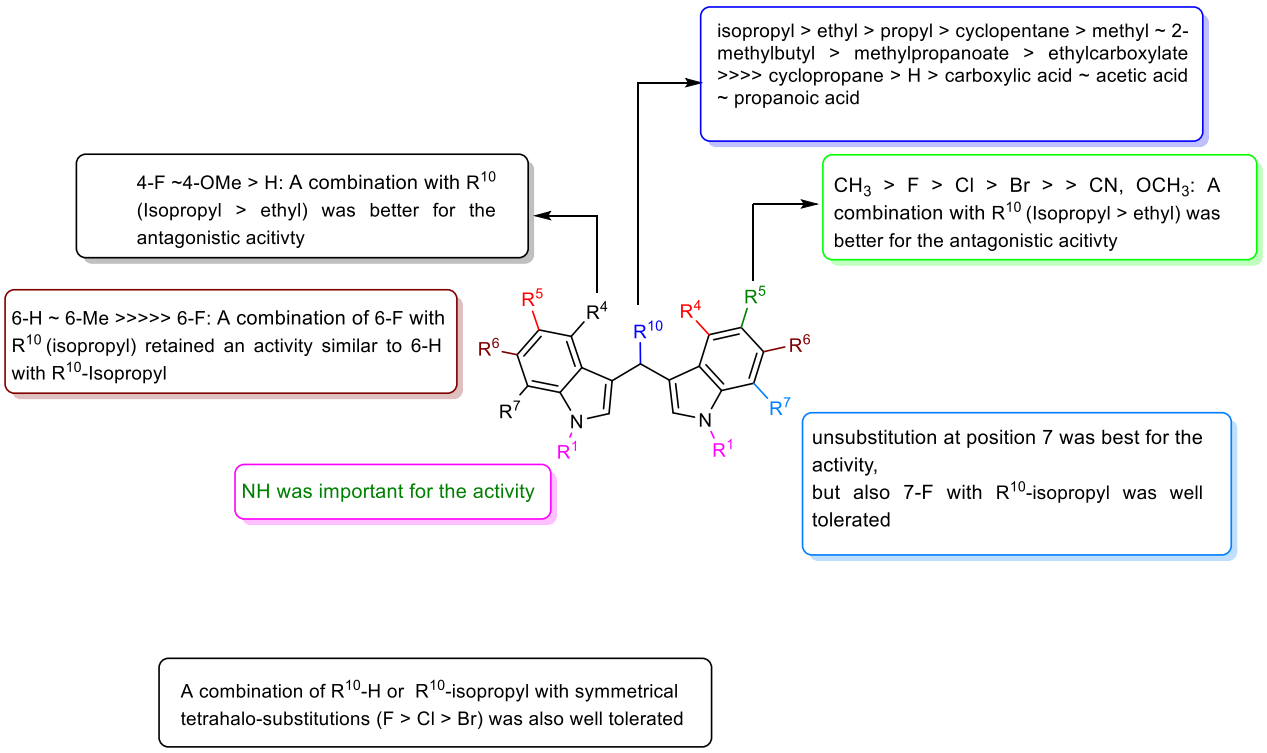

Figure 20: Structure-activity relationship of symmetrical diindolylmethanes derivatives combining 3,3'-cyclo(alkyl) substitution with various substitution combinations on the indole rings as antagonists of the human $P2Y_2$ receptor.

Scaffold B: aryl substituents

Several aryl substituents were also investigated at the 3,3'-methylene bridge of **115**. Their structure-activity relationship is illustrated in Figure 21. Coupling of 2-thienyl yielded **182** which was better tolerated as a $P2Y_2R$ antagonist (IC_{50} 9.79 µM) compared to the lead compound **115** and its derivative **121** (5,5'-dimethyl). Phenyl substitution (**183**) alone showed no advantage over the lead compound (**115**). However, further coupling of **183** with 4,4'-dimethoxy resulted in the more potent **184** (IC_{50} 4.11 µM). Comparing **183** and **184** with **117** reveals that the dimethoxy substituents are very important for $P2Y_2R$ antagonism. Various *N*-alkylphenyl derivatives (**186-191**) tested were all inactive, except **186** with 3,3'-(4-methylphenyl) substitution which showed moderate activity (IC_{50} 15.2 µM). Activity was abolished for *ortho*- and *meta*- methyl positions on the phenyl ring. Also, all the *N*-methoxyphenyl derivatives (**192-197**) except **194** were inactive. In comparison to **192** and **122**, it appears the potency of **194** (IC_{50} 10.4 µM) may have been

significantly improved by the 5,5'-dimethoxy substitution. 3,3'-Methoxyphenyl substitution may therefore be deleterious to $P2Y_2R$ antagonism in the symmetrical diindolylmethanes.

Derivatives with 4-hydroxyphenyl (**198**, IC_{50} 14.9 µM) and 4-fluorophenyl (**200**, IC_{50} 5.26 µM) were moderately potent whereas those with 4-chlorophenyl (**199**) and 4-nitrophenyl (**216**) lost activity.

Substitution with a 4-pyridyl group (**203**) showed no antagonism at the $P2Y_2R$. However, its derivatives with difluoro substitutions at 4,4'- (**204**), 5,5'- (**205**), 6,6'- (**207**) and 7,7'- (**208**) positions showed moderate potencies. Combination of the 4-pyridyl group with 5,5'-dichloro substituents (**206**) was not tolerated probably due to the larger size of the halogen. We observed that 3,3'-substitution with larger groups such as styryl (**209**), 4-phenoxybenzyl (**210**), 4-(1,3-benzodioxolyl) (**211**), naphthalenyl (**212-214**) abolished $P2Y_2R$ antagonism except for 3-indolyl (**215**) with a moderate potency of 12.3 µM.

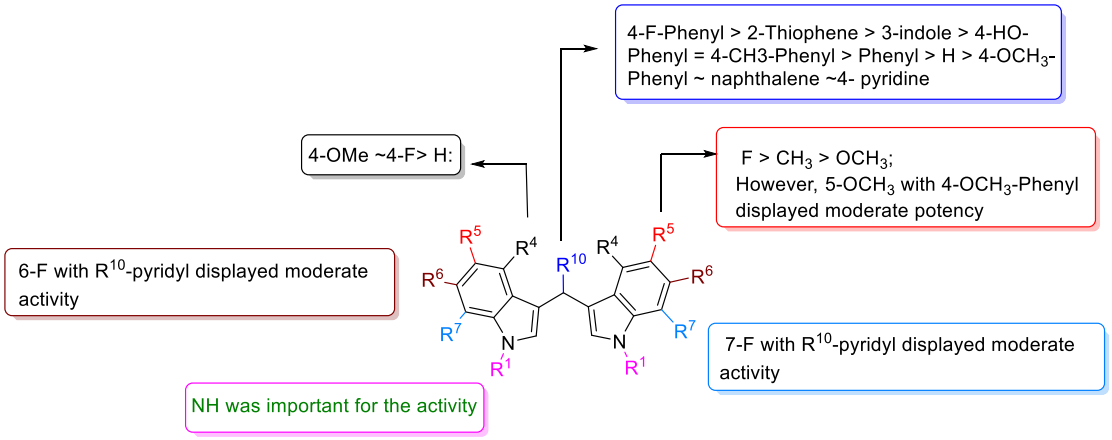

Figure 21: Structure-activity relationship of symmetrical diindolylmethane derivatives with 10-aryl substitutions as antagonists of the human $P2Y_2$ receptor.

Scaffold C

Here, we tested several diindolylmethanone derivatives (**217-233**) to ascertain their potency and SARs as $P2Y_2R$ antagonists. However, all of them showed loss of activity at the $P2Y_2R$ compared to the lead structure (**115**).

Also, based on insights from exploring various substitutions on the indolyl ring and at the C10 methylene linker of scaffolds A and B, we synthesized and investigated new unsymmetrically

substituted diindolylmethane derivatives (**234-253**) with substitution on various positions on just one indole ring. These can further be categorized as those with C10-substitution and those without. The first ones among the unsymmetrical series without C10-substitution is **234** with a CH_3 mono-substitution replacing one of the NH hydrogen of the indole rings. Compound **234** showed a steep increase in potency (IC_{50} 5.84 µM) compared to the inactive **144** with 1,1'-dimethyl substitutions. This implies that at least one unsubstituted NH group is required for antagonism by the diindolylmethane derivatives at the $P2Y_2R$. Other C10-unsubstituted DIM derivatives with mono-substitutions such as 5-OCH_3 (**235**), 5-F (**236**), 5-COOH (**239**), 5-$COOCH_3$ (**240**) and 6-CH_3 (**241**) were inactive whilst those with 5-Cl (**237**, IC_{50} 6.23 µM) and 5-Br (**238**, IC_{50} 7.56 µM) were moderately potent $P2Y_2R$ antagonists.

Furthermore, unsymmetrical C10-isopropyl-substituted DIM derivatives were also assessed. All such derivatives with mono-substitution (**242-245**) or di-substitutions (**246-248**) on one of the indole rings yielded potencies between 1.91 µM to 4.35 µM. Compound **247** (IC_{50} 1.91 µM) was the most potent diindolylmethane tested so far in this study. Exchanging the 4-F,5-F substituents of **247** for 4-Cl,5-Cl (**248**, IC_{50} 4.35 µM) reduced the activity by 2-fold although not significantly ($p > 0.05$).

Next, we explored the effect of tetra-substitution at the C10-positions on potency of the lead compound **115**. It appears at C10, tetra-substitution with methyl and 4-methylphenyl groups (**249**, IC_{50} 12.7 µM) are better tolerated than those with methyl and methoxyphenyl groups (**250** and **251**). This is consistent with data from compounds **186** and **192**. Tetra-substitution at position C10 therefore may not diminish antagonism of the DIM derivatives at the $P2Y_2R$. Moreover, tetra-substituted C10 may prolong the chemical stability of the diindolylmethane derivatives as an added advantage. Furthermore, we observed that substitution of one of the indole ring of DIM for 1*H*-pyrrolo[3,2-*c*]pyridine (**252** and **253**) abolishes activity. This underscores the importance of the indole ring to DIMs for $P2Y_2R$ antagonism. Figure 22 illustrates the SARs of scaffold C derivatives.

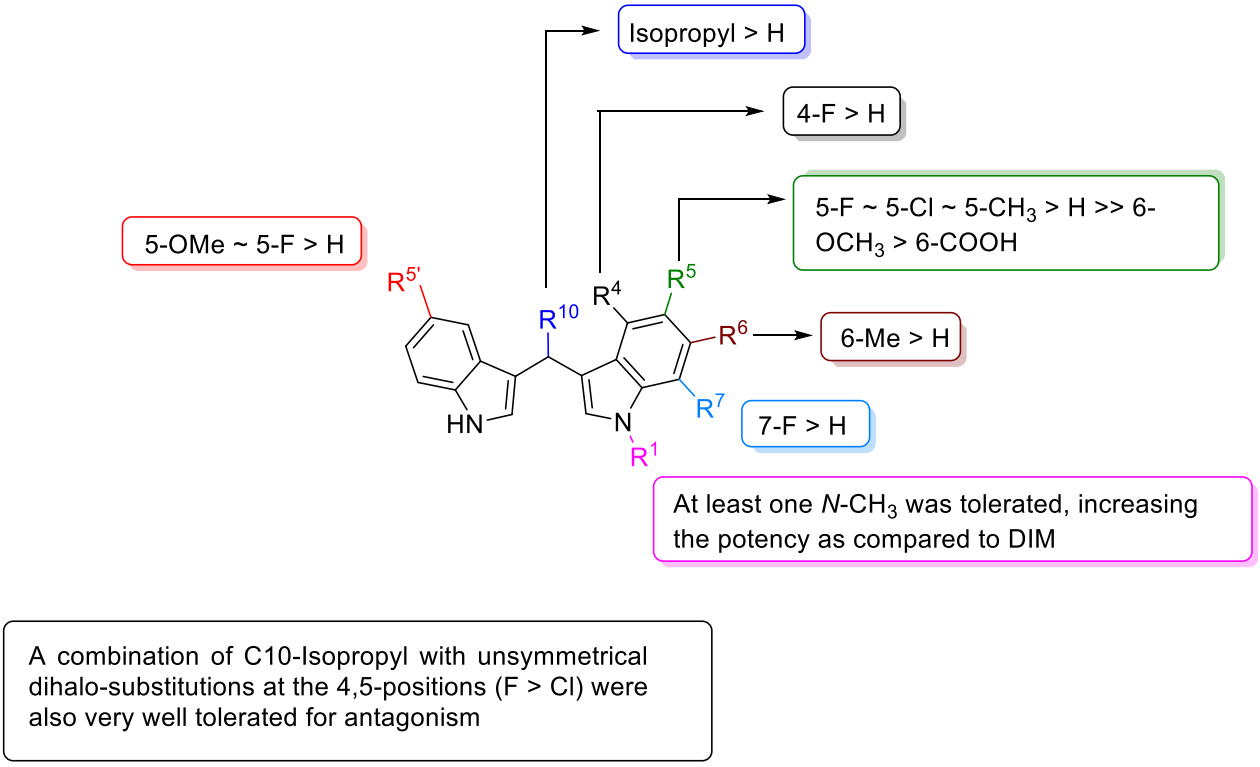

Figure 22: Structure-activity relationships of unsymmetrically substituted diindolylmethane derivatives as antagonists of the human $P2Y_2$ receptor.

Scaffold D

Diindolymethane derivatives with scaffold D are unsymmetrical and explore substitutions on both indole rings. We observed that the diindolylmethanone (**254-262**) were inactive at the $P2Y_2R$. However, unsymmetrical DIM derivatives with one indole ring bearing a 5-OCH_3 substitution (**263-268**) were moderately potent (IC_{50} values 6.17 µ - 9.04 µM).

Scaffold E and Scaffold F

Derivatives in these series are unsymmetrically substituted 2-indoline derivatives with a 3,3'-methene bridge at C10. The 3'-indolyl (**270-274**) as well as 3'-pyrrolyl (**277**) substituents abolished $P2Y_2R$ antagonism. Contrarily, compound with 5'- and 6'-indolyl derivatives (**275** and **276**) were moderately potent with IC_{50} values of 10.5 µ and 12.7 µM respectively. In comparison to **270-274**, the lack of steric hinderance from the carbonyl (2-keto) group on the special interactions of the two NH groups may have contributed to the enhanced potency of compounds **275** and **276.**

The derivatives based on scaffold F (**278-281**) are 3-ethyl-2-indolinone derivatives without the methene bridge. Interestingly, none of the derivatives of scaffold F was active at the $P2Y_2R$ as antagonists. This implies that the methene bridge may be important to the activity of these indolinone scaffolds (E and F) as antagonists of the $P2Y_2R$.

3.7.2 **Activity of DIM derivatives in β-arrestin assay**

Generally, halo-substituents introduced inhibition of $P2Y_2R$-mediated β-arrestin recruitment. For instance, at R^1 of scaffold A, 4-F derivative **118** showed a potency of **33.4** μM in the β-arrestin assay. The 4-Cl derivative was inactive probably due to its larger size. Derivatives with 4,4'-dichloro (**119**) and 4,4'-dinitro (**120**) substituents were inactive in both assays. Also, at 5,5'-positions β-arrestin inhibitory activity was only introduced by **123**, **124** and **125** with F, Cl and Br substitutions respectively (see Figure 23A). Similarly, among the derivatives with multiple halogen substitutions, **138** (4-Cl,6-Cl) showed the highest potency (IC_{50} = 8.54 μM) against $P2Y_2R$-induced β-arrestin activity. Others with weak potencies are **140** (5-Cl,7-Cl, IC_{50} 73.3 μM) and **143** (5-F,7-F, IC_{50} 37.2 μM)

Furthermore, substitution on the methylene bridge of scaffold B especially with aryl substituents also introduced inhibitory activity against β-arrestin recruitment. Among these, compounds **201** (4-fluorophenyl) and **213** (2-naphthalenyl) were the most selective at the $P2Y_2R$ for β-arrestin inhibitory activity with IC_{50} values of 10.4 μM and 14.8 μM respectively (see Figure 23B). Unsymmetrical mono-substitutions with 5-Cl (**237**) and 5-Br (**238**) led to slight enhancement of β-arrestin inhibitory activity relative to the lead compound **115**. Similarly, unsymmetrical dihalo-substituted products **267** (4,5-difluoro, IC_{50} 29.3 μM) and **268** (4,6-difluoro, IC_{50} 33.0 μM) showed better potencies than the lead compound in β-arrestin assays.

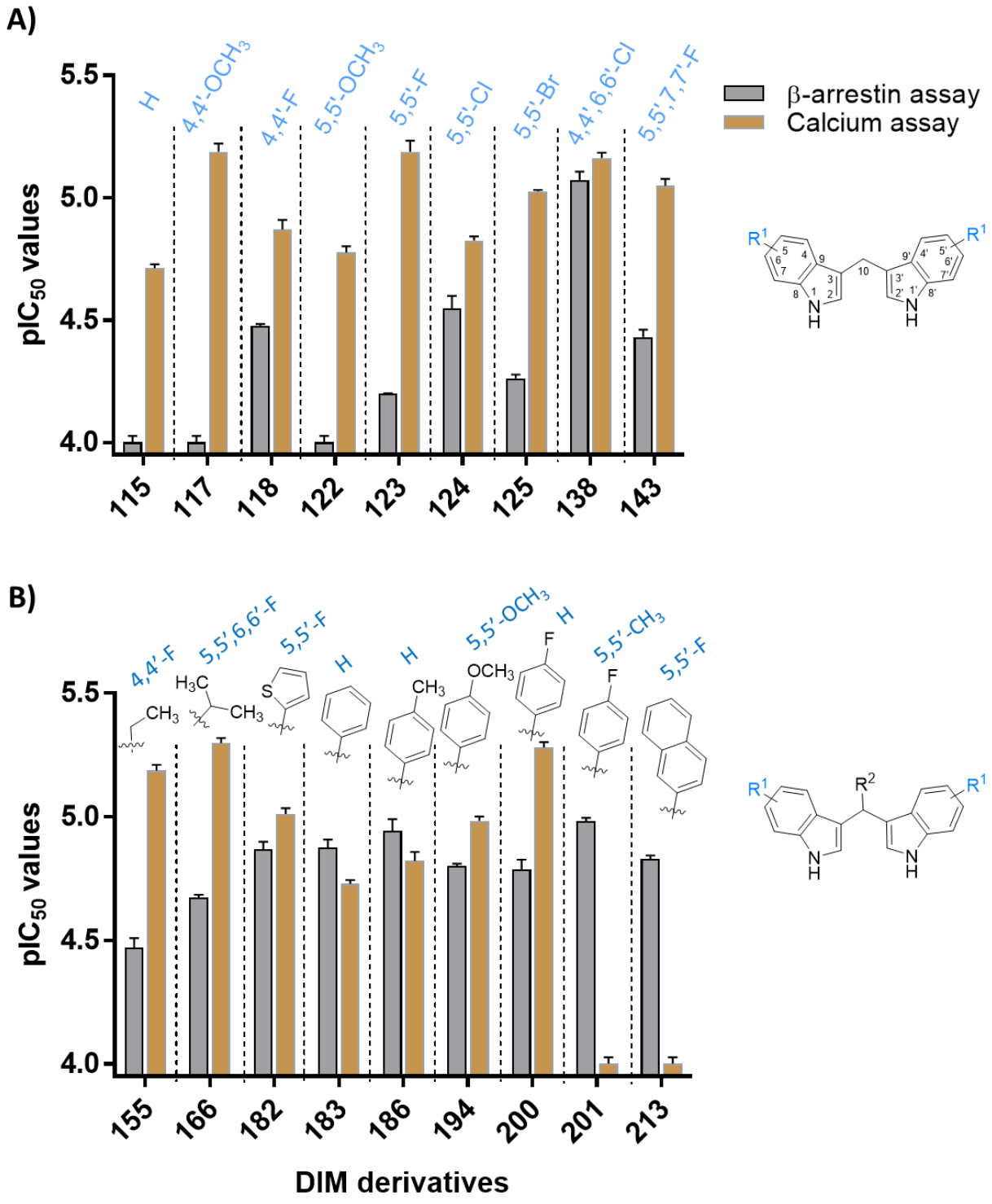

Figure 23: Bar charts illustrating pathway bias of the diindolylmethane (DIM) derivatives in blocking UTP activation of the human $P2Y_2$ receptor in β-arrestin assay and calcium assay. Compounds are more active in calcium assay (brown color) compared to β-arrestin assays (ash columns). Halo-substitutions appear to enhance inhibition against β-arrestin recruitment.

Our data indicates DIM derivatives show substantial differences in antagonizing UTP-mediated $P2Y_2R$ activation of G_q-proteins (in calcium assay) as compared to β-arrestin recruitment – a phenomenon known as functional bias (see Figure 24). For agonists, bias factors can be calculated.[206–209] Similarly, for antagonists, the different cellular backgrounds might influence the determined IC_{50} values. Pathway bias could be relevant to the development of drugs with less deleterious effects.[210]

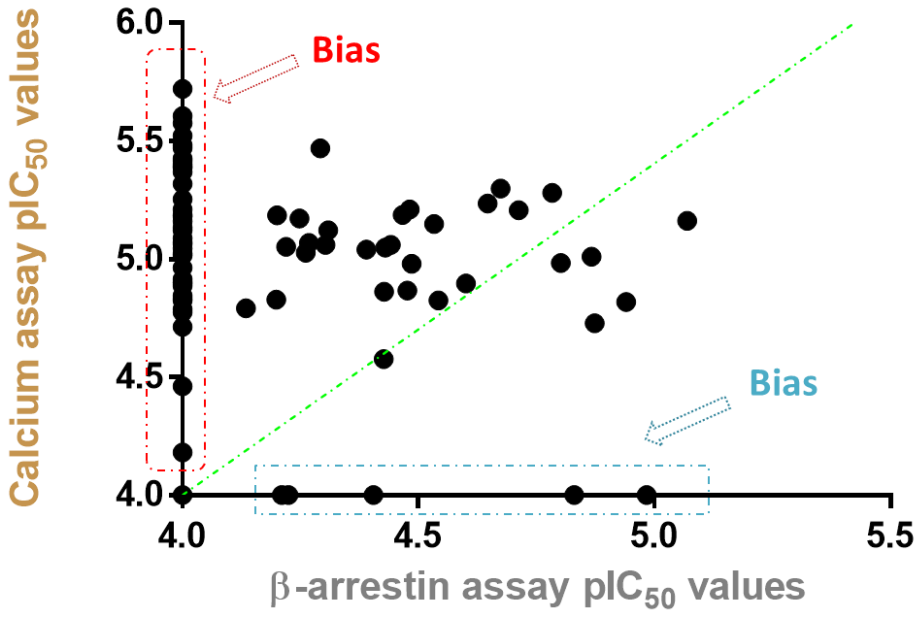

Figure 24: Scatter plot indicating functional bias of the diindolylmethane derivatives in inhibiting $P2Y_2R$ activation by UTP. Each black dot indicates the potencies of a compound. Those on the abscissa (highlighted by blue rectangle) are biased towards the β-arrestin pathway whilst the majority on the y-axis (red rectangle) antagonize only the G_q-protein activity.

However, the observed bias also raises the question: could the potencies of the DIM derivatives determined in calcium assays be due to artifacts from the assay? To eliminate such doubts, we screened some DIM derivatives at the human P2X4 receptor (P2X4R) in a calcium assay. We observed that most of these compounds, although active at the $P2Y_2R$, were completely inactive at the P2X4R. The potencies of DIMs at the $P2Y_2R$ are therefore likely a reflection of receptor-ligand interactions and not of artifacts of the calcium assay.

Next, we investigated the mechanism of inhibition for DIM derivative **159**, as a relatively potent and selective member of the DIM series. The Schild analysis showed that there was a significant reduction of the maximal UTP response with increasing concentrations of **159**, while the EC_{50} values for UTP concentration-response curves remained the same (see Figure 25B and Table 7). This indicates that compound **159** is probably a negative allosteric, non-competitive modulator.

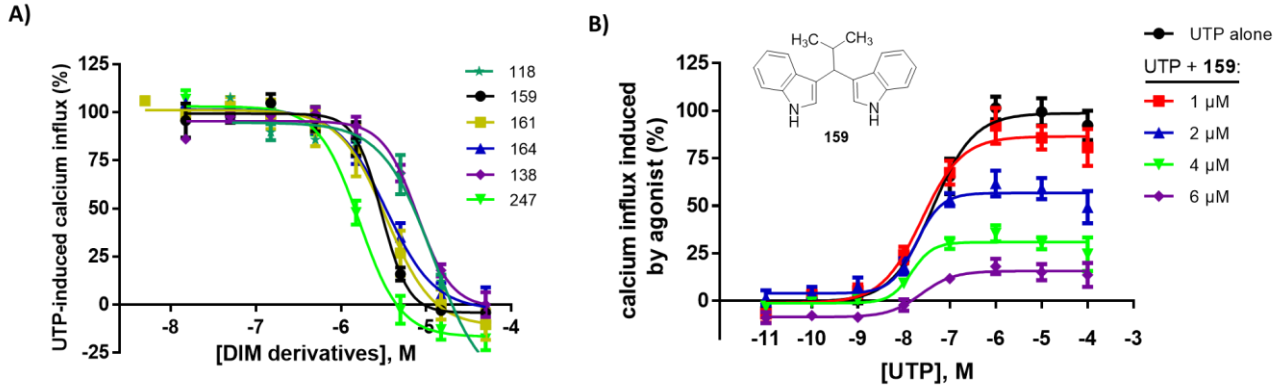

Figure 25: A. Concentration-dependent inhibition of UTP induced $P2Y_2R$ activation by DIM derivatives UTP. **B.** Schild analysis of UTP concentration-response curves in the presence of various concentrations antagonist **159** at the human $P2Y_2$ receptor.

Table 7: Potency of UTP at the $P2Y_2R$ in the presence of varying concentrations of antagonist **159** determined in calcium assays.

Concentration-response curve	**EC_{50}** ± SEM, µM (n = 3-4)
UTP alone	**0.0497** ± 0.0096
UTP + 1 µM **159**	**0.0281** ± 0.0072
UTP + 2 µM **159**	**0.0197** ± 0.0058
UTP + 4 µM **159**	**0.0177** ± 0.0036
UTP + 6 µM **159**	**0.0246** ± 0.0069

3.7.3 **Selectivity of DIM derivatives versus other GPCRs**

The diindolylmethane (DIM) derivatives, which had been reported as GPR84 agonists (by cAMP assay), were antagonists at the hP2Y$_2$R (in calcium assay). When tested as agonists at the P2Y$_2$R, they showed no activity (data not shown). We observed that whereas at the methylene bridge (C10) aryl or alkyl substituents (**149-216**) were not tolerated for agonism at GPR84, they resulted in moderately potent antagonists at hP2Y$_2$R. The most potent of there was **247** with IC$_{50}$ 1.91 µM (see Figure 26). The DIM derivatives with dimethyl substitutions at 1,1'- and 2,2'-positions were inactive at both the GPR84 and hP2Y$_2$ receptors. However, mono-substitution with *N*-CH$_3$ (**234**) was selective for only P2Y$_2$R. 2-Indolinone derivatives such **275** and **276** were also selective for only the P2Y$_2$R although only moderately potent with IC$_{50}$ values of 10.5 µM and 12.5 µM respectively.

The DIM derivatives were also tested at the cannabinoid CB$_1$ and CB$_2$ receptors by radio-ligand binding assays to ascertain their selectivity. Most derivatives showed similar potencies at CB$_1$ and CB$_2$ receptors. It appear both CB$_1$ and CB$_2$ receptors tolerate substitution at the methylene bridge like the P2Y$_2$R. Alkyl substituents at C10-position of DIM favor CB$_1$ interactions whilst CB$_2$ activity is enhanced by C10-aryl substituents and halogens on the indolyl rings. However a few compounds showed distinct selectivity for the P2Y$_2$R (see Figure 26). Alkyl substituents such as methyl (**150**, **152**), propyl (**157**) and isopropyl (**161**) groups at the C10-position were better tolerated by the P2Y$_2$R. The mono-substitution product **234** (*N*-CH$_3$) was selective for the P2Y$_2$R since it was inactive at CB$_1$ and CB$_2$ receptors. Derivatives of **234**, **275** and **276** could be developed as ligands selective for P2Y$_2$R over the CB$_1$ and CB$_2$ receptors. Although most of the DIM derivatives may be potent at CB$_1$ and CB$_2$ in binding assay, potency of ligands in binding assays do not always translate into functional activity. Moreover the DIM derivatives were reported as partial agonists of the cannabinoid receptors whereas our studies reveal they are antagonists at the P2Y$_2$R. Another possibility would be to optimize and use these compounds as multitarget ligands of the human P2Y$_2$R, GPR84, cannabinoid CB$_1$ and CB$_2$ receptors to treat various diseases.

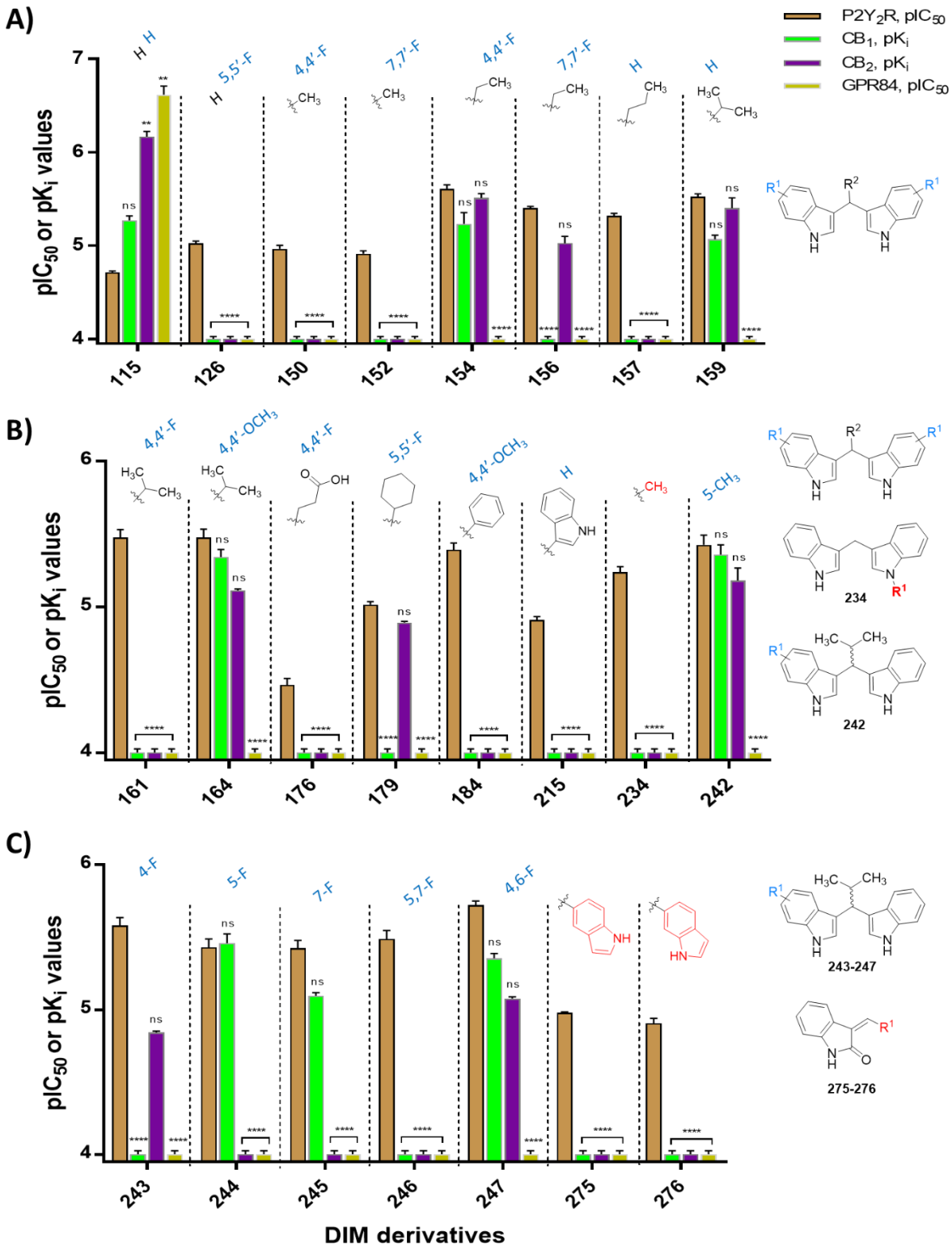

Figure 26: Selectivities of diindolylmethane derivatives for the $P2Y_2R$ against GPR84 and cannabinoids CB_1 and CB_2 receptors. Ligands were assessed by calcium assay ($P2Y_2R$, pIC_{50}),

cAMP assay (GPR84, pIC_{50}) and radioligand binding assay (CB_1 and CB_2, pK_i) respectively. Data represents means ± SEM (n = 4 – 6). The IC_{50} values are listed in Table 6. Statistical analysis was by one-way ANOVA with Dunnett's post-hoc test for multiple comparison: ^{ns} not significant; * $p \leq 0.05$; ** $p \leq 0.01$; *** $p \leq 0.001$; **** $p \leq 0.0001$.

3.8 **Discussion**

In the discovery of $P2Y_2R$ antagonists, we established and validated calcium and β-arrestin assays using standard agonists and antagonists of the $P2Y_2R$. The assays satisfied quality control metrics, such as the Z'-factor, and reproducibility tests during screening. Subsequently, we screened compound sub-libraries from the Pharma Zentrum Bonn and discovered several scaffolds as potential antagonists of the $P2Y_2R$. Two such scaffolds were further investigated, namely the urea- and diindolymethane derivatives.

The urea derivatives showed antagonistic but not agonistic activity by β-arrestin assays. Among the series, compound **84** was the most potent (IC_{50} = **1.31** µM) and the most selective antagonist against other GPCRs such as GPR18 and the cannabinoid CB_1 and CB_2 receptors. Other potent derivatives include compounds **76**, **85** and **90**. The SAR analysis indicates the urea group is very important for activity as replacement with amides led to a total loss of activity. Contrarily, the indolyl ring may be replaced with a 4-cyanophenyl moiety without significant reduction in potency. Despite their high molecular weight, the SAR analysis of these urea scaffolds present several opportunities for modification in order to increase potency and drug-like properties. Interestingly, these compounds were not active against UTP-h$P2Y_2R$ activation in calcium assays thus indicating functional bias. Compound **85** was determined to be an allosteric inhibitor using Schild analysis. The urea derivatives were are similar in structure to BPTU, a selective allosteric antagonist of the $P2Y_1R$. It would be interesting to investigate if **85** is also selective for the $P2Y_2R$ over the $P2Y_1R$ in functional β-arrestin assays.

The 3,3'-diindolylmethane scaffold was also found to be active as $P2Y_2R$ antagonist. The most potent DIM derivative synthesized was compound **247** (IC_{50} 1.91 µM), an unsymmetrical derivative with 3,3'-isopropyl and 4,6-difluoro substitutions. Several other derivatives including symmetrical DIM derivatives such as **123**, **153**, **159** and **183** were potent.

A few derivatives also showed considerable selectivity for $P2Y_2R$ over other GPCRs such as GPR84, P2X4R and the cannabinoid CB_1 and CB_2 receptors.

According to the SARs, alkyl substituents are preferred over aryl substituents at the C10-methylene bridge. Symmetrical and unsymmetrical substitutions on the indole rings, especially with fluoro, were well tolerated for antagonism. It appears that at least one amino (NH) hydrogen is required for activity. Analogs with 2-indolinone scaffolds such **275** and **276** were moderately potent and could be developed to be very selective. These compounds were found to be allosteric inhibitors and also demonstrated substantial bias for the G_q-protein pathway.

Allosteric ligands bind to sites in the receptor different from that of the endogenous orthosteric ligands. These binding sites have uniquely evolved for each receptor subtype and upon ligand binding modulate receptor response (positively or negatively) to the orthosteric ligands. The allosteric sites are saturable so they control the efficacy of receptor response and thus may mitigate the unwanted side effects of drugs. Another way by which allosteric modulators impact selectivity and control side effects is by stabilizing receptor conformations that lead to "signaling or functional bias".[210,211]

Allosteric ligands, including antagonists, which induce signaling bias in class A GPCRs have been widely reported, some of which are in clinical trials.[212] For instance, the biased angiotensin receptor antagonist TRV120027 has been reported to block G-protein-mediated vasoconstriction effects of angiotensin in heart failure whilst maintaining the beneficial effects of β-arrestin recruitment.[213] Also, the histaminic H_4 receptor (H_4R) antagonist JNJ7777120 only blocks the G-protein pathway but is a partial agonist for H_4R-mediated β-recruitment.[214] Other ligands that have demonstrated signaling bias include carvedilol (β-adrenergic receptor blocker)[215], bosentan and the cell penetrating peptide IC2B (both are endothelin receptor antagonists), and more recently the peptide antagonist X4-2-6 of the chemokine receptor CXCR4.[216,217] Therefore, the urea- and diindolylmethane scaffolds, found to exhibit biased allosterism are no exceptions and could be further developed into clinical drugs. However, for such biased ligands, it is recommended to confirm their activity directly in animal in vivo studies before proceeding further with the drug development process.[218]

In summary, we have developed novel scaffolds, urea- and diindolylmethane derivatives, as potent allosteric antagonists of the $P2Y_2R$. Further investigation of their binding sites is necessary for

ligand optimization. Additionally, it is our aim to develop orthosteric ligands of the $P2Y_2R$ receptor with better antagonistic profiles than that of AR-C118925.

4 Discovery of $P2Y_2R$ ligands through virtual screening

4.1 Introduction

In the previous chapter, we discussed how we randomly screened compound libraries for novel $P2Y_2R$ receptor antagonists. We discovered and characterized compounds **84** and **247** as allosteric antagonists with considerable potency. These allosteric modulators will be further optimized into potential drug candidates. However, there is also a need for competitive, orthosteric antagonists. Orthosteric ligands often have higher receptor affinities and possibly higher efficacies than allosteric ligands.[219] They may be more effective in reversing agonist effects, e.g. due to overdosing or poisoning.

Till today, the most potent and selective orthosteric antagonist of the $P2Y_2R$ with mid-nanomolar potency is AR-C118925 (**38**). However, due to its failure in clinical trials, AR-C118925 (**38**) is currently only used as a pharmacological tool. Therefore, in order to identify and develop novel, potent and selective orthosteric antagonists for the $P2Y_2R$, we resorted to the use of virtual screening methods.

Virtual screening (VS), also known as *in-silico* screening, has become an integral part of contemporary drug discovery, complementing *in vitro* screening. This computational tool reduces the huge chemical space to a single or manageable set of compounds that potentially interacts with a specific target in assay systems. All VS procedures involve use of predefined mathematical algorithms or metrics called "scoring functions" to run, filter and rank results of enquiries.[220]

Traditionally, there are two forms of virtual screening (VS): ligand-based virtual screening (LBVS) and structure-based virtual screening (SBVS). Ligand-based screening utilizes the topographical data of known drugs or active compounds at a given target, as descriptors to mine virtual libraries (VL) for potential hits for the said target. The basic assumption here is that compounds with similar surface properties have similar biological activities. LBVS does not require structural information of the target protein and involves methods like functional group similarity searches and pharmacophore mapping. Where there is no active compound as a template, machine learning protocols involving artificial neural networks as well as support vector machines have been used to generate and rank potential actives.[220,221] LBVS has been used to identify potent ligands for several GPCRs including chemokine receptor 5 (CCR5) inhibitors.[222]

Structure-based screening (SBVS), on the other hand, utilizes structural knowledge of the target protein to determine the protein-ligand interaction geometries, potential ligands and the binding affinities of such ligands. The protein structural data are usually available from experimental methods such as nuclear magnetic resonance or X-ray crystallography. Where structure of the target protein is unknown, a homology model is generated using the structure of one or more evolutionarily close proteins known as homologs. SBVS involves processes such as target protein and compound library preparation, docking of the ligands, post-processing and scoring of the results. Recent advancements such as ensemble docking (ED) and consensus induced-fit docking have reduced the past failures of SBVS.[223] Another complement to SBVS is *de novo* drug design where novel molecules, unavailable in compound libraries, are designed and tested based on knowledge of the protein binding site. Fragment-based screening is also a variant of SBVS that determines and combines functional groups relevant to ligand-target binding into new chemical entities.[224,225]

Compared to the traditional experimental methods, VS is a fast and cost-efficient way of generating potential drug leads. Also, it allows for a better understanding of the molecular interactions between ligands and receptors. However, VS could be plagued with false positive hits due to the use of inappropriate algorithms, inaccurate homology models or a general lack of experience. Also, ligand-receptor concepts such as entropy, flexibility and solvation have not fully and accurately been computed yet. The success of VS to generate good leads are usually case specific and the protocols non-transferable.[223] These limitations notwithstanding, major successful and inspiring VS-mediated drug discovery cases have been reported.[226,227]

Recently, a homology model of the $P2Y_2R$ built on the of the $P2Y_1R$ X-ray crystallographic structure was published.[183] Using this model, we undertook a virtual screening campaign at the $P2Y_2R$ with a virtual compound library (VL) from the ZINC database (http://zinc.docking.org/).[228] The VS was performed by Alexander Neumann and Dr. Vigneshwaran Namasivayam. The VS protocol used for the $P2Y_2R$ is described in detail under Materials and Methods. Briefly, compounds of the ZINC VL pre-filtered for drug-like properties were prepared for docking in a $P2Y_2R$ pocket defined by the binding geometrics of AR-C118925 (**38**). AR-C118925 (**38**) was previously characterized to be a competitive orthosteric antagonist of the $P2Y_2R$ binding to the same pocket as UTP (**1**).[229] After several steps of scoring, validation and visual inspection of hits,

57 compounds were finally purchased for preliminary in vitro screening against UTP-mediated $P2Y_2R$ activation. Hits from the in vitro screening were evaluated and cherry-picked. Subsequently, 42 more compounds were purchased and subjected to a second in vitro screening. These second set of compounds consisted of analogs of the cherry-picked hits from the first in vitro screening at the $P2Y_2R$. The VS workflow is summarized in Figure 27.

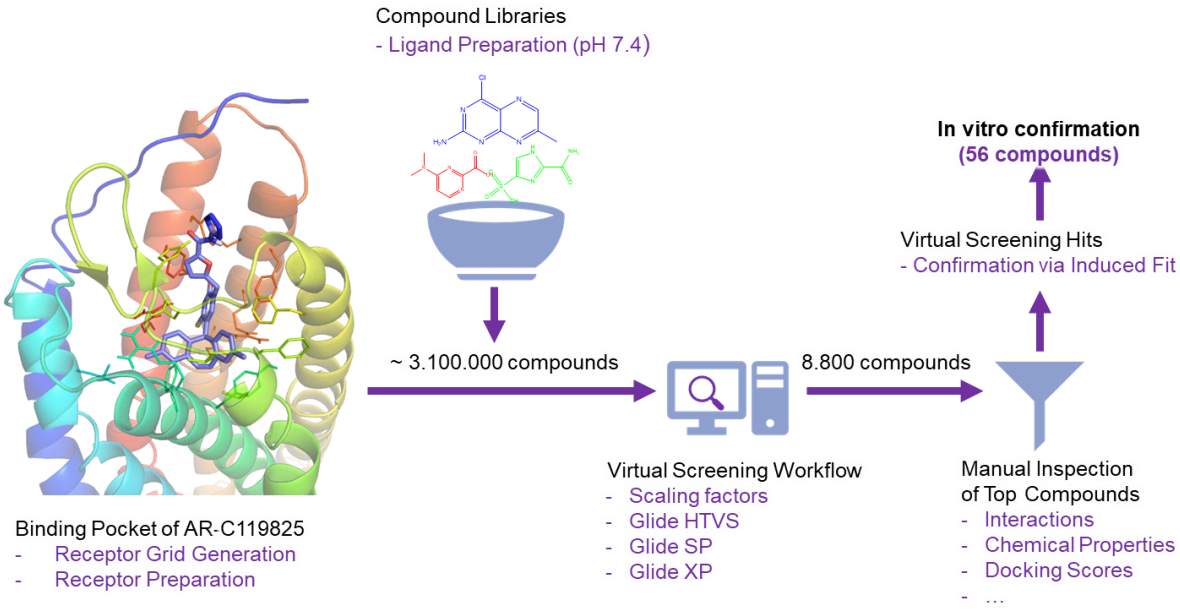

Figure 27: Schematic representation of virtual screening protocol used for identification of in-silico $P2Y_2R$ hits from the ZINC database.(credit: Alexander Neumann)

4.2 **Results**

In addition to the $P2Y_2R$, the compounds were also screened for selectivity at the human $P2Y_1$, $P2Y_4$ and $P2Y_6$ receptors using the agonists ADP, UTP and UDP, respectively. Calcium assays were used to screen the purchased compounds at all of the receptors which are recombinantly expressed in the 1321N1 astrocytoma cells. The 1321N1 astrocytoma cells express native muscarinic M_3 receptors (M_3R); therefore the VS hits were counter-screened at the M_3R against carbachol in calcium assays to eliminate false positives. Compounds which were hits on the M_3Rs were considered to have off-target effects and were hence discarded as artifacts. Additionally, the compounds were screened in β-arrestin assays at the human $P2Y_2$ and $P2Y_4$ receptors cloned into Chinese hamster ovary (CHO) K1 cells. The compounds were screened at 10 µM in both assay

systems as antagonists at the P2Y receptors. The threshold for selection of *in vitro* screening hits was set to 30 % inhibition. Figures 28 and 29 represents the results from the first and second screen campaign of the hits from VS campaigns. Dose-response curves were further performed for the *in vitro* hits; all test results are presented in Table 8.

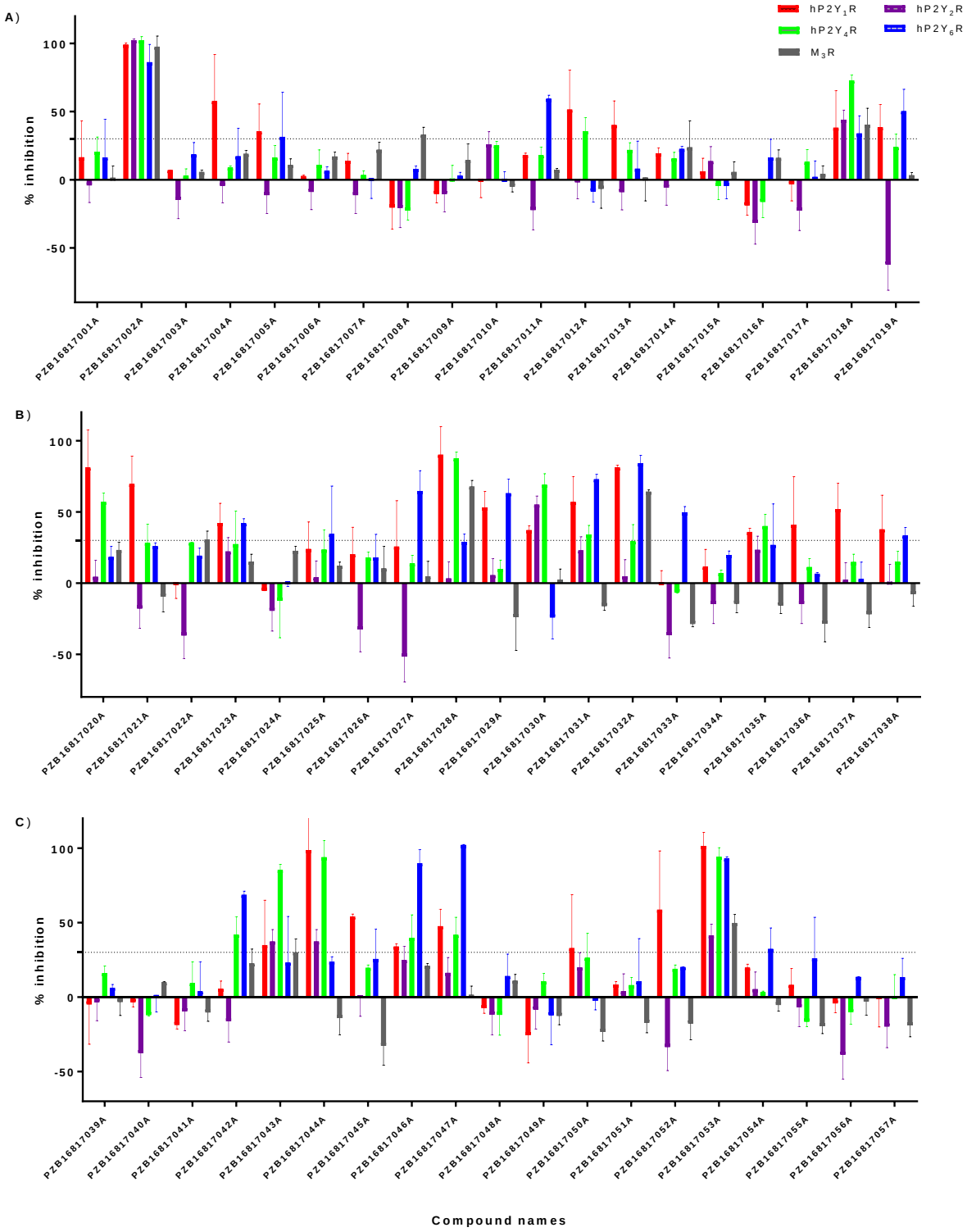

Figure 28: Results of in vitro screening of the first virtual screening hits as antagonists at the hP2Y and the muscarinic M_3 receptors as determined by calcium assays (n=3). Each bar represents the mean ± S.E.M of % inhibition values. The dotted black line indicates the 30 % inhibition threshold defined for a hit compound.

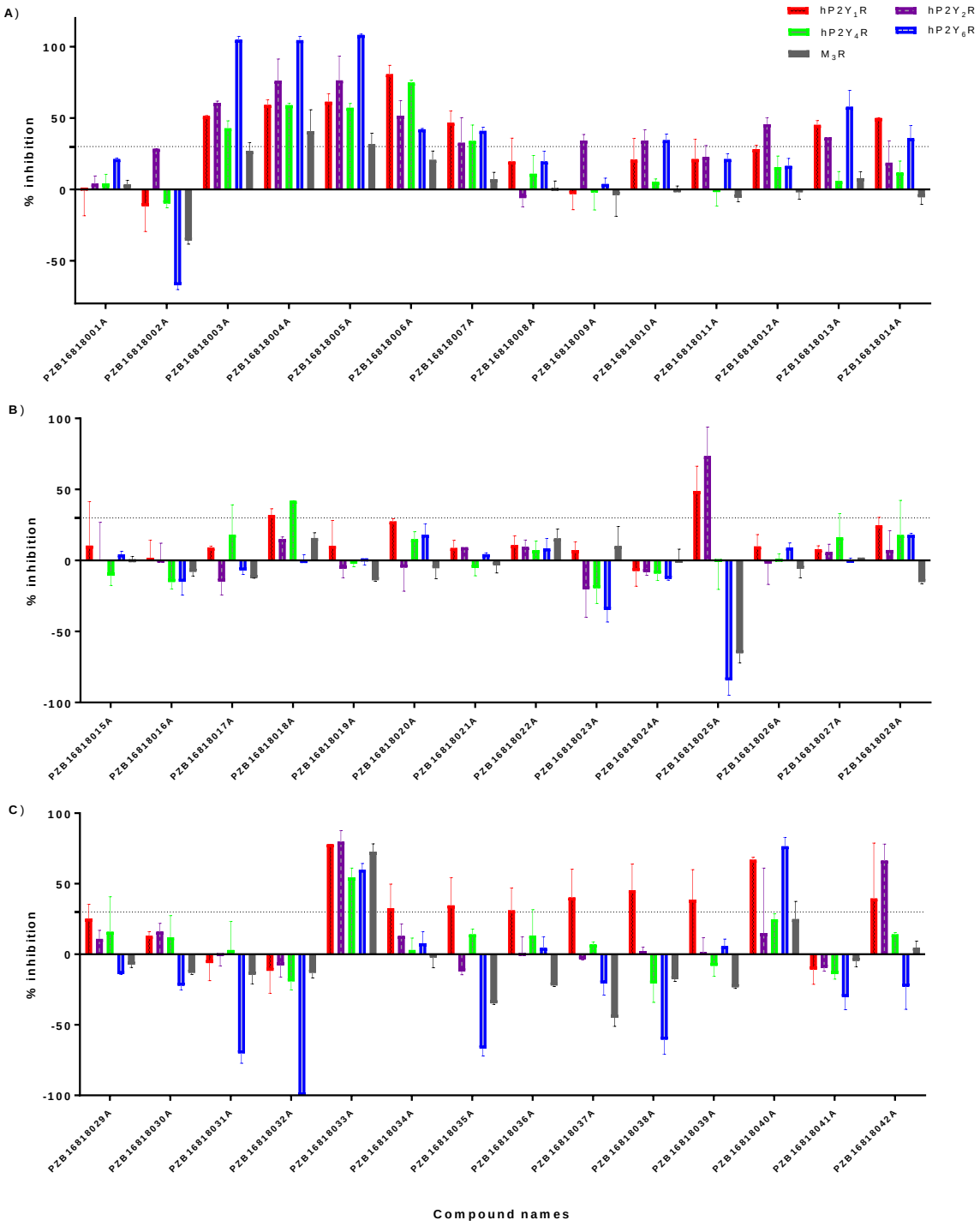

Figure 29: Results of second in vitro screening of the virtual screening hits as antagonists at the hP2Y and the muscarinic M_3 receptors as determined by calcium assays (n=3). Each bar represents the mean ± S.E.M of % inhibition values. The dotted black line indicates the 30 % inhibition threshold defined for a hit compound.

Table 8 : Potencies of in-silico hits as antagonists of the $P2Y_2R$ compared to their activity at selected $P2Y_1$-like receptors and at the acetylcholine M_3R. Biological assessment of the compounds was performed using calcium mobilization and β-arrestin recruitment assays.

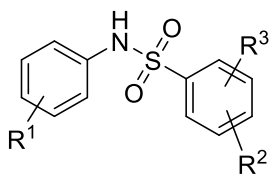

(283 - 285)
N-phenylbenzenesulfonamide derivatives

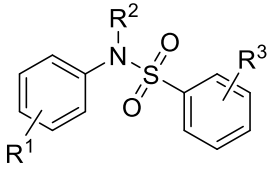

(286 - 289)
N-phenylbenzenesulfonamide derivatives

Cpd	Name	Structure			IC_{50} ± SEM [μM] (% inhibition at 10 μM); n = 3-4						
					hP2Y$_1$R[a]	**hP2Y$_2$R**[b]		**hP2Y$_4$R**[c]		**hP2Y$_6$R**[d]	**M$_3$R**[e]
		R^1	**R^2**	**R^3**	(Calcium assay)	Calcium assay	β-arrestin assay	Calcium assay	β-arrestin assay	(Calcium assay)	(Calc. assay)
283	PZB16 817004	***p***- COOH	H	***m***- 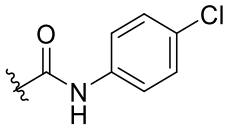	> 10 (7 %)	> 10 (-4 %)	> 10 (-1 %)	> 10 (9 %)	> 10 (-1 %)	> 10 (6 %)	> 10 (19 %)
284	PZB16 817006	***p***- Br	***o***- CH_3	***m***- 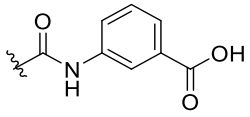	> 10 (3 %)	> 10 (-9 %)	> 10 (-6 %)	> 10 (11 %)	> 10 (-2 %)	> 10 (4 %)	> 10 (17 %)
285	PZB16 817022	***o***- 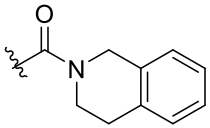	H	***p***- F	≤ 10 (34 %)	> 10 (-37 %)	> 10 (-10 %)	> 10 (28 %)	> 10 (-5 %)	< 10 (42 %)	≤ 10 (31 %)

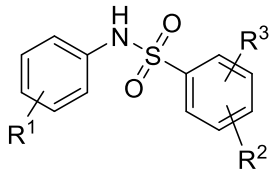

(283 - 285)
N-phenylbenzenesulfonamide derivatives

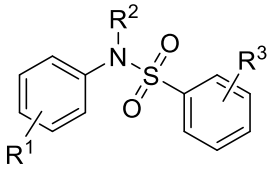

(286 - 289)
N-phenylbenzenesulfonamide derivatives

Cpd	Name	Structure			IC_{50} ± SEM [μM] (% inhibition at 10 μM); n = 3-4						
					hP2Y$_1$R[a]	**hP2Y$_2$R**[b]		**hP2Y$_4$R**[c]		**hP2Y$_6$R**[d]	**M$_3$R**[e]
		R^1	**R^2**	**R^3**	(Calcium assay)	Calcium assay	β-arrestin assay	Calcium assay	β-arrestin assay	(Calcium assay)	(Calc. assay)
286	PZB16 818008	H	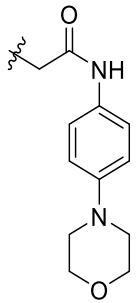	***p***- CH_3	> 10 (20 %)	> 10 (-6 %)	> 10 (4 %)	> 10 (11 %)	> 10 (9 %)	> 10 (19 %)	> 10 (1 %)
287	PZB16 818042	H	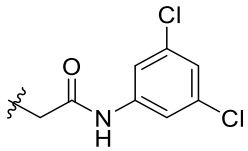	H	**7.19** ± 0.94	**8.34** ± 0.52	> 10 (10 %)	> 10 (14 %)	> 10 (34 %)	> 10 (-23 %)	> 10 (5 %)

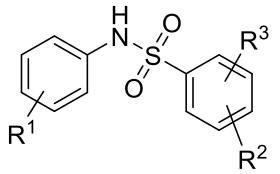

(283 - 285)
N-phenylbenzenesulfonamide derivatives

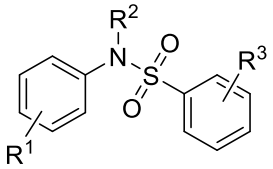

(286 - 289)
N-phenylbenzenesulfonamide derivatives

Cpd	Name	Structure			IC_{50} ± SEM [μM] (% inhibition at 10 μM); n = 3-4						
					hP2Y$_1$R[a]	**hP2Y$_2$R**[b]		**hP2Y$_4$R**[c]		**hP2Y$_6$R**[d]	**M$_3$R**[e]
		R^1	**R^2**	**R^3**	(Calcium assay)	Calcium assay	β-arrestin assay	Calcium assay	β-arrestin assay	(Calcium assay)	(Calc. assay)
288	PZB16 818030	***o***- Cl	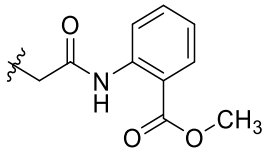	H	> 10 (13 %)	> 10 (16 %)	> 10 (-14 %)	> 10 (12 %)	> 10 (16 %)	> 10 (-22 %)	> 10 (-13 %)
289	PZB16 817042	***p***- Cl	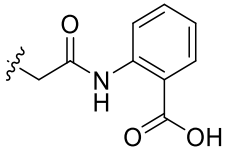	H	> 10 (5 %)	**30.3** ± 3.3	> 10 (14 %)	**30.7** ± 3.5	> 10 (1 %)	**36.8** ± 1.2	> 10 (23 %)

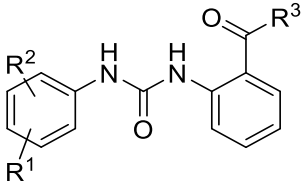

(**290 - 293**)
1,3-diphenylurea derivatives

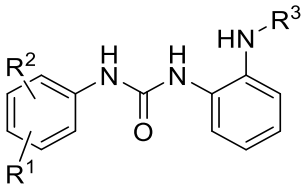

(**294 - 296**)
1,3-diphenylurea derivatives

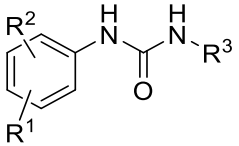

(**297 - 299**)
1-phenylurea derivatives

Cpd	Name	Structure			**IC$_{50}$** ± SEM [µM] (% inhibition at 10 µM); n = 3-4						
					hP2Y$_1$R[a]	**hP2Y$_2$R**[b]		**hP2Y$_4$R**[c]		**hP2Y$_6$R**[d]	**M$_3$R**[e]
		R^1	**R^2**	**R^3**	(Calcium assay)	Calcium assay	β-arrestin assay	Calcium assay	β-arrestin assay	(Calcium assay)	(Calc. assay)
290	PZB16 818011	H	***o***- F	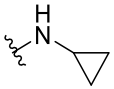	> 10 (21 %)	> 10 (23 %)	> 10 (-19 %)	> 10 (-2 %)	> 10 (-12 %)	> 10 (21 %)	> 10 (-6 %)
291	PZB16 817044	H	***m***- Cl	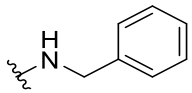	> 10 (23 %)	**46.2** ± 9.2	> 10 (-5 %)	**18.9** ± 6.2 (-3 %)	> 10 (-8 %)	> 10 (-1 %)	> 10 (-14 %)
292	PZB16 818018	***m***- Cl	***m***- Cl	OH	≈ 10 (29 %)	> 10 (15 %)	> 10 (-17 %)	≈ 10 (30 %)	> 10 (6 %)	> 10 (1 %)	> 10 (16 %)
293	PZB16 818021	***o***- Cl	***o***- Cl	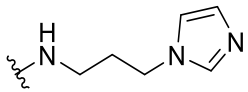	> 10 (9 %)	> 10 (9 %)	> 10 (-22 %)	> 10 (-5 %)	> 10 (-14 %)	> 10 (4 %)	> 10 (-3 %)

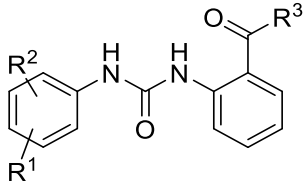

(**290 - 293**)
1,3-diphenylurea derivatives

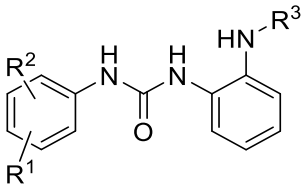

(**294 - 296**)
1,3-diphenylurea derivatives

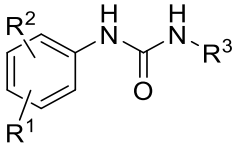

(**297 - 299**)
1-phenylurea derivatives

Cpd	Name	Structure			**IC$_{50}$** ± SEM [µM] (% inhibition at 10 µM); n = 3-4						
					hP2Y$_1$R[a]	**hP2Y$_2$R**[b]		**hP2Y$_4$R**[c]		**hP2Y$_6$R**[d]	**M$_3$R**[e]
		R^1	**R^2**	**R^3**	(Calcium assay)	Calcium assay	β-arrestin assay	Calcium assay	β-arrestin assay	(Calcium assay)	(Calc. assay)
294	PZB16 817018	H	H	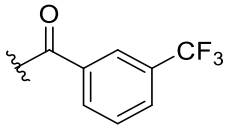	**11.9** ± 1.3	**6.83** ± 0.75	> 10 (-1 %)	**14.0** ± 0.2	**14.6** ± 0.8 (18 %)	> 10 (7 %)	> 10 (27 %)
295	PZB16 817020	H	H	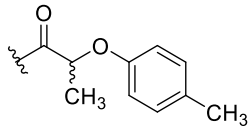	**16.6** ± 0.9	**11.0** ± 1.3 (32 %)	> 10 (-4 %)	**9.56** ± 1.97	**27.0** ± 8.0 (13 %)	**10.7** ± 1.1	> 10 (23 %)

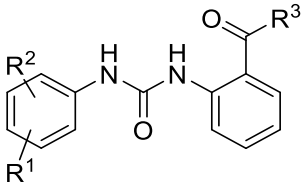

(**290 - 293**)
1,3-diphenylurea derivatives

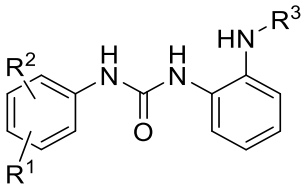

(**294 - 296**)
1,3-diphenylurea derivatives

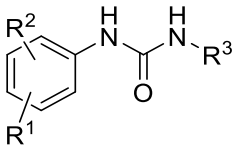

(**297 - 299**)
1-phenylurea derivatives

Cpd	Name	Structure			IC_{50} ± SEM [µM] (% inhibition at 10 µM); n = 3-4						
					hP2Y$_1$R[a]	**hP2Y$_2$R**[b]		**hP2Y$_4$R**[c]		**hP2Y$_6$R**[d]	**M$_3$R**[e]
		R^1	**R^2**	**R^3**	(Calcium assay)	Calcium assay	β-arrestin assay	Calcium assay	β-arrestin assay	(Calcium assay)	(Calc. assay)
296	PZB16 818026	H	H	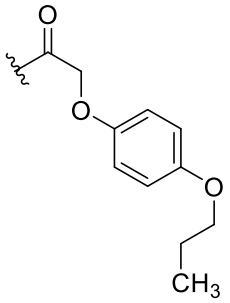	> 10 (10 %)	> 10 (-2 %)	> 10 (-19 %)	> 10 (1 %)	> 10 (4 %)	> 10 (9 %)	> 10 (-6 %)
297	PZB16 818012	H	***o***- 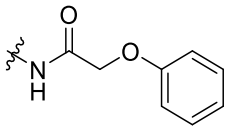	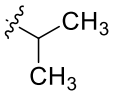	> 10 (28 %)	> 10 (1 %)	> 10 (-4 %)	> 10 (16 %)	> 10 (-12 %)	> 10 (16 %)	> 10 (-2 %)

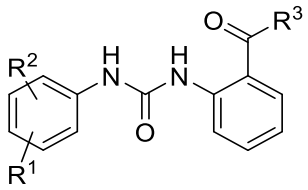

(**290 - 293**)
1,3-diphenylurea derivatives

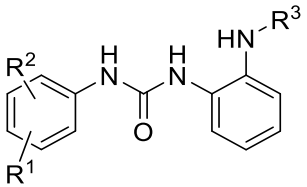

(**294 - 296**)
1,3-diphenylurea derivatives

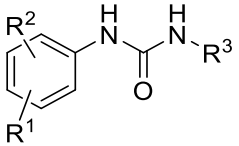

(**297 - 299**)
1-phenylurea derivatives

Cpd	Name	Structure			IC_{50} ± SEM [µM] (% inhibition at 10 µM); n = 3-4						
					hP2Y$_1$R[a]	**hP2Y$_2$R**[b]		**hP2Y$_4$R**[c]		**hP2Y$_6$R**[d]	**M$_3$R**[e]
		R^1	**R^2**	**R^3**	(Calcium assay)	Calcium assay	β-arrestin assay	Calcium assay	β-arrestin assay	(Calcium assay)	(Calc. assay)
298	PZB16 817014	H	***o***- 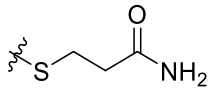	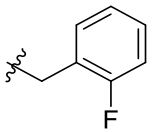	> 10 (28 %)	> 10 (-6 %)	> 10 (-8 %)	> 10 (16 %)	> 10 (3%)	> 10 (36 %)	> 10 (24 %)
299	PZB16 818033	***m***- CH_3	***o***- 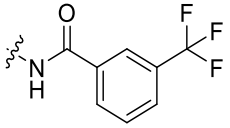	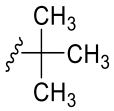	< 10 (78 %)	< 10 (80 %)	> 10 (36 %)	< 10 (54 %)	> 10 (39 %)	< 10 (60 %)	< 10 (73 %)

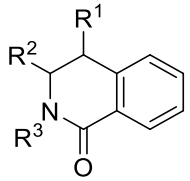

(**300**) PZB16817013

3,4-dihydroisoquinolin-1(2*H*)-one derivative

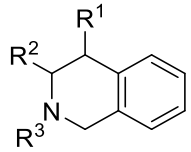

(**301**) PZB16817017

1,2,3,4-tetrahydroisoquinoline derivative

Cpd	Name	Structure			**IC$_{50}$** ± SEM [μM] (% inhibition at 10 μM); n = 3-4						
					hP2Y$_1$R[a]	**hP2Y$_2$R**[b]		**hP2Y$_4$R**[c]		**hP2Y$_6$R**[d]	**M$_3$R**[e]
		R^1	**R^2**	**R^3**	(Calcium assay)	Calcium assay	β-arrestin assay	Calcium assay	β-arrestin assay	(Calcium assay)	(Calc. assay)
300	PZB16 817013	COOH	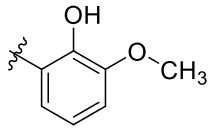	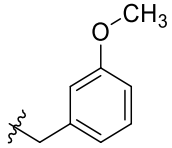	> 10 (8 %)	> 10 (-9 %)	> 10 (-2 %)	> 10 (22 %)	> 10 (-13 %)	> 10 (2 %)	> 10 (-1 %)
301	PZB16 817017	H	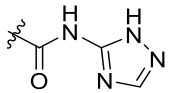	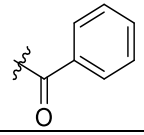	> 10 (-16 %)	> 10 (-23 %)	> 10 (-1 %)	> 10 (13 %)	> 10 (-8 %)	> 10 (10 %)	> 10 (4 %)

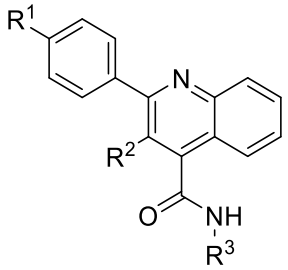

(**302 - 304**)

2-phenylquinoline-4-carboxamide derivatives

Cpd	Name	Structure			**IC$_{50}$** ± SEM [μM] (% inhibition at 10 μM); n = 3-4						
					hP2Y$_1$R[a]	**hP2Y$_2$R**[b]		**hP2Y$_4$R**[c]		**hP2Y$_6$R**[d]	**M$_3$R**[e]
		R^1	**R^2**	**R^3**	(Calcium assay)	Calcium assay	β-arrestin assay	Calcium assay	β-arrestin assay	(Calcium assay)	(Calc. assay)
302	PZB16 817032	H	H	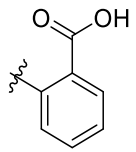	< 10 (50 %)	> 10 (5 %)	> 10 (4 %)	> 10 (29 %)	> 10 (11 %)	< 10 (82 %)	< 10 (64 %)
303	PZB16 818035	H	H	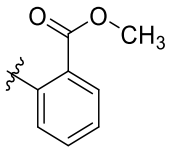	> 10 (-2 %)	> 10 (-12 %)	> 10 (-34 %)	> 10 (14 %)	> 10 (-4 %)	> 10 (-67 %)	> 10 (-35 %)
304	PZB16 818028	CH_3	CH_3	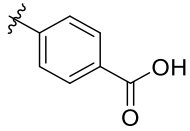	> 10 (25 %)	> 10 (7 %)	> 10 (-37 %)	> 10 (18 %)	> 10 (-3 %)	> 10 (18 %)	> 10 (-15 %)

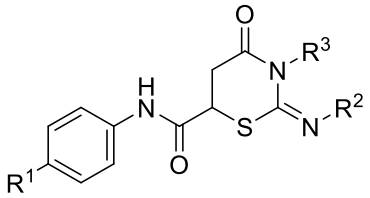

(**305 - 313**)

2-imino-4-oxo-*N*-phenyl-1,3-thiazinane-6-carboxamide derivatives

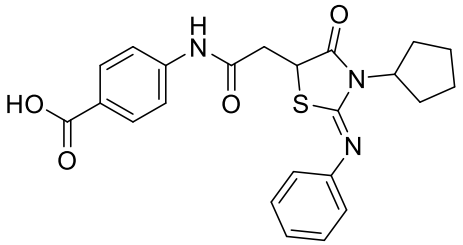

(**314**) PZB16817031

Cpd	Name	Structure			**IC$_{50}$** ± SEM [μM] (% inhibition at 10 μM); n = 3-4						
					hP2Y$_1$R[a]	**hP2Y$_2$R**[b]		**hP2Y$_4$R**[c]		**hP2Y$_6$R**[d]	**M$_3$R**[e]
		R^1	**R^2**	**R^3**	(Calcium assay)	Calcium assay	β-arrestin assay	Calcium assay	β-arrestin assay	(Calcium assay)	(Calc. assay)
305	PZB16 818034	F	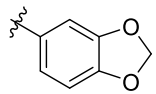	CH_3	**16.5** ± 0.5	> 10 (13 %)	> 10 (-40 %)	> 10 (3 %)	> 10 (-8 %)	> 10 (8 %)	> 10 (-2 %)
306	PZB16 817055	COOH	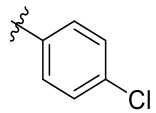	CH_3	> 10 (-28 %)	> 10 (-7 %)	> 10 (-12 %)	> 10 (-17 %)	> 10 (-15 %)	> 10 (-10 %)	> 10 (-20 %)
307	PZB16 817036	COOH	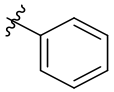	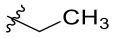	> 10 (-1 %)	> 10 (-15 %)	> 10 (-17 %)	> 10 (11 %)	> 10 (-13 %)	> 10 (7 %)	> 10 (-29 %)

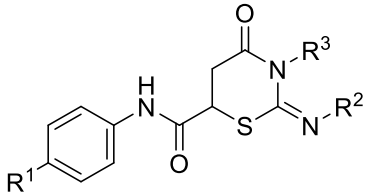

(**305 - 313**)

2-imino-4-oxo-*N*-phenyl-1,3-thiazinane-6-carboxamide derivatives

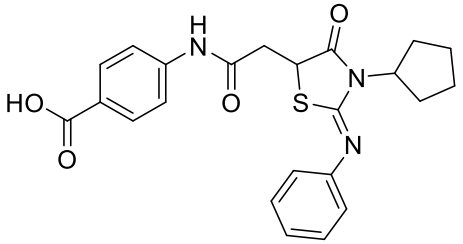

(**314**) PZB16817031

Cpd	Name	Structure			IC_{50} ± SEM [μM] (% inhibition at 10 μM); n = 3-4						
					hP2Y$_1$R[a]	**hP2Y$_2$R**[b]		**hP2Y$_4$R**[c]		**hP2Y$_6$R**[d]	**M$_3$R**[e]
					(Calcium assay)	Calcium assay	β-arrestin assay	Calcium assay	β-arrestin assay	(Calcium assay)	(Calc. assay)
		R^1	**R^2**	**R^3**							
308	PZB16 818040	COOH	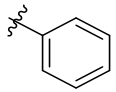	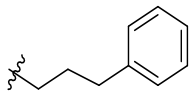	**6.68** ± 0.93	> 10 (15 %)	> 10 (-13 %)	> 10 (25 %)	> 10 (17 %)	**5.74** ± 0.49	> 10 (25 %)
309	PZB16 818039	COOH	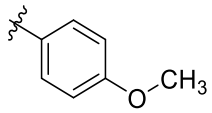	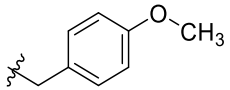	**11.1** ± 0.5	> 10 (1 %)	> 10 (-30 %)	> 10 (-8 %)	> 10 (-12 %)	> 10 (6 %)	> 10 (-23 %)
310	PZB16 817046	COOH	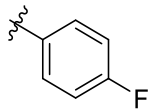	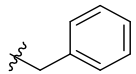	**10.8** ± 0.1	**9.87** ± 0.68	> 10 (-3 %)	**11.9** ± 0.6	> 10 (-5 %)	**4.92** ± 0.48	> 10 (21 %)
311	**PZB16 817047**	COOH	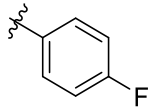	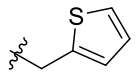	> 10 (3 %)	> 10 (16 %)	> 10 (-14 %)	≈ 10 (**42** %)	> 10 (-13 %)	**11.7** ± 0.4	> 10 (2 %)

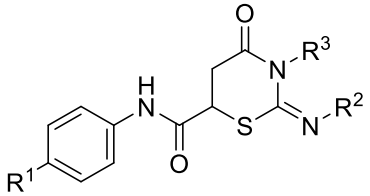

(**305 - 313**)

2-imino-4-oxo-*N*-phenyl-1,3-thiazinane-6-carboxamide derivatives

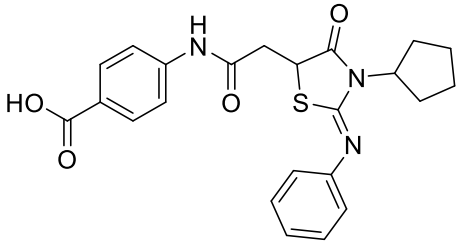

(**314**) PZB16817031

Cpd	Name	Structure			IC_{50} ± SEM [μM] (% inhibition at 10 μM); n = 3-4						
					hP2Y$_1$R[a]	**hP2Y$_2$R**[b]		**hP2Y$_4$R**[c]		**hP2Y$_6$R**[d]	**M$_3$R**[e]
		R^1	**R^2**	**R^3**	(Calcium assay)	Calcium assay	β-arrestin assay	Calcium assay	β-arrestin assay	(Calcium assay)	(Calc. assay)
312	PZB16 818031	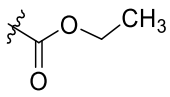	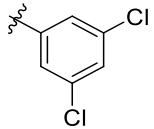	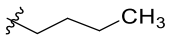	> 10 (-6 %)	> 10 (-1 %)	> 10 (-14 %)	> 10 (3 %)	> 10 (22 %)	> 10 (-70 %)	> 10 (-14 %)
313	PZB16 818032	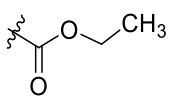	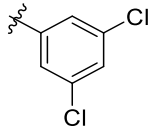	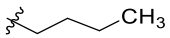	> 10 (-12 %)	> 10 (-8 %)	> 10 (-10 %)	> 10 (-19 %)	> 10 (30 %)	> 10 (-123 %)	> 10 (-13 %)
314	**PZB16 817031**	See structure above			> 10 (13 %)	> 10 (23 %)	> 10 (-22 %)	≈ 10 (**34** %)	> 10 (-4 %)	> 10 (11 %)	> 10 (-16 %)

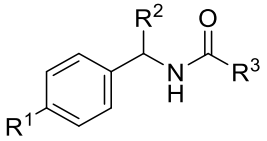

(**315 - 321**)

N-benzylacetamide derivatives

Cpd	Name	Structure			**IC$_{50}$** ± SEM [µM] (% inhibition at 10 µM); n = 3-4						
					hP2Y$_1$R[a]	**hP2Y$_2$R**[b]		**hP2Y$_4$R**[c]		**hP2Y$_6$R**[d]	**M$_3$R**[e]
		R^1	**R^2**	**R^3**	(Calcium assay)	Calcium assay	β-arrestin assay	Calcium assay	β-arrestin assay	(Calcium assay)	(Calc. assay)
315	PZB16 818016	H	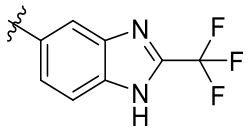	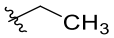	> 10 (2 %)	> 10 (1 %)	> 10 (-9 %)	> 10 (-15 %)	> 10 (4 %)	> 10 (-15 %)	> 10 (-8 %)
316	PZB16 818015	H	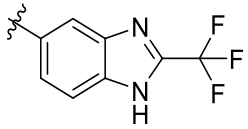		> 10 (10 %)	> 10 (1 %)	> 10 (-21 %)	> 10 (-11 %)	> 10 (25 %)	> 10 (4 %)	> 10 (1 %)
317	PZB16 817027	H	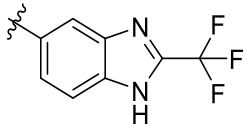	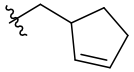	> 10 (1 %)	> 10 (-52 %)	> 10 (-5 %)	> 10 (14 %)	> 10 (5 %)	> 10 (19 %)	> 10 (5 %)

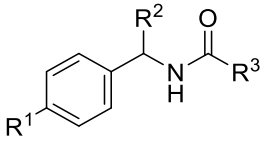

(**315 - 321**)

N-benzylacetamide derivatives

Cpd	Name	Structure			**IC$_{50}$** ± SEM [µM] (% inhibition at 10 µM); n = 3-4						
					hP2Y$_1$R[a]	**hP2Y$_2$R**[b]		**hP2Y$_4$R**[c]		**hP2Y$_6$R**[d]	**M$_3$R**[e]
		R^1	**R^2**	**R^3**	(Calcium assay)	Calcium assay	β-arrestin assay	Calcium assay	β-arrestin assay	(Calcium assay)	(Calc. assay)
318	PZB16 817026	F	CH_3	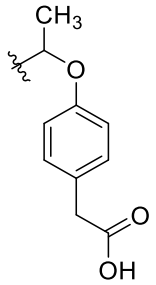	> 10 (11 %)	> 10 (-33 %)	> 10 (-13 %)	> 10 (18 %)	> 10 (3 %)	> 10 (8 %)	> 10 (10 %)
319	PZB16 817033	Cl	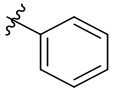	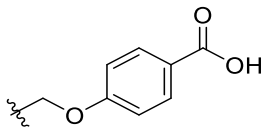	> 10 (-24 %)	> 10 (-37 %)	> 10 (-2 %)	> 10 (-6 %)	> 10 (-9 %)	> 10 (10 %)	> 10 (-29 %)

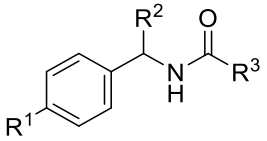

(**315 - 321**)
N-benzylacetamide derivatives

Cpd	Name	Structure			**IC$_{50}$** ± SEM [µM] (% inhibition at 10 µM); n = 3-4						
					hP2Y$_1$R[a]	**hP2Y$_2$R**[b]		**hP2Y$_4$R**[c]		**hP2Y$_6$R**[d]	**M$_3$R**[e]
		R^1	**R^2**	**R^3**	(Calcium assay)	Calcium assay	β-arrestin assay	Calcium assay	β-arrestin assay	(Calcium assay)	(Calc. assay)
320	PZB16 817019	COOH	H	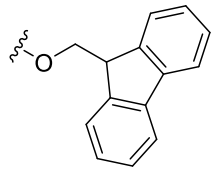	> 10 (-5 %)	> 10 (-62 %)	> 10 (-16 %)	> 10 (24 %)	> 10 (-11 %)	> 10 (27 %)	> 10 (3 %)
321	PZB16 817023	H	H	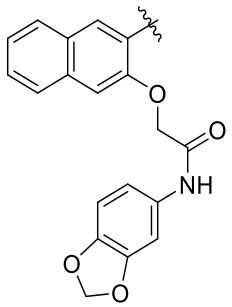	> 10 (-6 %)	> 10 (22 %)	> 10 (-4 %)	> 10 (27 %)	> 10 (-1 %)	> 10 (19 %)	> 10 (15 %)

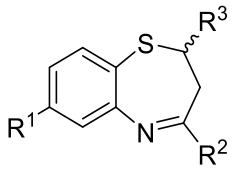

(**322 - 325**)

2,3-dihydrobenzo[*b*][1,4]thiazepine derivatives

Cpd	Name	Structure			**IC$_{50}$** ± SEM [µM] (% inhibition at 10 µM); n = 3-4						
					hP2Y$_1$R[a]	**hP2Y$_2$R**[b]		**hP2Y$_4$R**[c]		**hP2Y$_6$R**[d]	**M$_3$R**[e]
		R^1	**R^2**	**R^3**	(Calcium assay)	Calcium assay	β-arrestin assay	Calcium assay	β-arrestin assay	(Calcium assay)	(Calc. assay)
322	PZB16 818002	H	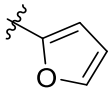	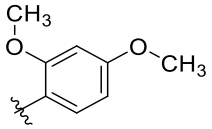	> 10 (-11 %)	> 10 (10 %)	> 10 (10 %)	> 10 (-10 %)	< 10 (**40** %)	> 10 (-67 %)	> 10 (-36 %)
323	PZB16 818023	H	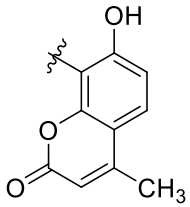	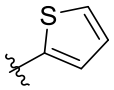	> 10 (7 %)	> 10 (-20 %)	> 10 (25 %)	> 10 (-19 %)	< 10 (**53** %)	> 10 (-35 %)	> 10 (10 %)

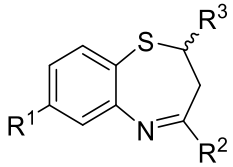

(**322 - 325**)

2,3-dihydrobenzo[*b*][1,4]thiazepine derivatives

Cpd	Name	Structure			**IC$_{50}$** ± SEM [µM] (% inhibition at 10 µM); n = 3-4						
					hP2Y$_1$R[a]	**hP2Y$_2$R**[b]		**hP2Y$_4$R**[c]		**hP2Y$_6$R**[d]	**M$_3$R**[e]
		R^1	**R^2**	**R^3**	(Calcium assay)	Calcium assay	β-arrestin assay	Calcium assay	β-arrestin assay	(Calcium assay)	(Calc. assay)
324	PZB16 817043		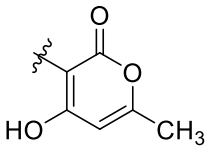	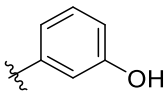	> 10 (4 %)	**10.9** ± 0.8	**26.0** ± 3.0 (26 %)	**18.4** ± 1.4	**12.4** ± 1.5 (31 %)	> 10 (19 %)	> 10 (30 %)
325	PZB16 818019		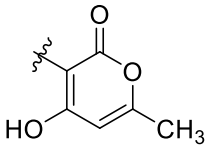	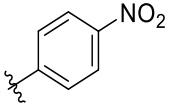	> 10 (10 %)	> 10 (-6 %)	> 10 (-14 %)	> 10 (-2 %)	> 10 (19 %)	> 10 (-1 %)	> 10 (-14 %)

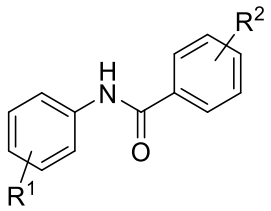

(**326 - 332**)

N-phenylbenzamide derivatives

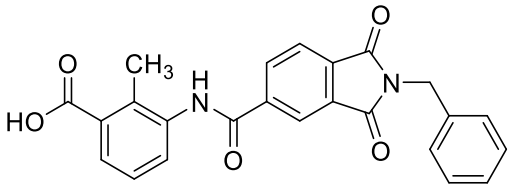

(**333**) PZB16817051

1,3-dioxo-*N*-phenylisoindoline-5-carboxamide derivative

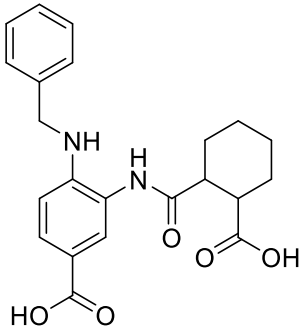

(**334**) PZB16817001

N-phenylcyclohexanecarboxamide derivative

Cpd	Name	Structure		IC_{50} ± SEM [μM] (% inhibition at 10 μM); n = 3-4						
				hP2Y$_1$R[a]	**hP2Y$_2$R**[b]		**hP2Y$_4$R**[c]		**hP2Y$_6$R**[d]	**M$_3$R**[e]
		R^1	**R^2**	(Calcium assay)	Calcium assay	β-arrestin assay	Calcium assay	β-arrestin assay	(Calcium assay)	(Calc. assay)
326	PZB16 817008	***o***- 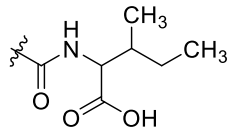	***p***- CH_3	> 10 (-23 %)	> 10 (-21 %)	> 10 (1 %)	> 10 (-23 %)	> 10 (10 %)	≈ 10 (29 %)	≈ 10 (33 %)
327	PZB16 818038	*o*- 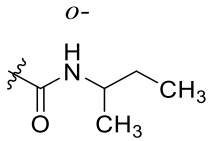	***p***- 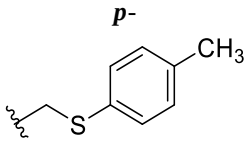	> 10 (-21 %)	> 10 (2 %)	> 10 (-26 %)	> 10 (-21 %)	> 10 (40 %)	> 10 (-60 %)	> 10 (-18 %)

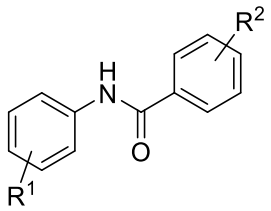

(**326 - 332**)

N-phenylbenzamide derivatives

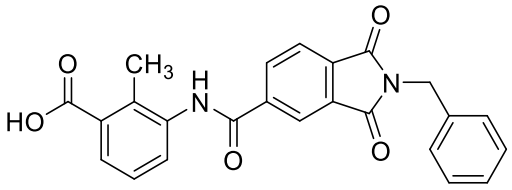

(**333**) PZB16817051

1,3-dioxo-*N*-phenylisoindoline-5-carboxamide derivative

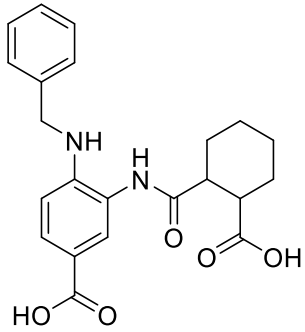

(**334**) PZB16817001

N-phenylcyclohexanecarboxamide derivative

Cpd	Name	Structure		**IC$_{50}$** ± SEM [µM] (% inhibition at 10 µM); n = 3-4						
				hP2Y$_1$R[a]	**hP2Y$_2$R**[b]		**hP2Y$_4$R**[c]		**hP2Y$_6$R**[d]	**M$_3$R**[e]
		R^1	**R^2**	(Calcium assay)	Calcium assay	β-arrestin assay	Calcium assay	β-arrestin assay	(Calcium assay)	(Calc. assay)
328	PZB16 817053	***o***- COOH	***o***- 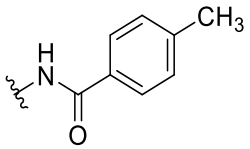	< 10 (70 %)	**5.76** ± 1.08 (41 %)	> 10 (10 %)	**3.46** ± 0.80 (94 %)	> 10 (-3 %)	< 10 (61 %)	**< 10 (50 %)**
329	PZB16 818036	***o***- COOH	***m***- 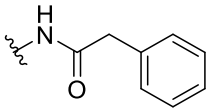	> 10 (5 %)	> 10 (1 %)	> 10 (-35 %)	> 10 (13 %)	> 10 (-16 %)	> 10 (5 %)	> 10 (-22 %)

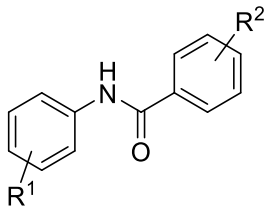

(**326 - 332**)

N-phenylbenzamide derivatives

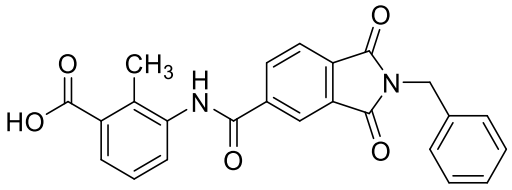

(**333**) PZB16817051

1,3-dioxo-*N*-phenylisoindoline-5-carboxamide derivative

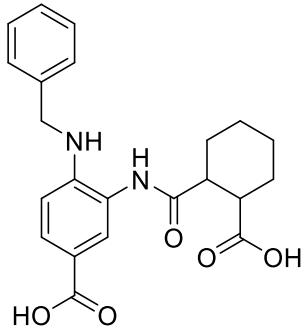

(**334**) PZB16817001

N-phenylcyclohexanecarboxamide derivative

Cpd	Name	Structure		**IC$_{50}$** ± SEM [μM] (% inhibition at 10 μM); n = 3-4						
				hP2Y$_1$R[a]	**hP2Y$_2$R**[b]		**hP2Y$_4$R**[c]		**hP2Y$_6$R**[d]	**M$_3$R**[e]
		R^1	**R^2**	(Calcium assay)	Calcium assay	β-arrestin assay	Calcium assay	β-arrestin assay	(Calcium assay)	(Calc. assay)
330	PZB16 818037	***o***- COOH	***p***- 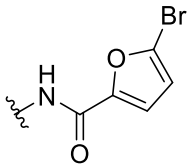	> 10 (-15 %)	> 10 (-4 %)	> 10 (-43 %)	> 10 (7 %)	> 10 (-26 %)	> 10 (-21 %)	> 10 (-45 %)
331	PZB16 817037	***m***- COOH	***m***- 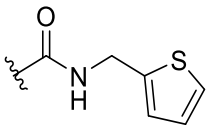	> 10 (11 %)	> 10 (2 %)	> 10 (-19 %)	> 10 (15 %)	> 10 (-19 %)	> 10 (2 %)	> 10 (-22 %)

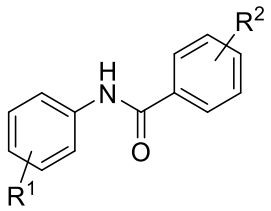

(**326 - 332**)

N-phenylbenzamide derivatives

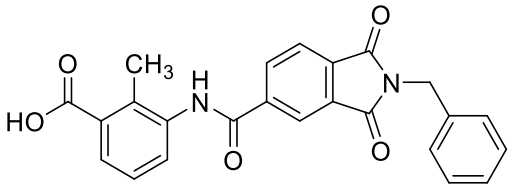

(**333**) PZB16817051

1,3-dioxo-*N*-phenylisoindoline-5-carboxamide derivative

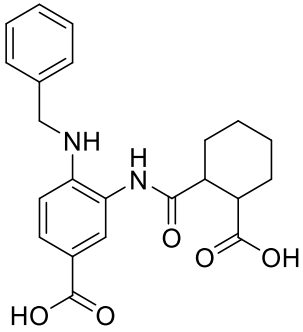

(**334**) PZB16817001

N-phenylcyclohexanecarboxamide derivative

Cpd	Name	Structure		IC_{50} ± SEM [μM] (% inhibition at 10 μM); n = 3-4						
				hP2Y$_1$R[a]	**hP2Y$_2$R**[b]		**hP2Y$_4$R**[c]		**hP2Y$_6$R**[d]	**M$_3$R**[e]
		R^1	**R^2**	(Calcium assay)	Calcium assay	β-arrestin assay	Calcium assay	β-arrestin assay	(Calcium assay)	(Calc. assay)
332	PZB16 817050	***p***- COOH	***m***- 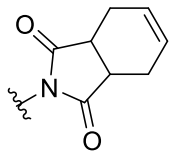	> 10 (5 %)	> 10 (20 %)	> 10 (-18 %)	> 10 (26 %)	> 10 (-16 %)	> 10 (-14 %)	> 10 (-23 %)
333	PZB16 817051	See structure above		> 10 (-5 %)	> 10 (4 %)	> 10 (-16 %)	> 10 (8 %)	> 10 (-13 %)	> 10 (-8 %)	> 10 (-17 %)
334	PZB16 817001	See structure above		> 10 (-23 %)	> 10 (-4 %)	> 10 (-1 %)	> 10 (21 %)	> 10 (-5 %)	> 10 (18 %)	> 10 (1 %)

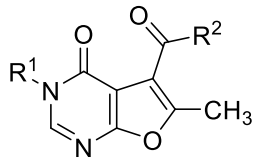

(**335 - 338**)

furo[2,3-*d*]pyrimidin-4(3*H*)-one derivatives

Cpd	Name	Structure		IC_{50} ± SEM [μM] (% inhibition at 10 μM); n = 3-4						
				hP2Y$_1$R[a]	**hP2Y$_2$R**[b]		**hP2Y$_4$R**[c]		**hP2Y$_6$R**[d]	**M$_3$R**[e]
		R^1	**R^2**	(Calcium assay)	Calcium assay	β-arrestin assay	Calcium assay	β-arrestin assay	(Calcium assay)	(Calc. assay)
335	PZB16 818001	CH_3	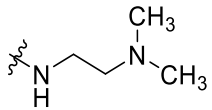	> 10 (-1 %)	> 10 (4 %)	> 10 (26 %)	> 10 (4 %)	> 10 (10 %)	> 10 (21 %)	> 10 (3 %)
336	PZB16 818007	H	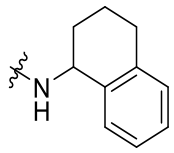	> 10 (30 %)	> 10 (13 %)	> 10 (-3 %)	> 10 (4 %)	> 10 (-10 %)	> 10 (-1 %)	> 10 (7 %)
337	PZB16 818017	H	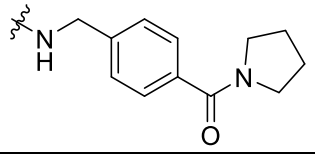	> 10 (9 %)	> 10 (-15 %)	> 10 (12 %)	> 10 (18 %)	> 10 (5 %)	> 10 (-7 %)	> 10 (-12 %)

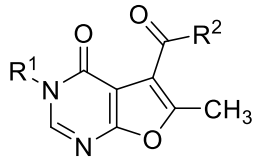

(**335 - 338**)

furo[2,3-*d*]pyrimidin-4(3*H*)-one derivatives

Cpd	Name	Structure		IC_{50} ± SEM [µM] (% inhibition at 10 µM); n = 3-4						
				hP2Y$_1$R[a]	**hP2Y$_2$R**[b]		**hP2Y$_4$R**[c]		**hP2Y$_6$R**[d]	**M$_3$R**[e]
		R^1	**R^2**	(Calcium assay)	Calcium assay	β-arrestin assay	Calcium assay	β-arrestin assay	(Calcium assay)	(Calc. assay)
338	PZB16 817030	H	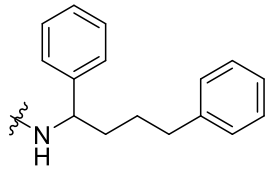	**6.62** ± 1.84	**2.95** ± 0.14 (37 %)	> 10 (-6 %)	**6.30** ± 2.04 (50 %)	**30.7** ± 0.9 (-5 %)	**9.16** ± 0.40 (24 %)	> 10 (2 %)

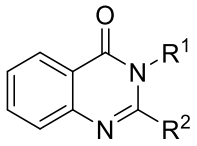

(**339 - 343**)
quinazolin-4(3*H*)-one derivatives

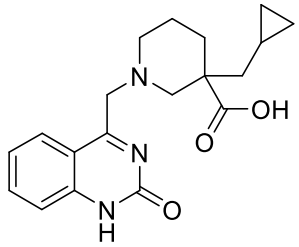

(**344**) PZB16817005
quinazolin-2(1*H*)-one dervative

Cpd	Name	Structure		IC_{50} ± SEM [µM] (% inhibition at 10 µM); n = 3-4						
				hP2Y$_1$R[a]	**hP2Y$_2$R**[b]		**hP2Y$_4$R**[c]		**hP2Y$_6$R**[d]	**M$_3$R**[e]
		R^1	**R^2**	(Calcium assay)	Calcium assay	β-arrestin assay	Calcium assay	β-arrestin assay	(Calcium assay)	(Calc. assay)
339	PZB16 817024	H	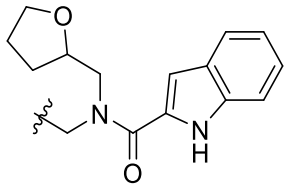	> 10 (-23 %)	> 10 (-19 %)	> 10 (-7 %)	> 10 (-12 %)	> 10 (-2 %)	> 10 (8 %)	> 10 (23 %)
340	PZB16 818006	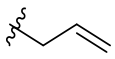	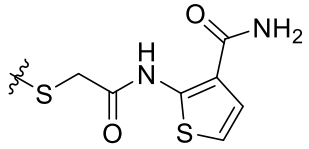	**5.89** ± 0.83	> 10 (21 %)	> 10 (-11 %)	**13.0** ± 0.9	> 10 (-9 %)	> 10 (2 %)	> 10 (21 %)
341	PZB16 818027	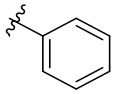	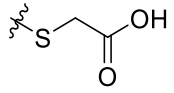	> 10 (8 %)	> 10 (6 %)	> 10 (-36 %)	> 10 (16 %)	> 10 (-16 %)	> 10 (1 %)	> 10 (1 %)

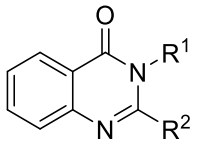

(**339 - 343**)
quinazolin-4(3*H*)-one derivatives

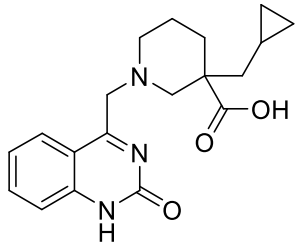

(**344**) PZB16817005
quinazolin-2(1*H*)-one dervative

Cpd	Name	Structure		**IC$_{50}$** ± SEM [µM] (% inhibition at 10 µM); n = 3-4						
				hP2Y$_1$R[a]	**hP2Y$_2$R**[b]		**hP2Y$_4$R**[c]		**hP2Y$_6$R**[d]	**M$_3$R**[e]
		R^1	**R^2**	(Calcium assay)	Calcium assay	β-arrestin assay	Calcium assay	β-arrestin assay	(Calcium assay)	(Calc. assay)
342	PZB16 818024	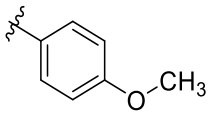	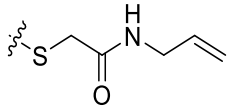	> 10 (-7 %)	> 10 (-7 %)	> 10 (-12 %)	> 10 (-9 %)	> 10 (-3 %)	> 10 (-13 %)	> 10 (1 %)
343	PZB16 817029	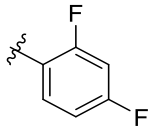	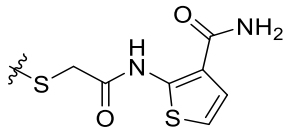	> 10 (-18 %)	> 10 (6 %)	> 10 (-8 %)	> 10 (10 %)	> 10 (-8 %)	> 10 (5 %)	> 10 (-24 %)
344	PZB16 817005	See structure above		> 10 (4 %)	> 10 (-11 %)	> 10 (-1 %)	> 10 (16 %)	> 10 (-9 %)	> 10 (1 %)	> 10 (11 %)

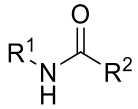

(**345 - 347**)
amide derivatives

Cpd	Name	Structure		IC_{50} ± SEM [µM] (% inhibition at 10 µM); n = 3-4						
				hP2Y$_1$R[a]	**hP2Y$_2$R**[b]		**hP2Y$_4$R**[c]		**hP2Y$_6$R**[d]	**M$_3$R**[e]
		R^1	**R^2**	(Calcium assay)	Calcium assay	β-arrestin assay	Calcium assay	β-arrestin assay	(Calcium assay)	(Calc. assay)
345	PZB16 817025	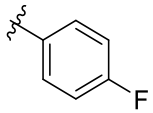	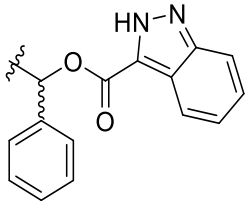	> 10 (25 %)	> 10 (4 %)	> 10 (-4 %)	> 10 (24 %)	> 10 (3 %)	> 10 (15 %)	> 10 (12 %)
346	PZB16 817057	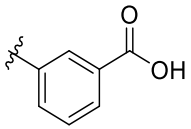	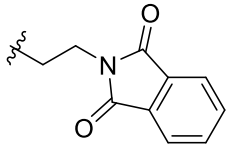	> 10 (-19 %)	> 10 (-20 %)	> 10 (-5 %)	> 10 (1 %)	> 10 (-24 %)	> 10 (-16 %)	> 10 (-19 %)
347	PZB16 817052	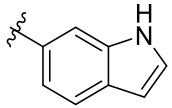	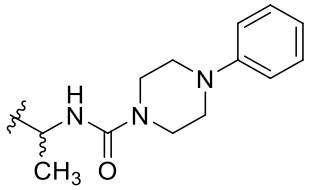	> 10 (4 %)	> 10 (-34 %)	> 10 (-12 %)	> 10 (19 %)	> 10 (-20 %)	> 10 (-3 %)	> 10 (-18 %)

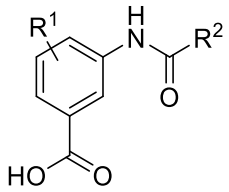

(**348 - 350**)

3-acetamidobenzoic acid derivatives

Cpd	Name	Structure		IC_{50} ± SEM [μM] (% inhibition at 10 μM); n = 3-4						
				hP2Y$_1$R[a]	**hP2Y$_2$R**[b]		**hP2Y$_4$R**[c]		**hP2Y$_6$R**[d]	**M$_3$R**[e]
		R^1	**R^2**	(Calcium assay)	Calcium assay	β-arrestin assay	Calcium assay	β-arrestin assay	(Calcium assay)	(Calc. assay)
348	PZB16 817045	H	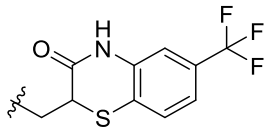	> 10 (2 %)	> 10 (-1 %)	> 10 (-17 %)	> 10 (20 %)	> 10 (-23 %)	> 10 (-9 %)	> 10 (-33 %)
349	PZB16 817049	***o***- OCH_3	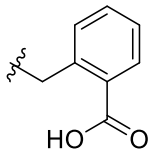	> 10 (-21 %)	> 10 (-8 %)	> 10 (-8 %)	> 10 (10 %)	> 10 (-14 %)	> 10 (1 %)	> 10 (-13 %)
350	PZB16 817040	***p***- Cl	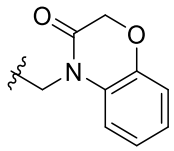	> 10 (-31 %)	> 10 (-38 %)	> 10 (-2 %)	> 10 (-12 %)	> 10 (-10 %)	> 10 (-9 %)	> 10 (10 %)

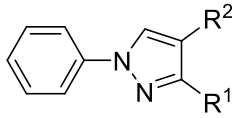

(**351 - 355**)

1-phenylpyrazole derivatives

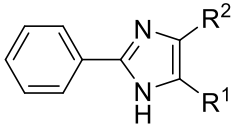

(**356**) PZB16817009

2-phenylimidazole derivative

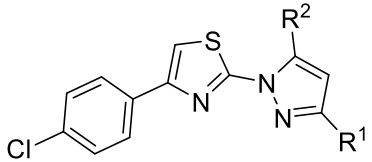

(**357**) PZB16818029

Cpd	Name	Structure		IC_{50} ± SEM [µM] (% inhibition at 10 µM); n = 3-4						
				hP2Y$_1$R[a]	**hP2Y$_2$R**[b]		**hP2Y$_4$R**[c]		**hP2Y$_6$R**[d]	**M$_3$R**[e]
		R^1	**R^2**	(Calcium assay)	Calcium assay	β-arrestin assay	Calcium assay	β-arrestin assay	(Calcium assay)	(Calc. assay)
351	PZB16 818025	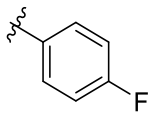	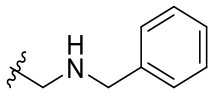	**13.4** ± 0.9	**8.60** ± 0.58	> 10 (13 %)	> 10 (-1 %)	> 10 (27 %)	> 10 (-84 %)	> 10 (-65 %)
352	PZB16 817021	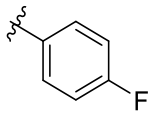	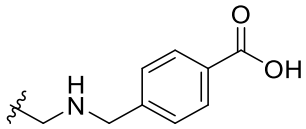	> 10 (17 %)	> 10 (-18 %)	> 10 (-13 %)	> 10 (28 %)	> 10 (-18 %)	> 10 (25 %)	> 10 (-9 %)
353	**PZB16 818009**	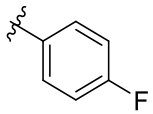	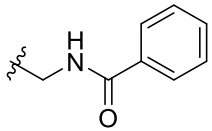	> 10 (-3 %)	> 10 (5 %)	> 10 (4 %)	> 10 (-2 %)	**< 10 (52 %)**	> 10 (4 %)	> 10 (-4 %)

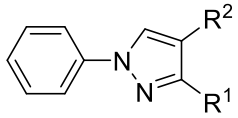

(**351 - 355**)

1-phenylpyrazole derivatives

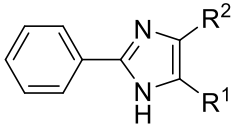

(**356**) PZB16817009

2-phenylimidazole derivative

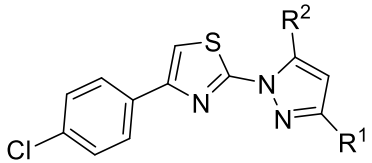

(**357**) PZB16818029

Cpd	Name	Structure		IC$_{50}$ ± SEM [µM] (% inhibition at 10 µM); n = 3-4						
				hP2Y$_1$R[a]	**hP2Y$_2$R**[b]		**hP2Y$_4$R**[c]		**hP2Y$_6$R**[d]	**M$_3$R**[e]
		R^1	**R^2**	(Calcium assay)	Calcium assay	β-arrestin assay	Calcium assay	β-arrestin assay	(Calcium assay)	(Calc. assay)
354	PZB16 818003	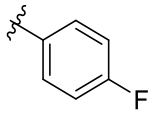	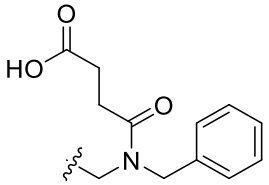	**10.0** ± 0.1	**10.6** ± 0.4	> 10 (-17 %)	**11.2** ± 0.4	**32.7** ± 2.4	**6.74** ± 0.93	> 10 (27 %)
355	PZB16 817039	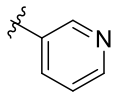	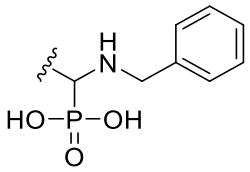	> 10 (-17 %)	> 10 (-3 %)	> 10 (-22 %)	> 10 (16 %)	> 10 (-12 %)	> 10 (3 %)	> 10 (-3 %)
356	PZB16 817009	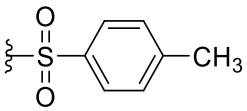	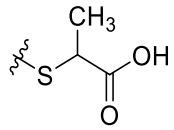	> 10 (-5 %)	> 10 (-10 %)	> 10 (2 %)	> 10 (1 %)	> 10 (-3 %)	> 10 (22 %)	> 10 (14 %)

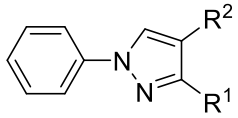

(**351 - 355**)

1-phenylpyrazole derivatives

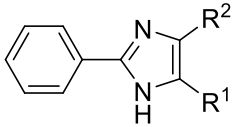

(**356**) PZB16817009

2-phenylimidazole derivative

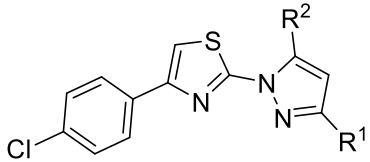

(**357**) PZB16818029

Cpd	Name	Structure		**IC$_{50}$** ± SEM [µM] (% inhibition at 10 µM); n = 3-4						
				hP2Y$_1$R[a]	**hP2Y$_2$R**[b]		**hP2Y$_4$R**[c]		**hP2Y$_6$R**[d]	**M$_3$R**[e]
		R^1	**R^2**	(Calcium assay)	Calcium assay	β-arrestin assay	Calcium assay	β-arrestin assay	(Calcium assay)	(Calc. assay)
357	PZB16 818029	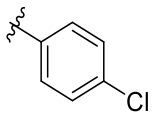		> 10 (25 %)	> 10 (11 %)	> 10 (-22 %)	> 10 (16 %)	> 10 (-13 %)	> 10 (-14 %)	> 10 (-7 %)

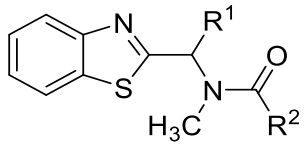

(**358 - 361**)

benzothiazole derivatives

Cpd	Name	Structure		IC_{50} ± SEM [µM] (% inhibition at 10 µM); n = 3-4						
				hP2Y$_1$R[a]	**hP2Y$_2$R**[b]		**hP2Y$_4$R**[c]		**hP2Y$_6$R**[d]	**M$_3$R**[e]
		R^1	**R^2**	(Calcium assay)	Calcium assay	β-arrestin assay	Calcium assay	β-arrestin assay	(Calcium assay)	(Calc. assay)
358	PZB16 818013	H	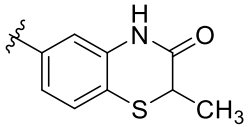	**21.3** ± 2.5	**16.6** ± 1.7	> 10 (-2 %)	> 10 (6 %)	> 10 (-24 %)	**7.36** ± 0.87	> 10 (5 %)
359	PZB16 818014	H	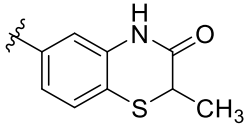	**11.2** ± 0.7	> 10 (19 %)	> 10 (-33 %)	> 10 (12 %)	> 10 (-20 %)	**10.7** ± 1.4	> 10 (-6 %)
360	PZB16 818010	H	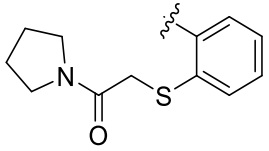	> 10 (21 %)	**21.9** ± 0.7	> 10 (-1 %)	> 10 (5 %)	> 10 (-1 %)	**28.7** ± 0.5	> 10 (1 %)
361	PZB16 817028	CH_3	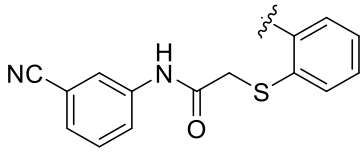	< 10 (66 %)	**9.26** ± 1.92	**13.5** ± 1.2 (9 %)	**2.80** ± 0.39	14.6 ± 2.8 (5 %)	< 10 (85 %)	**< 10 (68 %)**

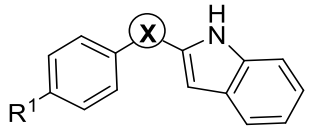

(**362 - 363**)

Cpd	Name	Structure		IC_{50} ± SEM [μM] (% inhibition at 10 μM); n = 3-4						
				hP2Y$_1$R[a]	**hP2Y$_2$R**[b]		**hP2Y$_4$R**[c]		**hP2Y$_6$R**[d]	**M$_3$R**[e]
		R^1	**X**	(Calcium assay)	Calcium assay	β-arrestin assay	Calcium assay	β-arrestin assay	(Calcium assay)	(Calc. assay)
362	PZB16 817048	OCH_3	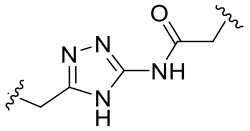	> 10 (-22 %)	> 10 (-12 %)	> 10 (-6 %)	> 10 (-12 %)	> 10 (-12 %)	> 10 (-3 %)	> 10 (11 %)
363	PZB16 817038	COOH	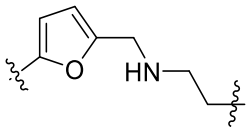	> 10 (20 %)	> 10 (1 %)	> 10 (-14 %)	> 10 (15 %)	> 10 (-8 %)	> 10 (12 %)	> 10 (-8 %)

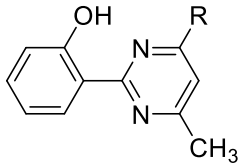

(**364**) PZB16817002

2-phenylpyrimidine derivative

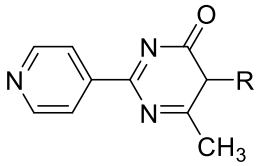

(**365**) PZB16817016

2-(pyridin-4-yl)pyrimidine derivative

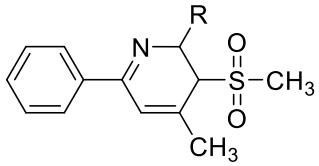

(**366**) PZB16818041

2-phenylpyridine derivative

Cpd	Name	Structure R	**IC$_{50}$** ± SEM [μM] (% inhibition at 10 μM); n = 3-4 **hP2Y$_1$R**[a] (Calcium assay)	**hP2Y$_2$R**[b] Calcium assay	 β-arrestin assay	**hP2Y$_4$R**[c] Calcium assay	 β-arrestin assay	**hP2Y$_6$R**[d] (Calcium assay)	**M$_3$R**[e] (Calc. assay)
364	PZB16 817002	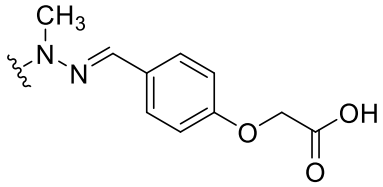	< 10 (79 %)	< 10 (102 %)	> 10 (24 %)	< 10 (102 %)	> 10 (15 %)	< 10 (58 %)	**< 10 (98 %)**
365	PZB16 817016	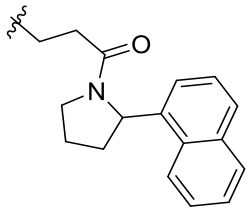	> 10 (-21 %)	> 10 (-32 %)	> 10 (2 %)	> 10 (-16 %)	> 10 (2 %)	> 10 (12 %)	> 10 (16 %)
366	PZB16 818041	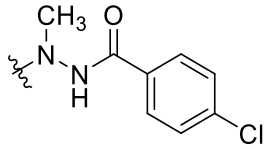	> 10 (-11 %)	> 10 (-10 %)	> 10 (15 %)	> 10 (-14 %)	> 10 (29 %)	> 10 (-30 %)	> 10 (-5 %)

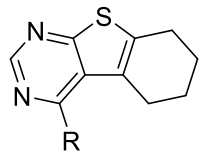

(**367 - 368**)

5,6,7,8-tetrahydrobenzo[4,5]thieno[2,3-*d*]pyrimidine derivatives

Cpd	Name	Structure R	**IC$_{50}$** ± SEM [µM] (% inhibition at 10 µM); n = 3-4						
			hP2Y$_1$R[a]	**hP2Y$_2$R**[b]		**hP2Y$_4$R**[c]		**hP2Y$_6$R**[d]	**M$_3$R**[e]
			(Calcium assay)	Calcium assay	β-arrestin assay	Calcium assay	β-arrestin assay	(Calcium assay)	(Calc. assay)
367	PZB16 818020	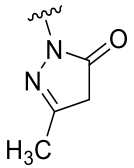	> 10 (28 %)	> 10 (-5 %)	> 10 (-25 %)	> 10 (15 %)	> 10 (21 %)	> 10 (18 %)	> 10 (-5 %)
368	PZB16 818022	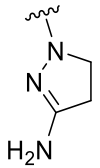	> 10 (11 %)	> 10 (10 %)	> 10 (-32 %)	> 10 (7 %)	> 10 (3 %)	> 10 (9 %)	> 10 (15 %)

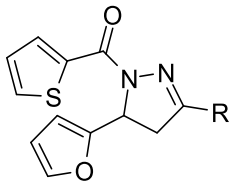

(**369 - 370**)
4,5-dihydro-1*H*-pyrazole derivatives

Cpd	Name	Structure R	**IC$_{50}$** ± SEM [µM] (% inhibition at 10 µM); n = 3-4 **hP2Y$_1$R**[a] (Calcium assay)	**hP2Y$_2$R**[b] Calcium assay	 β-arrestin assay	**hP2Y$_4$R**[c] Calcium assay	 β-arrestin assay	**hP2Y$_6$R**[d] (Calcium assay)	**M$_3$R**[e] (Calc. assay)
369	PZB16 818004	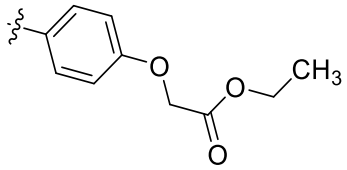	**2.66** ± 0.52	**3.07** ± 0.64	> 10 (4 %)	**1.94** ± 0.39	**25.8** ± 1.4	**1.79** ± 0.22	≈ 10 (29 %)
370	PZB16 818005	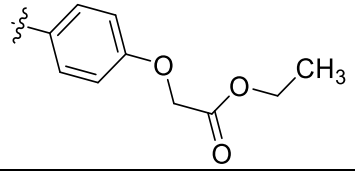	**4.39** ± 0.67	**4.02** ± 0.77	> 10 (-1 %)	**4.94** ± 0.87	**20.0** ± 3.6	**3.24** ± 0.14	≈ 10 (32 %)

Cpd	Name	Structure (371 -381)	IC_{50} ± SEM [µM] (% inhibition at 10 µM); n = 3-4						
			$hP2Y_1R$[a]	**$hP2Y_2R$**[b]		**$hP2Y_4R$**[c]		**$hP2Y_6R$**[d]	**M_3R**[e]
			(Calcium assay)	Calcium assay	β-arrestin assay	Calcium assay	β-arrestin assay	(Calcium assay)	(Calc. assay)
371	PZB16 817003	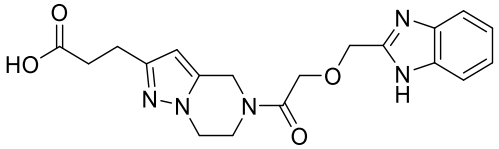	> 10 (-8 %)	> 10 (-15 %)	> 10 (-2 %)	> 10 (3 %)	> 10 (-10 %)	> 10 (4 %)	> 10 (6 %)
372	PZB168 17015	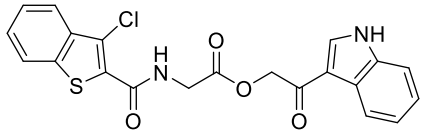	> 10 (-22 %)	> 10 (14 %)	> 10 (-10 %)	> 10 (-5 %)	> 10 (1 %)	> 10 (3 %)	> 10 (6 %)
373	PZB16 817007	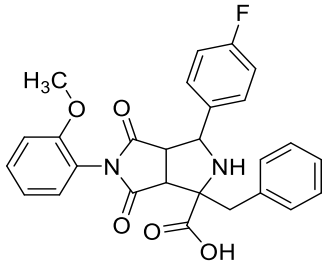	> 10 (-19 %)	> 10 (-11 %)	> 10 (-11 %)	> 10 (3 %)	> 10 (1 %)	≈ 10 (34 %)	> 10 (22 %)

Cpd	Name	Structure (371 -381)	IC_{50} ± SEM [µM] (% inhibition at 10 µM); n = 3-4						
			hP2Y$_1$R[a]	**hP2Y$_2$R**[b]		**hP2Y$_4$R**[c]		**hP2Y$_6$R**[d]	**M$_3$R**[e]
			(Calcium assay)	Calcium assay	β-arrestin assay	Calcium assay	β-arrestin assay	(Calcium assay)	(Calc. assay)
374	PZB16 817010	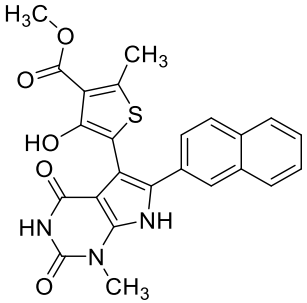	> 10 (3 %)	> 10 (26 %)	> 10 (4 %)	> 10 (25 %)	> 10 (12 %)	> 10 (18 %)	> 10 (-5 %)
375	PZB16 817011	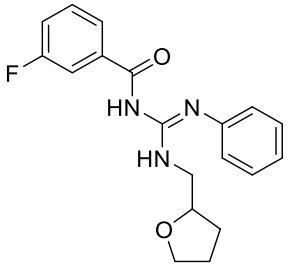	> 10 (-6 %)	> 10 (-22 %)	> 10 (5 %)	> 10 (18 %)	> 10 (3 %)	> 10 (-1 %)	> 10 (7 %)
376	PZB16 817034	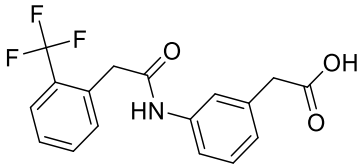	> 10 (-1 %)	> 10 (-15 %)	> 10 (-8 %)	> 10 (7 %)	> 10 (-13 %)	> 10 (-8 %)	> 10 (-14 %)

Cpd	Name	Structure (371 -381)	IC_{50} ± SEM [µM] (% inhibition at 10 µM); n = 3-4						
			hP2Y$_1$R[a]	**hP2Y$_2$R**[b]		**hP2Y$_4$R**[c]		**hP2Y$_6$R**[d]	**M$_3$R**[e]
			(Calcium assay)	Calcium assay	β-arrestin assay	Calcium assay	β-arrestin assay	(Calcium assay)	(Calc. assay)
377	PZB16 817035	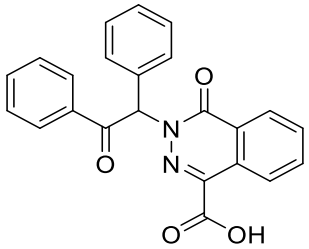	> 10 (17 %)	> 10 (23 %)	> 10 (-12 %)	> 10 (**40** %)	> 10 (-1 %)	> 10 (-12 %)	> 10 (-16 %)
378	PZB16 817041	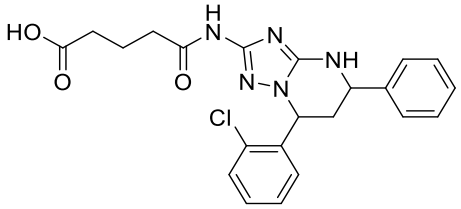	> 10 (-18 %)	> 10 (-10 %)	> 10 (-8 %)	> 10 (9 %)	> 10 (-14 %)	> 10 (-6 %)	> 10 (-10 %)
379	PZB168 17012	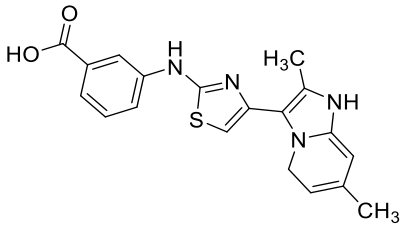	> 10 (13 %)	> 10 (-2 %)	> 10 (-3 %)	> 10 (**36** %)	> 10 (4 %)	> 10 (27 %)	> 10 (-7 %)

Cpd	Name	Structure (371 -381)	IC_{50} ± SEM [µM] (% inhibition at 10 µM); n = 3-4						
			hP2Y$_1$R[a]	**hP2Y$_2$R**[b]		**hP2Y$_4$R**[c]		**hP2Y$_6$R**[d]	**M$_3$R**[e]
			(Calcium assay)	Calcium assay	β-arrestin assay	Calcium assay	β-arrestin assay	(Calcium assay)	(Calc. assay)
380	PZB16 817054	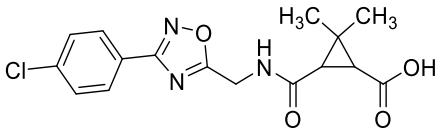	> 10 (17 %)	> 10 (5 %)	> 10 (-20 %)	> 10 (3 %)	> 10 (-24 %)	> 10 (-7 %)	> 10 (-5 %)
381	PZB16 817056	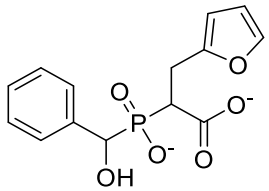	> 10 (-28 %)	> 10 (-39 %)	> 10 (-4 %)	> 10 (-10 %)	> 10 (-11 %)	> 10 (-17 %)	> 10 (-3 %)

Potencies of antagonists were determined against agonist EC_{80} concentrations in the respective assays. Antagonism was determined at the: [a]human P2Y$_1$R vs. ADP, [b]human P2Y$_2$ receptor vs. UTP in both calcium and β-arrestin assays, [c] human P2Y$_4$R vs UTP in both calcium and β-arrestin assays, [d]human P2Y$_6$R vs. UDP and [e]acetylcholine M$_3$R vs carbachol. All data are presented as mean from 3-4 independent assays.

4.2.1 **Hits from in vitro screening of compounds identified by virtual screening (VS)**

Most of the compounds tested were more active in calcium assays than in β-arrestin assays. To enable efficient comparison of data across P2Y receptor (P2YR) subtypes, we will focus on results from calcium assays.

Any compound that showed > 30 % inhibition at 10 µM was considered a hit. The hit rates from the initial in vitro screening of the VS compounds in calcium assays were as follows: 19 % at $P2Y_1R$, 7 % at $P2Y_2R$, 17 % at $P2Y_4R$ and 26 % at $P2Y_6R$. This was after exclusion of ligands which showed ≥ 30 % inhibitions at the muscarinic M_3R. The hit rate at the $P2Y_1R$ was about 3-fold as high as at the $P2Y_2R$, and this may not be surprising as the displayed $P2Y_2R$ homology model was built using structural data of the $P2Y_1R$. Dose-response curves were performed for each hit, after which some $P2Y_2R$ hits were cherry-picked, their analogues purchased and further screened. After the second screening, the hit rates were 33 % for the $P2Y_1R$, 21 % for $P2Y_2R$, 12 % for $P2Y_4R$ and 21 % for $P2Y_6R$. Although, the hit rate at the $P2Y_2R$ in the second screen indicates a slight increase in specificity, the $P2Y_1R$ unsurprisingly yielded the highest hit rate. There was a high attrition for active ligands after dose-response curves were performed for all the hits. The attrition rate was 10 % for $P2Y_1R$, 6 % for $P2Y_2R$, 13 % for $P2Y_4R$ and as high as 50 % for the $P2Y_6R$. This implies a high number of hit compounds were actually false positives. False positives may arise when compounds have poor aqueous solubility, have reactive moieties, interfere with signaling pathways or are just promiscuous aggregators. Also, we observed from screening that some compounds showed ≤ -30 % inhibitions and thus may be further developed as P2YR activators.

4.2.2 **Potency and selectivity of VS hits at the $P2Y_2R$**

At the $P2Y_2R$, most of the *N*-phenylbenzenesulfonamide derivatives (**283-289**) were inactive as antagonists. However, capping of the secondary sulfonamide yielded derivatives such as **287** and **289** with potencies of 8.34 µM and 30.3 µM respectively. Whereas **287** showed additional activity at only the $P2Y_1R$, **289** was non-selective vs. the $P2Y_4$ and $P2Y_6Rs$. Capping of the sulfonamide with phenylpropionamide bearing small groups such as chloro (**287**) were preferred to relatively larger ones such as -COOH (**289**) or $-COOCH_3$ (**288**).

Among the compounds with urea functionality, 1,3-diphenylurea derivatives (**290-296**) showed higher inhibitory potency at the $P2Y_2R$ than their 1-phenylurea analogs (**297-299**). Although inhibitory activities of 1-phenylurea derivatives were very high at the P2Y receptors, they were non-selective vs. the native M_3R, indicating potential off-target activity. We observed that diphenylurea derivatives with *N*-amido substitutions **294** (IC_{50} 6.83 µM) and **295** (IC_{50} 11.0 µM) were more potent that those with *C*-amido substituents such as **291** (IC_{50} 46.3 µM). The discrepancy might be due to different binding poses introduced by the *N*- or *C*-amido groups. Also, **294** and **295** with shorter and less flexible substituents than **291** may be better tolerated at the $P2Y_2R$. Generally, these diphenylurea were non-selective for the other P2YR tested. They may be further developed as potent and more drug-like pharmacological tools for the P2Y receptors than RB-2 (**30**) and suramin (**31**).

From certain scaffold series, there was only one potent hit at the $P2Y_2R$. For instance, compound **310** with a moderate potency of 9.87 µM is the only potent albeit non-selective carboxamide derivative at the $P2Y_2R$. Activity of **310** at the $P2Y_2R$ may have been introduced by the lipophilic phenyl groups. Among the benzothiazepine derivatives, only compound **324** (IC_{50} 10.9 µM) was moderately potent and relatively selective for the $P2Y_2R$ over the $P2Y_4R$.

The furopyrimidinone derivative **338** (IC_{50} 2.95 µM) was the most potent $P2Y_2R$ antagonist hit discovered from the current virtual screening campaign. However, it was not so selective over other P2Y receptors. It showed considerable potency at the $P2Y_1$ (IC_{50} 6.62 µM), $P2Y_4$ (IC_{50} 6.30 µM) and $P2Y_6$ (IC_{50} 9.16 µM) receptor subtypes. Compared to others in the same series, the flexibility of **338** may contribute to its antagonism at the P2Y receptors. Another scaffold, the phenylpyrazole, showed interesting $P2Y_2R$ activity. Compounds **351** (IC_{50} 8.60 µM) was additionally active at the $P2Y_1R$ whilst **354** (IC_{50} 10.6 µM) was non-selective vs. all of the investigated P2Y receptors. The phenylpyrazole derivatives are good small molecule leads for the development of $P2Y_2$-selective antagonists.

The benzothiazole derivatives **358** (IC_{50} 16.6 µM) and **360** (IC_{50} 21.9 µM) tested were also moderately potent at the $P2Y_2R$. However, these compounds showed a fair amount of structural rigidity and were not selective against other P2Y receptor subtypes. The 4,5-dihydropyrazole compounds **369** and **370** were also potent but non-selective $P2Y_2R$ antagonists. They have a similar scaffold as the phenylpyrazoles **351** and **354**.

The most potent hit at the $P2Y_2R$, **338**, was not the most selective. Selectivity of these VS compounds at the $P2Y_2R$ were poor. Although none of the $P2Y_2R$ hits was selective over all three other P2Y subtypes investigated, there were a few antagonists relatively selective over two receptor subtypes. These selective $P2Y_2$ antagonists (**287**, **291**, **324**, **351** and **360**) were only moderately potent and all were of different scaffolds (see Figure 30). Nevertheless, they could be good leads for developing novel $P2Y_2R$ orthosteric antagonists.

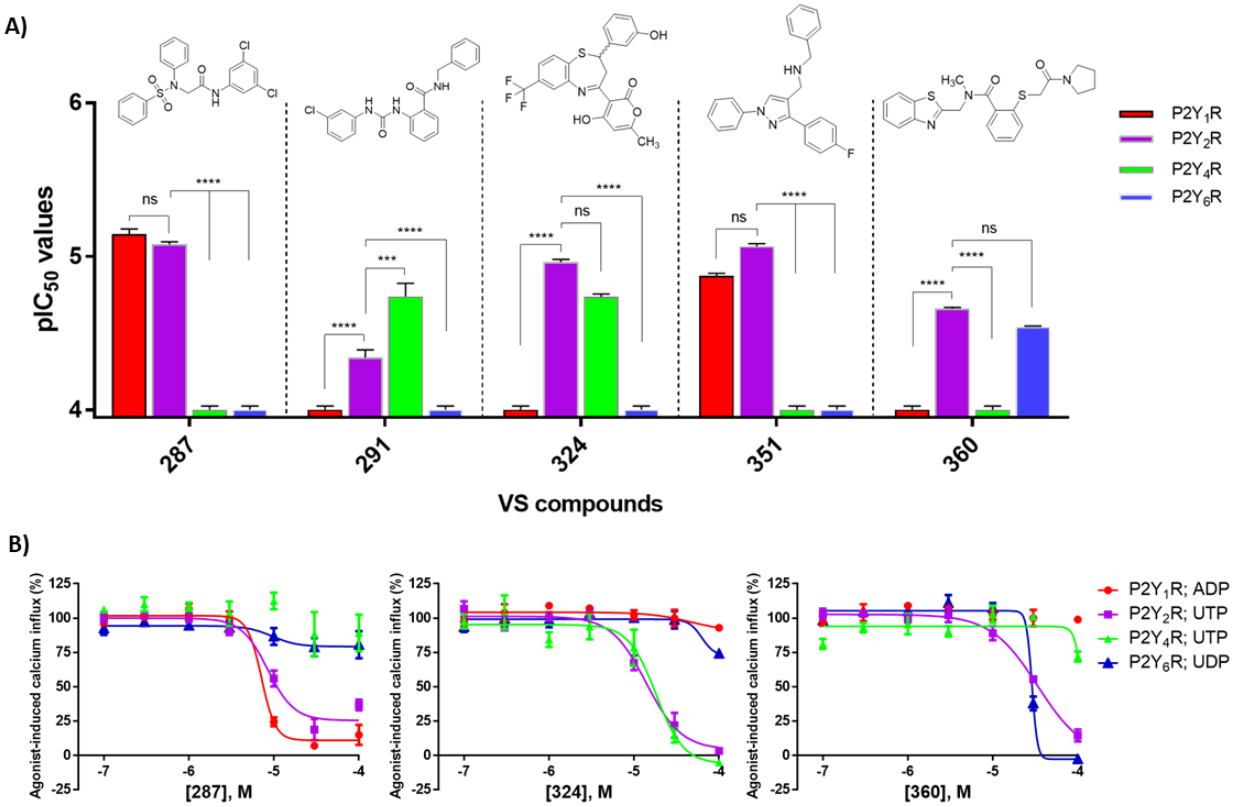

Figure 30: **A.** Bar graph showing potency and selectivity of some VS compounds as $P2Y_2R$ antagonists and **B.** dose-response curves of compounds **287**, **324** and **360** as antagonists at the P2YRs as determined by calcium assays. Data represent means ± SEM of 4-6 independent assays each in duplicate. Statistics by one-way ANOVA with Dunnett's post-hoc test for multiple in-row comparison: ^{ns} not significant; * $p \leq 0.05$; ** $p \leq 0.01$; *** $p \leq 0.001$; **** $p \leq 0.0001$.

The scaffolds investigated at the $P2Y_2R$ and other P2Y receptors, did not have many potent derivatives to warrant a clear structure-activity relationship (SAR) analysis. However, based on the inactive analogs of each hit and more importantly, based on our intuition and experience as medicinal chemists, we have put together a preliminary SAR for each P2Y receptor subtype. Figure

31 presents the preliminary SAR of the phenylpyrazole derivatives whilst Figure 32 shows some other potent scaffolds identified as $P2Y_2R$ antagonists.

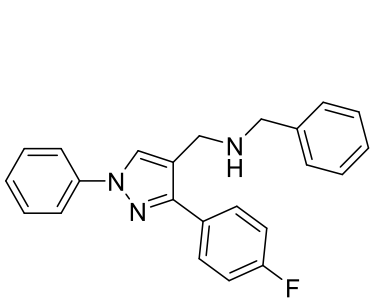

(**351**) PZB16818025

human $P2Y_1R$, IC_{50} = **13.4** ± 0.9 μM
human $P2Y_2R$, IC_{50} = **8.60** ± 0.58 μM
human $P2Y_4R$, IC_{50}> 10 μM
human $P2Y_6R$, IC_{50} > 10 μM
Muscarinic M_3R, IC_{50} > 10 μM

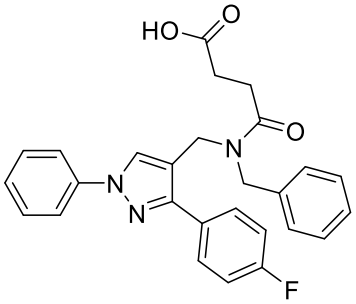

(**354**) PZB16818003

human $P2Y_1R$, IC_{50} = **10.0** ± 0.1 μM
human $P2Y_2R$, IC_{50} = **10.6** ± 0.4 μM
human $P2Y_4R$, IC_{50} = **11.2** ± 0.4 μM
human $P2Y_6R$, IC_{50} = **6.74** ± 0.93 μM
Muscarinic M_3R, IC_{50} > 10 μM

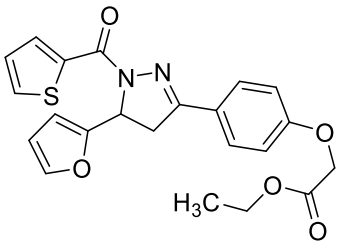

(**370**) PZB16818005

human $P2Y_1R$, IC_{50} = 4.**39** ± 0.67 μM
human $P2Y_2R$, IC_{50} = **4.02** ± 0.77 μM
human $P2Y_4R$, IC_{50} = **4.94** ± 0.87 μM
human $P2Y_6R$, IC_{50} = **3.24** ± 0.14 μM
Muscarinic M_3R, IC_{50} ~ 10 μM

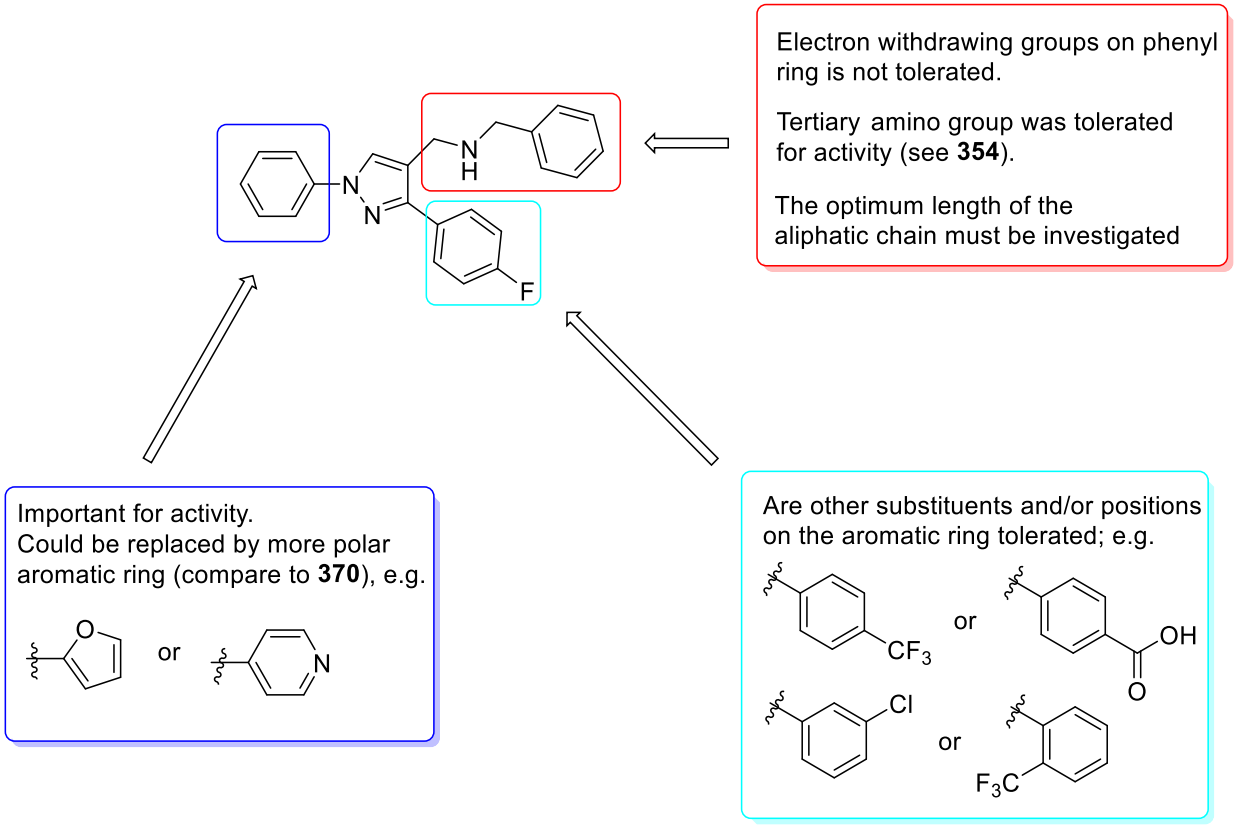

Figure 31: Scheme showing preliminary structure-activity relationships of phenylpyrazole derivatives as antagonists at the human $P2Y_2$ receptor as determined by intracellular calcium mobilization assay.

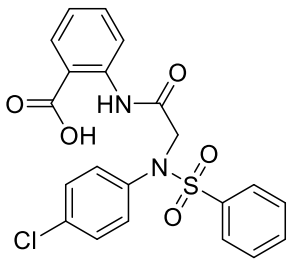

(**289**) PZB16817042

human P2Y$_1$R, IC$_{50}$ > 10 μM
human P2Y$_2$R, IC$_{50}$ = **30.3** ± 3.3 μM
human P2Y$_4$R, IC$_{50}$ = **30.7** ± 3.5 μM
human P2Y$_6$R, IC$_{50}$ = **36.8** ± 1.2 μM
Muscarinic M$_3$R, IC$_{50}$ > 10 μM

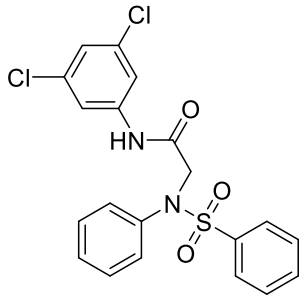

(**287**) PZB16818042

human P2Y$_1$R, IC$_{50}$ = **7.19** ± 0.94 μM
human P2Y$_2$R, IC$_{50}$ = **8.34** ± 0.52 μM
human P2Y$_4$R, IC$_{50}$ > 10 μM
human P2Y$_6$R, IC$_{50}$ > 10 μM
Muscarinic M$_3$R, IC$_{50}$ > 10 μM

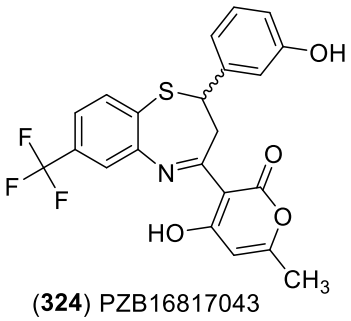

(**324**) PZB16817043

human P2Y$_1$R, IC$_{50}$ > 10 μM
human P2Y$_2$R, IC$_{50}$ = **10.9** ± 0.8 μM
human P2Y$_4$R, IC$_{50}$ = **18.4** ± 1.4 μM
human P2Y$_6$R, IC$_{50}$ > 10 μM
Muscarinic M$_3$R, IC$_{50}$ > 10 μM

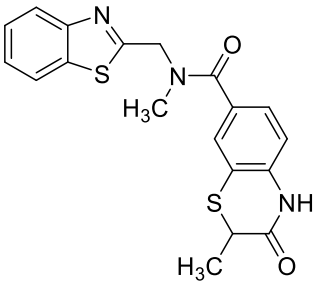

(**358**) PZB16818013

human P2Y$_1$R, IC$_{50}$ = **21.3** ± 2.5 μM
human P2Y$_2$R, IC$_{50}$ = **16.6** ± 1.7 μM
human P2Y$_4$R, IC$_{50}$ > 10 μM
human P2Y$_6$R, IC$_{50}$ = **7.36** ± 0.87 μM
Muscarinic M$_3$R, IC$_{50}$ > 10 μM

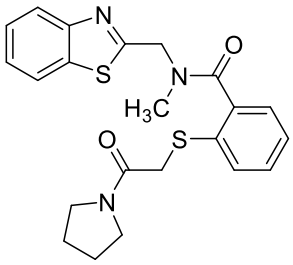

(**360**) PZB16818010

human P2Y$_1$R, IC$_{50}$ > 10 μM
human P2Y$_2$R, IC$_{50}$ = **21.9** ± 0.7 μM
human P2Y$_4$R, IC$_{50}$ > 10 μM
human P2Y$_6$R, IC$_{50}$ = **28.7** ± 0.5 μM
Muscarinic M$_3$R, IC$_{50}$ > 10 μM

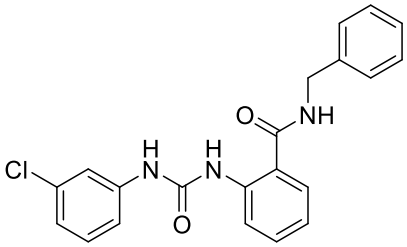

(**291**) PZB16817044

human P2Y$_1$R, IC$_{50}$ > 10 μM
human P2Y$_2$R, IC$_{50}$ = **46.2** ± 9.2 μM
human P2Y$_4$R, IC$_{50}$ = **18.9** ± 6.2 μM
human P2Y$_6$R, IC$_{50}$ > 10 μM
Muscarinic M$_3$R, IC$_{50}$ > 10 μM

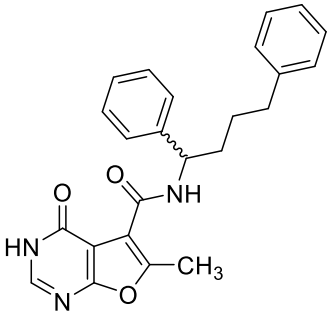

(**338**) PZB16817030

human P2Y$_1$R, IC$_{50}$ = **6.62** ± 1.84 μM
human P2Y$_2$R, IC$_{50}$ = **2.95** ± 0.14 μM
human P2Y$_4$R, IC$_{50}$ = **6.30** ± 2.04 μM
human P2Y$_6$R, IC$_{50}$ = **9.16** ± 0.40 μM
Muscarinic M$_3$R, IC$_{50}$ > 10 μM

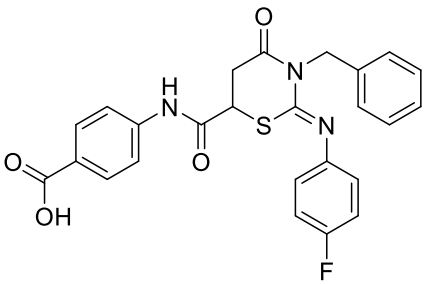

(**310**) PZB16817046

human P2Y$_1$R, IC$_{50}$ = **10.8** ± 0.1 μM
human P2Y$_2$R, IC$_{50}$ = **9.87** ± 0.68 μM
human P2Y$_4$R, IC$_{50}$ = **11.9** ± 0.6 μM
human P2Y$_6$R, IC$_{50}$ = **4.92** ± 0.48 μM
Muscarinic M$_3$R, IC$_{50}$ > 10 μM

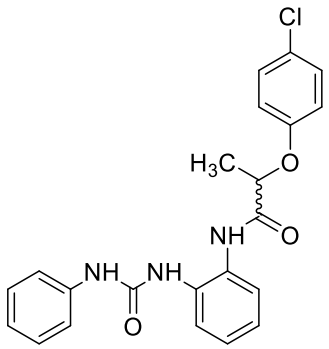

(**295**) PZB16817020

human P2Y$_1$R, IC$_{50}$ = **16.6** ± 0.9 μM
human P2Y$_2$R, IC$_{50}$ = **11.0** ± 1.3 μM
human P2Y$_4$R, IC$_{50}$ = **9.56** ± 1.97 μM
human P2Y$_6$R, IC$_{50}$ = **10.7** ± 1.1 μM
Muscarinic M$_3$R, IC$_{50}$ > 10 μM

Figure 32: Structures of some active scaffolds as antagonists at the human P2Y$_2$ receptor as determined by intracellular calcium mobilization assay.

4.2.3 **Potency and selectivity of VS hits at the $P2Y_1R$**

Various novel scaffolds were identified from the screen as potent $P2Y_1R$ antagonists. Compound **287** with a tertiary-substituted sulfonyl NH was the only *N*-phenylbenzenesulfonamide derivative that displayed moderate potency (IC_{50} 7.19 µM) as a $P2Y_1R$ antagonist. All the other *N*-phenylbenzenesulfonamide derivatives were inactive at the $P2Y_1R$.

The 1,3-diphenylurea derivatives, particularly, those with *N*-amido substitution on the phenyl ring such as **294** (IC_{50} 11.9 µM) and **295** (IC_{50} 16.6 µM) were identified as moderately potent $P2Y_1R$ antagonists. In contrast, all the *N*-phenylurea derivatives (**297-299**) were inactive. Also, urea analogs such as *N*-benzylacetamides (**315-321**), *N*-phenylbenzamides (**326-332**), amides (**345-347**) and acetamidobenzoic acid derivatives (**348-350**) were all inactive as $P2Y_1R$ antagonists. The 1,3-diaryl substituents of the urea group appear to be very important for $P2Y_1R$ activity. This is corroborated by previous reports of diarylurea derivatives which were very selective in antagonizing $P2Y_1R$ activation by ADP.[230] BPTU (**9**), the most potent one among them, was later identified through X-ray crystallography to bind to an allosteric pocket of the $P2Y_1R$.[125] Compounds **294** and **295** of the current study have a similar structure as BPTU (**9**) and may therefore be allosteric modulators. However, in contrast to BPTU, **294** and **295** are non-selective $P2Y_1R$ antagonists.

Furthermore, the carboxamide derivatives **305**, **308**, **309** and **310** were identified as novel $P2Y_1R$ antagonists with moderate potencies of 16.5 µM, 6.68 µM, 11.1 µM and 10.8 µM respectively. Whereas **308** and **310** were non-selective, compounds **305** and **309** showed distinct selectivity for the $P2Y_1R$. It appears that polar aromatic substitutions on the imino NH of these scaffolds may be responsible for their antagonism. Additionally, with reference to **305**, short alkyl substituents on the thiazinanone moiety may confer $P2Y_1R$ selectivity to these ligands. Furthermore, we present their preliminary SAR and explored their potential for development into drug candidates in Figure 34 below.

Other scaffolds discovered as $P2Y_1R$ antagonist were the quinazoline derivative **340** (IC_{50} 5.89 µM) and the phenylpyrazoles **351** (IC_{50} 13.4 µM) and **354** (IC_{50} 10.0 µM). Benzothiazole derivatives **358** and **359**, and the non-selective dihydropyrazole derivatives (**369** and **370**) were also active (see Figure 35).

Although these scaffold were considerably potent as hit compounds at the P2Y$_1$R, they were non-selective at other P2Y receptor subtypes. Generally, the carboxamides (**305** and **309)** were more selective than any other scaffold as P2Y$_1$R antagonists. Figure 33 shows the scaffolds that are relatively selective for the P2Y$_1$R.

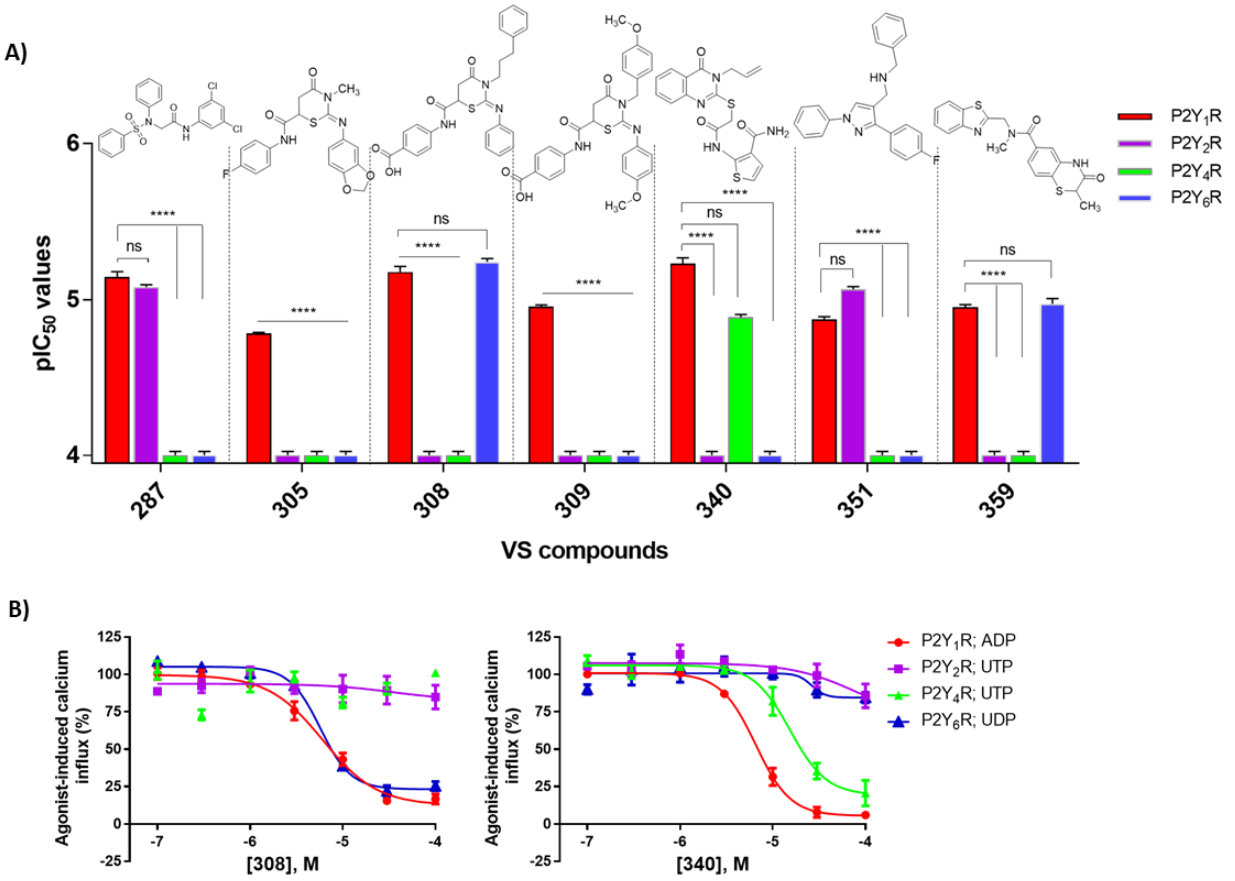

Figure 33: **A.** Bar graph showing potency and selectivity of some VS compounds as P2Y$_1$R antagonists and **B.** dose-response curves of compounds **308** and **340** as antagonists at the P2YRs as determined by calcium assays. Data represent means ± SEM of 4-6 independent assays each in duplicate. Statistics by one-way ANOVA with Dunnett's post-hoc test for multiple in-row comparison: ^{ns} not significant; * $p \leq 0.05$; ** $p \leq 0.01$; *** $p \leq 0.001$; **** $p \leq 0.0001$.

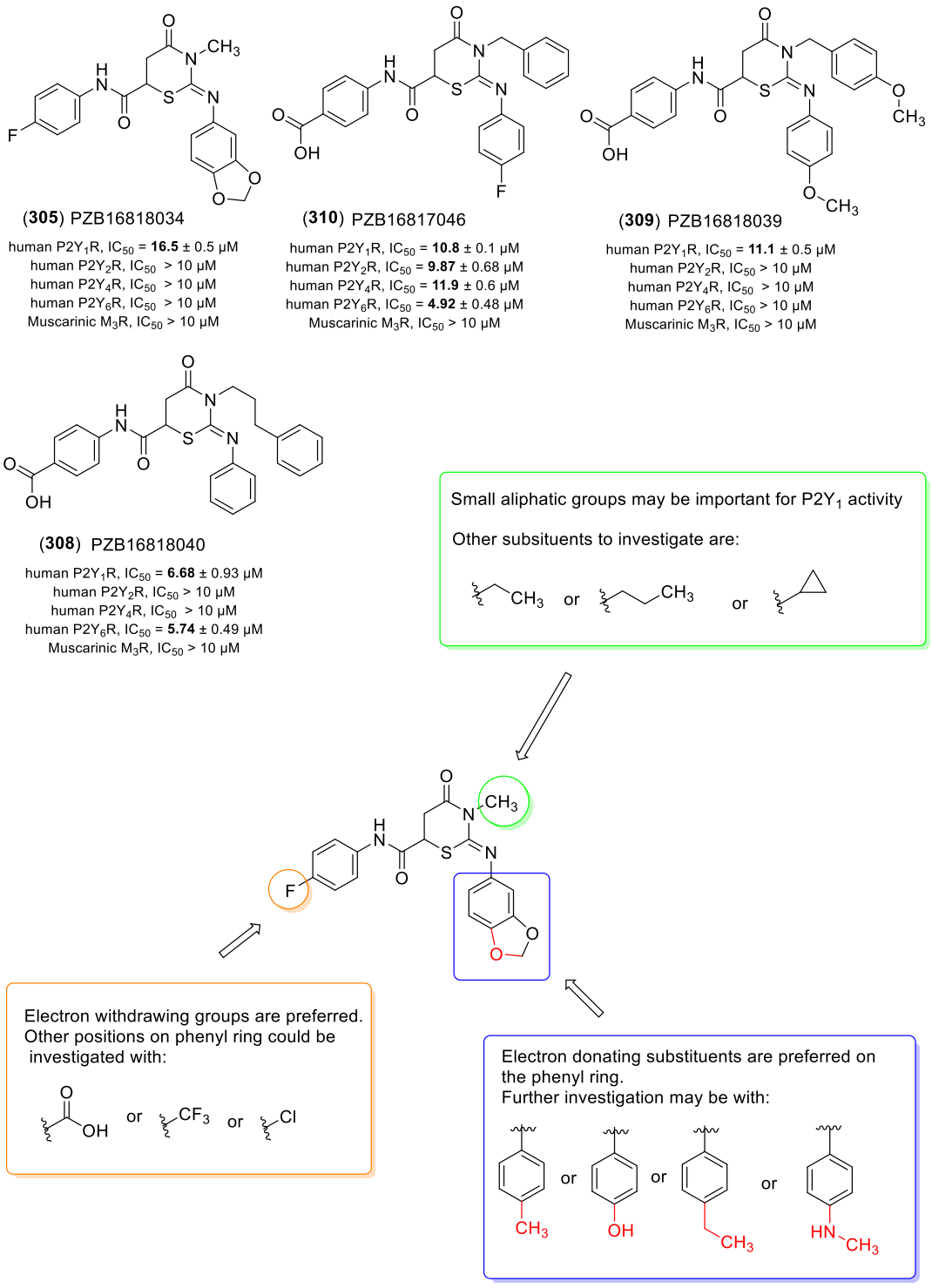

Figure 34: Scheme showing preliminary structure-activity relationships of the carboxamide derivatives as antagonists at the human $P2Y_1$ receptor as determined by intracellular calcium mobilization assay.

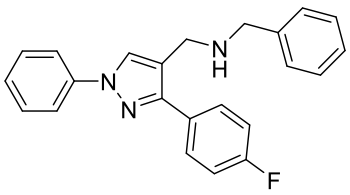

(**351**) PZB16818025

human P2Y$_1$R, IC$_{50}$ = **13.4** ± 0.9 μM
human P2Y$_2$R, IC$_{50}$ = **8.60** ± 0.58 μM
human P2Y$_4$R, IC$_{50}$> 10 μM
human P2Y$_6$R, IC$_{50}$ > 10 μM
Muscarinic M$_3$R, IC$_{50}$ > 10 μM

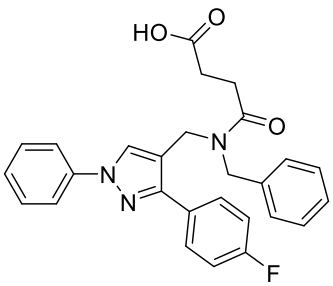

(**354**) PZB16818003

human P2Y$_1$R, IC$_{50}$ = **10.0** ± 0.1 μM
human P2Y$_2$R, IC$_{50}$ = **10.6** ± 0.4 μM
human P2Y$_4$R, IC$_{50}$ = **11.2** ± 0.4 μM
human P2Y$_6$R, IC$_{50}$ = **6.74** ± 0.93 μM
Muscarinic M$_3$R, IC$_{50}$ > 10 μM

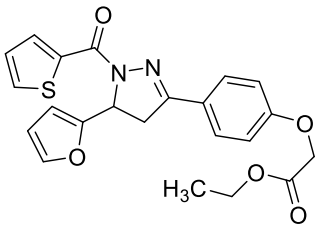

(**370**) PZB16818005

human P2Y$_1$R, IC$_{50}$ = 4.**39** ± 0.67 μM
human P2Y$_2$R, IC$_{50}$ = **4.02** ± 0.77 μM
human P2Y$_4$R, IC$_{50}$ = **4.94** ± 0.87 μM
human P2Y$_6$R, IC$_{50}$ = **3.24** ± 0.14 μM
Muscarinic M$_3$R, IC$_{50}$ ~ 10 μM

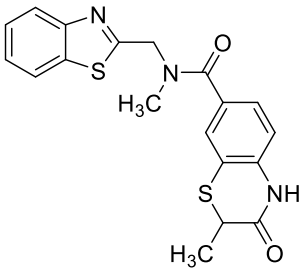

(**359**) PZB16818014

human P2Y$_1$R, IC$_{50}$ = **11.2** ± 0.7 μM
human P2Y$_2$R, IC$_{50}$ > 10 μM
human P2Y$_4$R, IC$_{50}$ > 10 μM
human P2Y$_6$R, IC$_{50}$ = **10.7** ± 1.4 μM
Muscarinic M$_3$R, IC$_{50}$ > 10 μM

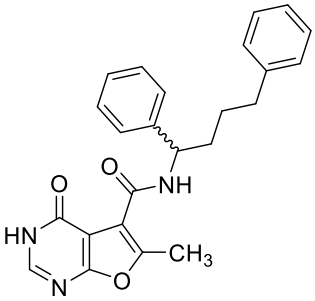

(**338**) PZB16817030

human P2Y$_1$R, IC$_{50}$ = **6.62** ± 1.84 μM
human P2Y$_2$R, IC$_{50}$ = **2.95** ± 0.14 μM
human P2Y$_4$R, IC$_{50}$ = **6.30** ± 2.04 μM
human P2Y$_6$R, IC$_{50}$ = **9.16** ± 0.40 μM
Muscarinic M$_3$R, IC$_{50}$ > 10 μM

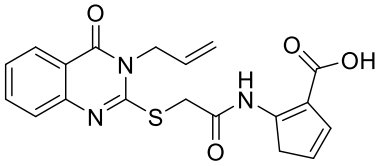

(**340**) PZB16818006

human P2Y$_1$R, IC$_{50}$ = **5.89** ± 0.83 μM
human P2Y$_2$R, IC$_{50}$ > 10 μM
human P2Y$_4$R, IC$_{50}$ = **13.0** ± 0.9 μM
human P2Y$_6$R, IC$_{50}$ > 10 μM
Muscarinic M$_3$R, IC$_{50}$ > 10 μM

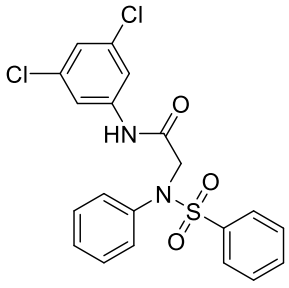

(**297**) PZB16818042

human P2Y$_1$R, IC$_{50}$ = **7.19** ± 0.94 μM
human P2Y$_2$R, IC$_{50}$ = **8.34** ± 0.52 μM
human P2Y$_4$R, IC$_{50}$ > 10 μM
human P2Y$_6$R, IC$_{50}$ > 10 μM
Muscarinic M$_3$R, IC$_{50}$ > 10 μM

Figure 35: Structures of some active scaffolds as antagonists at the human P2Y$_1$ receptor as determined by intracellular calcium mobilization assay.

4.2.4 **Potency and selectivity of VS hits at the P2Y$_4$R**

Unlike at the P2Y$_1$- and P2Y$_2$Rs, where a scaffold may yield more than one hit to allow SAR analysis, at the P2Y$_4$R most scaffolds yielded only a single hit. These "stand-alones" include the carboxamide **310**, benzothiazepine **324**, quinazoline **340**; phenylpyrazole **354** and benzothiazole **361**. The exceptions were the diphenylurea and the non-selective dihydropyrazole derivatives **369** and **370**.

Three diphenylurea derivatives (**291**, **294** and **295**) were identified as P2Y$_4$R antagonists. Compound **291** is a *C*-amido derivative which although less potent (IC$_{50}$ 18.9 µM), was more selective than the *N*-amido derivatives **294** (IC$_{50}$ 14.0 µM) and **295** (IC$_{50}$ 9.56 µM).

Again, only a few ligands (of different scaffolds) were selective for the P2Y$_4$R as illustrated in Figure 36. Other potent P2Y$_4$R antagonist are shown in Figure 37 below.

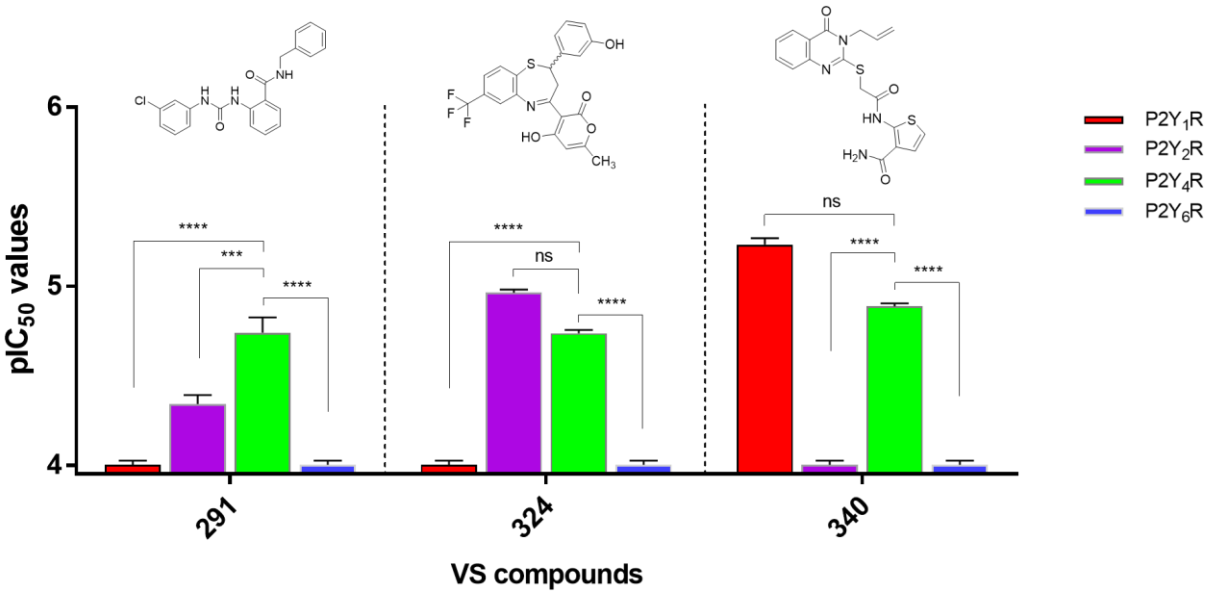

Figure 36: Bar graph showing potency and selectivity of some VS compounds as P2Y$_4$R antagonists in calcium assays. Data represents mean ± SEM of 3-4 independent assays. Statistics by two-way ANOVA with Dunnett's post-hoc test for multiple in-row comparison: ^{ns} not significant; * $p \leq 0.05$; ** $p \leq 0.01$; *** $p \leq 0.001$; **** $p \leq 0.0001$.

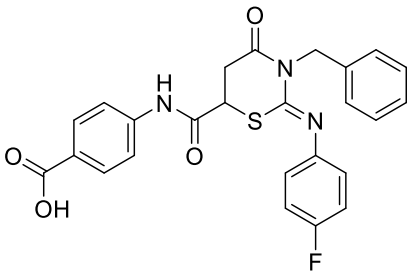

(**310**) PZB16817046

human $P2Y_1R$, IC_{50} = **10.8** ± 0.1 μM
human $P2Y_2R$, IC_{50} = **9.87** ± 0.68 μM
human $P2Y_4R$, IC_{50} = **11.9** ± 0.6 μM
human $P2Y_6R$, IC_{50} = **4.92** ± 0.48 μM
Muscarinic M_3R, IC_{50} > 10 μM

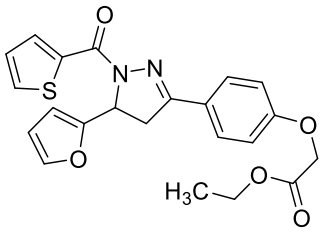

(**370**) PZB16818005

human $P2Y_1R$, IC_{50} = 4.**39** ± 0.67 μM
human $P2Y_2R$, IC_{50} = **4.02** ± 0.77 μM
human $P2Y_4R$, IC_{50} = **4.94** ± 0.87 μM
human $P2Y_6R$, IC_{50} = **3.24** ± 0.14 μM
Muscarinic M_3R, IC_{50} ~ 10 μM

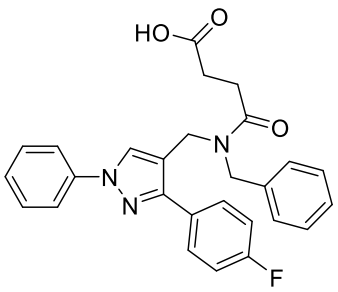

(**354**) PZB16818003

human $P2Y_1R$, IC_{50} = **10.0** ± 0.1 μM
human $P2Y_2R$, IC_{50} = **10.6** ± 0.4 μM
human $P2Y_4R$, IC_{50} = **11.2** ± 0.4 μM
human $P2Y_6R$, IC_{50} = **6.74** ± 0.93 μM
Muscarinic M_3R, IC_{50} > 10 μM

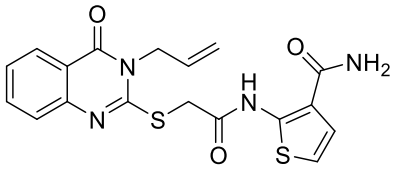

(**340**) PZB16818006

human $P2Y_1R$, IC_{50} = **5.89** ± 0.83 μM
human $P2Y_2R$, IC_{50} > 10 μM
human $P2Y_4R$, IC_{50} = **13.0** ± 0.9 μM
human $P2Y_6R$, IC_{50} > 10 μM
Muscarinic M_3R, IC_{50} > 10 μM

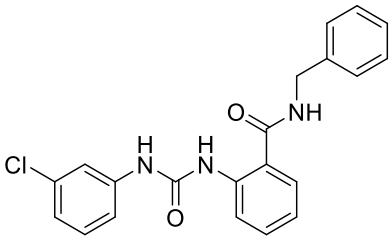

(**291**) PZB16817044

human $P2Y_1R$, IC_{50} > 10 μM
human $P2Y_2R$, IC_{50} = **46.2** ± 9.2 μM
human $P2Y_4R$, IC_{50} = **18.9** ± 6.2 μM
human $P2Y_6R$, IC_{50} > 10 μM
Muscarinic M_3R, IC_{50} > 10 μM

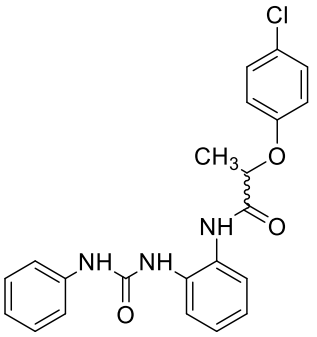

(**295**) PZB16817020

human $P2Y_1R$, IC_{50} = **16.6** ± 0.9 μM
human $P2Y_2R$, IC_{50} = **11.0** ± 1.3 μM
human $P2Y_4R$, IC_{50} = **9.56** ± 1.97 μM
human $P2Y_6R$, IC_{50} = **10.7** ± 1.1 μM
Muscarinic M_3R, IC_{50} > 10 μM

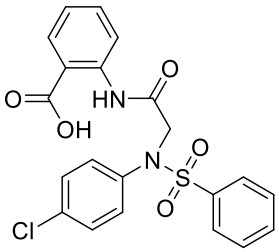

(**289**) PZB16817042

human $P2Y_1R$, IC_{50} > 10 μM
human $P2Y_2R$, IC_{50} = **30.3** ± 3.3 μM
human $P2Y_4R$, IC_{50} = **30.7** ± 3.5 μM
human $P2Y_6R$, IC_{50} = **36.8** ± 1.2 μM
Muscarinic M_3R, IC_{50} > 10 μM

Figure 37: Structures of some active scaffolds as antagonists at the human $P2Y_4$ receptor as determined by intracellular calcium mobilization assay.

4.2.5 **Potency and selectivity of VS hits at the P2Y$_6$R**

The P2Y$_6$R presents a case similar to that of the P2Y$_4$R. Here, the stand-alone hits include the phenylbenzenesulfonamide **289**, diphenylurea **295**, furopyrimidinone **338** and phenylpyrazole derivative **354**. None of these were selective for the P2Y$_6$R.

The potent carboxamides were **308** (IC$_{50}$ 5.74 µM), **310** (IC$_{50}$ 4.92 µM) and **311** (IC$_{50}$ 11.7 µM). These compounds were relatively selective for the P2Y$_6$R over the other P2Y receptor subtypes (Figure 38). Contrary to the P2Y$_1$R, we propose selectivity at the P2Y$_6$R is conferred by aromatic groups on the nitrogen (N) atom of the thiazinanone moiety (see Figure 39). Another set of compounds that showed moderate potency at the P2Y$_6$R are the benzothiazole derivatives **359** (IC$_{50}$ 10.7 µM) and **360** (IC$_{50}$ 28.7 µM). Also, **359** and **360** displayed appreciable selectivity for the P2Y$_6$R (see Figures 38 and 40).

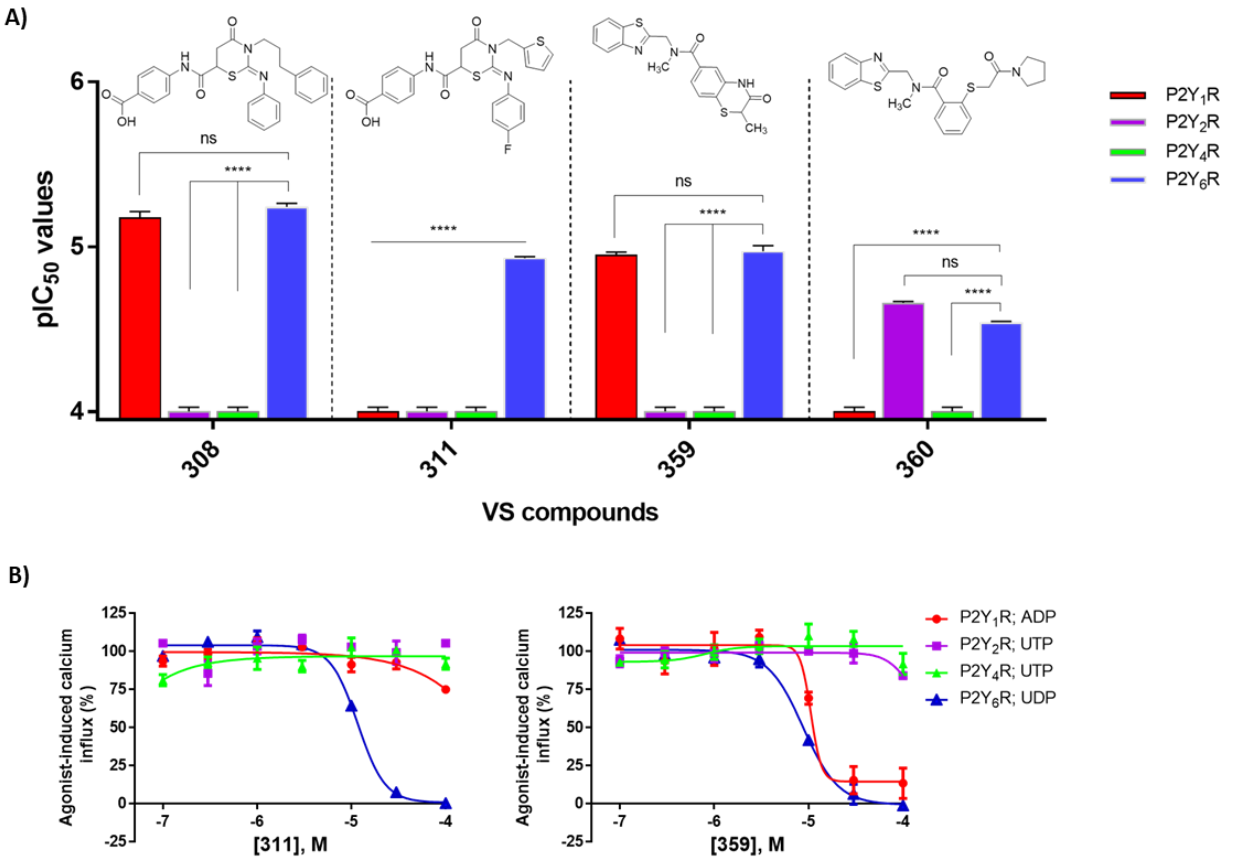

Figure 38: **A.** Bar graph showing potency and selectivity of some VS compounds as P2Y$_6$R antagonists and **B.** dose-response curves of compounds **311** and **359** as antagonists at the P2YRs as determined by calcium assays. Data represent means ± SEM of 4-6 independent assays each in

duplicate. Statistics by two-way ANOVA with Dunnett's post-hoc test for multiple in-row comparison: ns not significant; * $p \leq 0.05$; ** $p \leq 0.01$; *** $p \leq 0.001$; **** $p \leq 0.0001$.

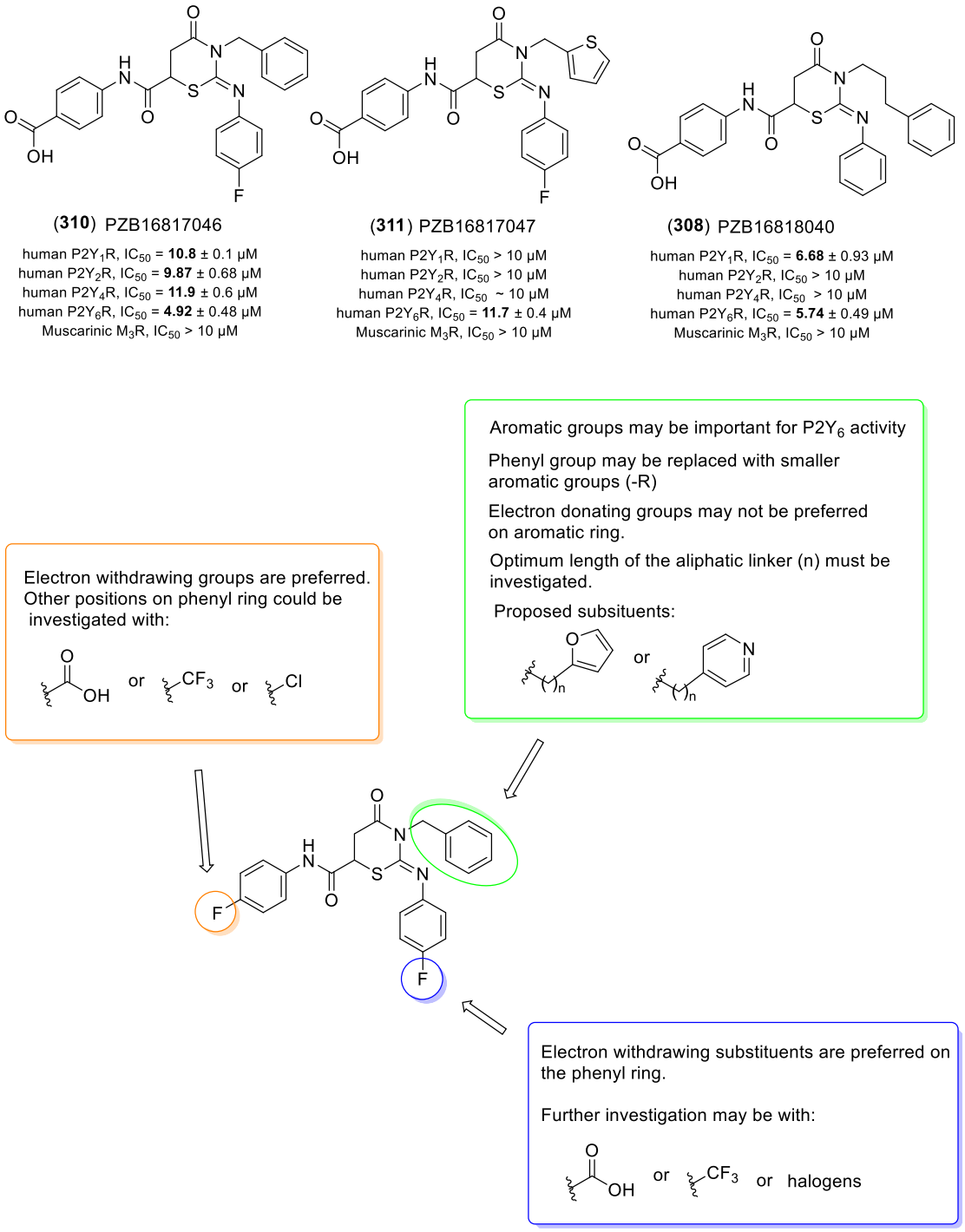

Figure 39: Scheme showing preliminary structure-activity relationships of the carboxamide derivatives as antagonists at the human $P2Y_6$ receptor as determined by intracellular calcium mobilization assay.

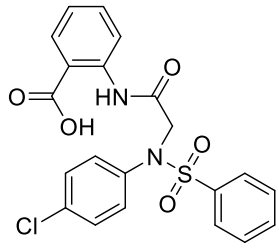

(**289**) PZB16817042

human $P2Y_1R$, IC_{50} > 10 μM
human $P2Y_2R$, IC_{50} = **30.3** ± 3.3 μM
human $P2Y_4R$, IC_{50} = **30.7** ± 3.5 μM
human $P2Y_6R$, IC_{50} = **36.8** ± 1.2 μM
Muscarinic M_3R, IC_{50} > 10 μM

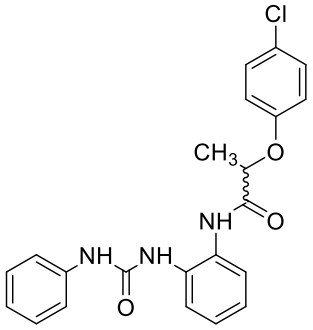

(**295**) PZB16817020

human $P2Y_1R$, IC_{50} = **16.6** ± 0.9 μM
human $P2Y_2R$, IC_{50} = **11.0** ± 1.3 μM
human $P2Y_4R$, IC_{50} = **9.56** ± 1.97 μM
human $P2Y_6R$, IC_{50} = **10.7** ± 1.1 μM
Muscarinic M_3R, IC_{50} > 10 μM

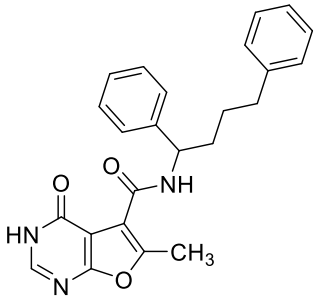

(**338**) PZB16817030

human $P2Y_1R$, IC_{50} = **6.62** ± 1.84 μM
human $P2Y_2R$, IC_{50} = **2.95** ± 0.14 μM
human $P2Y_4R$, IC_{50} = **6.30** ± 2.04 μM
human $P2Y_6R$, IC_{50} = **9.16** ± 0.40 μM
Muscarinic M_3R, IC_{50} > 10 μM

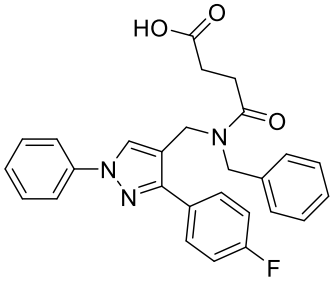

(**354**) PZB16818003

human $P2Y_1R$, IC_{50} = **10.0** ± 0.1 μM
human $P2Y_2R$, IC_{50} = **10.6** ± 0.4 μM
human $P2Y_4R$, IC_{50} = **11.2** ± 0.4 μM
human $P2Y_6R$, IC_{50} = **6.74** ± 0.93 μM
Muscarinic M_3R, IC_{50} > 10 μM

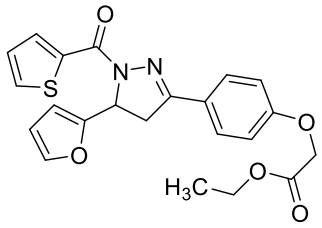

(**370**) PZB16818005

human $P2Y_1R$, IC_{50} = 4.**39** ± 0.67 μM
human $P2Y_2R$, IC_{50} = **4.02** ± 0.77 μM
human $P2Y_4R$, IC_{50} = **4.94** ± 0.87 μM
human $P2Y_6R$, IC_{50} = **3.24** ± 0.14 μM
Muscarinic M_3R, IC_{50} ~ 10 μM

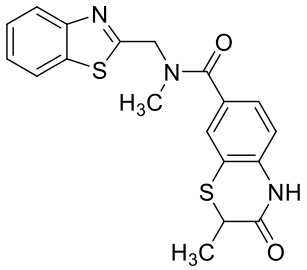

(**358**) PZB16818013

human $P2Y_1R$, IC_{50} = **21.3** ± 2.5 μM
human $P2Y_2R$, IC_{50} = **16.6** ± 1.7 μM
human $P2Y_4R$, IC_{50} > 10 μM
human $P2Y_6R$, IC_{50} = **7.36** ± 0.87 μM
Muscarinic M_3R, IC_{50} > 10 μM

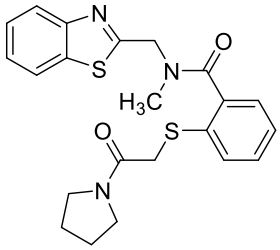

(**360**) PZB16818010

human $P2Y_1R$, IC_{50} > 10 μM
human $P2Y_2R$, IC_{50} = **21.9** ± 0.7 μM
human $P2Y_4R$, IC_{50} > 10 μM
human $P2Y_6R$, IC_{50} = **28.7** ± 0.5 μM
Muscarinic M_3R, IC_{50} > 10 μM

Figure 40: Structures of some active scaffolds as antagonists at the human $P2Y_6$ receptor as determined by intracellular calcium mobilization assay.

4.3 **Discussion**

From the biological assessment of the VS compounds, we observed various patterns of activity. Several scaffolds were inactive at all the P2Y receptors whilst other scaffolds such the carboxamides (**305-313**) consisted of enough potent derivatives to allow preliminary SAR analysis. A handful of compounds such as **291**, **324** and **340** were the only potent compounds from their respective scaffolds. These compounds with isolated activities could be described as displaying activity cliffs, however more analogues need to be investigated together with computer-aided docking analysis to confirm this assertion.[231] Furthermore, we observed that within the series for certain scaffolds, minor differences between derivatives influenced P2Y receptor subtype selectivity (compare **308-311**). Although this appears baffling, Stumpfe *et al.* studied such a phenomenon, described as structure-selectivity relationship (SSR) and concluded in their works that no simple rules govern SSR and that structural similarity alone is insufficient to predict selectivity for a particular receptor.[232–234] Lastly, we identified compounds such as **289**, **295**, **310**, **354**, and **369**, among others which showed considerable potency at two or more of the P2Y subtypes studied. To treat disease conditions such as cancer, Alzheimer's, atherosclerosis and cystic fibrosis, which involves multiple P2Y receptor targets (refer to Table 1 under chapter 1), we propose such non-selective ligands as potential multitarget drugs.

Some marketed drugs have been shown to solicit their biological effects by acting additionally on off-targets, and although not so designed, this may contribute to their therapeutic effects.[235] Multitarget ligands (MTL) are particularly useful as therapeutic agents for diseases such as Alzheimer's, with multi-variant causes. Such MTLs simultaneously modulate the various targets implicated in the disease-state. MTLs may have low affinity or efficacy for each targeted pathway but their additive or synergistic effect on mitigating disease progression could be very profound. The low efficacy of MTLs on each distinct target also implies a very high safety profile for use in patients. In contrast, single-target ligands require very high affinities for treatment hence may have numerous safety issues.[236,237] Additionally, multitarget drugs may improve patient compliance to taking medicines and eliminate over-burdening them with pills, the so-called polypharmacy, as practiced currently in the health sector. The rational discovery and design of multitarget ligands include screening focused libraries of known actives for one receptor at other targeted receptors for cross-activities. This is essentially a selectivity screening, as performed in this study, except that the motive is different. We would optimize the potency and drug-like properties of these serendipitous non-selective ligands at each P2Y receptor subtype into potential multiligand drug

candidates – a very daunting challenge though. However successful reports include dual angiotensin (AT_1)/endothelin (ET_A) receptor antagonists for controlling hypertension[238], and the marketed drug Ziprasidone, a dopamine D_2/serotonin 5-HT_2 antagonist for treating schizophrenia.[239] Furthermore, in case these discovered VS compounds cannot be optimized sufficiently to meet clinical requirements, they could be used as useful pharmacological tools to further research in the field of purinergic signaling.

4.4 **Conclusion and outlook**

Using virtual screening techniques coupled to biological evaluation, we identified potent but weakly selective $P2Y_2R$ antagonists. Additionally, we identified novel scaffolds as $P2Y_1$, $P2Y_4$ and $P2Y_6R$ selective antagonists. These novel P2Y hits are less potent than the current pharmacological tools including **13**, **15** and **38**, used to investigate the $P2Y_6$, $P2Y_4$ and $P2Y_2Rs$, respectively. However, they are good non-nucleotide leads with moderately drug-like properties that could be further optimized. Also, we discovered during in vitro screening that the $P2Y_1R$ instead of $P2Y_2R$ had the highest number of potent hits. Among several reasons, the discrepancy may be due to use of inappropriate scoring algorithms for virtual screening or the use of an unrefined $P2Y_2R$ homology model. To undertake rational design of selective $P2Y_2R$ antagonists using computational tools, the homology model of the $P2Y_2R$ may have to be further validated and fine-tuned. Also, we would test more analogues of some of the potent scaffolds such as the carboxamides and phenylpyrazoles that show great promise as drug leads for P2YR-mediated diseases.

Furthermore, we discovered various moderately potent but non-selective scaffolds by serendipity, which could be re-designed into multitarget ligands of the P2Y receptors for treating conditions such as cancer, Alzheimer's and cystic fibrosis.

5 Site-directed mutagenesis studies

5.1 Introduction

In the design of selective ligands for GPCRs, 3D structural knowledge of target proteins have become an indispensable tool. Methods including X-ray crystallography and Nuclear Magnetic Resonance (NMR) spectroscopy are used to generate such structural data and additionally, they provide information on receptor conformational changes and ligand binding pose. However, despite their relevance, these methods are tedious, time-consuming and expensive to perform. Also, whilst the former requires the use of pure crystallized proteins which are very difficult to degenerate, use of the latter is limited to small to medium sized proteins of high concentrations only.[240,241] Due to these limitations, only a handful of GPCR have their 3D structures elucidated. Consequently, researchers use known X-ray crystal structures of closely related proteins as templates to generate homology models for their target proteins.

In the previous chapter, virtual screening (VS) was performed using the $P2Y_2R$ homology model published by Rafehi et al.[183] The VS hits were tested in vitro by calcium assays and several were moderately potent antagonists were discovered. However, these $P2Y_2R$ antagonists were not selective over the $P2Y_4R$. The human $P2Y_2R$ is closely related to the human $P2Y_4R$. Both receptors share the highest amino acid sequence identity among the $P2Y_2R$ subtypes (53 %), compared to sequence identities of 34 % for $P2Y_2/P2Y_1$, 38 % for $P2Y_2/P2Y_6$ and 21 % for $P2Y_2/P2Y_{12}$.

In order to be able to design ligands for the $P2Y_2$ and $P2Y_4Rs$, there is the need to knowledge of the topography of the agonist binding site of these receptors is required. To this end, we employed molecular modeling and site-directed mutagenesis studies. While the X-ray crystallographic structures of the $P2Y_2$ and $P2Y_4R$ are currently unavailable, those of the $P2Y_1$ and $P2Y_{12}R$ have been published.[125,242]

Recently, a $P2Y_2R$ homology model based on the X-ray crystal structures of the human $P2Y_1$ and $P2Y_{12}R$. Preliminary data from site-directed mutagenesis studies coupled with docking studies of UTP (**1**), Ap_4A (**27**) and AR-C118925 (**38**) (Figure 41) into the model shed a new light on key interactions with amino acids in the orthosteric binding pocket of the $P2Y_2R$.[183] The docking results suggested a binding mode of agonists similar to that of 2Me-SADP (**5**) and 2Me-SATP at the

human $P2Y_{12}R$,[243] which differed from the binding mode of nucleotide antagonist MRS2500 (**6**) in complex with the human $P2Y_1R$.[125]

Moreover, we published a homology model of the human $P2Y_4R$ and used it to predict the binding site of the anthraquinone (AQ) antagonists.[139] In the present study, we performed site-directed mutagenesis to address specific questions related to the selective ligand binding at the closely related P2Y receptor subtypes. Specifically, we addressed the questions of agonist binding modes and agonist discrimination e.g. ATP versus UTP as well as the binding modes of antagonists.

5.2 **Results**

5.2.1 **Docking studies**

Using the previously reported $P2Y_2$ and $P2Y_4R$ homology models, docking was performed as previously described.[244] Briefly, Asp185 ($P2Y_2R$) and Aps187 ($P2Y_4R$) were used as centroids to dock ligands within a box of side length 25.0 Å into the putative orthosteric sites. The ligands docked were included agonists such as UTP (**1**), ATP (**2**), MRS4062 (**14**) and Ap_4A (**27**), and antagonists such as the AQ derivatives RB-2 (**30**), PSB-09114 (**37**), PSB-16133 (**15**), PSB-16135 (**16**) and PSB-1699 (**17**), and the selective $P2Y_2R$ antagonist AR-C118925 (**38**) (see Figure 41). After exclusion of alternative binding sites, the best docking poses were selected based on the Induced Fit Docking (IFD) scores and Prime Energy values. The homology modeling and docking studies were performed by Dr. Vigneshwaran Namasivayam and Alexander Neumann.

According to the docking studies, all four agonist have a similar binding pose in the $P2Y_2R$ orthosteric pocket. The hydroxyl groups of the ribose moiety likely forms hydrogen bonds with Arg110 and Asp185. The phosphate groups of all agonists interact with common residues including Arg177, His184, Asp185, Arg265, Arg272, Lys289 and Arg292. Additionally, the δ-phosphate group of Ap_4A may have ionic interactions with Arg26 and Arg177 (Figure 42). However, interactions of the nucleobases differ slightly. While the uracil ring of UTP and the adenine group of ATP bind in a pocket of formed by clusters of the aromatic residues Phe113, Tyr114, Leu177, Tyr118, and Phe261, the second adenine ring of Ap_4A may bind in a domain close to the *N*-terminus and the extracellular lumen.[183] In contrast, docking studies suggest the phenylpropyl moiety of MRS4062 binds in the same pocket as the nucleobase of UTP and ATP while its pyrimidine moiety is displaced towards Phe113 and Tyr114.

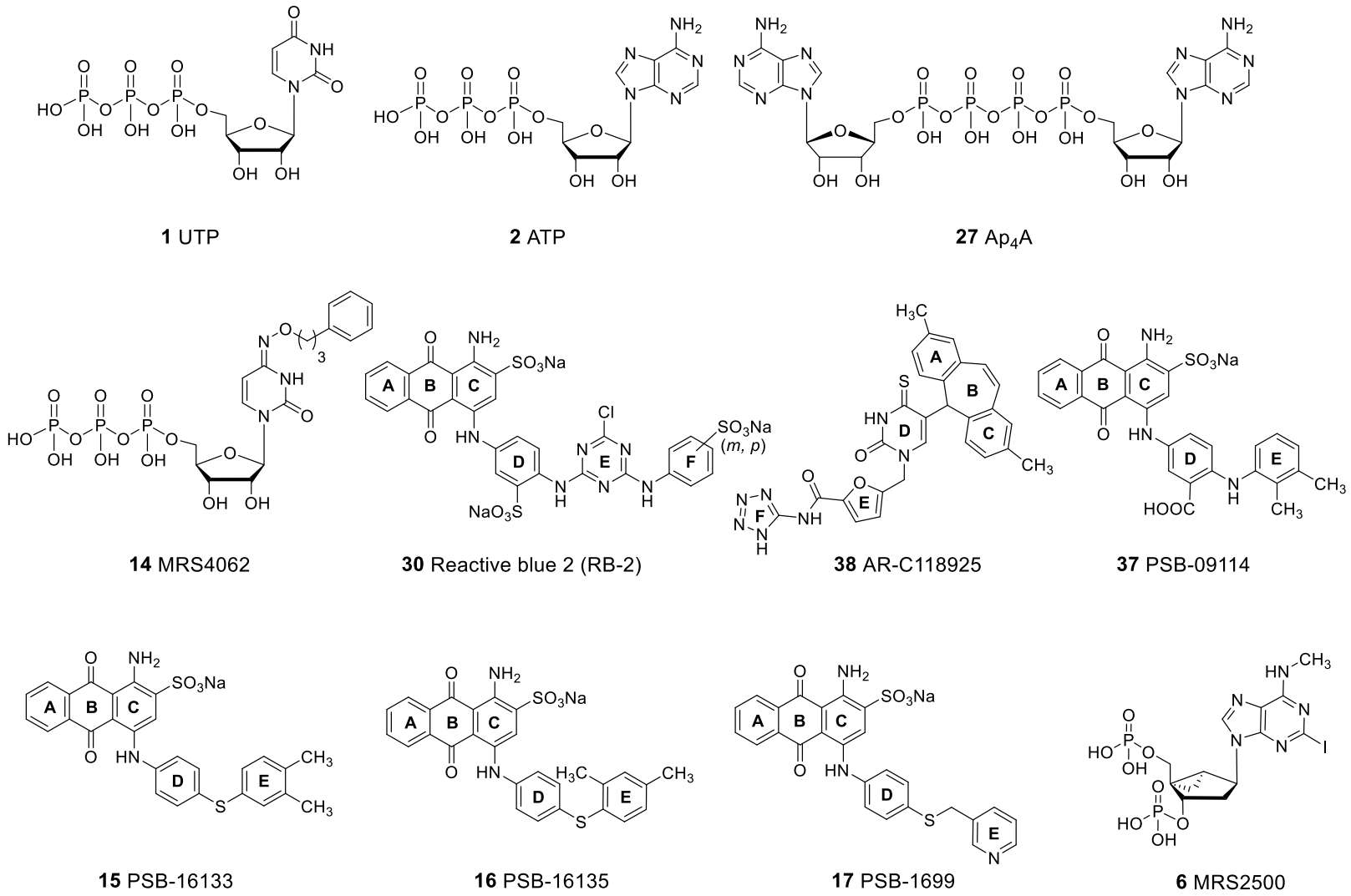

Figure 41: Structures of selected P2Y ligands.

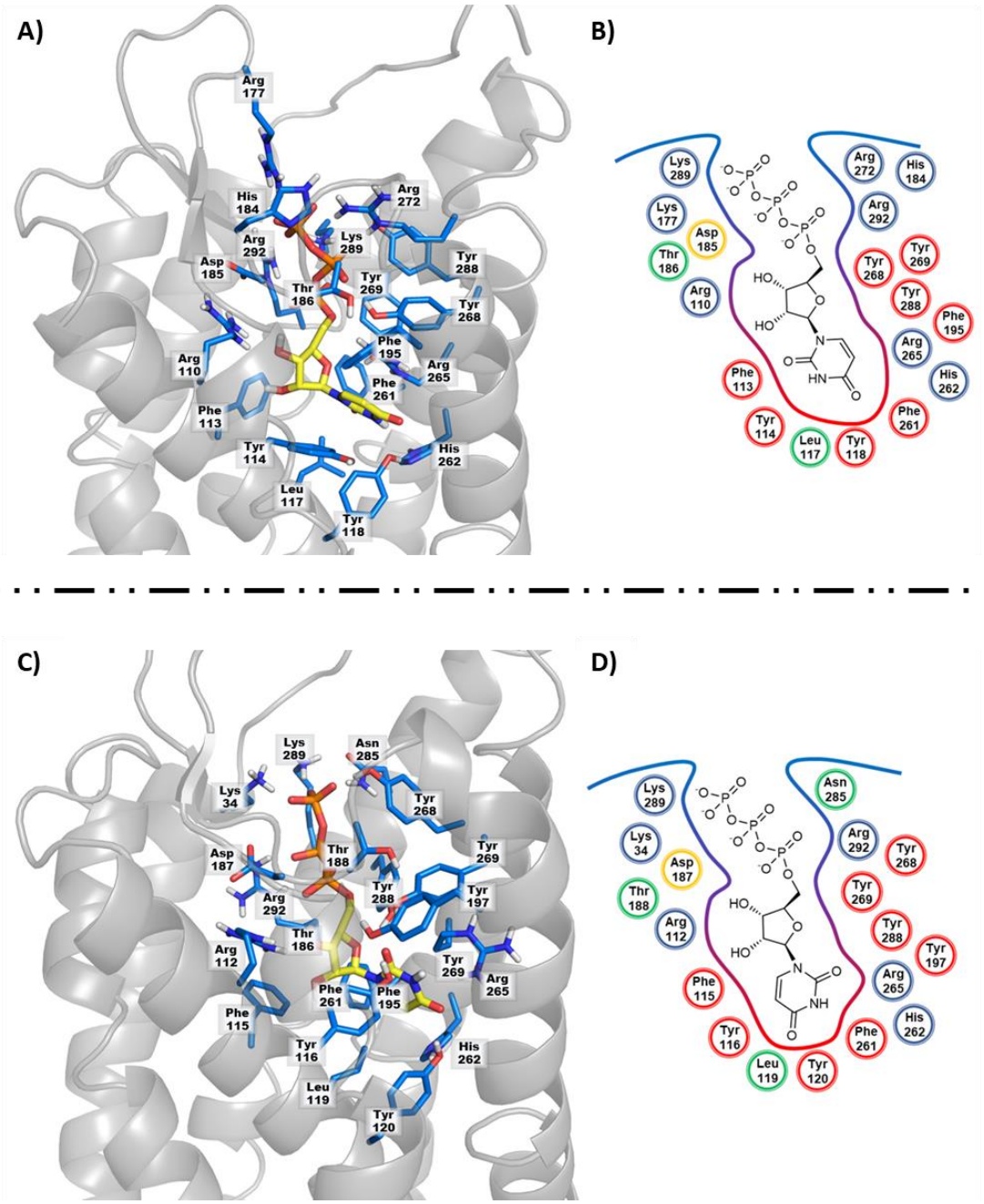

Figure 42: Putative binding mode of UTP in the homology model of **A.** the human $P2Y_2R$ and **C.** the human $P2Y_4$ receptors. The P2Y receptors (gray) are displayed in cartoon representation, the amino acid residues (blue) and UTP (yellow) are shown as stick models. Oxygen atoms are colored in red, nitrogen atoms in blue, phosphorus atoms in orange. Schematic 2D representation of the binding pocket of B. $P2Y_2R$ and D. $P2Y_4R$ are also shown. Charged, basic residues are colored in blue, aromatic residues in red, the conserved aspartic acid residue in ECL2 involved in the ionic

lock with Arg292 in yellow, other residues in the binding pocket in green.(credit: Alexander Neumann)

At the human $P2Y_4R$, UTP binds in a mode similar to that at the $P2Y_2R$ (see Figure 42). The uracil nucleobase binds in a lipophilic region consisting of aromatic (Phe115, Tyr116, Tyr120, Tyr197, Phe261) and lipophilic (Leu119, Val204, Met205) residues. The phosphate groups are accommodated in a negatively charged binding cleft formed by residues including Lys289, Asp187, Tyr268, Asn285 and Arg292. Also, MRS4062 binds in a similar mode as UTP. The phenyl group binds in a cleft formed by several aromatic residues Tyr116, Tyr120, Tyr197 and Phe200.

Based on the docking studies, amino acid residues in the binding pocket of both the $P2Y_2$ and $P2Y_4$ receptors were selected for mutagenesis studies. Molecular Dynamics simulations suggested an ionic lock between an aspartic acid in the extracellular loop 2 (ECL2) and an arginine of TM VII to play a key role in $P2Y_1R$ activation; agonist broke the ionic lock between Asp204 and Arg310, while antagonists stabilized the interaction preventing receptor activation.[245] Mutagenesis studies on the human $P2Y_1R$ identified both residues to play a key role in agonist-induced receptor activation.[246] In our previous studies we were able to confirm $P2Y_2$-Arg292 as an important residue for agonist interactions, which is the analogous residue to $P2Y_1$-Arg310. To further investigate the role of an ionic lock between ECL2 and TM VII in the $P2Y_2R$, we constructed a $P2Y_2$-D185A mutant. $P2Y_2$-R110A, an already published mutant, was also investigated in this report for its possible amino acid interactions with the recently published ligands, particularly MRS4062. $P2Y_2$-Phe113 is likely present in the orthosteric binding site of the $P2Y_2R$ and thus was mutated to alanine and tyrosine. $P2Y_2$-Phe195 is placed close to the ECL2 at the upper part of TM V and one of the non-conserved residues in the assumed orthosteric binding pocket of $P2Y_2$ and $P2Y_4R$, thus making the residue interesting for its role in discrimination between UTP and ATP. At $P2Y_4R$, Asn170 was selected as it is close to the putative orthosteric binding site and is replaced by valine in the $P2Y_2R$. Arg194 was found to play a role in ligand acceptance at the $P2Y_2R$ although being displaced from the putative orthosteric binding site. A second ionic lock close to ECL2 in TM V was proposed to modify the flexibility of the loop, resulting in decreased potencies of agonists. Therefore, we decided to investigate Arg190, Glu193 and Asp195 of TM V as those were likely to form an analogous ionic lock in $P2Y_4R$. Finally, Tyr197 and Phe200 of $P2Y_4R$ were selected as candidates for mutagenesis studies, as they are close to the putative orthosteric binding site. The mutants were recombinantly expressed in 1321N1 astrocytoma cells and their effects on the presently docked

ligands were studied by intracellular calcium mobilization assay. The tested agonists were UTP (**1**), ATP (**2**), Ap_4A (**27**), and MRS4062 (**14**). The investigated antagonists were AQ derivatives: RB-2 (**30**), PSB-09114 (**37**), PSB-16133 (**15**), PSB-16135 (**16**), and PSB-1699 (**17**) and the uracil-derived AR-C118925 (**38**). Our ligand selection was based on both their structural diversity, size and unique pharmacological profiles at either the wildtype (wt) $P2Y_2$ or $P2Y_4$Rs.

5.2.2 **Site-Directed Mutagenesis**

Several mutagenesis studies of the binding sites of the human and rat $P2Y_2$R have been reported, however, little is known about the binding pocket of the human $P2Y_4$R (see Figure 43).[140,183,247] Mutation of positively charged $P2Y_2$R residues His262, Arg265 and Arg292 to leucine or isoleucine diminished UTP and ATP potency and led to the conclusion of that these residues interact with the triphosphate groups of the nucleotide.[247] Further studies by Hillman et al. and Rafehi et al. revealed new insights into the $P2Y_2$R orthosteric agonist binding sites and the likely ligand binding pose. Mutation of aromatic residues including Tyr114, Tyr118, Tyr198, Phe261 and Tyr288 were found to stabilize agonist binding and activation. Exchange of charged residues like Arg194 and Arg272 (known as the gatekeeper) were found to drastically decrease agonism.[140,183]

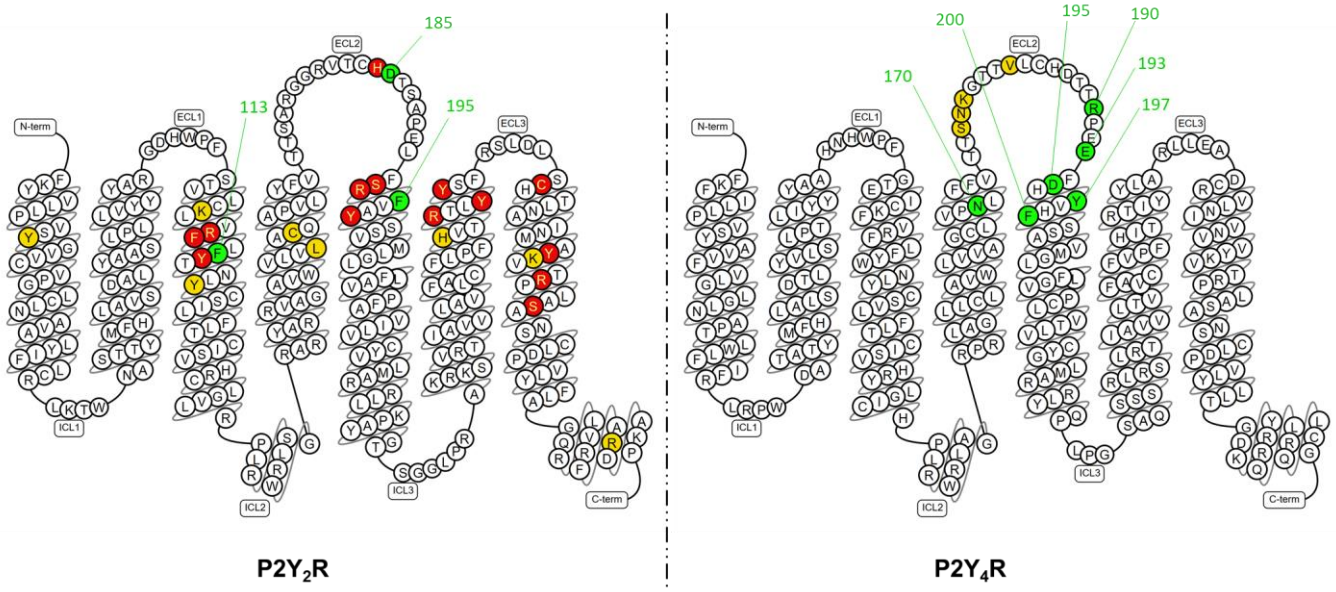

Figure 43: Snake representation of the $P2Y_2$R and the $P2Y_4$R showing relative positions of the amino acids that when mutated had no effect on agonist activity (yellow) or decreased agonist activity (red). Amino acids in green are those studied in this dissertation. Snake diagram was generated from gpcrdb.org.[8]

At the $P2Y_4R$, the amino acids Ser333 and Ser334 located in the intracellular C-terminus were reported to regulate agonist-dependent receptor phosphorylation, desensitization and internalization.[248] A comparative study between the N-terminus and extracellular loop 2 (ECL2) of the rat and human $P2Y_4R$ chimeras had been conducted, and the amino acids Asn177, Ile183, and Leu190 in the ECL2 to the ability of the rat $P2Y_4R$ to accept ATP as an agonist while the $hP2Y_4R$ is activated only by UTP but not by ATP.[249]

In the current study, however, we performed a comparative study of the binding pockets of to explain ligand discrimination so far. A total of 13 amino acid residues in the binding pocket of both the $P2Y_2R$ and the $P2Y_4R$ receptors were selected for mutagenesis studies. As described in Materials and Methods, the coding sequence of the $P2Y_2$ and $P2Y_4Rs$ were cloned into the plasmid vector pUC19 and using whole plasmid PCR, point mutations that led to the desired mutations were introduced. From pUC19, the cDNAs were cloned into the pLXSN retroviral expression vector featuring a hemagglutinin (HA) epitope sequence at the N-terminus of the receptor. The wt and mutant receptors were then stably transfected into 1321N1 astrocytoma cells and their cell surface expression levels quantified by enzyme-linked immunosorbent assay (ELISA). The effects of these mutant receptors on selected ligands were then determined by calcium assays.

5.2.3 **Receptor expression**

Since the level of cell surface receptor expression directly affects the potency of GPCR agonists in functional assays,[250,251] expression levels were determined by enzyme-linked immunosorbent assay (ELISA) with an antibody against the HA tag. Previous reports had shown that the HA-tag does not interfere with ligand-receptor pharmacology.[140,183] All data were normalized to the expression of the wt receptor (see Figure 44 and Appendix Table S1 for expression values).

Cell surface expression of the $P2Y_2R$ mutants was between 16 % and 125 % relative to that of the wt receptor (100 %). The least expressed receptor was the $P2Y_2R$-F113Y mutant (16 %), which is a highly conserved amino acid among the two P2YR subtypes (see Figure 44). In contrast to F113Y, the $P2Y_2R$-mutant F113A showed high expression (125 %). $P2Y_2R$-R110A mutant displayed a high cell surface expression (74 %) similar as in a previous study.[183] Cell surface expression of the $P2Y_4R$ mutants was between 56 % (Y197A) and 144 % (F200Y) relative to that of the wt $P2Y_4R$ (100 %).

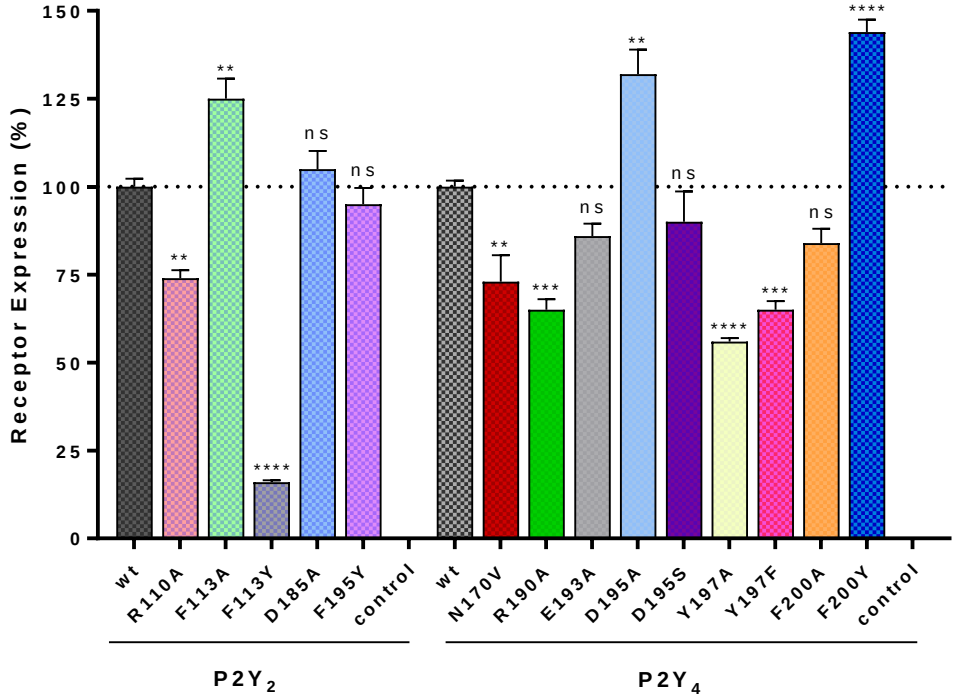

Figure 44: Cell surface receptor expression levels as determined by ELISA with antibodies interacting with the HA tag fused to the N-terminus of the $P2Y_2$ and $P2Y_4$Rs. Data represent means ± SEM of 3-4 independent experiments (in duplicates). Expression rates of the mutants were determined relative to the wt (100 %). Statistically analyzed by one-way ANOVA with Dunnett's post-hoc test: ^{ns} not significant; * $p \leq 0.05$; ** $p \leq 0.01$; *** $p \leq 0.001$; **** $p \leq 0.0001$.

5.2.4 **Analysis of agonist activities**

Four agonists, UTP (**1**), ATP (**2**), Ap_4A (**27**) and MRS4062 (**14**), were selected for testing at the receptors based on their structures and their pharmacology. UTP is an agonist for both receptors. ATP and Ap_4A only activate the $P2Y_2R$ while MRS4062 was reported to be selective for the $P2Y_4R$. The ligands were assessed by measuring intracellular calcium concentrations using the fluorescent calcium-chelating dye Fluo-4. 1321N1 Astrocytoma cells natively express muscarinic M_3R which is also G_q protein-coupled and therefore, like the $P2Y_2$ and $P2Y_4$ receptors, also lead to intracellular calcium release upon activation. Carbachol, a muscarinic M_3R agonist was therefore

used as an internal standard to which all data were normalized. In addition, data for all agonist efficacies at each mutant were normalized to UTP efficacy at the corresponding wt receptors. Concentration-response curves are shown in Figures 45, 47 and 48, pEC_{50} values and efficacies are presented in Figures 46 and 49 while EC_{50} values are collected in Tables S2 and S3 of Appendix.

5.2.4.1 Evaluation of agonists at the $P2Y_2R$

UTP. UTP (**1**) displayed an EC_{50} value of 82 nM at the human $P2Y_2R$, which is consistent with previous reports in calcium assays.[140,183] There was a rightward shift of the dose-response curves for most of the mutants relative to the wt receptor, except for the F195Y mutant at which UTP showed an EC_{50} value of 23 nM (see Figures 45 and 46; Table S2). There was no significant difference ($p \leq 0.05$) between the potencies at the wt and at the F113Y receptor mutant despite its comparatively lower expression level (16 % of the wt $P2Y_2R$). The R110A mutation resulted in a complete loss of receptor activation for all four tested agonists. The potency of UTP decreased 300-fold decrease at the F113A mutant (EC_{50} 250000 nM, $p \leq 0.0001$, ****) whereas at the D185A mutant it decreased 7-fold compared to that at the wt $P2Y_2R$ (606 nM vs 82 nM). There was a 3-fold increase in UTP potency at the F195Y mutant (EC_{50} 203 nM, $p \leq 0.01$, **). The efficacies of UTP at the $P2Y_2$ mutants ranged between 33 - 170 % compared to the wt $P2Y_2R$. There was a significant change in UTP efficacy for the F113A (170 %, $p \leq 0.0001$, ****) and the F113Y (33 %, $p \leq 0.0001$, ****) mutants compared to the wt receptor (see Figure 46).

ATP. ATP (**2**) was about equipotent to UTP at the human wt $P2Y_2R$ (EC_{50}: 102 nM) with similar efficacy (see Table S2). Similar to UTP, dose-response curves were slightly rightward-shifted for ATP at most of the mutants (i.e. F113A, F113Y, D185A and F195Y), with significant differences in potencies (see Figures 45 and 46). Like UTP, ATP was completely inactive at the R110A mutant although this mutant was highly expressed. Also, the receptor mutants F113A and F113Y showed appreciable differences in ATP activity as compared to the wt $P2Y_2R$. At F113A, ATP (**2**) was significantly 200-fold less potent (EC_{50} 20500 nM, $p \leq 0.0001$, ****) compared to the wt receptor, whereas the F113Y mutation resulted in only a 2-fold non-significant decrease in potency (EC_{50} 219 nM, $p \leq 0.05$, ^{ns}). Disruption of the ionic lock in the D185A mutant led to a 21-fold reduction in ATP potency (EC_{50} 2160 nM, $p \leq 0.0001$, ****) relative to the wt $P2Y_2R$. The efficacy of ATP (**2**) was significantly different from that at the wt $P2Y_2R$ (set at 100 %) at the F113A (185 %, $p \leq$

0.0001, ****) and F113Y (31 %, $p \leq 0.0001$, ****) mutants. Residues Arg110, Phe113 and to a lesser extent Asp185 are important for $P2Y_2R$ activation by UTP and ATP.

Ap_4A. The EC_{50} value of Ap_4A (**27**) at the wt $P2Y_2R$ amounted to 69.5 nM with 88 % efficacy, similar to the previously reported values.[183] Ap_4A (**27**) was completely inactive at the other $P2Y_2R$ mutants (i.e. R110A, F113A, F113Y and D185A) except for the F195Y mutant, at which it showed a 3-fold decrease in potency from 69.5 nM at the wt to 194 nM ($p \leq 0.001$, ***), and a moderate reduction in efficacy to 67 % ($p \leq 0.05$, *) (see Figures 45 and 46).

MRS4062. The wt $P2Y_2R$ was activated by the $P2Y_4R$ agonist MRS4062 (**14**) with an EC_{50} value of 535 nM and 88 % efficacy compared to UTP. MRS4062 was 10-fold more potent at the F113Y receptor mutant (EC_{50} 54.6 nM, $p \leq 0.0001$, ****), 3-fold more potent at the F195Y receptor mutant (EC_{50} 178 nM, $p \leq 0.001$, ***) and completely inactive at all other investigated $P2Y_2R$ mutants (Figures 45 and 46). MRS4062 (**14**) showed moderate efficacies at the F113Y mutant (20 %, $p \leq$ 0.0001, ****) and at the F195Y mutant (71 %, $p \leq 0.001$, ***) compared to that at the wt $P2Y_2R$.

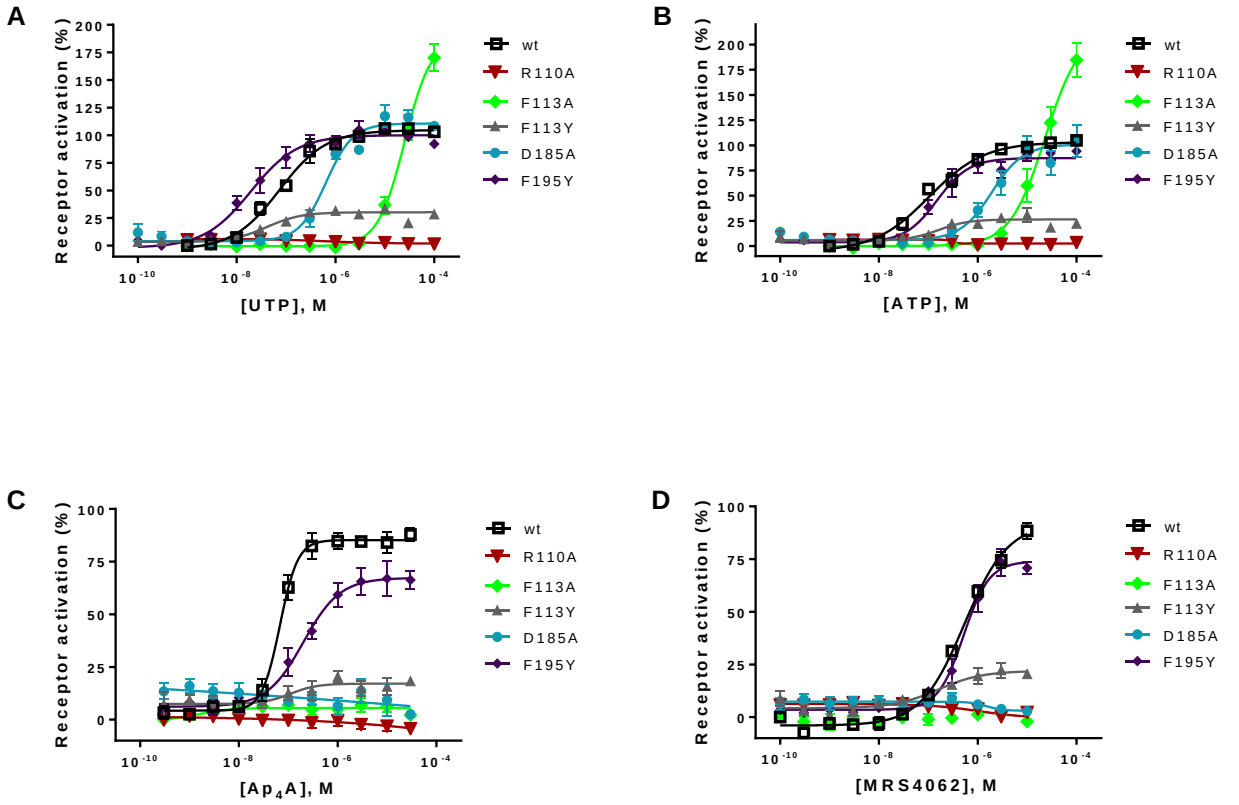

Figure 45: Dose-response curves of **(A)** UTP **(B)** ATP **(C)** Ap_4A and **(D)** MRS4062 determined by calcium mobilization assays on the wt and mutant $P2Y_2Rs$ expressed in 1321N1 astrocytoma cells. Each data point represents the mean ± SEM of 4 – 6 independent determinations each in duplicate. EC_{50} values are reported in Appendix Table S2.

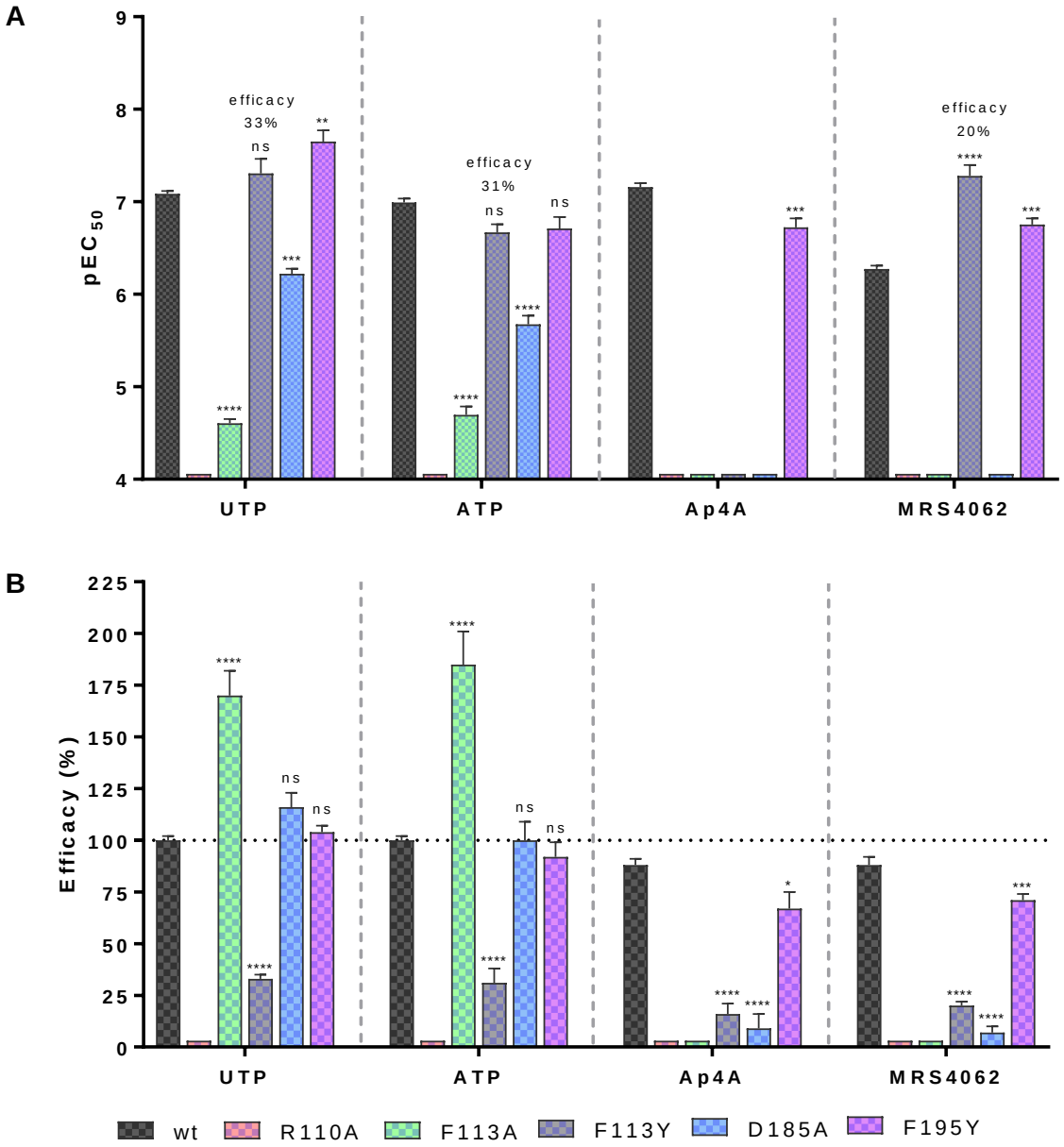

Figure 46: A. Potencies and **B.** efficacies of the agonists determined in calcium mobilization assays on the human $P2Y_2R$ (wt and mutants) expressed in 1321N1 astrocytoma cells. Data represent means ± SEM (n = 4 – 6) performed in duplicates. One-way ANOVA with Dunnett's post-hoc test: ^{ns} not significant; * $p \leq 0.05$; ** $p \leq 0.01$; *** $p \leq 0.001$; **** $p \leq 0.0001$.

5.2.4.2 Evaluation of agonists at the $P2Y_4R$

UTP. In comparison to the wt $P2Y_4R$ (EC_{50} = 135 nM), UTP showed no significant difference in potency for the $P2Y_4R$ mutants except at the R190A mutant (EC_{50} 1980 nM, $p \leq 0.0001$, ****), (see Figures 47 and 48; Table S3). There were, however, differences in agonist efficacies (Figure 49). Notably, there was a slight decrease in UTP (potency at Y197A (411 nM, 3-fold) and F200A (284 nM, 2-fold) with significantly reduced efficacy to 56 % ($p \leq 0.001$, ***) and 24 % ($p \leq 0.0001$, ****) respectively. UTP (**1**) was least potent at the R190A mutant with a 15-fold decrease (EC_{50} 1980 nM, $p \leq 0.0001$, ****) and 53 % efficacy ($p \leq 0.001$, ***) compared to the wt $P2Y_4R$.

ATP. ATP was inactive at the wt $P2Y_4R$ as previously described.[140,243] Interestingly, ATP showed some activity at the $P2Y_4R$ mutant Y197A with an EC_{50} value of 11,900 nM and an efficacy of 32 %. ATP was inactive at all the other investigated $P2Y_4R$ mutants (see Figures 48 and 49, Appendix Table S3).

Ap_4A. At the human wt $P2Y_4R$ and its mutants, Ap_4A (**27**) was completely inactive as an agonist as previously reported.[140,243] (see Appendix Table S3).

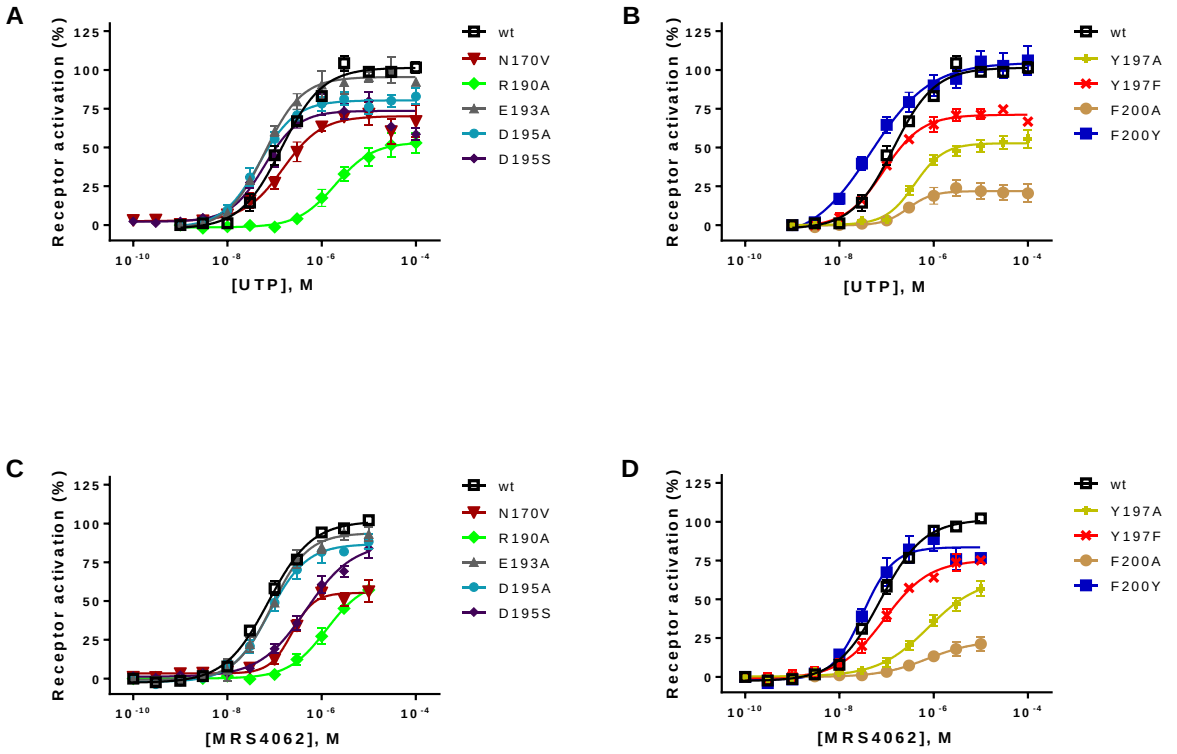

Figure 47: Dose-response curves of UTP (**A** and **B**) and MRS4062 (**C** and **D**) determined by calcium mobilization assay on the $P2Y_4Rs$ (wt and mutants) expressed in 1321N1 astrocytoma cells. Each data point represents means ± SEM of 4 – 6 independent determinations each in duplicate. EC_{50} values are reported in Appendix Table S3, pEC_{50} values are shown in Figure 49.

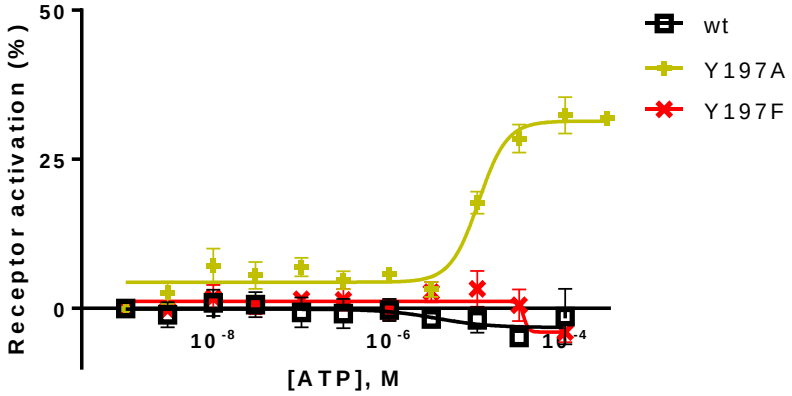

Figure 48: Concentration-response curves of ATP on the wt $P2Y_4R$ and the $P2Y_4R$ mutants Y197A and Y197F expressed in 1321N1 astrocytoma cells as determined by calcium mobilization assay. Replacement of Tyr197 in the wt $P2Y_4R$ by alanine (Y197A), but not by phenylalanine (Y197F),

led to a receptor activated by ATP. Each data point represents means ± SEM of 4 – 6 independent determinations each in duplicate. EC_{50} values are reported in Appendix Table S3, pEC_{50} values are shown in Figure 49.

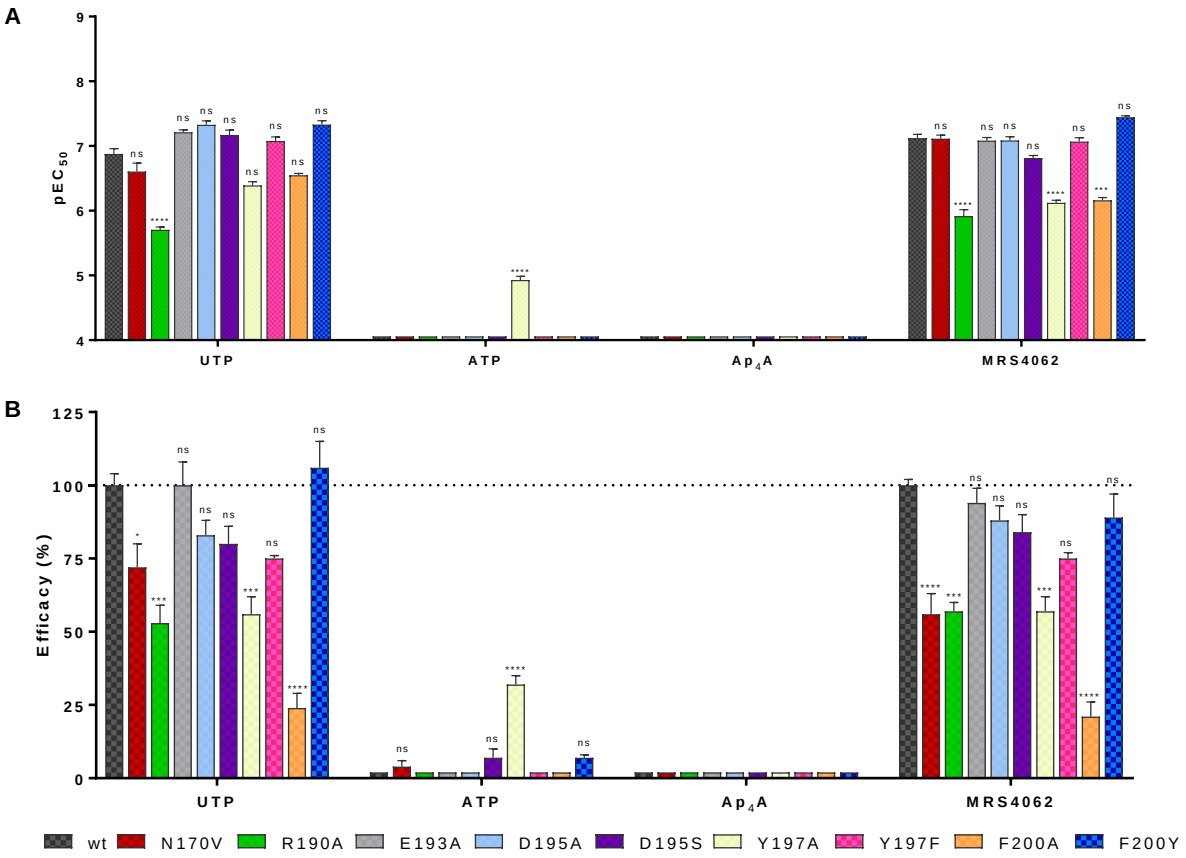

Figure 49: A. Potencies and **B.** efficacies of agonists determined in calcium mobilization assays at the wt $P2Y_4R$ and $P2Y_4R$ mutants expressed in 1321N1 astrocytoma cells. EC_{50} values are presented in Appendix Table S3. Data represent means ± SEM from 4-6 separate experiments performed in duplicates. Statistical analysis was done by one-way ANOVA with Dunnett's post-hoc test: ^{ns} not significant; * $p \leq 0.05$; ** $p \leq 0.01$; *** $p \leq 0.001$; **** $p \leq 0.0001$.

MRS4062. MRS4062 (**14**) was 7-fold more selective for the wt $P2Y_4R$ (76.1 nM, 100 % efficacy) versus the wt $P2Y_2R$ (535 nM, 88 % efficacy) confirming previously published data.[138] Compared to the wt $P2Y_4R$, the potency of MRS4062 (**14**) was significantly reduced at the R190A mutant (EC_{50} 1240 nM, 16-fold), the Y197A mutant (EC_{50} 757 nM, 10-fold), and the F200A (EC_{50} 694 nM, 9-fold). The efficacies at these mutants were also significantly decreased to 57 % ($p \leq 0.001$,

) for the R190A, and to 21 % for the Y197A mutants, and ($p \leq 0.0001$, *). MRS4062 also showed reduced efficacy at the N170V receptor mutant (56 %, $p \leq 0.0001$, ****) although its potency was unchanged compared to the wt $P2Y_4R$ (see Figures 47 and 49, Appendix Table S3).

5.2.5 **Analysis of antagonist activities**

Selected antagonists were tested in calcium assays at the wt $P2Y_2$ and $P2Y_4R$ and their mutants. Recombinant 1321N1 cells were pre-incubated with different concentrations of antagonist followed by receptor stimulation by agonist at its EC_{80} concentration to obtain concentration-dependent inhibition curves. We tested the non-selective P2YR antagonist reactive blue 2 (RB-2), the smaller AQs, PSB-09144 (**37**), PSB-16133 (**15**), PSB-16135 (**16**) and PSB-1699 (**17**), as well as AR-C118925 (**38**), a potent and selective $P2Y_2R$ antagonist. These antagonists have been proposed to bind to the orthosteric site of the $P2Y_2R$.[183] In contrast, at the $P2Y_4R$, RB-2 and other AQ derivatives were reported to be bind to an allosteric pocket in close proximity to the orthosteric site. However, experimental evidence for this hypothesis is still lacking and the individual interaction partners in the receptor protein have not been confirmed so far. We therefore set out to investigated the proposed different binding modes of the AQ derivatives by our mutational approach (see Appendix Figure S1 and Tables S4, respectively, for dose-response curves and IC_{50} values of antagonist at the human $P2Y_2R$; for those at the $P2Y_4R$, see Appendix Figures S2 and S3, and Table S5).

5.2.5.1 Evaluation of antagonists at the $P2Y_2R$ mutants

Reactive blue 2. At the wt $P2Y_2R$, the P2YR antagonist RB-2 displayed potency in the low micromolar range (5990 nM) consistent with reported values.[139,140] There was, however, a 3- and 4-fold reduction in RB-2 potency at the mutants F113Y (23500 nM, $p \leq 0.0001$, ****) and F195Y (18000 nM, $p \leq 0.01$, **), respectively (Figure 50). In contrast, RB-2 was 3-fold more potent at D185A (IC_{50} 1730 nM, $p \leq 0.001$, ***). RB-2 appear to have a pharmacological activity different from those of the other anthraquinones at the $P2Y_2R$ mutants studied.

Further anthraquinone derivatives. PSB-09114 (**37**), PSB-16133 (**15**) and PSB-16135 (**16**), showed no significant differences in potencies at the wt $P2Y_2R$ as compared to the mutant receptors F113A and F195Y. However, at the $P2Y_2R$ mutants F113Y and D185A, the potencies of these AQ were appreciably increased. PSB-09114 (**37**) was 3-fold more potent at the F113Y (IC_{50} 550 nM, $p \leq 0.05$, *) and 9-fold more potent at the D185A receptor mutant (170 nM, $p \leq 0.01$, **). Similarly, PSB-16133 (**15**) was 5- to 7-fold more potent, and PSB-16135 (**16**) was about 2-fold more potent at the F113Y (1380 nM, $p \leq 0.01$, **) and D185A (1200 nM, $p \leq 0.01$, **) mutants over the wt (Figure 50 and Table S4). Interestingly, the AQ derivative PSB-1699 (**17**), with an extra methylene linker to ring E, showed a completely different pattern. Contrary to the former AQ derivatives **15, 16** and **37**, PSB-1699 (**17**, IC_{50} 3190 nM) at the wt $P2Y_2R$ showed no inhibition of UTP-induced receptor activation at the F113A and F195Y receptor mutants while it maintained potency similar to that at the wt $P2Y_2R$ for the F113Y and D185A receptor mutants.

AR-C118925. The potency of the UTP-derived $P2Y_2R$-selective antagonist AR-C118925 (**38**) was in the low nanomolar range as previously reported. [229] Interestingly, there was no significant difference in AR-C118925 potency at the $P2Y_2R$ mutants (Figure 50, see Table S4).

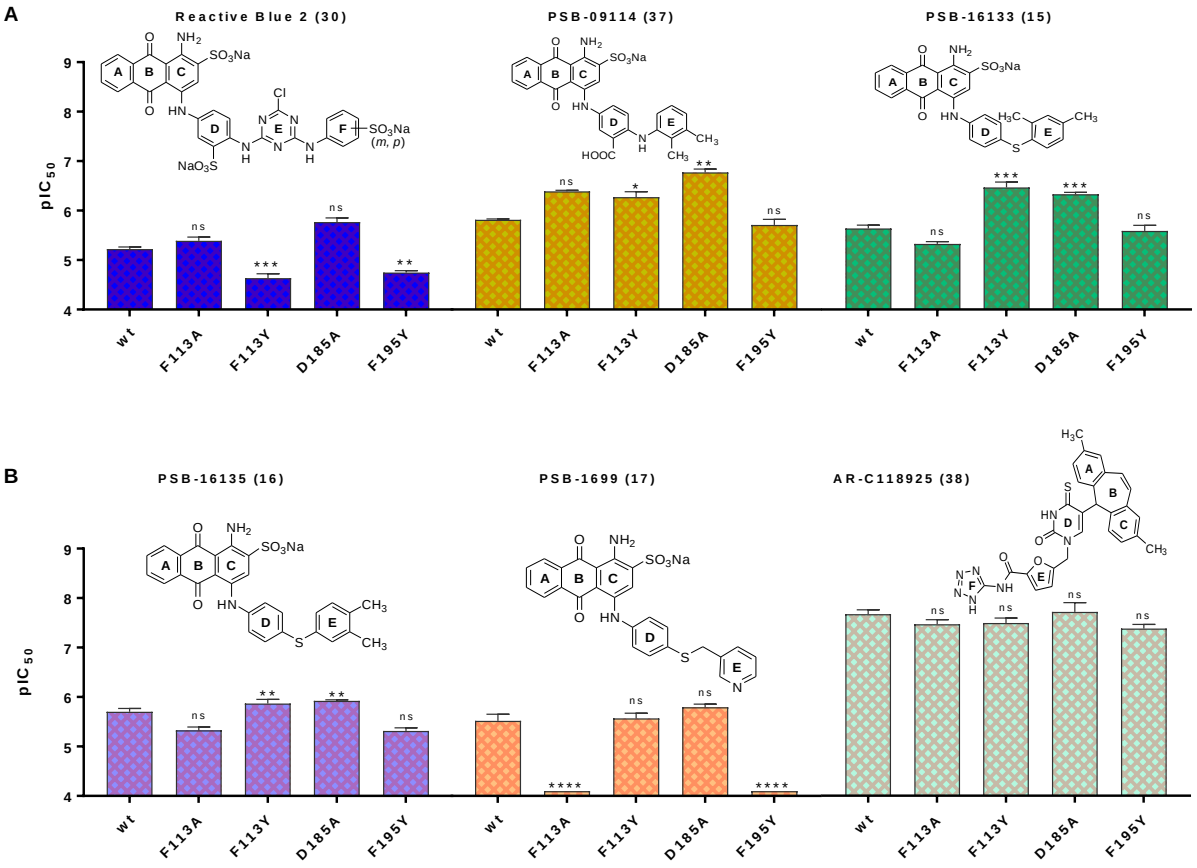

Figure 50: Potencies of Reactive blue 2 (RB-2, purified), PSB-09114, and PSB-16133, PSB-16135, PSB-1699 and AR-C118925 determined by calcium mobilization assays at the human wt $P2Y_2R$ and its mutants expressed in 1321N1 astrocytoma cells. Data represent mean pIC_{50} values ± SEM of 3 – 5 independent determinations each in duplicates vs. UTP at its EC_{80} value for the respective cell line. IC_{50} values are reported in Appendix Table S4. Concentration-response curves are shown in Appendix Figure S1.

5.2.5.2 Evaluation of antagonists at the $P2Y_4R$ mutants

Reactive-blue 2. RB-2 (**30**) was about 6-fold more potent at the wt $P2Y_4R$ (IC_{50} 1050 nM) as compared to the wt $P2Y_2R$ (IC_{50} = 5990 nM). In comparison to the wt $P2Y_4R$, RB-2 (**30**) was 2-fold less potent at the D195S mutant (2260 nM, $p \leq 0.05$, *), 3-fold less potent at the Y197F mutant (3300 nM, $p \leq 0.001$, ***) and 4-fold less potent at the F200Y mutant (4170 nM, $p \leq 0.0001$, ****).

At the N170V mutant, RB-2 was 2-fold more potent (477 nM, $p \leq 0.05$, *). There was no significant change in potency of RB-2 at the other mutants (see Figure 51 and Table S5).

Further anthraquinone derivatives. There were no significant or only moderate differences between the potencies of PSB-09114 (**37**), PSB-16133 (**15**) and PSB-16135 (**16**) at the wt $P2Y_4R$ and the investigated $P2Y_4R$ mutants (see Figure 51 and Table S5). PSB-09114 (**37**) was 5-fold less potent at the N170V (2260 nM, $p \leq 0.0001$, ****) and the F200Y (2090 nM, $p \leq 0.0001$, ****) mutants, and 2-fold less potent at the E193A (1010 nM, $p \leq 0.01$, **) and the Y197F (913 nM, $p \leq 0.01$, **) mutants compared to the wt $P2Y_4R$. PSB-16133 (**15**) showed a significant, 3-fold decrease in potency at the Y197F (4770 nM, $p \leq 0.05$, *) and the F200Y (5430 nM, $p \leq 0.01$, **) mutants, whereas its potency increased 5-fold at R190A (260 nM, $p \leq 0.001$, ***) and 8-fold at the Y197A mutant (2260 nM, $p \leq 0.0001$, ****). The potency of PSB-16135 (**16**) was 3-fold lower at the R190A (4980 nM, $p \leq 0.01$, **), the E193A (4330 nM, $p \leq 0.05$, *) and the F200Y (5690 nM, $p \leq 0.01$, **) receptor mutants. At the Y197A mutant, PSB-16135 displayed a 6-fold increase in potency (303 nM, $p \leq 0.0001$, ****).

Interestingly, as observed at the $P2Y_2R$, PSB-1699 (**17**) also displayed a different trend from the other AQ derivatives at the $P2Y_4R$ as well. PSB-1699 (**17**) activity was completely abolished at the R190A, D195A, F200A, and F200Y receptor mutants. At the Y197F receptor mutant, there was a 6-fold decrease in potency while it was 3-fold more potent at at N170V (537 nM, $p \leq 0.0001$, ****) and the D195S $P2Y_4R$ mutant (504 nM, $p \leq 0.0001$, ****) relative to the wt $P2Y_4R$.

AR-C118925. In the current study, AR-C118925 (**38**) was determined to be about 270-fold selective for the $P2Y_2R$ (IC_{50} = 21 nM) over $P2Y_4R$. These data confirm the previously published selectivity profile of AR-C118925 (**38**).[229] With the exception of F200A which showed no significant difference in the potency of AR-C118925 relative to the wt $P2Y_4R$, mutation of the $P2Y_4R$ significantly affected AR-C118925 potency (Figure 51). Most mutations led towards a reduction in potency of the antagonist. Inhibitory activity of **38** against UTP was lost in the N170V, D195S and F200Y receptor mutants. AR-C118925 showed a 2-fold decrease in potency at the R190A mutant (10900 nM, $p \leq 0.01$, **) and the E193A mutant (12700 nM, $p \leq 0.001$, ***), two amino acids predicted to form ionic locks in the $P2Y_4R$. In contrast, **38** was more potent at the D195A and Y197A mutants than at the wt $P2Y_4R$ with IC_{50} values of 1470 nM ($p \leq 0.0001$, ****) and 1960 nM ($p \leq 0.0001$, ****), respectively.

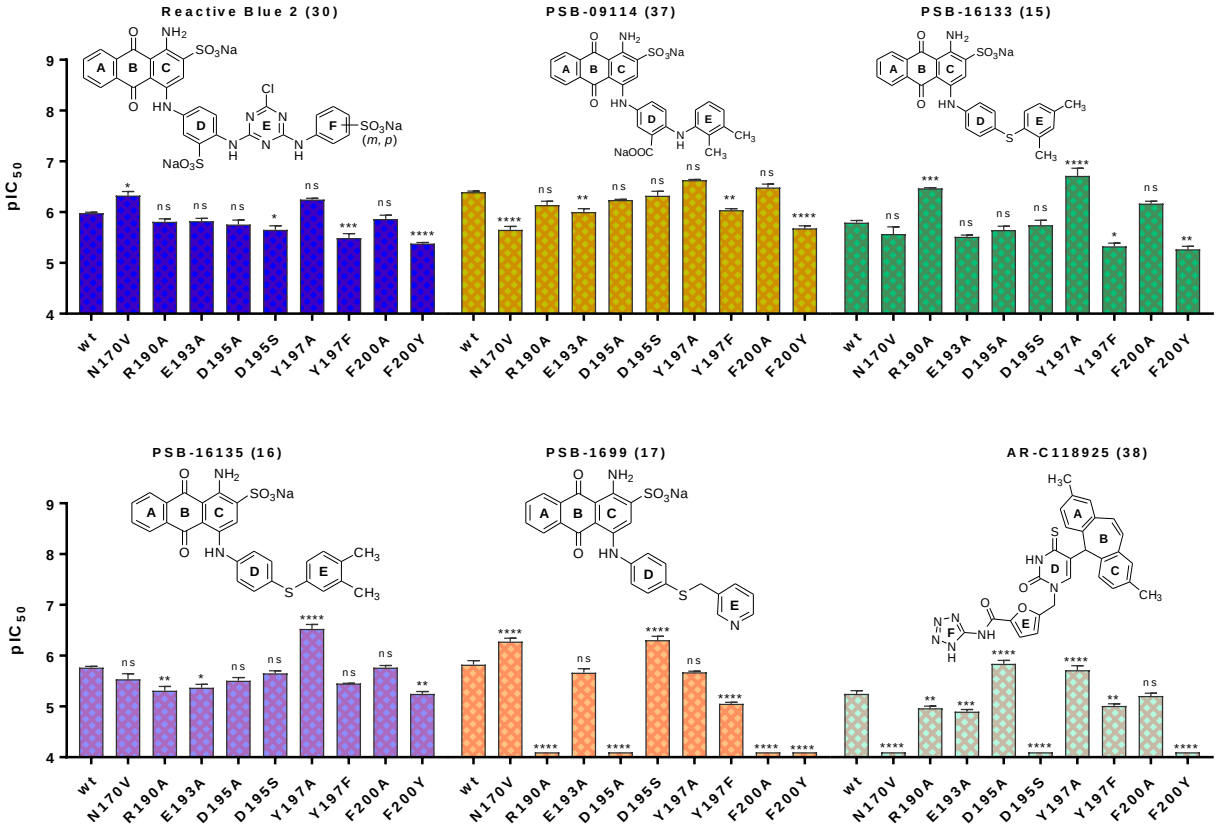

Figure 51: Potencies of Reactive blue 2 (RB-2, purified), PSB-09114, and PSB-16133, PSB-16135, PSB-1699 and AR-C118925 as determined by calcium mobilization assays at the human wt $P2Y_4R$ and its mutants expressed in 1321N1 astrocytoma cells. Data represent mean pIC_{50} values ± SEM of 3 – 5 independent determinations each in duplicates vs. UTP (EC_{80} value for the respective cell line). IC_{50} values are reported in Appendix Table S5. Concentration-response curves are shown in Appendix Figure S2 and S3.

5.3 **Discussion of mutagenesis data**

A combination of site-directed mutagenesis, calcium mobilization assays and homology modeling was employed to identify residues from the putative binding pockets of the human $P2Y_2R$ and $P2Y_4$ receptors important for ligand recognition and activity. Interpretation of mutagenesis data was done together with Dr. Vigneshwaran Namasivayam and Alexander Neumann.

5.3.1 **Agonists at the human $P2Y_2R$**

As previously confirmed for UTP and Ap_4A, mutation of the key residue Arg110 also led to complete abolishment of ATP and MRS4062 activity, which was expected since the ribose moiety of MRS4062 was at the same position as that of UTP in our model forming hydrogen bonds between the 3′-hydroxy group and Arg110 (Figure 42). Mutation of Phe113 to alanine led to a significant decrease in potency for all investigated agonists. The nucleobases of the endogenous agonists UTP, ATP and Ap_4A likely form π-π-interactions with Phe113. In the case of MRS4062 no π-π-interactions with the nucleobase were observed for the rotamers in the module due to its shifted position in the binding pocket close to TM V (see Figure 52). While still in proximity, the aromatic network of Phe113, Tyr114, Tyr118 and Phe261 might be essential for ligand binding, as mutation of residues Tyr114, Tyr118 and Phe261in previous studies reduced the potency of the agonists.[140,183] The theory of an aromatic network in the orthosteric binding site is supported by the observation that the F113Y mutant had no significant effect on agonist potencies. The D185A mutation led to a moderate, non-significant decrease in potency of UTP and ATP at the $P2Y_2R$. Interestingly, the same mutation resulted in a complete loss of Ap_4A and MRS4062 activity. Ap_4A possesses an additional (δ-)phosphate in close proximity to the ionic lock between Asp185 and Arg292, while the phosphate groups of MRS4062 are shifted towards TM VII possibly allowing additional ionic and hydrogen bond interactions with those residues, resulting in different interaction patterns as compared to UTP and ATP. Mutation of Phe195 to tyrosine had only little effect on UTP and ATP potency and efficacy.

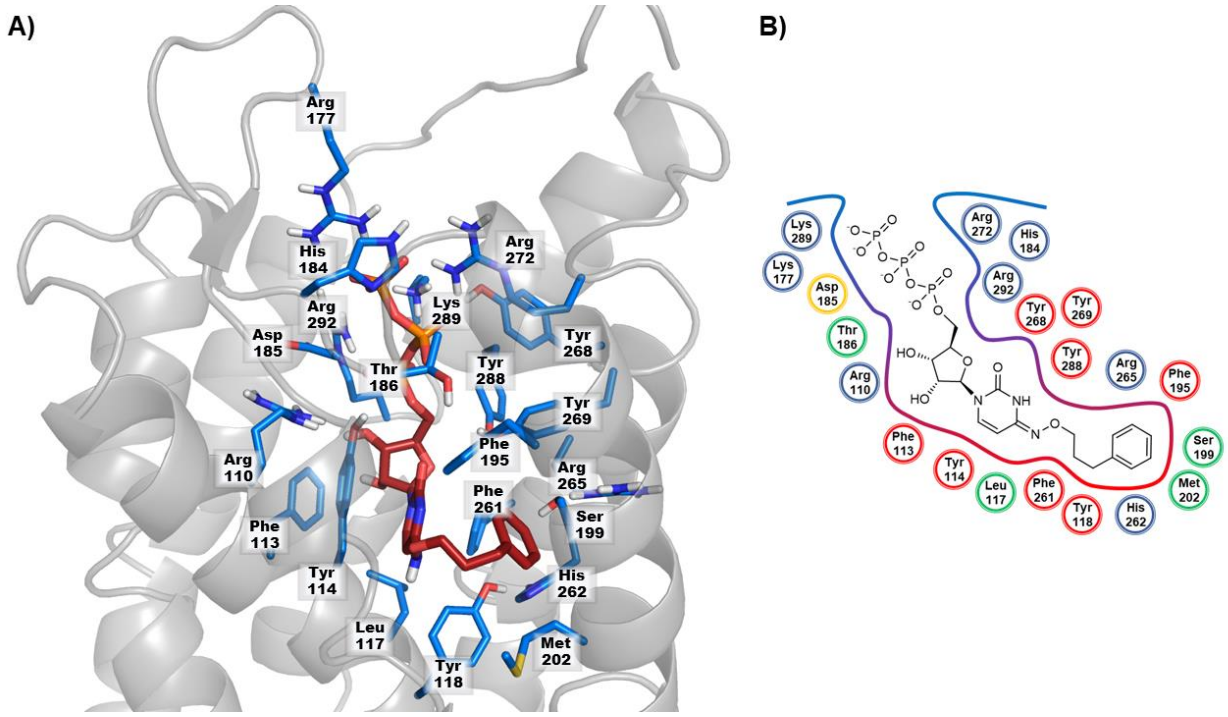

Figure 52: Putative binding mode of MRS4062 in the homology model of the human $P2Y_2R$. (**A**) Docked pose of MRS4062 with the important residues in the binding pocket shown. MRS4062 is colored in red. (**B**) Schematic 2D representation of the binding pocket. See Figure 42 for the color code. (credit: Alexander Neumann)

In case of Ap_4A, potency and efficacy were slightly decreased, while for MRS4062 potency was increased and the efficacy was decreased. As we did not observe different interactions for Phe195 with Ap_4A as compared to ATP in the model, the small difference in agonist potency could be explained by modulation of ECL2 flexibility resulting in weaker interactions with the larger agonist Ap_4A. The increase in MRS4062 potency at the F195Y mutant may be explained by additional hydrogen bonds between the introduced hydroxy group of the tyrosine and O^2 of the pyrimidine moiety.

The efficacy profiles were similar between the agonists UTP and ATP, and Ap_4A and MRS4062, respectively (see Figure 46). However, the mutations F113A and D185A led to different pharmacological responses as illustrated in Figures 45 and 46. While the F113A mutant resulted in a significant increase in efficacy for UTP and ATP, receptor activation response by Ap_4A and MRS4062 was drastically impaired. Since ATP and Ap_4A likely share the same binding mode based on the collected data, the difference in the pharmacological profiles can be explained by different modes of receptor activation. This includes different ionic and hydrogen bond interaction

patterns involving the ionic lock between Asp185 and Arg292 and other residues close to the ionic lock within in the aromatic network of the orthosteric binding site. This is further supported by a decrease in efficacy of Ap_4A and MRS4062 at the D185A mutant, while no changes in efficacies for UTP and ATP could be observed. It is possible, that the formation of the ionic lock between Asp185 and Arg292 induces a specific rotamer of Arg292 which is needed for proper interactions with the phosphate groups. Since Ap_4A possesses an additional δ-phosphate group, and MRS4062 likely has a different interaction patterns due to its shifted position in the binding pocket, they might form additional interactions with the proper rotamer of Arg292, which are not present in the case of UTP and ATP. Therefore, potencies and efficacies of Ap_4A and MRS4062 are affected more strongly than those of UTP and ATP at the D185A mutant, since two phosphate groups are likely involved in the interaction with Arg292.

Although there were only slight changes in potencies and efficacies of agonists were determined for the F195Y mutant, different trends were observed for ATP, UTP and Ap_4A. When mutated to tyrosine, the potency of UTP and MRS4062 slightly increased while it decreased for ATP and Ap_4A. Our docking studies suggest that the nucleobase binds close to Phe195 which would allow π-π-interactions of varying magnitudes with the adenine and uracil derivatives, respectively. Since the space in the investigated lipophilic binding pocket is limited, the size and functionality of residues might be crucial for ligand discrimination. $Phe195^{5.35}$ (Ballesteros-Weinstein numbering) is conserved in mouse and rat $P2Y_2R$, but exchanged by the larger tyrosine in the $P2Y_4R$ ($Tyr197^{5.35}$). As discussed below, mutation of Tyr197 to alanine introduced ATP-sensitivity into the $P2Y_4R$, probably due to the increase in available space, but since it was not crucial for ATP agonism at the $P2Y_2R$, we expect several residues besides the $Phe195^{5.35}$ to be responsible for accepting both ATP and UTP by the $P2Y_2R$.

5.3.2 **Antagonists at the human $P2Y_2R$**

Anthraquinone derivatives. The mutation of Phe113 to alanine had no significant effect on the potency of the antagonists except for PSB-1699 (**17**), where it led to a complete loss of antagonistic activity. In the case of PSB-1699, the distance between Phe113 and ring E amounts to approximately 3.6 Å according to our model, thus allowing π-π-interactions (see Figure 53). In the complexes of the other AQ antagonists, namely PSB-16133 (**15**) and PSB-16135 (**16**), the distance

of ring E and Phe113 is approximately 5.1 Å, leading to the assumption that no π-π-interactions can be formed. π-π-Interactions between ring E of PSB-1699 and Phe113 are further supported by the fact that the F113Y mutant showed no decrease in potency. We observed significant increases or trends towards increased potency of the investigated AQ antagonists at the D185A mutant. The mutation of Asp185 to alanine would break the ionic lock with Arg292 thus allowing rotamers to form additional interactions with the sulfonate of ring C. We observed a complete loss of inhibitory potency of PSB-1699 (**17**) at the F195Y mutant and a significant decrease in RB-2 potency, while the potency of AQ derivatives PSB-09114 (**37**), PSB-16133 (**15**), and PSB-16135 (**16**) was unaffected. The additional methylene linker in PSB-1699 of ring E increases the flexibility of the molecule and could thereby allow π-π-interactions with Phe195. As previously proposed by our group, the larger RB-2 appears to have a different binding mode compared to the other AQ derivatives. The orthosteric binding site is most likely composed of several lipophilic and aromatic residues which is a repelling environment for the sulfonate on ring F of RB-2. In our previously published study, the Y114F mutation showed increased potency of several AQ derivatives, but had no effect on RB-2, further supporting the orthosteric binding of smaller AQ derivatives without a charged group on ring D.

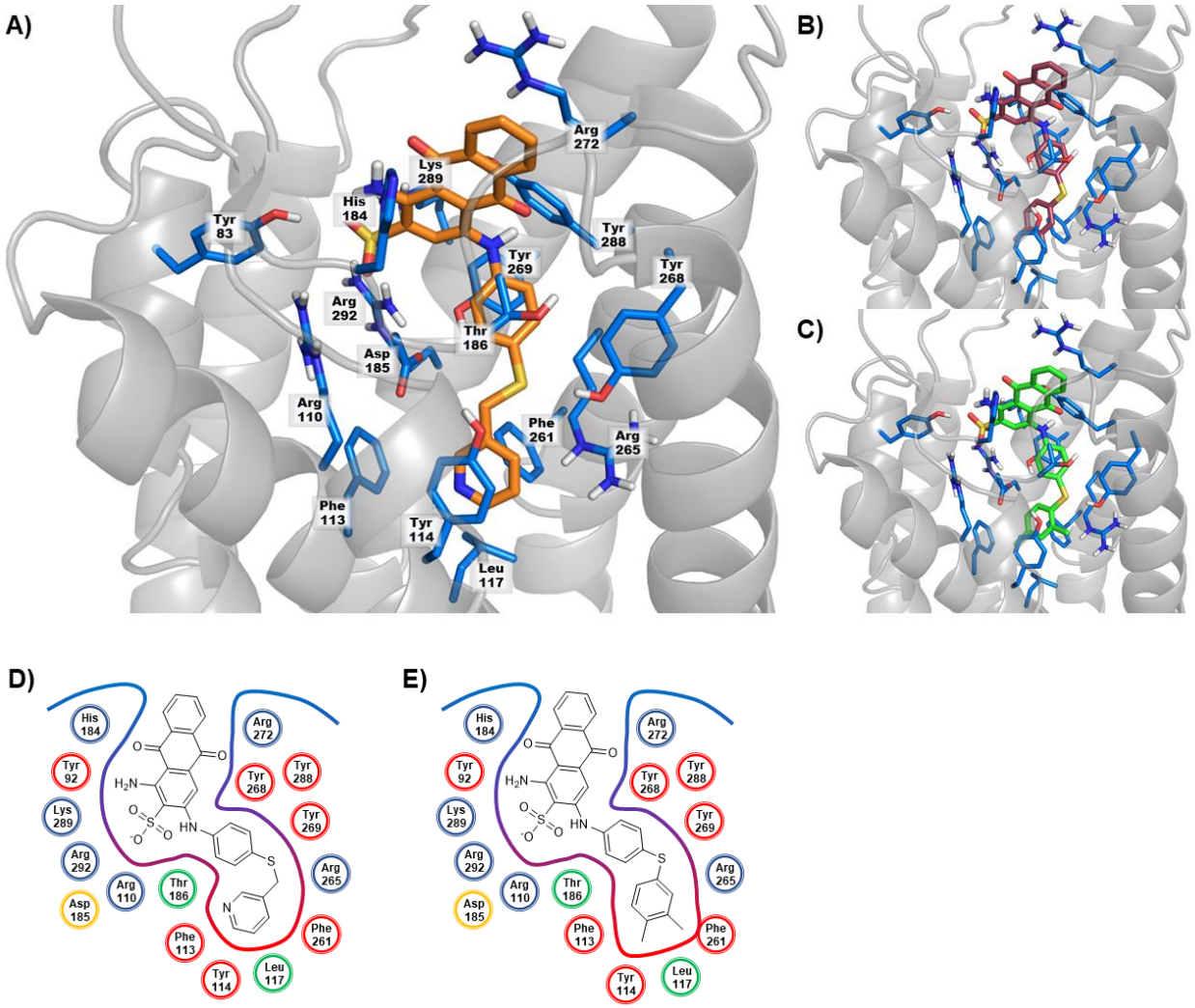

Figure 53: Putative binding mode of anthraquinone derived antagonists in the homology model of the human $P2Y_2R$. (**A**) Docked pose of PSB-1699 with the important residues in the binding pocket shown. The human $P2Y_2R$ (gray) is displayed in cartoon representation, the amino acid residues (blue) and PSB-1699 (orange) are shown as stick models. Oxygen atoms are colored in red, nitrogen atoms in blue, phosphorus atoms in orange, sulfur atoms in yellow. (**B**) Binding mode of PSB-16133. (**C**) Binding mode of PSB-16135. Schematic 2D representation of the binding pocket of PSB-1699 (**D**) and PSB-16133 (**E**). Charged, basic residues are colored in blue, aromatic residues in red, the conserved aspartic acid residue in ECL2 involved in the ionic lock in yellow, other residues in the binding pocket in green. (credit: Alexander Neumann)

5.3.3 **Agonists at the human $P2Y_4R$**

UTP. A significant change in UTP potency was observed for the $P2Y_4R$ R190A mutant, while no changes were observed for the E193A, D195A/S mutants. Although distant from the orthosteric binding site, Arg194 still modulated agonist potency, indicating a different mode of modulation rather than direct interaction between agonist and residue side-chain, e.g. by the increased flexibility of ECL2 resulting in less active receptor conformations. We could neither confirm Glu193 nor Asp195 as the major interaction partners for Arg190. Other residues of TM V such as Glu192 are conceivable as ionic interaction partners for Arg194. Mutations of Asn170, Tyr197 and Phe200 had no effect on agonist potency.

ATP. The human wt $P2Y_4R$ is activated by UTP but not by ATP. We were able to introduce ATP-sensitivity into the $P2Y_4R$ by mutating $Tyr197^{5.35}$ to alanine. The tyrosine residue in position 5.35 is conserved in mouse, rat and human $P2Y_4R$. It is exchanged by a phenylalanine in the $P2Y_2R$, but mutation of Tyr197 to phenylalanine had no effect on ATP recognition. As discussed, the aromatic side-chain of the 5.35 position might be involved in π-π-interactions with the nucleobase. This is supported by the findings that the Y197A mutant led to a significant decrease in UTP potency whereas the decrease in potency was not significant for the Y197F mutant. Similar interactions are likely for the agonists at the $P2Y_2R$ with $Phe195^{3.35}$. Although not solely responsible for ATP recognition, Tyr197 might contribute to ligand recognition by different mechanisms. The Tyr197 residue could act as a molecular switch for ATP activity at the $P2Y_4R$. Molecular switches are a cluster of highly conserved amino acid interactions in GPCR families which, when disrupted by ligands, lead to receptor activation but are stabilized by antagonists and inverse agonists.[252] Such molecular switches have been reported for rhodopsin, β_2-adrenergic, angiotensin AT_1, thyrotropin, serotonin and muscarinic M_3 receptors; they could be located anywhere in the receptor such as in the transmembrane domains, in intracellular loop and/or extracellular loop regions.[253–258] Modulating effects of the Y197A mutants on the flexibility of the ECL2 should not be disregarded, as the mutant was still insensitive towards Ap_4A stimulation.

Our docking results and the improved homology model indicate that the available space is an important factor in ligand recognition for both investigated receptors. At the $P2Y_4R$ Met205 of TM

V appears to be directed towards TM VI, while at the $P2Y_2R$ Met202 is likely directed towards TM IV (see Figure 52 and 54). Several rotamer combinations exist for Met205 and Arg265, where both residues interact through hydrogen bonds, or fewer rotamers are feasible for Arg265 concerning Met205 in its proximity, resulting in overall reduced space in the orthosteric binding site. At the $P2Y_2R$, more rotamers of Arg265 are conceivable, as Met202 projects outwards of the orthosteric binding site, where it can form interactions with Cys164 and Gln165. The additionally available space, as in the Y197A mutant, could therefore be important in accepting ATP.

MRS4062. The phenylpropyloxime substituent of MRS4062 (**14**) showed a similar binding pose in the model of $P2Y_4R$ as in the $P2Y_2R$ (see Figure 54). In our docking studies, MRS4062 displayed a somewhat larger shift towards TM VII than in the $P2Y_2R$. The R190A mutant showed a significant decrease in agonist potency compared to the wt $P2Y_4R$, most likely for the same reasons as in the case of UTP, namely Arg190 is part of an ionic lock with Asp195 which has been broken. Decreases in potency were also observed for the Y197A and F200A mutants, which were not different from those for UTP, indicating that the phenylpropyl substituent forms π-π-interactions with both Tyr197 and Phe200. This is supported by aromatic mutations Y197F and F200Y, which had no effect on the potency of MRS4062.

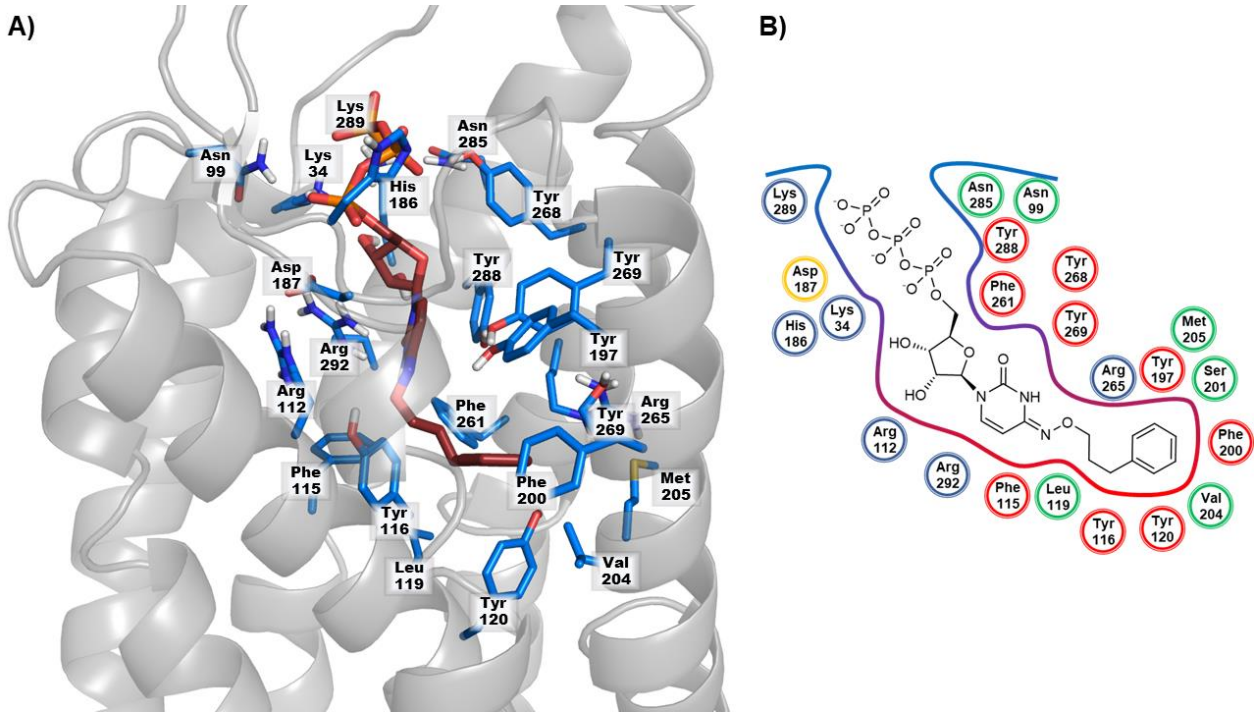

Figure 54: Putative binding mode of MRS4062 in the homology model of the human $P2Y_4R$. (**A**) Docked pose of MRS4062 with the important residues in the binding pocket shown. MRS4062 is colored in red. (**B**) Schematic 2D representation of the binding pocket. See Figure 42 for color code. (credit: Alexander Neumann)

Marouka *et al.* had developed MRS4062 and reported on its selectivity for the human $P2Y_4$ over the $P2Y_2R$. Based on a homology model of the two receptors built on the X-ray crystal structure of the CXCR4 chemokine receptor, they predicted that the phenyl moiety of the N^4-phenylpropoxy group of MRS4062 may project from the $P2Y_4$ binding pocket into a cavity in the ECL2 surrounded by Thr182 and Leu184. According to that study, this cavity is surrounded by bulky amino acids Arg180 and Thr182 in the $P2Y_2R$ which might explain the difference in selectivity.[138] Our current results which could be based on the recently published X-ray structure of the more closely related $P2Y_1R$ came to the conclusion that the phenylpropyloxime moiety binds deep in the pocket towards the intracellular region and interacts with Tyr116, Tyr120, Tyr197 and Phe200.

5.3.4 **Antagonists at the human $P2Y_4R$**

Anthraquinone derivatives. As previously reported, the AQ derivatives are most likely allosteric antagonists at the human $P2Y_4R$. They were proposed to bind close to the ECL2, as in the $P2Y_2R$, where the sulfonate of ring C can interact with charged residues including Lys34, Asp187 and Arg292 (see Figure 53). Ring D is most likely stabilized by interactions with His186 and Tyr288, while ring E binds close to TM V and VI, where it is stabilized through π-π-stacking with Tyr269 and Tyr288, and probably through cation-π-interactions with Arg265. The putative orthosteric binding site is blocked by the hydroxy group of Tyr197.

At the $P2Y_4R$, RB-2 (**30**) as well as its smaller derivatives showed significant decreases in potency at the F200Y mutant. The Y197F mutation led to a decrease of potencies of RB-2 (**30**), PSB-09114 (**37**), PSB-16133 (**15**) and PSB-1699 (**17**). Since the mutation of Tyr197 and Phe200 to alanine had no negative impact on the potencies of the investigated antagonists, we assume that no π-π-interactions between the residues and aromatic rings of the anthraquinone structure are formed, which is consistent with our proposed docking position. Due to several aromatic residues of TM V, VI and VII we expect an aromatic network, which plays a role in ligand recognition and rotamer stabilization. The aromatic network could stabilize a rotamer of Tyr197 thus modifying the flexibility of ECL2, resulting in low but significant decreases in antagonist potencies. The results indicated that the larger RB-2 interacts similarly as the smaller AQ derivatives with the $P2Y_4R$, while it has a different binding mode at the $P2Y_2R$. It appears that RB-2 can form ionic interactions between its sulfonate at the terminal ring F and Arg265 in the putative allosteric binding pocket of $P2Y_4R$, while no such interactions were observed for the $P2Y_2R$.

Interestingly, PSB-1699 (**17**) shows a different profile than the other AQ derivatives. Here, the R190A, D195A and F200A/Y mutants led to complete abolishment of the ligand's antagonistic activity. The main difference between PSB-1699 and the other investigated AQ antagonists included an additional methylene linker connecting the thioether and ring E, resulting in higher molecule flexibility and at the same time requirement of more space. Therefore, changes in the flexibility of ECL2 could greatly affect the potency of PSB-1699. As mentioned above, Arg190 could possibly be involved in an ionic lock close to the extracellular space modulating the flexibility of ECL2. Although only the mutation of Arg190 affected agonist potency, it is possible that Asp195 affects antagonist potency through ionic interactions with Arg190. The larger decrease

in potency at the F200A/Y mutant could be explained by the extended projection of ring E which demands proper interactions in the aromatic network.

AR-C118925. Large decreases in potency of AR-C118925 (**38**) were observed at the N170V, D195S and F200Y mutants, minor changes at the R190A, E193A, Y197F and F200A mutants, and significant increases in potency at D195A and Y197A mutants. Asn170 is placed at TM IV very close to the nucleotide binding pocket. Our homology model and docking results suggest that hydrogen bonds may be formed with Tyr116, leading to the assumption that Asn170 is involved in regulation of the aromatic network. Increases in space in the binding pocket through mutation of Tyr197 or Phe200 to alanine had no negative impact on the potency of AR-C118925, while substitution with the respective other aromatic amino acids led to a decrease, indicating that the resulting additional space after mutation to alanine benefits binding, while proper aromatic stacking plays a key role in ligand acceptance. Since the mutation of residues likely involved in the ionic lock of TM V affected AR-C118925 potency, it is possible that ECL2 is involved in ligand recognition and/or binding. The selectivity of AR-C118925 for the $P2Y_2R$ could be explained through increased lipophilicity or favorable aromatic stacking in the binding cavity for the dibenzocycloheptenyl moiety, as Asn170 of $P2Y_4R$ is replaced by a valine, and Tyr197 is replaced by a phenylalanine in the $P2Y_2R$.

5.4 **Conclusions**

Our docking and mutagenesis results suggest a binding mode of agonists at both, $P2Y_2$ and $P2Y_4R$, comparable to that of agonists at the human $P2Y_{12}R$, where the phosphate groups interact with negatively charged residues, and a lipophilic binding pocket accommodates the nucleobase. The putative agonist binding mode at $P2Y_2$ and $P2Y_4R$ differs from the one observed in the X-ray crystal structure of human $P2Y_1R$ in complex with the nucleotide antagonist MRS2500 (**6**). The investigated agonists contain a triphosphate chain, while the MRS2500 (**6**) antagonist contains 3'-, 5'- phosphate groups, resulting in different binding modes. The proper binding conformation of both, agonists and antagonists, is likely induced through an aromatic network consisting of residues of TM III, V and VI. The $P2Y_2R$ may be privileged to accept ATP and other adenine nucleotide-derived agonists due to a more spacious nucleobase binding cavity, caused by a replacement of a methionine residue by valine, and a swap of tyrosine to phenylalanine between $P2Y_4$ and $P2Y_2R$ at position 5.35. Residues close to the ECL2, distant from the putative orthosteric binding site,

modulate agonist and antagonist effects at the human $P2Y_4R$, which is consistent with previous observations for the human $P2Y_2R$. Ligand recognition is therefore not only limited to the orthosteric binding site but can also be altered through interactions between residues close to the ECL2, which might affect loop flexibility. UTP and ATP share a common pharmacological profile of full agonists at the $P2Y_2R$, while Ap_4A (**27**) and MRS4062 (**14**) acting as partial agonists appear to induce a different active receptor conformer. The investigated AQ antagonists share a similar binding cavity for the anthraquinone core, whereas substituents (rings D and E) project towards an allosteric binding domain ($P2Y_4R$) or reach the orthosteric nucleobase-binding site ($P2Y_2R$).

Antagonist AR-C118925 likely binds to the orthosteric site at both receptor subtypes. ECL2 possibly plays a key role in binding of AR-C118925 in the case of the $P2Y_4R$ while no similar observations were made for the investigated mutants of $P2Y_2R$. The selectivity for $P2Y_2R$ could be explained by increased lipophilicity in the binding pocket resulting in tighter binding and stronger Van-der-Waals forces.

Altogether, the data from the current work provides further insights into the architecture of ligand-receptor interactions and ligand selectivity of the $P2Y_2$ and $P2Y_4R$. Our docking studies using homology models succeeded in predicting key residues with direct ligand interactions and those remote to the orthosteric binding site. The findings and the refined homology models will aid future rational structure-based ligand design.

6 Summary and outlook

The P2Y receptors (P2Y) are nucleotide-activated GPCRs that are important (potential) drug targets for the treatment of common diseases such as thrombosis, (neuro)inflammation and cancer. However, several of the P2YR subtypes lack potent or selective ligands with suitable properties for use as pharmacological tools or drugs. The aim of this dissertation therefore was to identify and characterize novel non-nucleotide ligands with a particular focus on the $P2Y_2R$. Among the P2Y receptor subtypes, $P2Y_2R$ shares the highest sequence identity (53 %) with the $P2Y_4R$. This poses a challenge for $P2Y_2R$ ligand selectivity. Therefore, with the aim to gain valuable insights into ligand binding and receptor activation that could aid the design of selective ligands, we additionally performed site-directed mutagenesis studies of the human $P2Y_2$ and $P2Y_4R$.

Discovery of $P2Y_2$ receptor antagonists by screening

We established calcium mobilization and β-arrestin recruitment assays to perform high-throughput screening (HTS) in search for novel $P2Y_2R$ antagonists. The assays were validated using the endogenous $P2Y_2R$ agonists UTP (**1**), ATP (**2**) and Ap_4A (**27**), and the potent and selective $P2Y_2R$ antagonist AR-C118925 (**38**). We screened about 6400 compounds from 22 sub-libraries of the PZB compound library using calcium mobilization and β-arrestin assays. The average Z'-factors were 0.53 and 0.61, respectively, for calcium and β-arrestin assays, indicating suitability for HTS. Each plate was screened twice at 10 µM or 5 µM concentration, respectively. Among the various scaffolds discovered as hits (with ≥ 50 % inhibition at 10 µM) were the urea and diindolylmethane scaffolds. Further investigation of the urea derivatives (**52-114**), revealed compound **85** as the most potent antagonist (IC_{50} 1.31 µM, see Figure 55). We discovered that compound **85** allosterically inhibited $P2Y_2R$ activation by UTP with an affinity (pA_2 value) of 5.48. Moreover, **85** was only active in β-arrestin assays and inactive in calcium assays. This is not untypical of allosteric modulators.[211,259] Compound **85** was relatively selective over other GPCRs including GPR18, tested in the same assay system. The structure-activity relationship (SAR) analysis of the urea derivatives is summarized in Figure 55. Several potent derivatives of **85** could be developed.

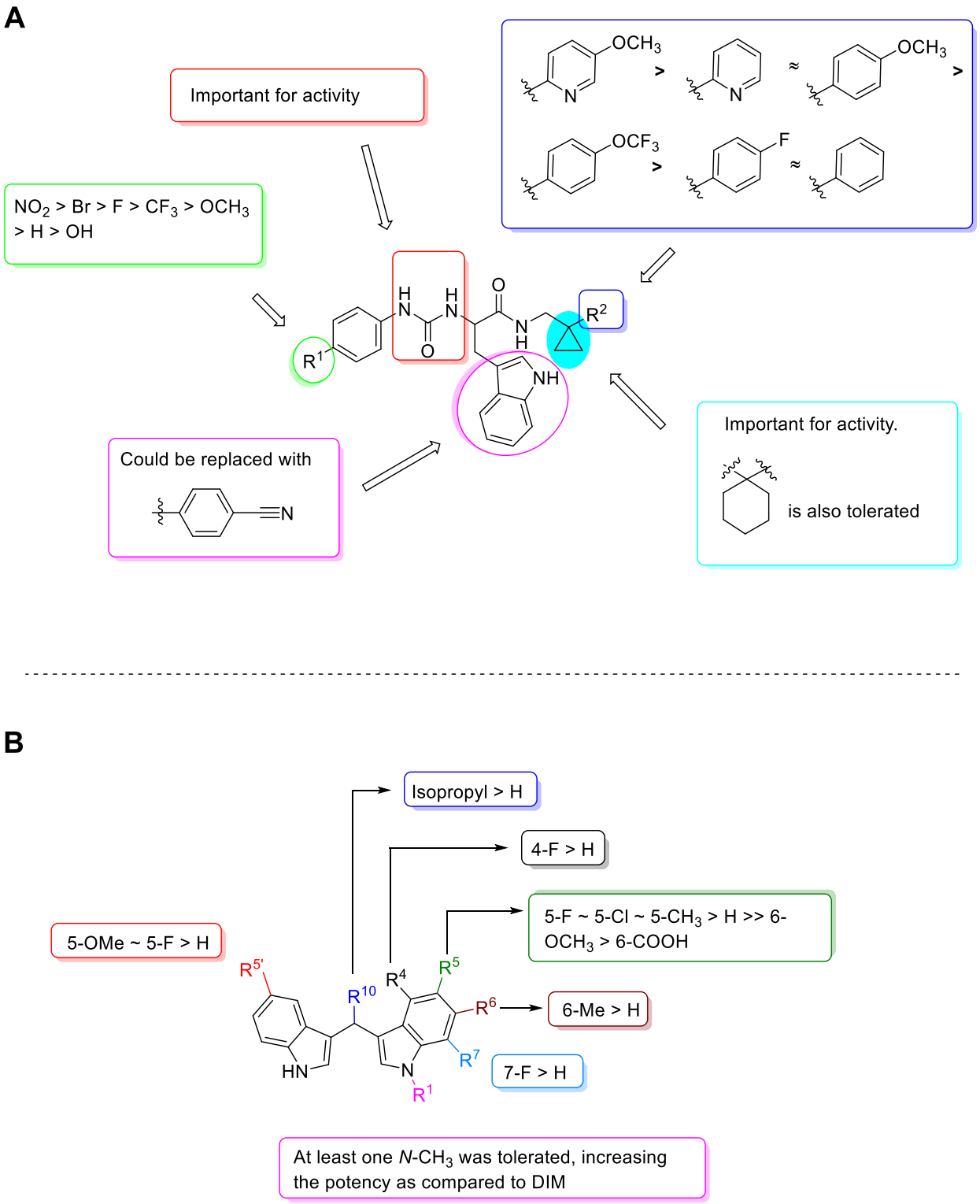

Figure 55: Structure-activity relationships of **A.** urea derivatives, and **B.** unsymmetrical diindolymethane derivatives as antagonists of the human $P2Y_2R$.

The investigated diindolylmethane (DIM) library (**115-282**), consisted of both symmetrically and unsymmetrically substituted DIMs. Compound **247**, an unsymmetrical DIM derivative, was the most potent $P2Y_2$ receptor antagonist of this series (IC_{50} 1.91 µM), being about 10-fold more potent than the lead compound **115** (19.4 µM). The SARs for the various DIM derivatives are summarized in Figure 51. They were found to be negative allosteric modulators of the $P2Y_2R$, mostly displaying functional bias towards the G_q pathway over the β-arrestin pathway (see Figures 24 and 25). They were relatively selective for the human $P2Y_2R$ over other GPCRs including the cannabinoid CB_1 and CB_2 receptors. So far, we have successfully discovered and characterized allosteric ligands for the $P2Y_2R$ which could be further optimized. Moreover, wehave proceeded to search for novel orthosteric antagonists for the $P2Y_2R$.

Discovery of $P2Y_2$ receptor antagonists by virtual screening

To discover novel orthosteric antagonists for the $P2Y_2R$, we performed virtual screening (VS) of on-line compound libraries using a $P2Y_2R$ homology model in complex with the orthosteric antagonist AR-C118925 (**38**).[183] The VS hits were subsequently validated experimentally in $P2Y_2R$ calcium assays and further screened for selectivity versus $P2Y_1$-, $P2Y_4$- and $P2Y_6$Rs. As a result, we discovered novel scaffolds as antagonists for each of these P2YR subtypes with potencies in the lower micromolar range. To the best of our knowledge, none of these scaffolds have so far been reported as antagonists for P2YRs. Some of the antagonists interact with several P2YR subtypes and might be developed as multitarget drugs. Selective ligands for the $P2Y_1R$ (**305** and **309**) and the $P2Y_6R$ (**311**) were also identified. Optimization of the newly discovered scaffolds is warranted and could be supported by structural knowledge of the orthosteric binding site. The SARs of some of the most prominent scaffolds for the development of $P2Y_2$- and $P2Y_6R$ antagonists are depicted in Figure 56.

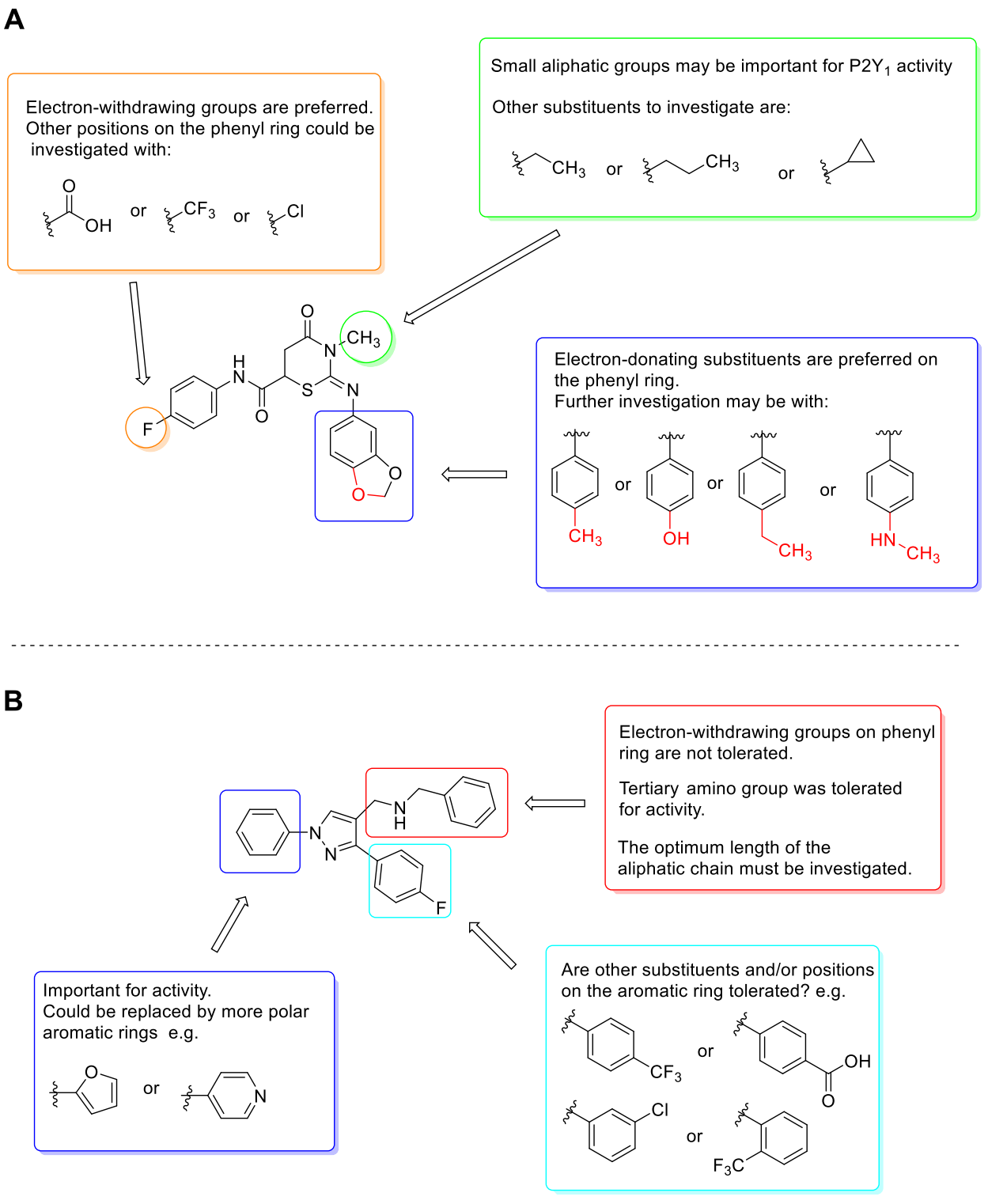

Figure 56: Preliminary structure-activity relationships of **A.** carboxamide derivatives and **B.** phenylpyrazole derivatives as antagonists of the $P2Y_1R$ and the $P2Y_2R$ respectively.

Mutagenesis studies of the human $P2Y_2$ and $P2Y_4$ receptor

In order to better understand the binding pockets of the $P2Y_2$- and $P2Y_4$Rs, we carried out a series of mutagenesis studies using PCR, bacterial transformation and retroviral expression of receptors. Expression was confirmed by ELISA and the mutant receptors were functionally characterized. Structurally diverse agonists, namely UTP, ATP, Ap_4A and MRS4062, and antagonists, i.e. several anthraquinone (AQ) derivatives and AR-C118925, were employed to investigate their interactions. Altogether, 4 new mutants of the $P2Y_2$R and 9 new mutants of the $P2Y_4$R were studied.

At the $P2Y_2$R, interactions of the residues Phe113 and Phe195 with agonists were found to be important for receptor activation. Mutation of these residues to alanine significantly reduced the potency of all agonists tested. Disruption of the ionic lock formed by Asp185 completely abolished the activity Ap_4A and MRS4062. With the exception of PSB-1699, the potency of the AQ derivatives were significantly reduced at the F113Y and D185A receptor mutants.

At the $P2Y_4$R, UTP and MRS4062 were found to bind in the same pocket (see Figure 57). The receptor mutant R190A and Y197A led to a decrease in the potency of both UTP and MRS4062. Additionally, MRS4062 displayed reduced potency at the F200Y receptor mutant compared to the wt $P2Y_4$R. In contrast, mutation of Tyr197 to alanine resulted in a $P2Y_4$R mutant that could be activated by ATP.

The anthraquinones were found to bind in an allosteric pocket of the $P2Y_4$R whereas in the $P2Y_2$R they were observed to bind in the orthosteric pocket. The potencies of the anthraquinones and AR-C118925 decreased significantly at the $P2Y_4$R after disruption of the ionic locks formed by Arg190, Glu193 and Asp195. Also, mutation of the aromatic residues Tyr197 and Phe200 in the $P2Y_4$R completely abolished the activity of PSB-1699. Our data suggest that aromatic π-π interactions between the dibenzocycloheptenyl moiety of AR-C118925 and residues such as $Val168^{4.60}$ and $Phe195^{5.35}$ of the $P2Y_2$R account for selectivity of AR-C118925 for the $P2Y_2$- over the $P2Y_4$R. At the $P2Y_4$R, the dibenzocycloheptenyl moiety of AR-C118925 interacts with the slightly more polar $Asn170^{4.60}$ and $Tyr197^{5.35}$ residues instead.

The data acquired in the study was used to further improve the $P2Y_2$R homology model and for providing experimental evidence to validate and fine-tune the $P2Y_4$R homology model

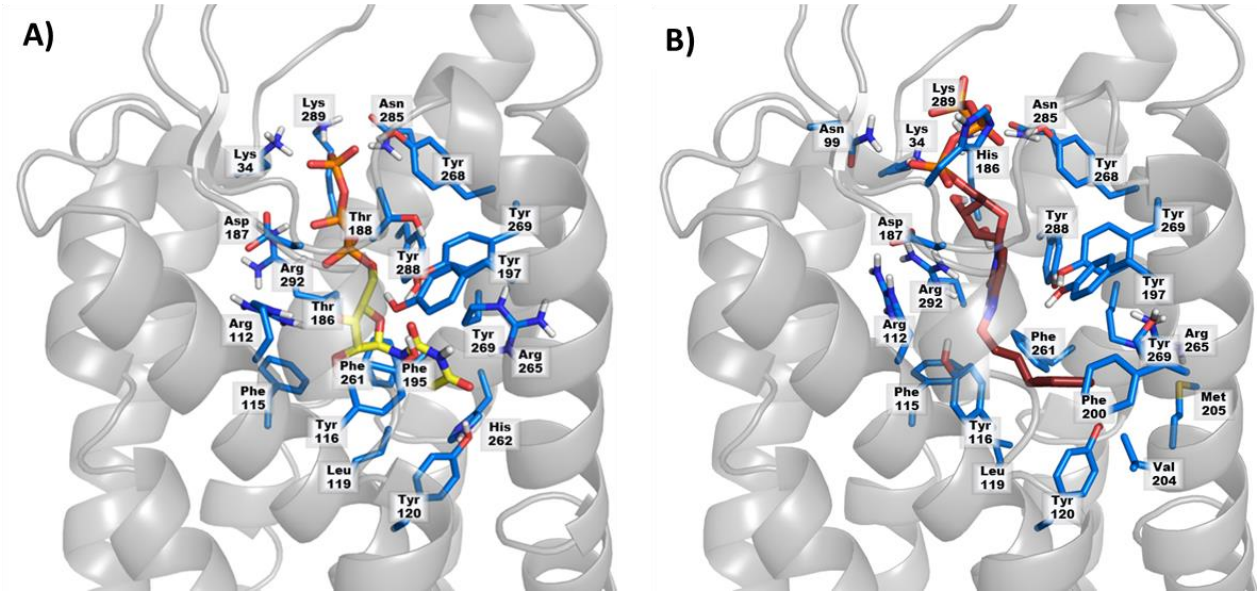

Figure 57: Docking poses of **A.** UTP (yellow) and **B.** MRS4062 (red) with the important residues in the putative binding pocket the human $P2Y_4R$ (gray).

Conclusions and outlook

Several new scaffolds for $P2Y_2R$ antagonists and also for $P2Y_1$-, $P2Y_4$-, and $P2Y_6R$ antagonists have been identified and characterized, which are suitable as lead structures for optimization. The obtained mutagenesis data of the $P2Y_2$- and $P2Y_4Rs$ provide structural information to support future drug development efforts.

7 Materials and Methods

7.1 Materials

7.1.1 Chemicals

24-well plates for ELISA assays	Sadstedt Ag & Co., Nuembrecht, Germany
ABTS chromophore (2,2′-azino-bis-3-ethylbenzothiazoline-6- sulfonic acid)	Calbiochem, Darmstadt, Germany
ADP	Sigma Aldrich Chemie GmbH, Taufkirchen, Germany
Agarose TE	Biozym Scientific GmbH, Hessisch-Oldendorf, Germany
All primers for molecular biology	MWG Biotech, Ebersberg, Germany
Ampicillin sodium	Carl Roth GmbH & Co. KG, Karlsruhe, Germany
Ap_4A	Sigma-Aldrich, St. Luis, USA
ATP	Carl Roth GmbH & Co. KG, Karlsruhe
Bovine serum albumin (BSA)	Carl Roth GmbH & Co. KG, Karlsruhe, Germany
$CaCl_2$	Sigma Aldrich Chemie GmbH, Taufkirchen, Germany
Carbachol	Alfa Aesar ThermoFisher GmbH, Kandel, Germany
CHAPS	Sigma Aldrich Corp., St. Louis, MO, USA
D-glucose	Sigma Aldrich Chemie GmbH, Taufkirchen, Germany
DMEM/F-12	Gibco®, Life Technologies, Thermo Fisher Scientific, Waltham, MA, USA
DMSO	AppliChem GmbH, Darmstadt, Germany
DMSO, cell culture grade	AppliChem GmbH, Darmstadt, Germany
DNA polymerase Pyrobest	TaKaRa Bio Inc., Kusatsu, Japan
Dulbecco's Modified Eagle Medium (DMEM)	Gibco®, Life Technologies, ThermoFisher Scientific, Waltham, MA, USA
Dulbecco's Modified Eagle Medium (DMEM)	Gibco® Invitrogen GmbH, Darmstadt, Germany

EDTA-sodium	Carl Roth GmbH & Co. KG, Karlsruhe, Germany
Ethanol, absolute	VWR International GmbH, Darmstadt, Germany
F-12 (Nutri-Mix)	Gibco®, Life Technologies, ThermoFisher Scientific, Waltham, MA, USA
FCS (fetal calf serum)	Sigma Aldrich Chemie GmbH, Taufkirchen, Germany
Fluo-4 AM cell permanent dye 10 x 50 µg	Invitrogen GmbH, Darmstadt, Germany
Galacton Star™	Applied Biosystems, ThermoFisher Scientific
Geneticin® (G 418) 100 mg/ml	Invitrogen GmbH, Darmstadt, Germany
Glacial acetic acid	Carl Roth GmbH & Co. KG, Karlsruhe, Germany
Glycerol	Sigma Aldrich Corp., St. Louis, MO, USA,
Hemagglutinin- (HA)-specific mouse monoclonal antibody (HA.11)	Covance, Berkeley, CA, USA
HEPES	Carl Roth GmbH & Co. KG, Karlsruhe, Germany
Hydrochloric acid 37 %	AppliChem GmbH, Darmstadt, Germany
Hygromycin	InvivoGen, San Diego, CA, USA
Isopropanol, absolute	VWR International GmbH, Darmstadt, Germany
K_2HPO_4	Carl Roth GmbH & Co. KG, Karlsruhe, Gemany
Kanamycin sulphate	Carl Roth GmbH & Co. KG, Karlsruhe, Germany
KH_2PO_4	Carl Roth GmbH & Co. KG, Karlsruhe, Gemany
LB agar	Carl Roth GmbH & Co. KG, Karlsruhe, Germany
LB medium	Carl Roth GmbH & Co. KG, Karlsruhe, Germany
Lipofectamine™	Thermo Fisher Scientific, Waltham, MA, USA
LumaSafe™	Perkin-Elmer, Waltham, MA, USA
Magnesium acetate [$Mg(OAc)_2$]	Carl Roth GmbH & Co. KG, Karlsruhe, Germany
Magnesium chloride [$MgCl_2$]	Sigma Aldrich Chemie GmbH, Taufkirchen, Germany
Magnesium sulfate [$MgSO_4$]	Sigma Aldrich Chemie GmbH, Taufkirchen, Germany
Methylparaben	Acros Organics, ThermoFisher Scientific, Waltham, MA, USA

MicroScint 25™	Perkin-Elmer, Waltham, MA, USA
MRS4062	Tocris Bioscience, Bristol, UK
Opti-MEM	Gibco®, Life Technologies, Thermo Fisher Scientific, Waltham, MA, USA
Paneticin G418 100 mg/ml	PANBiotech GmbH, Aidenbach, Germany
Penicillin-streptomycin (10 000 I.E./ml, 10 mg/ml)	Gibco® Invitrogen GmbH, Darmstadt
Phenol red solution 0.5 %	Sigma Aldrich Chemie GmbH, Taufkirchen, Germany
Plasmocin 2.5 mg/ml	Invitrogen GmbH, Darmstadt, Germany
Pluronic F-127	Sigma Aldrich Chemie GmbH, Taufkirchen, Germany
Polyethyleneimine (PEI) 50%	Fluka, Sigma Aldrich Corp., St. Louis, MO, USA
Potassium chloride [KCl]	Fluka, Sigma Aldrich Chemie GmbH, Taufkirchen, Germany
Purelab® Plus water	ELGA LabWater, Celle, Germany
Restriction enzymes	New England Biolabs, Ipswich, MA, USA
Sodium bicarbonate [$NaHCO_3$]	Sigma Aldrich Chemie GmbH, Taufkirchen, Germany
Sodium chloride [NaCl]	Carl Roth GmbH & Co. KG, Karlsruhe
Sodium dihydrogen phosphate [NaH_2PO_4]	Carl Roth GmbH & Co. KG, Karlsruhe
Sodium hydroxide	Sigma Aldrich Chemie GmbH, Taufkirchen, Germany
Sodium tartrate	Riedel-de-Haen, Seelze, Germany
TRIS-HCl	Carl Roth GmbH & Co. KG, Karlsruhe, Germany
Triton X-100	Sigma Aldrich Corp., St. Louis, MO, USA
Tropix® Emerald II	Applied Biosystems, ThermoFisher Scientific
Trypsin	PANBiotech GmbH, Aidenbach, Germany
UDP	Carl Roth GmbH & Co. KG, Karlsruhe, Gemany
Ultraglutamin / L-Glutamin	Gibco®, Life Technologies, ThermoFisher Scientific, Waltham, MA, USA

UTP	Sigma Aldrich Chemie GmbH, Taufkirchen, Germany

7.1.2 **Laboratory consumables**

Bacterial tubes, 4 ml	Sarstedt, Numbrecht, Germany
Biozym® steril pipette tips	Biozym Scientific GmbH, Hessisch Oldendorf, Germany
Combitips advanced® for Eppendorf	Eppendorf AG, Hamburg, Germany
Corning® 3340 CellBind 96 well plates, sterile	Sigma Aldrich Chemie GmbH, Taufkirchen, Germany
Cryo vials	Sarstedt, Numbrecht, Germany
Cuvettes for UV-Vis photometry	Ratiolab, Dreieich, Germany
Disposable petri-dishes (25 cm^2), sterile and disposable	Sarstedt, Numbrecht, Germany
Disposable pipettes 1, 5, 10 and 25 ml	Sarstedt, Nümbrecht, Germany
Falcons 15 ml and 50 ml	Corning Science Tanaulipas, Mexiko, USA
Falcons 15 ml, 120 x 17 mm	Sarstedt, Nümbrecht, Germany
Falcons 50 ml, 114 x 28 mm	Sarstedt, Nümbrecht, Germany
GF/B filters	Whatman GE Healthcare, Little Chalfont, UK
GF/C filters	Perkin-Elmer, Waltham, MA, USA
Megablocks	VWR International, Darmstadt, Germany
Microtubes 2 ml	Corning Science Tanaulipas, Mexiko, USA
Multipette® E3 5 ml, 2.5 ml and 1 ml	Eppendorf AG, Hamburg, Germany
NUNClon™ Delta Surface	Thermo Fisher Scientific, Rosenkilde, Denmark
Pipette tips 10, 100 and 1000 µl	Sarstedt, Nümbrecht, Germany
Pipette tips 5000 µl	Sarstedt, Nümbrecht, Germany
Reservoirs 50ml, nonsterile and sterile	VWR International GmbH, Darmstadt, Germany
Ritips® 0.5 ml, 1 ml, 2.5 ml and 5 ml	Ritter GmbH Medical, Schwabmünchen, Germany

Rotilabo® microtest plates, V bottom, 96 well	Carl Roth GmbH & Co. KG, Karlsruhe, Germany
Safe Seal® microtubes 1.5 and 5 ml	Eppendorf AG, Hamburg, Germany
Scinti-Vials, 3.5 ml, 10 ml	VWR International, Darmstadt, Germany;
Sterile, disposable pipettes 1, 5, 10 and 25 ml	Sarstedt, Numbrecht, Germany
TipOne filter tips sterile 10, 100 and 1000 µl	STARLAB GmbH, Hamburg, Germany
Tissue culture 96 well plates, sterile	Greiner Bio-one GmbH, Frickenhausen, Germany
Tissue Culture Flask 25, 75 und 175 cm^2	Sarstedt, Nümbrecht, Germany

7.1.3 **Laboratory devices**

Accu-Jet® pipetting controller	Brand, Wertheim, Germany
Analytical balance 440-47N (max. 2000 g)	Kern & Sohn GmbH, Balingen-Frommern, Germany
Analytical balance CP225D	Sartorius, Göttingen, Germany
Axiovert 25 microscope	Carl Zeiss AG, Oberkochen, Germany
Beckman centrifuge Avanti J-20 I	Beckman, Brea, CA, USA
Biometra® Thermocycler	Biometra GmbH, Göttingen, Germany
Brandel Harvester (48 and 96)	Brandel, Gaithersberg, MD, USA
Eppendorf Easypet®3 pipetting aid	Eppendorf AG, Hamburg, Germany
Eppendorf Multipette® E3/E3x	Eppendorf AG, Hamburg, Germany
Eppendorf Multipette® plus	Eppendorf AG, Hamburg, Germany
Eppendorf Research® plus pipettes 0.5-10 µl, 2-20 µl, 10-100 µl, 20-200 µl, 100-1000 µl and 500-5000 µl	Eppendorf AG, Hamburg, Germany
Eppendorf Xplorer® electronic pipettes 0.5-10 µl, 10-100 µl and30-300 µl	Eppendorf AG, Hamburg, Germany
FlexStation® 3 multi-mode microplate reader	Molecular Devices Corporation, Sunnyvale CA (USA)
Freezer -20°C	Bosch GmbH, Stuttgart, Germany

Fridge	Bosch GmbH, Stuttgart, Germany
Hettich centrifuge for falcons	Hettich, Tuttlingen, Germany
Hettich centrifuge for microliter tubes	Hettich, Tuttlingen, Germany
Hund microscope	Helmut Hund GmbH, Wetzlar
IKA® Vortex 3	IKA®-Werke GmbH & Co. KG, Staufen, Germany
Micro 200 centrifuge	Hettich Holding GmbH & Co.oHG, Kirchlengern, Germany
Mithras Multimode Microplate Reader LB 940	Berthold Technologies, Bad Wildbad, Germany
Neubauer Counting chamber 10 mm^2/ 0.0025 mm^2	Paul Marienfeld GmbH & Co. KG, Lauda Konigshofen, Germany
Neubauer Counting chamber 10 mm^2/0,0025 mm^2	Paul Marienfeld GmbH & Co. KG, Lauda Königshofen, Germany
NOVOstar® fluorescence plate reader	BMG Labtech GmbH, Ortenberg
NUNC® BIOFLOW workbench	Nunc GmbH & Co. KG, Langenselbold, Germany
NUNC® Safe flow 1.2 workbench	Nunc GmbH & Co. KG, Langenselbold, Germany
pH 197 measuring instrument	Wissenschaftlich-Technische Werkstätten GmbH, Weilheim
pH electrode SenTix 41	Wissenschaftlich-Technische Werkstätten GmbH, Weilheim
pH-Meter	Mettler-Toledo, Columbus, OH, USA
Purelab® Plus water purification plant	ELGA LabWater, Celle, Germany
RCT Basic hot plate stirrer	IKA Labortechnik, Staufen, Germany
Rotofix 32 centrifuge	Hettich, Tuttlingen, Germany
Sanyo Ultra Low Freezer -80°C	Ewald Innovationstechnik GmbH, Bad Nenndorf, Germany
Scaltec SBC 42 balance (min. 0,02 g, max. 120 g)	Scaltec Instruments GmbH, Göttingen, Germany
Shaker Thermostat	Elmi, Riga, Latvia.
Systec 3850 ELV autoclave	Systec, Wettenberg, Germany
Topcount NXT	Perkin-Elmer, Waltham, MA, USA
Tricarb 2900TR, luminescence Counter	Perkin-Elmer, Waltham, MA, USA
Ultrasonic bath	Bandelin electronic, Berlin, Germany

UltraTurrax	IKAR-Werke GmbH & Co. KG, Staufen, Germany
UV/Vis spectrometer	Beckman, Brea, CA, USA

7.2 **Methods**

7.2.1 **Molecular biology**

7.2.1.1 Polymerase Chain Reaction (PCR)

PCR primers were designed to either amplify plasmid DNA or introduce point mutations during site directed mutagenesis studies. The primers were synthesized at MWG Biotech, Ebersberg, Germany. The mastermix used for the PCR consisted of:

template DNA (~ 12 ng)	1 µL
forward primer (~ 10 pM)	2.5 µL
reverse primer (~ 10 pM)	2.5 µL
10X-pyrobest-buffer	2.5 µl
1.25 DMSO (sterile)	1.25 µl
dNTP mix (2.5 mM stock)	2.5 µl
PCR water to…	25 µL
pyrobest-polymerase	0.25 µL

The PCR was performed as follows: 30 s at 98 °C, 30 cycles each consisting of 10 s at 98 °C, 40 s at appropriate annealing temperature (T_m, ºC), and 5 min of primer extension at 72 °C. The final products were stored at 4 °C.

7.2.1.2 Agarose gel electrophoresis

Agarose gel from Biozym LE Agarose was dissolved by boiling in Tris acetated EDTA (TAE) buffer to yield a 1 % concentration. After cooling the clear solution to about 60 ºC, gel red staining solution from Biotium was added to a final concentration of 1: 10,000, mixed and the resulting solution transferred into a gel holder. The appropriate comb is inserted and the gel is allowed to set. The set gel was transferred into an electrophoresis chamber and submerged in 1x TAE buffer. The comb is then removed and the wells loaded with the prepared dna samples premixed with 6x loading dye. DNA markers (lambda, λ and phi, ϕ) were used as controls were necessary. Electrophoresis was carried out at 110 V for 45 min. DNA bands were visualized and analyzed

under exposure to UV light using the Geldoc from Bio-Rad. If the DNA was to be extracted, the bands of interest were cut out.

7.2.1.3 Preparation of competent bacteria

To a volume of 40 ml LB medium, 4 ml overnight culture (without antibiotics) of untransformed Top 10 *E. coli* bacteria was added and grown at 37 ºC, 220 rpm to an optical density (OD) of 0.5 at a wavelength of 550 nm. The culture was centrifuged at 1700 g, 4 °C for 20 min. The supernatant was then removed and the bacteria pellet was resuspended in 20 ml of sterile, ice cold 0.1 M $CaCl_2$ solution and incubated for 30 min on ice. The suspension was then centrifuged again (1700 x g, 4 °C, 20 min), the bacteria pellet resuspended in 2 ml of CaCl2 solution. Then 0.5 ml of sterile glycerol was added and of 100 µL aliquots were prepared and stored at –80 °C

7.2.1.4 Bacterial transformation

Competent 10 (E. *coli*) cells in Eppendorf tubes were thawed on ice for 30 min. The plasmid DNA (1 µL) of interest was added and the mixture was heat shocked at 42 ºC for 45s on a thermomixer. The tubes were place again on ice for 3-5 min. 1 ml of antibiotic-free LB medium was added and the mixture incubated at 37 ºC for 1 hr with shaking at 500 rpm on a Thermomixer. Afterwards, 500 µL of the mixture was added to 5 ml of ampicillin-selective LB medium and incubated at 37 ºC overnight. Alternatively, 250 µL to 500 µL of the transformed bacteria could be spread on an antibiotic selective agar-plate using a sterile Drigalski-spatula. After air drying, the agar plates are incubated inverted at 37 °C overnight for selection of single bacterial colonies.

7.2.1.5 Preparation of bacterial glycerol stocks

To preserve transformed bacterial clones carrying the desired plasmid DNA for a long time, 200 µL of sterile glycerol was added to 800 µL of overnight culture, mixed well and portions aliquoted. Aliquots were stored at either -20 °C or -80°C. To re-culture such bacteria stock, an aliquots is thawed and ice and using a sterile pipette tip, a small drop is added to the appropriate selective LB-medium under conditions. The suspension is then incubated overnight at 37 °C with agitation.

7.2.1.6 Enzyme restriction digest

All restriction ezymes for DNA digestion were bought from New England Biolabs (NEB). DpnI enzyme which recognizes methylated DNA (from bacteria) was used to cut methylated DNA templates used for PCR. Digestion of plasmid DNA to achieve sticky ends was performed with restriction endonucleases such as XhoI, MluI, EcoRI and HindIII. Two of these enzymes were only used together for double digestion when they have compatible buffers. The Cutsmart buffer from NEB is commonly useful in double digestion. The general protocol consists of a mixture 1 µL of enzymes to 1 µg (max) of DNA, 1 µL of 10X CutSmart buffer and making up the volume to 10 µL. The mixture is then incubated at 37 °C for 1 hr on a heat block. Controls consisted of samples lacking either the DNA plasmid of interest or the restriction enzymes.

7.2.1.7 Ligation

Ligation is the covalent bonding of two cohesive (sticky) ends of two DNA strands. We used the T4 DNA ligase from NEB for our ligation. 2 µL of the T4 DNA ligase buffer (10X) was added to a mixture of vector DNA and insert DNA (1:3 molar ratio) in total reaction volume of 20 µL nuclease-free water. 1 µL of the T4 DNA ligase is added and the mixture incubated at 16 °C overnight. The ligase was heat inactivated at 65°C for 10 min. The final mixture was used to transform bacteria which is incubated overnight on an agar plate for selection of single clones.

7.2.1.8 Single colony picking and growth

From an overnight culture on an agar plate, single transformed bacteria clones were randomly picked with pipette tips and transferred to 4 ml of ampicillin-selective LB-medium under sterile conditions. Extreme caution was take in order not to pick more than one colony into a single tube. The samples were appropriately labelled and incubated overnight (18 h) at 37 °C with shaking at 220 rpm. For DNA minipreps, 4 ml bacteria culture was used but for midipreps or larger scales DNA isolation, the bacterial colony were transferred into a 150 ml LB-medium containing heat-sterilized Erlenmeyer flask and shaken overnight at 37 °C.

7.2.1.9 Miniprep and midiprep

Miniprep and midiprep were used to purify small (up to 25 µg) and large (up to 1000 µg) amounts of DNA from bacteria culture using ZR Plasmid Miniprep™-Classic and, PureLink™ HiPure Plasmid Filter Purification Kits from Zymo Research Corp. and Invitrogen respectively. These experiments are dependent on alkaline lysis of bacteria cell wall for DNA extraction. The experiments were performed according to manufacturers' protocol. All DNA isolated from mini- or midipreps were validated by sequencing at GATC Biotech (Cologne, Germany).

7.2.1.10 DNA Recovery

This is to recover plasmid DNA from bands cut from agorose gel after electrophoresis. This was performed according to the manufacturer's protocol using Zymoclean™ Gel DNA Recovery Kit from Zymo Research Corp.

7.2.2 Computational methods

7.2.2.1 Homology modeling

Previously we reported on both homology models of the human $P2Y_2$ and $P2Y_4R$.[139,183] Both were based on the X-ray crystal structure of the human $P2Y_1R$ in complex with the nucleotide antagonist MRS2500 (PDB-ID: 4XNW).[125] The sequences for the human $P2Y_1$ (Uniprot-ID: P47900), $P2Y_2$ (P41231) and $P2Y_4R$ (P51582) were retrieved from the UniProt sequence database (http://www.uniprot.org). The sequences of the human $P2Y_2$ and $P2Y_4R$ were respectively aligned with that of the X-ray crystal structure of the human $P2Y_1R$ after removal of the engineered fusion partner rubredoxin between Lys247 and Pro253 in the ICL3 of the $P2Y_1R$ using Clustal Omega, with corresponding sequence similarities of 28% ($P2Y_2R$) and 32% ($P2Y_4R$).[260] With the human $P2Y_1R$ as template, we generated 500 models using the standard comparative modeling by the automodel class available for MODELLER.[244] To ensure correct tertiary protein structure we induced disulfide bridges between the highly conserved cysteines; for the $P2Y_2R$ the two disulfide bridges Cys25-Cys278 and Cys106-Cys183, and for the $P2Y_4R$ the two bridges Cys27-Cys278 and Cys108-Cys185. The generated models were analyzed and the best model of the human $P2Y_2$ and $P2Y_4R$ was used for molecular docking studies, based on the DOPE- and GA341-score, PROSA II

Z-score, and Ramachandran plots. The homology modelling and docking studies were performed by Alexander Neumann and Dr. Vigneshwaran Namasivayam.

7.2.2.2 Docking Studies

Prior to docking, the selected homology models of the human $P2Y_2$ and $P2Y_4R$ were prepared using the Protein Preparation Wizard module implemented in Schrödinger.[261,262] In the first step for protein preparation, we preprocessed the structure using the standard protocol; assigning bond orders, using the CCD database, adding hydrogens, creating disulfide bonds, generating het states using the implemented Epik module for prediction of the structure protonation state at pH 7.4. The second step involved H-bond assignment optimization by considering sample water orientations and using the PROPKA package to determine the protein protonation state at pH 7.4. In the third and final protein preparation step we performed restrained minimization, covering heavy atoms to 0.30 Å RMSD using the Liquid Simulations Version 3 (OPLS3) force-field.

Rotamers of side chains were examined using the rotamer library module implemented in Molecular Operating Environment (MOE 2014.09, Chemical Computing Group Inc., Montreal, Canada). The selected agonists and antagonists were docked into the putative orthosteric binding site of the receptor, based on previously published mutagenesis and docking data. Prior to docking all ligands were preprocessed using the Ligand Preparation module implemented in Schrödinger for proper protonation states. Docking was performed using Induced Fit Docking (IFD) and Glide as implemented in Schrödinger release 2016.[263] In the first step of IFD, Glide ligand docking were performed by removing the side chains of the amino acids in the selected binding pocket. In the second phase of docking, the Prime was applied to refine the nearby residues and optimize the side chains. In the final docking phase, the ligand was re-docked into all induced fit protein structures that were within 30 kcal⁄mol of the lowest energy structure, by using the Glide XP scoring function. The receptor center was specified on the position of the aspartic acid Asp185 ($P2Y_2R$) and Asp187 ($P2Y_4R$), a residue most likely involved in receptor activation as discussed below, to limit the docking to the putative orthosteric binding site. The putative orthosteric binding site was derived from the X-ray crystal structure of the human $P2Y_{12}R$ in complex with the orthosteric agonists 2MeSADP and 2MeSATP (PDB-IDs: 4PXZ, 4PY0).[85] Ligands with a size of 25.0 Å were docked. We take into account, that our docking procedure limits the investigated area to a specific area of the receptor and thus other binding sites for the studied ligands are conceivable.

During the docking simulations, the receptor and the ligands were selected flexibly. Following docking, the resulting poses of the best model was selected using the IFD scores and Prime Energy as representative values. The conformations of the docked ligands within an energy window of 2.5 kcal/mol were considered. For Glide docking, the following standard parameters were selected: receptor van der Waals scaling, 0.50; ligand van der Waals scaling, 0.50; a maximum of 20 poses per ligand. Residues within 5.0 Å of the ligand poses were refined, and the side chains were optimized. The best docking pose was selected based on the IFD score and Prime Energy values.

In the case of the MRS4062 (**14**) no conclusive docking position at the $P2Y_4R$ were achievable due to sterical hindrance by Tyr116. Therefore, we introduced a computational Y116A mutant to increase the space of the binding cavity and docked MRS4062 with the described procedure. The best docking pose was selected and the Y116A mutation was reverted. The Tyr116 rotamer with the lowest energy value was selected for the final docking pose.

During the docking of the anthraquinone antagonists, the highest-ranked protein complex of $P2Y_2R$ with PSB-16133 was considered a template for further dockings, since we expected the ligands to have a similar binding mode with the induced rotamers. Afterwards the ligands were redocked with the most reasonable docking pose using extra precision (XP) glide docking. The top scoring docking poses were evaluated with their scores and Prime Energy. The homology modelling and docking studies were performed by Alexander Neumann and Dr. Vigneshwaran Namasivayam.

7.2.3 **Site-directed mutagenesis**

The sequences of the human $P2Y_2$ ($hP2Y_2$) and the human $P2Y_4$ ($hP2Y_4$) receptors used in the site-directed mutagenesis studies were taken from the Uniprot database, with respective IDs **P41231** and **P51582**.[264] Whole plasmid recombinant polymerase chain reaction (PCR) using the appropriate primers was performed on puc19 vector to introduce the desired point mutations. The PCR was performed as described above. The PCR products were treated with DpnI enzymes to digest the template plasmid, then purified and used to transform competent *E. coli*. Each receptor (*wt* and mutant) cDNA was isolated from individual clones and recombinantly cloned into the mammalian retroviral vector pLXSN with the influenza hemagglutinin (HA) epitope engineered to the N-terminus. All DNA sequencing data were generated by GATC Biotech (Cologne, Germany).

7.2.4 **Retroviral transfection**

A day before transfection, 1.5 x 10^6 GP+envAM12 packaging cells were seeded into a small 25 cm^2 cell culture flask with a DMEM medium supplemented with 10 % FCS and 100 U/ml penicillin G and 100 µg/ml streptomycin. A few hours before the transfection, the medium was changed to 6.25 µl of DMEM medium containing only 10 % FCS. Transfection involves the delivery of a total of 10 µg DNA – 6.25 µg of receptor-containing plasmid-DNA and 3.75 µg of the vesicular stomatitis virus G protein (VSV-G) - into the packaging cells using Lipofectamine 2000. After incubating the transfected cells at 37 °C for 12 -15 h, the medium was changed to 3 ml DMEM supplemented with 10 % FCS, 100 U/ml penicillin G, 100 µg/ml streptomycin and 5 mM sterile aqueous solution of sodium butyrate. The cells were then incubated at 32°C with 5 % CO_2 for 48 h during which the viruses with integrated receptor DNA are cultivated. The viruses were harvested after 48 h and used to infect *wt* 1321N1 astrocytoma cells. About 24 h before infection 5 x 10^5 1321N1 astrocytoma cells were seeded in a 25 cm^2 in DMEM medium with 10 % FCS, 100 U/ml penicillin G and 100 µg/ml streptomycin and incubated at 37 °C. On the day of infection, the medium is removed from the astrocytoma cells and discarded. The medium (containing viruses) were removed from the GP+envAM12 cells, filtered through a 0.22 µm filter onto the astrocytoma cells and fortified with 6 µl sterilized polybrene solution (4 mg/ml in water). The astrocytoma cells were then incubated at 37 °C for 2½ h after which the medium was changed for 5 ml of DMEM medium containing 10 % FCS, 100 U/ml penicillin G and 100 µg/ml streptomycin. The medium was replaced after 48 h of incubation to DMEM with 10 % FCS, 100 U/ml penicillin G, 100 µg/ml streptomycin and 800 µg/ml G418 for selection of cells expressing the receptor.

7.2.5 **Cell culturing**

The 1321N1 astrocytoma cell lines stably transfected with human $P2Y_1R$, $P2Y_2R$, $P2Y_4R$ and $P2Y_6Rs$ used for screening were received from Dr. Muhammad Rafehi. These cell lines and the untransfected 1321N1 cell lines were cultured in in DMEM supplemented with 1% ultraglutamine, 10% FCS, 100 U/mL penicillin G, and 100 µg/mL streptomycin.

Astrocytoma cell lines stably transfected with either the P2Y receptor wild-types or receptor mutants used for site-directed mutagenesis studies were cultured in the DMEM described above

but fortified with 800 µg/mL Geneticin (G418). The GP+envAM12 packaging cells were maintained in HXM media containing DMEM supplemented with 1% ultraglutamine, 10% FCS, 100 U/mL penicillin G, 100 µg/mL streptomycin, 15 µg/mL hypoxanthine, 250 µg/ mL xanthine, 25 µg/mL mycophenolic acid, and 200 µg/mL hygromycin B.

CHO-K1 cells stably transfected with human $P2Y_2R$ and $P2Y_4Rs$ used in β-arrestin recruitment assays were received from Dr. Aliaa Abdelrahman and Dr. Muhammad Rafehi respectively. These cell lines were cultured in Opti-Mem medium supplemented with 2% FCS, 100 U/ml Penicillin, 100 µg/ml Streptomycin, 800 µg/ml Geneticin and 300 µg Hygromycin. All cells were grown at 37 °C in 96 % humidified air and 5-10 % CO_2 concentration.

7.2.6 **Cell surface enzyme-linked immunosorbent assay (ELISA)**

The 1321N1 astrocytoma cell-line expressing the various wt or mutant receptors were seeded in duplicates at a density of 150,000 cells per well in a 12-well plate 24 h before the assay. The medium was removed and the cells were washed with PBS. 500 µL of 1% bovine serum albumin (BSA) in PBS was added for 5 min to block nonspecific cell surface binding. Next, 300 µL of a 1 : 1000 dilution of the HA-specific mouse monoclonal antibody (HA.11) solution in DMEM containing 1 % BSA was added to each well and the mixture was incubated at room temperature (rt) for 1 h. The cells were washed three times with 500 µL of PBS, fixed with 500 µL of 4 % paraformaldehyde (PFA) in PBS, pH 7.3, washed again with 500 µL of PBS and blocked with 500 µL of 1 % BSA in PBS for 10 min. The cells were then incubated at rt for 1 h with 300 µL of peroxidase-conjugated goat anti-mouse IgG antibody of a 1:2500 dilution ratio in DMEM supplemented with 1 % BSA. After further washing with 500 µL PBS for four times, the cells were incubated with 300 µl of the substrate, ABTS solution, for 45 min at rt. Finally, 170 µL aliquots of the supernatant ABTS solution was then transferred into 96-well plate, and the absorbance was measured at 405 nm by a PHERAstar microplate reader (BMG Laboratory Technologies, Offenburg, Germany). The whole assay, except for the addition of antibodies and the substrate reaction, was performed on ice and with freshly prepared cold buffers.

7.2.7 **Pharmacological assays**

7.2.7.1 Measurement of intracellular calcium concentrations

About 16 - 24 h before the assay, the growth medium was removed from a T175 ml flask with approximately 80–90 % cell confluency. The cells were washed with phosphate-buffered saline (PBS containing 137 mM NaCl, 2.7 mM KCl, 4.3 mM Na_2HPO_4, and 1.47 mM KH_2PO_4, at pH 7.3). The cells were then detached with trypsin-EDTA and re-suspended in supplemented DMEM (see above). To each well of the sterile black 96-well polystyrene plate with a transparent flat bottom (Corning 3340), about 60,000 cells in 200 µL DMEM growth medium were added and incubated at 37 °C, 96 % humidity and 10 % CO_2. Prior to the assay, the growth medium was removed completely and the adherent cells were incubated with 40 µl of loading dye, consisting of 15 µL fluo-4 acetoxymethyl ester (1 mM solution in dimethyl sulfoxide, DMSO) and 15 µL Pluronic F-127 (25 % w/v in DMSO) in 4970 µL Hank's Balanced Salt Solution (HBSS) buffer, in each well, for 1 h. After incubation, the excess dye was removed, and cells were further incubated in HBSS buffer at rt for 30 min before the addition of agonists. For assessment of antagonist potencies, the cells were pre-incubated with the antagonists in HBSS buffer during the 30 min incubation before addition of the agonist at its EC_{80} concentration. All dilutions used for dose-response curves were performed on a log-scale. The final concentration in each well was 200 µL, and final DMSO concentration was maintained at 0.5 %. The measurement of fluorescence intensities was performed on a Novostar plate reader (BMG LabTechnologies, Offenburg, Germany) at 520 nm for 30 s at 0.4 s intervals after excitation at 485 nm. For all assays 100 µM carbachol, inducing intracellular Ca^{2+} release by activating the natively expressed G_q protein-coupled muscarinic M_3 receptor (M_3R) of 132N1 astrocytoma cells, was used as a positive control. The maximal carbachol response was set as 100 % and employed for normalization of all other responses.

7.2.7.2 β-Arrestin recruitment assays

About 18-24 h before the assay, confluent CHO-K1 cells with the receptor of interest were harvested with dissociation buffer [500 ml PBS, 10 mM D-glucose and 2 mM EDTA] into a 15 ml falcon tube and centrifuged at 2000g for 5 min. After removal of the supernatant, the cells were re-suspended in culture medium, seeded in a 96-well plate at 20,000 cells/90 µL/well and incubated overnight (37 ºC, 5 % CO_2). At the time of assay, cells were incubated with 5 µL of antagonists

pre-diluted in Opti-Mem (without supplements) to yield the desired final concentration and incubated as 37 ºC for 60 min. The final DMSO concentration did not exceed 1%. 5 µL of agonist (diluted in Opti-Mem) is then added to make up the final assay volume to 100 µL and incubated at rt. for 90 min. For agonist dose response curves the addition of antagonists is skipped. After the 90 min incubation, 50 µL of the detection reagent, in accordance to the DiscoverX PathHunter® assay system, is added and further incubated for 60 min at rt. after which chemiluminescence is measured using the Mitras from Berthold. The detection reagent consists of 220 Galacton Star®, 1100 µL of Emerald II® and 4150 µL of lysis buffer.

7.2.7.3 Cyclic AMP (cAMP) assays

The cyclic AMP assays were performed at GPR84 receptor as previously described.[76] About 24 h before the assay, CHO-K1 cells stably transfected with GPR84 cells were seeded into a 24-well plate at a density of 200000 cells/well. The culture medium was removed and the cells were washed and incubated with 190 µL/well HBSS buffer [NaCl (13 mM), HEPES (20 mM), glucose (5.5 mM), KCl (5.4 mM), $NaHCO_3$ (4.2 mM), $CaCl_2 \times 2\ H2O$ (1.25 mM), $MgSO_4$ (0.8 mM), $MgCl_2$ (1 mM), KH_2PO_4 (0.44 mM), and Na_2HPO4 (0.34 mM) dissolved in deionized autoclaved water, pH 7.4] for 2 h. Afterwards, the cAMP phosphodiesterase inhibitor Ro-20-1724 (4-(3-butoxy-4-methoxybenzyl)-2-imodazolidinone), the test compounds (antagonists and/or agonists) and forskolin, each dissolved in 10 % DMSO/90 % sterile HBSS (pH 7.4), were added in a stepwise manner to yield a final DMSO concentration of 1.9 %. First, the suspension was incubated for 10 min after the addition 20 µL of Ro-20-1724 (final concentration of 40 µM), then for 5 min after the addition of test compounds (antagonists were added at the desired concentration 20 min before addition of agonists) and lastly for another 15 min after adding forskolin (final concentration of 10 µM) in the presence or absence (controls) of test compounds. The supernatant is then removed and the cells are lyzed with 500 µL of hot lysis buffer (100 °C; 4 mM EDTA, 0.01% Triton X-100). This stops the accumulation of celluar cAMP. To 50 µL aliquouts of cell suspension in 2.5 mLeppindorf tubes, 30 µL [^{3}H]cAMP and 40 µL cAMP-binding protein (50 µg/well) obtained from bovine adrenal cortex, were added and the suspension incubated on ice for 1 h. Using a Brandel 48-channel cell harvester, the bound radioligand is separated from the free radioligand by rapid filtration through GF/B glass fiber filters. After incubating the filters with 3 ml scintillation cocktail, radioactivity is measured using the liquid scintillation counter (TRICARB 2900TR, Packard/Perkin-Elmer). The forskolin-induced increase in cAMP concentration in the presence of

agonists was expressed as percentage of the response to forskolin in the absence of agonists (% of control). Three independent experiments were performed, each in duplicate by Katharina Sylvester and Dr. Meryem Koese.

7.2.7.4 Radioligand binding assays at CB_1 and CB_2 recepters and at GPR84

Competition binding assays were performed using [^{3}H](-)-cis-3-[2-hydroxy-4-(1,1-dimethylheptyl)phenyl]-trans-4-(3-hydroxypropyl)cyclohexanol ([^{3}H] (CP55,940)) in concentration at 0.1 nM and 2nM [^{3}H]PSB-1584 as hot ligands at the cannabinoid (CB_1 and CB_2) receptors and at GPR84 respectively. Cell membrane preparations expressing either human CB_1, CB_2 or GPR84 receptors were obtained as previously described.[265] The test compounds were screened at 5 µM at CB_1 and CB_2, but at 10 µM at GPR84. The final DMSO concentration did not exceed 2.5 %.

Binding was performed using 96-well megablocks with each well containing 15 µL of the test compound in DMSO, 60 µL of the hot ligand in assay buffer, and 60 µL of receptor membrane preparation to 465 µL of assay buffer. The assay buffer consists of 50 mM TRIS, 3 mM MgCl2, 0.1% BSA in water maintained at pH 7.4. Total binding was determined in the absence of the test compound with 2.5 % DMSO whilst non-specific bibding was determined using the unlabeled Cp55,940 and PSB1584. The mixture was then incubated at rt for 120 min, after which it was rapidly filtered using a 96-channel harvester through GF/C glass fiber filters that were presoaked with 0.3% aqueous polyethyleneimine solution for 30 minutes. Using ice cold assay buffer, the filters were washed three times and then dried at 50 ºC for 90 min. Subsequently, the filters were incubated in 50 µL scintillation cocktail for 10 hr after which radioactivity was measured in a Topcount® Microplate Scintillation and Luminescence Counter. Subsequently, the data were analyzed using GraphPad Prism 4 (San Diego, CA, USA). For test compounds with > 50 %, full inhibition curves were used to determine the K_i. These assays were performed at the cannabinoid receptors by Andhika B. Mahardika and Dr. Clara Schroeder, and at the GPR84 receptor by Katharina Sylvester and Dr. Meryem Koese.

7.2.7.5 Data Analysis

All data from pharmacological assays were analyzed using Microsoft® Excel and Graphpad® Prism 4.02. Additionally, data from screening compound libraries were managed with MarvinView

v15.2.23 and Instant Jchem v5.3.4 from ChemAxon Kft and Informatic Matters Ltd., Budapest, Hungary For analysis of DNA sequences, we used software DNATrans v2.3.0.1 (Pharmazeutische Chemie I, Bonn, Germany) and Chromas Lite version 2.01 (Technelysium Pty Ltd, Australia).

8 References

(1) Rosenbaum, D. M.; Rasmussen, S. G. F.; Kobilka, B. K. The structure and function of G-protein-coupled receptors. *Nature* **2014**, *459*, 356–363.

(2) Hill, S. J. G-protein-coupled receptors: past, present and future. *Br. J. Pharmacol.* **2006**, *147*, 27–37.

(3) Albert, A. D.; Litman, B. J. Independent structural domains in the membrane protein bovine rhodopsin. *Biochemistry* **1978**, *17*, 3893–3900.

(4) Hargrave, P. A.; Mcdowell, J. H.; Curtis, D. R.; Wang, J. K.; Juszczak, E.; Fong, S.-L.; Rao, J. K. M.; Argos, P. The structure of bovine rhodopsin. *Biophys Struct Mech* **1983**, *9*, 235–244.

(5) Fredriksson, R. The G protein-coupled receptors in the human genome form five main families. phylogenetic analysis, paralogon groups, and fingerprints. *Mol. Pharmacol.* **2003**, *63*, 1256–1272.

(6) Santos, R.; Ursu, O.; Gaulton, A.; Bento, A. P.; Donadi, R. S.; Bologa, C. G.; Karlsson, A.; Al-Lazikani, B.; Hersey, A.; Oprea, T. I.; Overington, J. P. A comprehensive map of molecular drug targets. *Nat. Rev. Drug Discov.* **2016**, *16*, 19–34.

(7) Hauser, A. S.; Attwood, M. M.; Rask-Andersen, M.; Schiöth, H. B.; Gloriam, D. E. Trends in GPCR drug discovery: new agents, targets and indications. *Nat. Rev. Drug Discov.* **2017**, *16*, 829–842.

(8) Szekeres, P. G. Functional assays for identifying ligands at orphan G protein-coupled receptors. *Recept. Channels* **2002**, *8*, 297–308.

(9) Zhang, R.; Xie, X. Tools for GPCR drug discovery. *Acta Pharmacol. Sin.* **2012**, *33*, 372–384.

(10) Serezani, C. H.; Ballinger, M. N.; Aronoff, D. M.; Peters-Golden, M. Cyclic AMP: master regulator of innate immune cell function. *Am. J. Respir. Cell Mol. Biol.* **2008**, *39*, 127–132.

(11) Milligan, G.; Kostenis, E. Heterotrimeric G-proteins: a short history. *Br. J. Pharmacol.* **2006**, *147*.

(12) Siehler, S. Cell-based assays in GPCR drug discovery. *Biotechnol. J.* **2008**, *3*, 471–483.

(13) Smrcka, A. V. G protein βγ subunits: central mediators of G protein-coupled receptor signaling. *Cellular and molecular life sciences : CMLS*. 2008, pp 2191–2214.

(14) Neptune, E. R.; Bourne, H. R. Receptors induce chemotaxis by releasing the beta-gamma

subunit of G_i, not by activating G_q or G_s. *Proc. Natl. Acad. Sci.* **1997**, *94*, 14489–14494.

(15) Ma, Q.; Ye, L.; Liu, H.; Shi, Y.; Zhou, N. An overview of Ca^{2+} mobilization assays in GPCR drug discovery. *Expert Opin. Drug Discov*. **2017**, *12*, 511–523.

(16) Violin, J. D.; Lefkowitz, R. J. β-arrestin-biased ligands at seven-transmembrane receptors. *Trends Pharmacol. Sci.* **2007**, *28*, 416–422.

(17) Oakley, R. H.; Laporte, S. A.; Holt, J. A.; Caron, M. G.; Barak, L. S. Differential affinities of visual arrestin, β-arrestin1, and β-arrestin2 for G protein-coupled receptors delineate two major classes of receptors. *J. Biol. Chem*. **2000**, *275*, 17201–17210.

(18) Vincent, F.; Loria, P.; Pregel, M.; Stanton, R.; Kitching, L.; Nocka, K.; Doyonnas, R.; Steppan, C.; Gilbert, A.; Schroeter, T.; Peakman, M. C. Developing predictive assays: the phenotypic screening "rule of 3." *Sci. Transl. Med.* **2015**, *7*, 1–5.

(19) Sams-Dodd, F. Target-based drug discovery: is something wrong? *Drug Discov. Today* **2005**, *10*, 139–147.

(20) Aparoy, P.; Reddy, K. K.; Reddanna, P. Structure and ligand based drug design strategies in the development of novel 5-lox inhibitors. *Curr Med Chem* **2012**, *19*, 3763–3778.

(21) Entzeroth, M.; Flotow, H.; Condron, P. Overview of high-throughput screening. *Curr. Protoc. Pharmacol.* **2009**, No. SUPPL. 44, 1–27.

(22) Eglen, R. M. Functional G protein-coupled receptor assays for primary and secondary screening. *Comb. Chem. High Throughput Screen.* **2005**, *8*, 311–318.

(23) Thomsen, W.; Frazer, J.; Unett, D. Functional assays for screening GPCR targets. *Curr. Opin. Biotechnol.* **2005**, *16*, 655–665.

(24) Chen, L.; Jin, L.; Zhou, N. An update of novel screening methods for GPCR in drug discovery. *Expert Opin. Drug Discov*. **2012**, *7*, 791–806.

(25) Trinquet, E.; Bouhelal, R.; Dietz, M. Monitoring G_q-coupled receptor response through inositol phosphate quantification with the IP-one assay. *Expert Opin. Drug Discov*. **2011**, *6*, 981–994.

(26) Hill, S. J.; Baker, J. G.; Rees, S. Reporter-gene systems for the study of G-protein-coupled receptors. *Curr. Opin. Pharmacol.* **2001**, *1*, 526–532.

(27) Degorce, F. HTRF: a technology tailored for drug discovery - a review of theoretical aspects and recent applications. *Curr. Chem. Genomics* **2009**, *3*, 22–32.

(28) Eglen, R. M. An overview of high throughput screening at G protein coupled receptors. *Front. Drug Des. Discov*. **2005**, *1*, 97–111.

(29) Bootman, M. D.; Rietdorf, K.; Collins, T.; Walker, S.; Sanderson, M. Ca^{2+}-sensitive fluorescent dyes and intracellular Ca^{2+} imaging. *Cold Spring Harb. Protoc.* **2013**, *8*, 83–99.

(30) Zhu, T.; Fang, L. Y.; Xie, X. Development of a universal high-throughput calcium assay for G protein-coupled receptors with promiscuous G-protein $G\alpha_{15/16}$. *Acta Pharmacol. Sin.* **2008**, *29*, 507–516.

(31) Woszczek, G.; Fuerst, E. Ca^{2+} mobilization assays in GPCR drug discovery. *Methods Mol. Biol.* **2015**, *1272*, 79–89.

(32) Miret, J. J.; Zhang, J.; Min, H.; Lewis, K.; Roth, M.; Charlton, M.; Bauer, P. H. Multiplexed G-protein-coupled receptor Ca^{2+} flux assays for high-throughput screening. *J. Biomol. Screen.* **2005**, *10*, 780–787.

(33) Brini, M.; Marsault, R.; Bastianutto, C.; Alvarez, J.; Pozzan, T.; Rizzuto, R. Transfected aequorin in the measurement of cytosolic Ca^{2+} concentration [Ca^{2+}]. a critical evaluation. *Journal of Biological Chemistry*. 1995, pp 9896–9903.

(34) Bovolenta, S.; Foti, M.; Lohmer, S.; Corazza, S. Development of a Ca^{2+}-activated photoprotein, Photina®, and its application to high-throughput screening. *J. Biomol. Screen.* **2007**, *12*, 694–704.

(35) Le Poul, E.; Hisada, S.; Mizuguchi, Y.; Dupriez, V. J.; Burgeon, E.; Detheux, M. Adaptation of aequorin functional assay to high throughput screening. *J. Biomol. Screen.* **2002**, *7*, 57–65.

(36) Stables, J.; Green, A.; Marshall, F.; Fraser, N.; Knight, E.; Sautel, M.; Milligan, G.; Lee, M.; Rees, S. A bioluminescent assay for agonist activity at potentially any G protein-coupled receptor. *Anal. Biochem.* **1997**, *252*, 115–126.

(37) Laptenok, S. P.; Van Stokkum, I. H. M.; Borst, J. W.; Van Oort, B.; Visser, A. J. W. G.; Van Amerongen, H. Disentangling picosecond events that complicate the quantitative use of the calcium sensor YC3.60. *J. Phys. Chem. B* **2012**, *116*, 3013–3020.

(38) Qian, Y.; Rancic, V.; Wu, J.; Ballanyi, K.; Campbell, R. E. A bioluminescent Ca^{2+} indicator based on a topological variant of GCaMP6s. *ChemBioChem* **2018**.

(39) Williams, C. cAMP detection methods in hts: selecting the best from the rest. *Nat. Rev. Drug Discov.* **2004**, *3*, 125–135.

(40) Audinot, V.; Beauverger, P.; Lahaye, C.; Suply, T.; Rodriguez, M.; Ouvry, C.; Lamamy, V.; Imbert, J.; Rique, H.; Nahon, J. L.; Galizzi, J. P.; Canet, E.; Levens, N.; Fauchère, J. L.; Boutin, J. A. Structure-activity relationship studies of melanin-concentrating hormone

(MCH)-related peptide ligands at SLC-1, the human MCH receptor. *J. Biol. Chem*. **2001**, *276*, 13554–13562.

(41) Kariv, I.; Stevens, M. E.; Behrens, D. L.; Oldenburg, K. R. High throughput quantitation of cAMP production mediated by activation of seven transmembrane domain receptors. *J. Biomol. Screen.* **1999**, *4*, 27–32.

(42) Kahl, S. D.; Felder, C. C. Scintillation proximity assay. *Curr. Protoc. Neurosci.* **2005**, *Chapter 7*, Unit 7.15.

(43) Prystay, L.; Gagné, A.; Kasila, P.; Yeh, L. A.; Banks, P. Homogeneous cell-based fluorescence polarization assay for the direct detection of cAMP. *J. Biomol. Screen.* **2001**, *6*, 75–82.

(44) Allen, M.; Hall, D.; Collins, B.; Moore, K. A homogeneous high throughput nonradioactive method for measurement of functional activity of G_s-coupled receptors in membranes. *J. Biomol. Screen.* **2002**, *7*, 35–44.

(45) Hunter, M. R.; Glass, M. Increasing the flexibility of the LANCE cAMP detection kit. *J. Pharmacol. Toxicol. Methods* **2015**, *71*, 42–45.

(46) Gabriel, D.; Vernier, M.; Pfeifer, M. J.; Dasen, B.; Tenaillon, L.; Bouhelal, R. High throughput screening technologies for direct cyclic AMP measurement. *Assay Drug Dev. Technol.* **2003**, *1*, 291–303.

(47) Zhao, X.; Jones, A.; Olson, K. R.; Peng, K.; Wehrman, T.; Park, A.; Mallari, R.; Nebalasca, D.; Young, S. W.; Xiao, S. H. A homogeneous enzyme fragment complementation-based β-arrestin translocation assay for high-throughput screening of G-protein-coupled receptors. *J. Biomol. Screen.* **2008**, *13*, 737–747.

(48) Neumann, S.; Eliseeva, E.; McCoy, J. G.; Napolitano, G.; Giuliani, C.; Monaco, F.; Huang, W.; Gershengorn, M. C. A new small-molecule antagonist inhibits Graves' disease antibody activation of the TSH receptor. *J. Clin. Endocrinol. Metab.* **2011**, *96*, 548–554.

(49) Avanzato, D.; Genova, T.; Fiorio Pla, A.; Bernardini, M.; Bianco, S.; Bussolati, B.; Mancardi, D.; Giraudo, E.; Maione, F.; Cassoni, P.; Castellano, I.; Munaron, L. Activation of P2X7 and $P2Y_{11}$ purinergic receptors inhibits migration and normalizes tumor-derived endothelial cells via cAMP signaling. *Sci. Rep.* **2016**, *6*, 1–15.

(50) Tomankova, H.; Valuskova, P.; Varejkova, E.; Rotkova, J.; Benes, J.; Myslivecek, J. The M_2 muscarinic receptors are essential for signaling in the heart left ventricle during restraint stress in mice. *Stress* **2015**, *18*, 208–220.

(51) Reinscheid, R. K.; Kim, J.; Zeng, J.; Civelli, O. High-throughput real-time monitoring of G_s-coupled receptor activation in intact cells using cyclic nucleotide-gated channels. *Eur. J. Pharmacol.* **2003**, *478*, 27–34.

(52) Visegrády, A.; Boros, A.; Némethy, Z.; Kiss, B.; Keseru, G. M. Application of the BD ACTOne™ technology for the high-throughput screening of G_s-coupled receptor antagonists. *J. Biomol. Screen.* **2007**, *12*, 1068–1073.

(53) Golla, R.; Seethala, R. A homogeneous enzyme fragment complementation cyclic AMP screen for GPCR agonists. *J. Biomol. Screen.* **2002**, *7*, 515–525.

(54) Buccioni, M.; Marucci, G.; Ben, D. D.; Giacobbe, D.; Lambertucci, C.; Soverchia, L.; Thomas, A.; Volpini, R.; Cristalli, G. Innovative functional cAMP assay for studying G protein-coupled receptors: application to the pharmacological characterization of GPR17. *Purinergic Signal.* **2011**, *7*, 463–468.

(55) Goulding, J.; May, L. T.; Hill, S. J. Characterisation of endogenous A_{2A} and A_{2B} receptor-mediated cyclic AMP responses in HEK 293 cells using the GloSensor™ biosensor: evidence for an allosteric mechanism of action for the A_{2B}-selective antagonist PSB 603. *Biochem. Pharmacol.* **2018**, *147*, 55–66.

(56) Pantel, J.; Williams, S. Y.; Mi, D.; Sebag, J.; Corbin, J. D.; Weaver, C. D.; Cone, R. D. Development of a high throughput screen for allosteric modulators of melanocortin-4 receptor signaling using a real time cAMP assay. *Eur. J. Pharmacol.* **2011**, *660*, 139–147.

(57) Gilissen, J.; Geubelle, P.; Dupuis, N.; Laschet, C.; Pirotte, B.; Hanson, J. Forskolin-free cAMP assay for G_i-coupled receptors. *Biochem. Pharmacol.* **2015**, *98*, 381–391.

(58) Barak, L. S.; Salahpour, A.; Zhang, X.; Masri, B.; Sotnikova, T. D.; Ramsey, A. J.; Violin, J. D.; Lefkowitz, R. J.; Caron, M. G.; Gainetdinov, R. R. Pharmacological characterization of membrane-expressed human trace amine-associated receptor 1 (TAAR1) by a bioluminescence resonance energy transfer cAMP biosensor. *Mol. Pharmacol.* **2008**, *74*, 585–594.

(59) Violin, J. D.; DiPilato, L. M.; Yildirim, N.; Elston, T. C.; Zhang, J.; Lefkowitz, R. J. B2-adrenergic receptor signaling and desensitization elucidated by quantitative modeling of real time cAMP dynamics. *J. Biol. Chem.* **2008**, *283*, 2949–2961.

(60) DiPilato, L. M.; Cheng, X.; Zhang, J. Fluorescent indicators of cAMP and Epac activation reveal differential dynamics of cAMP signaling within discrete subcellular compartments. *Proc. Natl. Acad. Sci.* **2004**, *101*, 16513–16518.

(61) Southern, C.; Cook, J. M.; Neetoo-Isseljee, Z.; Taylor, D. L.; Kettleborough, C. A.; Merritt, A.; Bassoni, D. L.; Raab, W. J.; Quinn, E.; Wehrman, T. S.; Davenport, A. P.; Brown, A. J.; Green, A.; Wigglesworth, M. J.; Rees, S. Screening β-arrestin recruitment for the identification of natural ligands for orphan G-protein–coupled receptors. *J. Biomol. Screen.* **2013**, *18*, 599–609.

(62) Oakley, R. H.; Hudson, C. C.; Cruickshank, R. D.; Meyers, D. M.; Payne Jr., R. E.; Rhem, S. M.; Loomis, C. R. The cellular distribution of fluorescently labeled arrestins provides a robust, sensitive, and universal assay for screening G protein-coupled receptors. *Assay Drug Dev Technol* **2002**, *1*, 21–30.

(63) Garippa, R. J.; Hoffman, A. F.; Gradl, G.; Kirsch, A. High-throughput confocal microscopy for β-arrestin-green fluorescent protein translocation G protein-coupled receptor assays using the Evotec Opera. *Methods Enzymol.* **2006**, *414*, 99–120.

(64) Oakley, R. H.; Hudson, C. C.; Sjaastad, M. D.; Loomis, C. R. The ligand-independent translocation assay: an enabling technology for screening orphan G protein-coupled receptors by arrestin recruitment. *Methods Enzymol.* **2006**, *414*, 50–63.

(65) Kocan, M.; See, H. B.; Seeber, R. M.; Eidne, K. A.; Pfleger, K. D. G. Demonstration of improvements to the bioluminescence resonance energy transfer (BRET) technology for the monitoring of G protein-coupled receptors in live cells. *J. Biomol. Screen.* **2008**, *13*, 888–898.

(66) Kamal, M.; Marquez, M.; Vauthier, V.; Leloire, A.; Froguel, P.; Jockers, R. Improved donor/acceptor BRET couples for monitoring β-arrestin recruitment to G protein-coupled receptors. *Biotechnol. J.* **2009**, *4*, 1337–1344.

(67) Hamdan, F. F.; Audet, M.; Garneau, P.; Pelletier, J.; Bouvier, M. High-throughput screening of G protein-coupled receptor antagonists using a bioluminescence resonance energy transfer 1-based β-arrestin2 recruitment assay. *J. Biomol. Screen.* **2005**, *10*, 463–475.

(68) Vrecl, M.; Jorgensen, R.; Pogačnik, A.; Heding, A. Development of a BRET2 screening assay using β-arrestin 2 mutants. *J. Biomol. Screen.* **2004**, *9*, 322–333.

(69) Hanson, B. J.; Wetter, J.; Bercher, M. R.; Kopp, L.; Fuerstenau-Sharp, M.; Vedvik, K. L.; Zielinski, T.; Doucette, C.; Whitney, P. J.; Revankar, C. A homogeneous fluorescent live-cell assay for measuring 7-transmembrane receptor activity and agonist functional selectivity through beta-arrestin recruitment. *J. Biomol. Screen.* **2009**, *14*, 798–810.

(70) Kunapuli, P.; Ransom, R.; Murphy, K. L.; Pettibone, D.; Kerby, J.; Grimwood, S.; Zuck, P.;

Hodder, P.; Lacson, R.; Hoffman, I.; Inglese, J.; Strulovici, B. Development of an intact cell reporter gene β-lactamase assay for G protein-coupled receptors for high-throughput screening. *Anal. Biochem*. **2003**, *314*, 16–29.

(71) Doucette, C.; Vedvik, K.; Koepnick, E.; Bergsma, A.; Thomson, B.; Turek-Etienne, T. C. Kappa opioid receptor screen with the tangog™ β-arrestin recruitment technology and characterization of hits with second-messenger assays. *J. Biomol. Screen.* **2009**, *14*, 381–394.

(72) Iwai, H.; Züger, S.; Jin, J.; Tam, P. H. Highly efficient protein trans-splicing by a naturally split DnaE intein from Nostoc punctiforme. *FEBS Lett*. **2006**, *580*, 1853–1858.

(73) Zhang, Y.; Yang, W.; Chen, L.; Shi, Y.; Li, G.; Zhou, N. Development of a novel DnaE intein-based assay for quantitative analysis of G-protein-coupled receptor internalization. *Anal. Biochem*. **2011**, *417*, 65–72.

(74) Kim, S. B.; Ozawa, T.; Watanabe, S.; Umezawa, Y. High-throughput sensing and noninvasive imaging of protein nuclear transport by using reconstitution of split Renilla luciferase. *Proc. Natl. Acad. Sci.* **2004**, *101*, 11542–11547.

(75) Zhang, Q.; Zheng, Y.-W.; Coughlin, S. R.; Shu, X. A rapid fluorogenic GPCR-β-arrestin interaction assay. *Protein Sci.* **2018**, *27*, 874–879.

(76) Pillaiyar, T.; Köse, M.; Sylvester, K.; Weighardt, H.; Thimm, D.; Borges, G.; Förster, I.; Von Kügelgen, I.; Müller, C. E. Diindolylmethane derivatives: potent agonists of the immunostimulatory orphan G protein-coupled receptor GPR84. *J. Med. Chem*. **2017**, *60*, 3636–3655.

(77) Schoeder, C. T.; Kaleta, M.; Mahardhika, A. B.; Olejarz-maciej, A.; Łażewska, D.; Kieć-kononowicz, K.; Müller, C. E. Structure-activity relationships of imidazothiazinones and analogs as antagonists of the cannabinoid-activated orphan G protein-coupled receptor GPR18. *Eur. J. Med. Chem*. **2018**, *155*.

(78) Burnstock, G. Purinergic receptors. *J. theor. Biol.* **1976**, *62*, 491–503.

(79) Jacobson, K. a.; Boeynaems, J. M. P2Y nucleotide receptors: promise of therapeutic applications. *Drug Discov. Today* **2010**, *15*, 570–578.

(80) Brunschweiger, A.; Müller, C. E. P2 receptors activated by uracil nucleotides - an update. **2006**, 763–771.

(81) von Kugelgen, I.; Harden, T. K. *Molecular Pharmacology, Physiology, and Structure of the P2Y Receptors*; 2011; Vol. 61.

(82) Pérez-Sen, R.; Gómez-Villafuertes, R.; Ortega, F.; Gualix, J.; Delicado, E. G.; Miras-Portugal, M. T. An update on $P2Y_{13}$ receptor signalling and function. In *Advances in experimental medicine and biology*; 2017; Vol. 1051, pp 139–168.

(83) Yu, J.; Ciancetta, A.; Dudas, S.; Duca, S.; Lottermoser, J.; Jacobson, K. A. Structure-guided modification of heterocyclic antagonists of the $P2Y_{14}$ receptor. *J. Med. Chem.* **2018**, *61*, acs.jmedchem.8b00168.

(84) Jacobson, K. A.; Müller, C. E. Medicinal chemistry of adenosine, P2Y and P2X receptors. *Neuropharmacology* **2016**, *104*, 31–49.

(85) Zhang, J.; Zhang, K.; Gao, Z.-G.; Paoletta, S.; Zhang, D.; Han, G. W.; Li, T.; Ma, L.; Zhang, W.; Müller, C. E.; Yang, H.; Jiang, H.; Cherezov, V.; Katritch, V.; Jacobson, K. a; Stevens, R. C.; Wu, B.; Zhao, Q. Agonist-bound structure of the human $P2Y_{12}$ receptor. *Nature* **2014**, *509*, 119–122.

(86) van der Kant, R.; Vriend, G. Alpha-bulges in G protein-coupled receptors. *Int. J. Mol. Sci.* **2014**, *15*, 7841–7864.

(87) Isberg, V.; de Graaf, C.; Bortolato, A.; Cherezov, V.; Katritch, V.; Marshall, F. H.; Mordalski, S.; Pin, J.-P.; Stevens, R. C.; Vriend, G.; Gloriam, D. E. Generic GPCR residue numbers – aligning topology maps while minding the gaps. *Trends Pharmacol. Sci.* **2015**, *36*, 22–31.

(88) Rafehi, M.; Müller, C. E. Tools and drugs for uracil nucleotide-activated P2Y receptors. *Pharmacol. Ther.* **2018**, *190*, 24–80.

(89) Yelovitch, S.; Barr, H. M.; Camden, J.; Weisman, G. A.; Shai, E.; Varon, D.; Fischer, B. Identification of a promising drug candidate for the treatment of type 2 diabetes based on a $P2Y_1$ receptor agonist. *J. Med. Chem.* **2012**, *55*, 7623–7635.

(90) Wei, Q.; Costanzi, S.; Liu, Q.-Z.; Gao, Z.-G.; Jacobson, K. A. Activation of the $P2Y_1$ receptor induces apoptosis and inhibits proliferation of prostate cancer cells. *Biochem. Pharmacol.* **2011**, *82*, 418–425.

(91) Zhou, Q.; Xu, C.; Cheng, X.; Liu, Y.; Yue, M.; Hu, M.; Luo, D.; Niu, Y.; Ouyang, H.; Ji, J.;

Hu, H. Platelets promote cartilage repair and chondrocyte proliferation via ADP in a rodent model of osteoarthritis. *Platelets* **2016**, *27*, 212–222.

(92) Parr, C. E. Cloning and expression of a human P2U nucleotide receptor, a target for cystic fibrosis pharmacotherapy. *Proc. Natl. Acad. Sci.* **1994**, *91*, 3275–3279.

(93) Fujihara, T.; Murakami, T.; Fujita, H.; Nakamura, M. Improvement of corneal barrier function by the $P2Y_2$ agonist INS365 in a rat dry eye model. *Invest. Ophthalmol. Vis. Sci.* **2001**, *42*, 96–100.

(94) Donnelly, L. E.; Rogers, D. F. Therapy for chronic obstructive pulmonary disease in the 21st century. *Drugs* **2003**, *63*, 1973–1998.

(95) Vanderstocken, G.; Van de Paar, E.; Robaye, B.; di Pietrantonio, L.; Bondue, B.; Boeynaems, J. M.; Desmecht, D.; Communi, D. Protective role of $P2Y_2$ receptor against lung infection induced by pneumonia virus of mice. *PLoS One* **2012**, *7*, e50385.

(96) Ajit, D.; Woods, L. T.; Camden, J. M.; Thebeau, C. N.; El-Sayed, F. G.; Greeson, G. W.; Erb, L.; Petris, M. J.; Miller, D. C.; Sun, G. Y.; Weisman, G. A. Loss of $P2Y_2$ nucleotide receptors enhances early pathology in the TgCRND8 mouse model of Alzheimer's disease. *Mol. Neurobiol.* **2014**, *49*, 1031–1042.

(97) Cohen, R.; Shainberg, A.; Hochhauser, E.; Cheporko, Y.; Tobar, A.; Birk, E.; Pinhas, L.; Leipziger, J.; Don, J.; Porat, E. UTP reduces infarct size and improves mice heart function after myocardial infarct via $P2Y_2$ receptor. *Biochem. Pharmacol.* **2011**.

(98) Ghanem, E.; Robaye, B.; Leal, T.; Leipziger, J.; Van Driessche, W.; Beauwens, R.; Boeynaems, J.-M. The role of epithelial $P2Y_2$ and $P2Y_4$ receptors in the regulation of intestinal chloride secretion. *Br. J. Pharmacol.* **2005**, *146*, 364–369.

(99) Li, H. -q.; Chen, C.; Dou, Y.; Wu, H. -j.; Liu, Y. -j.; Lou, H.-F.; Zhang, J. -m.; Li, X. -m.; Wang, H.; Duan, S. $P2Y_4$ receptor-mediated pinocytosis contributes to amyloid beta-induced self-uptake by microglia. *Mol. Cell. Biol.* **2013**, *33*, 4282–4293.

(100) Schreiber, R.; Kunzelmann, K. Purinergic $P2Y_6$ receptors induce Ca^{2+} and CFTR dependent Cl^- secretion in mouse trachea. *Cell. Physiol. Biochem.* **2005**, *16*, 99–108.

(101) Wan, H.; Xie, R.; Xu, J.; He, J.; Tang, B.; Liu, Q.; Wang, S.; Guo, Y.; Yang, X.; Dong, T. X.; Carethers, J. M.; Yang, S.; Dong, H. Anti-proliferative effects of nucleotides on gastric cancer via a novel $P2Y_6$/SOCE/Ca^{2+}/β-catenin pathway. *Scientific Reports*. 2017.

(102) Bar, I.; Guns, P.; Metallo, J.; Boeynams, J.; Bult, H.; Robaye, B. Knockout mice reveal a role for $P2Y_6$ receptor in macrophages , endothelial cells , and vascular smooth muscle cells.

Mol. Pharmacol. **2008**, *74*, 777–784.

(103) Shinozaki, Y.; Kashiwagi, K.; Namekata, K.; Takeda, A.; Ohno, N.; Robaye, B.; Harada, T.; Iwata, T.; Koizumi, S. Purinergic dysregulation causes hypertensive glaucoma-like optic neuropathy. *JCI Insight* **2017**, *2*, 1–14.

(104) Ohtani, M.; Suzuki, J.-I.; Jacobson, K. a; Oka, T. Evidence for the possible involvement of the $P2Y_6$ receptor in Ca^{2+} mobilization and insulin secretion in mouse pancreatic islets. *Purinergic Signal.* **2008**, *4*, 365–375.

(105) Reichenbach, N.; Delekate, A.; Breithausen, B.; Keppler, K.; Poll, S.; Schulte, T.; Peter, J.; Plescher, M.; Hansen, J. N.; Blank, N.; Keller, A.; Fuhrmann, M.; Henneberger, C.; Halle, A.; Petzold, G. C. $P2Y_1$ receptor blockade normalizes network dysfunction and cognition in an Alzheimer's disease model. *J. Exp. Med.* **2018**, *215*, 1649–1663.

(106) Krügel, U.; Köles, L.; Illés, P. Integration of neuronal and glial signalling by pyramidal cells of the rat prefrontal cortex; control of cognitive functions and addictive behaviour by purinergic mechanisms. *Neuropsychopharmacol. Hung.* **2013**, *15*, 206–213.

(107) Hechler, B.; Freund, M.; Ravanat, C.; Magnenat, S.; Cazenave, J. P.; Gachet, C. Reduced atherosclerotic lesions in $P2Y_1$/apolipoprotein E double-knockout mice: the contribution of non-hematopoietic-derived $P2Y_1$ receptors. *Circulation* **2008**, *118*, 754–763.

(108) Léon, C.; Hechler, B.; Freund, M.; Eckly, A.; Vial, C.; Ohlmann, P.; Dierich, A.; Lemeur, M.; Cazenave, J.; Gachet, C. Defective platelet aggregation and increased resistance to thrombosis in purinergic $P2Y_1$ receptor – null mice. *J. Clin. Invest.* **1999**, *104*, 1731–1737.

(109) Luo, Y.; Feng, C.; Wu, J.; Wu, Y.; Liu, D.; Wu, J.; Dai, F.; Zhang, J. Erratum to: $P2Y_1$, $P2Y_2$, and TRPV1 receptors are increased in diarrhea-predominant irritable bowel syndrome and $P2Y_2$ correlates with abdominal pain. *Dig. Dis. Sci.* **2016**, *61*, 3639.

(110) Müller, T.; Robaye, B.; Vieira, R. P.; Ferrari, D.; Grimm, M.; Jakob, T.; Martin, S. F.; Di Virgilio, F.; Boeynaems, J. M.; Virchow, J. C.; Idzko, M. The purinergic receptor $P2Y_2$ receptor mediates chemotaxis of dendritic cells and eosinophils in allergic lung inflammation. *Allergy Eur. J. Allergy Clin. Immunol.* **2010**, *65*, 1545–1553.

(111) Schumacher, D.; Strilic, B.; Sivaraj, K. K.; Wettschureck, N.; Offermanns, S. Report platelet-derived nucleotides promote tumor-cell transendothelial migration and metastasis via $P2Y_2$ receptor. *Cancer Cell* **2013**, *24*, 130–137.

(112) Magni, G.; Merli, D.; Verderio, C.; Abbracchio, M. P.; Ceruti, S. $P2Y_2$ receptor antagonists as anti-allodynic agents in acute and sub-chronic trigeminal sensitization: role of satellite

glial cells. *Glia* **2015**, *63*, 1256–1269.

(113) Dixon, C. J.; Bowler, W. B.; Littlewood-Evans, A.; Dillon, J. P.; Bilbe, G.; Sharpe, G. R.; Gallagher, J. A. Regulation of epidermal homeostasis through $P2Y_2$ receptors. *Br. J. Pharmacol.* **1999**, *127*, 1680–1686.

(114) Adamson, S. E.; Montgomery, G.; Seaman, S. A.; Peirce-cottler, S. M.; Leitinger, N. Myeloid $P2Y_2$ receptor promotes acute inflammation but is dispensable for chronic high-fat diet-induced metabolic dysfunction. *Purinergic Signal.* **2018**, *14*, 19–26.

(115) Stachon, P.; Geis, S.; Peikert, A.; Heidenreich, A.; Michel, N. A.; Ünal, F.; Hoppe, N.; Dufner, B.; Schulte, L.; Marchini, T.; Cicko, S.; Ayata, K.; Zech, A.; Wolf, D.; Hilgendorf, I.; Willecke, F.; Reinöhl, J.; Mühlen, C. Von; Bode, C.; Idzko, M.; Zirlik, A. Extracellular ATP induces vascular inflammation and atherosclerosis via purinergic receptor Y_2 in mice. *Arterioscler. Thromb. Vasc. Biol.* **2016**, *36*, 1577–1586.

(116) Wesselius, A.; Bours, M. J. L. Association of $P2Y_2$ receptor SNPs with bone mineral density and osteoporosis risk in a cohort of Dutch fracture patients. *Purinergic Signal.* **2013**, *9*, 41–49.

(117) Zizzo, M. G.; Mastropaolo, M.; Grählert, J.; Mulè, F.; Serio, R. Pharmacological characterization of uracil nucleotide-preferring P2Y receptors modulating intestinal motility: a study on mouse ileum. *Purinergic Signal.* **2012**, *8*, 275–285.

(118) Delbro, D. S.; Nylund, G.; Nordgren, S. Demonstration of $P2Y_4$ purinergic receptors in the HT-29 human colon cancer cell line. *Auton. Autacoid Pharmacol.* **2005**, *25*, 163–166.

(119) Guns, P.-J. D.; Hendrickx, J.; Van Assche, T.; Fransen, P.; Bult, H. P2Y receptors and atherosclerosis in apolipoprotein e-deficient mice. *Br. J. Pharmacol.* **2010**, *159*, 326–336.

(120) Azimi, I.; Beilby, H.; Davis, F. M.; Marcial, D. L.; Kenny, P. A.; Thompson, E. W.; Roberts-Thomson, S. J.; Monteith, G. R. Altered purinergic receptor-Ca^{2+} signaling associated with hypoxia-induced epithelial-mesenchymal transition in breast cancer cells. *Mol. Oncol.* **2016**, *10*, 166–178.

(121) Steculorum, S. M.; Paeger, L.; Bremser, S.; Evers, N.; Hinze, Y.; Idzko, M.; Kloppenburg, P.; Brüning, J. C. Hypothalamic UDP increases in obesity and promotes feeding via $P2Y_6$-dependent activation of AgRP neurons. *Cell* **2015**, *162*, 1404–1417.

(122) Barragán-Iglesias, P.; Mendoza-Garcés, L.; Pineda-Farias, J. B.; Solano-Olivares, V.; Rodríguez-Silverio, J.; Flores-Murrieta, F. J.; Granados-Soto, V.; Rocha-González, H. I. Participation of peripheral $P2Y_1$, $P2Y_6$ and $P2Y_{11}$ receptors in formalin-induced inflammatory pain in rats. *Pharmacol. Biochem. Behav.* **2015**, *128*, 23–32.

(123) Orriss, I. R.; Wang, N.; Burnstock, G.; Arnett, T. R.; Gartland, A.; Robaye, B.; Boeynaems, J. M. The $P2Y_6$ receptor stimulates bone resorption by osteoclasts. *Endocrinology* **2011**, *152*, 3706–3716.

(124) Von Kügelgen, I.; Hoffmann, K. Pharmacology and structure of p2y receptors. *Neuropharmacology* **2016**, *104*, 50–61.

(125) Zhang, D.; Gao, Z.-G.; Zhang, K.; Kiselev, E.; Crane, S.; Wang, J.; Paoletta, S.; Yi, C.; Ma, L.; Zhang, W.; Han, G. W.; Liu, H.; Cherezov, V.; Katritch, V.; Jiang, H.; Stevens, R. C.; Jacobson, K. a.; Zhao, Q.; Wu, B. Two disparate ligand-binding sites in the human $P2Y_1$ receptor. *Nature* **2015**, *520*, 317–321.

(126) Moore, D. J.; Chambers, J. K.; Wahlin, J. P.; Tan, K. B.; Moore, G. B.; Jenkins, O.; Emson, P. C.; Murdock, P. R. Expression pattern of human P2Y receptor subtypes: a quantitative reverse transcription-polymerase chain reaction study. *Biochim. Biophys. Acta* **2001**, *1521*, 107–119.

(127) Maruoka, H.; Barrett, M. O.; Ko, H.; Tosh, D. K.; Melman, A.; Burianek, L. E.; Balasubramanian, R.; Berk, B.; Costanzi, S.; Harden, T. K.; Jacobson, K. A. Pyrimidine ribonucleotides with enhanced selectivity as $P2Y_6$ receptor agonists: novel 4-alkyloxyimino, (*S*)-methanocarba, and 5'-triphosphate gamma-ester modifications. *J. Med. Chem.* **2010**, *53*, 4488–4501.

(128) El-Tayeb, A.; Qi, A.; Müller, C. E. Synthesis and structure-activity relationships of uracil nucleotide derivatives and analogues as agonists at human $P2Y_2$, $P2Y_4$, and $P2Y_6$ receptors. *J. Med. Chem.* **2006**, *49*, 7076–7087.

(129) Brüser, A.; Zimmermann, A.; Crews, B. C.; Sliwoski, G.; Meiler, J.; König, G. M.; Kostenis, E.; Lede, V.; Marnett, L. J.; Schöneberg, T. Prostaglandin E2 glyceryl ester is an endogenous agonist of the nucleotide receptor $P2Y_6$. *Sci. Rep.* **2017**, *7*, 1–15.

(130) Mamedova, L. K.; Joshi, B. V; Gao, Z.-G.; von Kügelgen, I.; Jacobson, K. A. Diisothiocyanate derivatives as potent, insurmountable antagonists of $P2Y_6$ nucleotide receptors. *Biochem. Pharmacol.* **2004**, *67*, 1763–1770.

(131) Köttgen, M.; Löffler, T.; Jacobi, C.; Nitschke, R.; Pavenstädt, H.; Schreiber, R.; Frische, S.; Nielsen, S.; Leipziger, J. $P2Y_6$ receptor mediates colonic NaCl secretion via differential activation of cAMP-mediated transport. *J. Clin. Invest.* **2003**, *111*, 371–379.

(132) Müller, T.; Fay, S.; Vieira, R. P.; Karmouty-Quintana, H.; Cicko, S.; Ayata, C. K.; Zissel, G.; Goldmann, T.; Lungarella, G.; Ferrari, D.; Di Virgilio, F.; Robaye, B.; Boeynaems, J.-M.; Lazarowski, E. R.; Blackburn, M. R.; Idzko, M. $P2Y_6$ receptor activation promotes inflammation and tissue remodeling in pulmonary fibrosis. *Front. Immunol.* **2017**, *8*.

(133) Steculorum, S. M.; Timper, K.; Engström Ruud, L.; Evers, N.; Paeger, L.; Bremser, S.; Kloppenburg, P.; Brüning, J. C. Inhibition of $P2Y_6$ signaling in AgRP neurons reduces food intake and improves systemic insulin sensitivity in obesity. *Cell Rep.* **2017**, *18*, 1587–1597.

(134) Clouet, S.; Di Pietrantonio, L.; Daskalopoulos, E.-P.; Esfahani, H.; Horckmans, M.; Vanorlé, M.; Lemaire, A.; Balligand, J.-L.; Beauloye, C.; Boeynaems, J.-M.; Communi, D. Loss of mouse $P2Y_6$ nucleotide receptor is associated with physiological macrocardia and amplified pathological cardiac hypertrophy. *J. Biol. Chem.* **2016**, *291*, 15841–15852.

(135) Matos, J. E.; Robaye, B.; Boeynaems, J. M.; Beauwens, R.; Leipziger, J. K^+ secretion activated by luminal $P2Y_2$ and $P2Y_4$ receptors in mouse colon. *J. Physiol.* **2005**, *564*, 269–279.

(136) Ward, M. M.; Puthussery, T.; Fletcher, E. L. Localization and possible function of $P2Y_4$ receptors in the rodent retina. *Neuroscience* **2008**, *155*, 1262–1274.

(137) Tran, M. D. P2 receptor stimulation induces amyloid precursor protein production and secretion in rat cortical astrocytes. *Neurosci. Lett.* **2011**, *492*, 155–159.

(138) Maruoka, H.; Jayasekara, M. P. S.; Barrett, M. O.; Franklin, D. A.; Sonia Castro, D.; Kim, N.; Costanzi, S.; Harden, T. K.; And; A., K. J. Pyrimidine nucleotides with 4-alkyloxyimino and terminal tetraphosphate δ-ester modifications as selective agonists of the $P2Y_4$ receptor. *J. Med. Chem.* **2011**, *54*, 4018–4033.

(139) Rafehi, M.; Malik, E. M.; Neumann, A.; Abdelrahman, A.; Hanck, T.; Namasivayam, V.; Müller, C. E.; Baqi, Y. Development of potent and selective antagonists for the UTP-activated $P2Y_4$ receptor. *J. Med. Chem.* **2017**, *60*, 3020–3038.

(140) Hillmann, P.; Ko, G. Y.; Spinrath, A.; Raulf, A.; Von Kügelgen, I.; Wolff, S. C.; Nicholas,

R. a.; Kostenis, E.; Höltje, H. D.; Müller, C. E. Key determinants of nucleotide-activated G protein-coupled $P2Y_2$ receptor function revealed by chemical and pharmacological experiments, mutagenesis and homology modeling. *J. Med. Chem.* **2009**, *52*, 2762–2775.

(141) Bagchi, S.; Liao, Z.; Gonzalez, F. A.; Chorna, N. E.; Seye, C. I.; Weisman, G. A.; Erb, L. The $P2Y_2$ nucleotide receptor interacts with alphav integrins to activate go and induce cell migration. *J. Biol. Chem.* **2005**, *280*, 39050–39057.

(142) Liao, Z.; Seye, C. I.; Weisman, G. a; Erb, L. The $P2Y_2$ nucleotide receptor requires interaction with alpha v integrins to access and activate G_{12}. *J. Cell Sci.* **2007**, *120*, 1654–1662.

(143) Eun, S. Y.; Ko, Y. S.; Park, S. W.; Chang, K. C.; Kim, H. J. $P2Y_2$ nucleotide receptor-mediated extracellular signal-regulated kinases and protein kinase C activation induces the invasion of highly metastatic breast cancer cells. *Oncol. Rep.* **2015**, *34*, 195–202.

(144) Li, W.-H.; Qiu, Y.; Zhang, H.-Q.; Tian, X.-X.; Fang, W.-G. $P2Y_2$ receptor and EGFR cooperate to promote prostate cancer cell invasion via ERK1/2 pathway. *PLoS One* **2015**, *10*, 1–15.

(145) Xie, R.; Xu, J.; Wen, G.; Jin, H.; Liu, X.; Yang, Y.; Ji, B.; Jiang, Y.; Song, P.; Dong, H.; Tuo, B. The $P2Y_2$ nucleotide receptor mediates the proliferation and migration of human hepatocellular carcinoma cells induced by ATP. *J. Biol. Chem.* **2014**, *289*, 19137–19149.

(146) Erb, L.; Cao, C.; Ajit, D.; Weisman, G. a. P2Y receptors in Alzheimer's disease. *Biol. Cell* **2015**, *107*, 1–21.

(147) León-Otegui, M.; Gómez-Villafuertes, R.; Díaz-Hernández, J. I.; Díaz-Hernández, M.; Miras-Portugal, M. T.; Gualix, J. Opposite effects of P2X7 and $P2Y_2$ nucleotide receptors on α-secretase-dependent APP processing in Neuro-2a cells. *FEBS Lett.* **2011**, *585*, 2255–2262.

(148) Lai, M. K. P.; Tan, M. G. K.; Kirvell, S.; Hobbs, C.; Lee, J.; Esiri, M. M.; Chen, C. P.; Francis, P. T. Selective loss of $P2Y_2$ nucleotide receptor immunoreactivity is associated with Alzheimer's disease neuropathology. *J. Neural Transm.* **2008**, *115*, 1165–1172.

(149) Séror, C.; Melki, M.-T.; Subra, F.; Raza, S. Q.; Bras, M.; Saïdi, H.; Nardacci, R.; Voisin, L.; Paoletti, A.; Law, F.; Martins, I.; Amendola, A.; Abdul-Sater, A. a; Ciccosanti, F.; Delelis, O.; Niedergang, F.; Thierry, S.; Said-Sadier, N.; Lamaze, C.; Métivier, D.; Estaquier, J.; Fimia, G. M.; Falasca, L.; Casetti, R.; Modjtahedi, N.; Kanellopoulos, J.; Mouscadet, J.-F.; Ojcius, D. M.; Piacentini, M.; Gougeon, M.-L.; Kroemer, G.; Perfettini,

J.-L. Extracellular ATP acts on $P2Y_2$ purinergic receptors to facilitate HIV-1 infection. *J. Exp. Med.* **2011**, *208*, 1823–1834.

(150) Önnheim, K.; Christenson, K.; Gabl, M.; Burbiel, J. C.; Müller, C. E.; Oprea, T. I.; Bylund, J.; Dahlgren, C.; Forsman, H. A novel receptor cross-talk between the ATP receptor $P2Y_2$ and formyl peptide receptors reactivates desensitized neutrophils to produce superoxide. *Exp. Cell Res.* **2014**, *323*, 209–217.

(151) Gabl, M.; Winther, M.; Welin, A.; Karlsson, A.; Oprea, T.; Bylund, J.; Dahlgren, C.; Forsman, H. $P2Y_2$ receptor signaling in neutrophils is regulated from inside by a novel cytoskeleton-dependent mechanism. *Exp. Cell Res.* **2015**, *336*, 242–252.

(152) Wang, S.; Iring, A.; Strilic, B.; Albarrán Juárez, J.; Kaur, H.; Troidl, K.; Tonack, S.; Burbiel, J. C.; Müller, C. E.; Fleming, I.; Lundberg, J. O.; Wettschureck, N.; Offermanns, S. $P2Y_2$ and G_q/G_{11} control blood pressure by mediating endothelial mechanotransduction. *J. Clin. Invest.* **2015**, *125*, 3077–3086.

(153) Yashima, S.; Shimazaki, A.; Mitoma, J.; Nakagawa, T.; Abe, M.; Yamada, H.; Higashi, H. Close association of B2 bradykinin receptors with $P2Y_2$ ATP receptors. *J. Biochem.* **2015**, *158*, 155–163.

(154) Hochhauser, E.; Cohen, R.; Waldman, M.; Maksin, A.; Isak, A.; Aravot, D.; Jayasekara, P. S.; Müller, C. E.; Jacobson, K. A.; Shainberg, A. $P2Y_2$ receptor agonist with enhanced stability protects the heart from ischemic damage in vitro and in vivo. *Purinergic Signal.* **2013**, *9*, 633–642.

(155) Cressman, V. L.; Lazarowski, E.; Homolya, L.; Boucher, R. C.; Koller, B. H.; Grubb, B. R. Effect of loss of $P2Y_2$ receptor gene expression on nucleotide regulation of murine epithelial Cl^- transport. *J. Biol. Chem.* **1999**, *274*, 26461–26468.

(156) El-tayeb, A.; Qi, A.; Nicholas, R. a. Structural modifications of ump, udp, and utp leading to subtype-selective agonists for $P2Y_2$, $P2Y_4$, and $P2Y_6$ receptors. *J. Med. Chem.* **2011**, *54*, 2878–2890.

(157) Lazarowski, E. R.; Watt, W. C.; Stutts, M. J.; Brown, H. A.; Boucher, R. C.; Harden, T. K. Enzymatic synthesis of UTPγS, a potent hydrolysis resistant agonist of P2U-purinoceptors. *Br. J. Pharmacol.* **1996**, *117*, 203–209.

(158) Ko, H.; Carter, R. L.; Cosyn, L.; Petrelli, R.; de Castro, S.; Besada, P.; Zhou, Y.; Cappellacci, L.; Franchetti, P.; Grifantini, M.; Van Calenbergh, S.; Harden, T. K.; Jacobson, K. A. Synthesis and potency of novel uracil nucleotides and derivatives as $P2Y_2$ and $P2Y_6$ receptor

agonists. *Bioorg. Med. Chem.* **2008**, *16*, 6319–6332.

(159) Van Poecke, S.; Barrett, M. O.; Santhosh Kumar, T.; Sinnaeve, D.; Martins, J. C.; Jacobson, K. A.; Kendall Harden, T.; Van Calenbergh, S. Synthesis and $P2Y_2$ receptor agonist activities of uridine 5'-phosphonate analogues. *Bioorg. Med. Chem.* **2012**, *20*, 2304–2315.

(160) Davenport, R. J.; Diaz, P.; Galvin, F. C. a; Lloyd, S.; Mack, S. R.; Owens, R.; Sabin, V.; Wynn, J. Novel nucleotide triphosphates as potent $P2Y_2$ agonists with enhanced stability over UTP. *Bioorganic Med. Chem. Lett.* **2007**, *17*, 558–561.

(161) Fonseca, B.; Martínez-Águila, A.; Díaz-Hernández, M.; Pintor, J. Diadenosine tetraphosphate contributes to carbachol-induced tear secretion. *Purinergic Signal.* **2015**, *11*, 87–93.

(162) Shaver, S. R.; Rideout, J. L.; Pendergast, W.; Douglass, J. G.; Brown, E. G.; Boyer, J. L.; Patel, R. I.; Redick, C. C.; Jones, A. C.; Picher, M.; Yerxa, B. R. Structure–activity relationships of dinucleotides: potent and selective agonists of P2Y receptors. *Purinergic Signal.* **2005**, *1*, 183–191.

(163) Keating, G. M. Diquafosol ophthalmic solution 3 %: a review of its use in dry eye. *Drugs* **2015**, *75*, 911–922.

(164) Yerxa, B. R.; Sabater, J. R.; Davis, C. W.; Stutts, M. J.; Picher, M.; Jones, A. C.; Cowlen, M. Pharmacology of ins37217 [P^1-(uridine 5')-P^4-(2'-deoxycytidine 5') tetraphosphate, tetrasodium salt], a next-generation $P2Y_2$ receptor agonist for the treatment of cystic fibrosis. *J. Pharmacol. Exp. Ther.* **2002**, *302*, 871–880.

(165) Nichols, K. K.; Yerxa, B.; Kellerman, D. J. Diquafosol tetrasodium: a novel dry eye therapy. *Expert Opin. Investig. Drugs* **2004**, *13*, 47–54.

(166) Deterding, R.; Retsch-Bogart, G.; Milgram, L.; Gibson, R.; Daines, C.; Zeitlin, P. L.; Milla, C.; Marshall, B.; LaVange, L.; Engels, J.; Mathews, D.; Gorden, J.; Schaberg, A.; Williams, J.; Ramsey, B. Safety and tolerability of denufosol tetrasodium inhalation solution, a novel $P2Y_2$ receptor agonist: results of a phase 1/phase 2 multicenter study in mild to moderate cystic fibrosis. *Pediatr. Pulmonol.* **2005**, *39*, 339–348.

(167) Moss, R. B. Pitfalls of drug development: lessons learned from trials of denufosol in cystic

fibrosis. *J. Pediatr.* **2013**, *162*, 676–680.

(168) Sakuma, K.; Nakagawa, H.; Oikawa, T.; Noda, M.; Ikeda, S. Effects of 4(1*H*)-quinolinone derivative, a novel non-nucleotide allosteric purinergic $P2Y_2$ agonist, on cardiomyocytes in neonatal rats. *Sci. Rep.* **2017**, *7*, 1–10.

(169) Robaye, B.; Boeynaems, J.-M.; Communi, D. Slow desensitization of the human $P2Y_6$ receptor. *Eur. J. Pharmacol.* **1997**, *329*, 231–236.

(170) Jacobson, K. a.; Jarvis, M. F.; Williams, M. Purine and pyrimidine (P2) receptors as drug targets. *J. Med. Chem.* **2002**, *45*, 4057–4093.

(171) Sauer, R.; El-Tayeb, A.; Kaulich, M.; Müller, C. E. Synthesis of uracil nucleotide analogs with a modified, acyclic ribose moiety as $P2Y_2$ receptor antagonists. *Bioorg. Med. Chem.* **2009**, *17*, 5071–5079.

(172) Kaulich, M.; Streicher, F.; Mayer, R.; Mueller, I.; Mueller, C. E. Flavonoids - novel lead compounds for the development of $P2Y_2$ receptor antagonists. *Drug Dev. Res.* **2003**, *59*, 72–81.

(173) Magni, G.; Ceruti, S. P2Y purinergic receptors: new targets for analgesic and antimigraine drugs. *Biochem. Pharmacol.* **2013**, *85*, 466–477.

(174) Burnstock, G. Purine and pyrimidine receptors. *Cell. Mol. Life Sci.* **2007**, *64*, 1471–1483.

(175) Weyler, S.; Baqi, Y.; Hillmann, P.; Kaulich, M.; Hunder, A. M.; Müller, I. a; Müller, C. E. Combinatorial synthesis of anilinoanthraquinone derivatives and evaluation as non-nucleotide-derived $P2Y_2$ receptor antagonists. *Bioorg. Med. Chem. Lett.* **2008**, *18*, 223–227.

(176) Kindon, N.; Davis, A.; Dougall, I.; Dixon, J.; Johnson, T.; Walters, I.; Thom, S.; McKechnie, K.; Meghani, P.; Stocks, M. J. From UTP to AR-C118925, the discovery of a potent non nucleotide antagonist of the $P2Y_2$ receptor. *Bioorganic Med. Chem. Lett.* **2017**, *27*, 4849–4853.

(177) Meghani, P. 2002. The design of $P2Y_2$ antagonists for the treatment of inflammatory diseases. In *Poster presentation*; 224th ACS National Meeting: Boston, MA, United States, 2002.

(178) Kemp, P. a.; Sugar, R. a.; Jackson, A. D. Nucleotide-mediated mucin secretion from

differentiated human bronchial epithelial cells. *Am. J. Respir. Cell Mol. Biol.* **2004**, *31*, 446–455.

(179) Purgatorio, R.; de Candia, M.; De Palma, A.; De Santis, F.; Pisani, L.; Campagna, F.; Cellamare, S.; Altomare, C.; Catto, M. Insights into structure-activity relationships of 3-arylhydrazonoindolin-2-one derivatives for their multitarget activity on β-amyloid aggregation and neurotoxicity. *Molecules* **2018**, *23*, 1544.

(180) Panek, D.; Więckowska, A.; Pasieka, A.; Godyń, J.; Jończyk, J.; Bajda, M.; Knez, D.; Gobec, S.; Malawska, B. Design, synthesis, and biological evaluation of 2-(benzylamino-2-hydroxyalkyl)isoindoline-1,3-diones derivatives as potential disease-modifying multifunctional anti-Alzheimer agents. *Molecules* **2018**, *23*, 1–15.

(181) Oset-Gasque, M. J.; Marco-Contelles, J. Alzheimer's disease, the "one-molecule, one-target" paradigm, and the multitarget directed ligand approach. *ACS Chem. Neurosci.* **2018**, *9*, 401–403.

(182) Xie, H.; Xu, X.; Chen, J.; Li, L.; Wang, J.; Fang, T.; Zhou, L.; Wang, H.; Zheng, S. Rational design of multifunctional small-molecule prodrugs for simultaneous suppression of cancer cell growth and metastasis in vitro and in vivo. *Chem. Commun.* **2016**, *52*, 5601–5604.

(183) Rafehi, M.; Neumann, A.; Baqi, Y.; Malik, E. M.; Wiese, M.; Namasivayam, V.; Müller, C. E. Molecular recognition of agonists and antagonists by the nucleotide-activated G protein-coupled $P2Y_2$ receptor. *J. Med. Chem.* **2017**, *60*, 8425–8440.

(184) Iversen, P. W.; Beck, B.; Chen, Y.-F.; Dere, W.; Devanarayan, V.; Eastwood, B. J.; Farmen, M. W.; Iturria, S. J.; Montrose, C.; Moore, R. A.; Weidner, J. R.; Sittampalam, G. S. *HTS Assay Validation*; Eli Lilly & Company and the National Center for Advancing Translational Sciences, 2004.

(185) Zhang, J.-H.; Chung; Oldenburg. A simple statistical parameter for use in evaluation and validation of high throughput screening assays. *J. Biomol. Screen.* **1999**, *4*, 67–73.

(186) Keseru, G. M.; Makara, G. M. Hit discovery and hit-to-lead approaches. *Drug Discov. Today* **2006**, *11*, 741–748.

(187) Boucher, H. W.; Groll, A. H.; Chiou, C. C.; Walsh, T. J. Newer systemic antifungal agents. *Drugs* **2004**, *64*, 1997–2020.

(188) Pilmis, B.; Jullien, V.; Sobel, J.; Lecuit, M.; Lortholary, O.; Charlier, C. Antifungal drugs during pregnancy: an updated review. *J. Antimicrob. Chemother.* **2015**, *70*, 14–22.

(189) Seidler, J.; McGovern, S. L.; Doman, T. N.; Shoichet, B. K. Identification and prediction of

promiscuous aggregating inhibitors among known drugs. *J. Med. Chem*. **2003**, *46*, 4477–4486.

(190) Paila, Y. D.; Pucadyil, T. J.; Chattopadhyay, A. The cholesterol-complexing agent digitonin modulates ligand binding of the bovine hippocampal serotonin 1A receptor. *Mol. Membr. Biol.* **2009**, *22*, 241–249.

(191) Tan, S. M.-L.; Li, F.; Rajendran, P.; Kumar, A. P.; Hui, K. M.; Sethi, G. Identification of beta-escin as a novel inhibitor of signal transducer and activator of transcription 3/Janus-activated kinase 2 signaling pathway that suppresses proliferation and induces apoptosis in human hepatocellular carcinoma cells. *J. Pharmacol. Exp. Ther.* **2010**, *334*, 285–293.

(192) Zhou, X.; Fu, F.; Li, Z.; Dong, Q.; He, J.; Wang, C. Escin, a natural mixture of triterpene saponins, exhibits antitumor activity against hepatocellular carcinoma. *Planta Med.* **2009**, *75*, 1580–1585.

(193) Kakumoto, M.; Sakaeda, T.; Takara, K.; Nakamura, T.; Kita, T.; Yagami, T.; Kobayashi, H.; Okamura, N.; Okumura, K. Effects of carvedilol on MDR1-mediated multidrug resistance: comparison with verapamil. *Cancer Sci.* **2003**, *94*, 81–86.

(194) Stama, M. L.; Ślusarczyk, J.; Lacivita, E.; Kirpotina, L. N.; Schepetkin, I. A.; Chamera, K.; Riganti, C.; Perrone, R.; Quinn, M. T.; Basta-Kaim, A.; Leopoldo, M. Novel ureidopropanamide based n-formyl peptide receptor 2 (FPR2) agonists with potential application for central nervous system disorders characterized by neuroinflammation. *Eur. J. Med. Chem*. **2017**, *141*, 703–720.

(195) Aggarwal, B. B.; Ichikawa, H. Molecular targets and anticancer potential of indole-3-carbinol and its derivatives. *Cell Cycle* **2005**, *4*, 1201–1215.

(196) Chen, I.; Safe, S.; Bjeldanes, L. Indole-3-carbinol and diindolylmethane as aryl hydrocarbon (AH) receptor agonists and antagonists in T47D human breast cancer cells. *Biochem. Pharmacol.* **1996**, *51*, 1069–1076.

(197) Ali, S.; Banerjee, S.; Ahmad, A.; El-Rayes, B. F.; Philip, P. A.; Sarkar, F. H. Apoptosis-inducing effect of erlotinib is potentiated by 3,3′-diindolylmethane in vitro and in vivo using an orthotopic model of pancreatic cancer. *Mol. Cancer Ther.* **2008**, *7*.

(198) Cho, S. D.; Chintharlapalli, S.; Abdelrahim, M.; Papineni, S.; Liu, S.; Guo, J.; Lei, P.; Abudayyeh, A.; Safe, S. 5,5′-Dibromo-bis(3′-indolyl)methane induces Krüppel-like factor 4 and p21 in colon cancer cells. *Mol. Cancer Ther.* **2008**, *7*.

(199) Lei, P.; Abdelrahim, M.; Cho, S. D.; Liu, S.; Chintharlapalli, S.; Safe, S. 1,1-Bis(3’-indolyl)-

1-(p-substituted phenyl)methanes inhibit colon cancer cell and tumor growth through activation of c-jun n-terminal kinase. *Carcinogenesis* **2008**, *29*, 1139–1147.

(200) Choi, K.-M.; Yoo, H.-S. 3,3′-diindolylmethane enhances glucose uptake through activation of insulin signaling in 3T3-L1 adipocytes. *Obesity* **2018**, *26*, 1153–1160.

(201) Danne, A. B.; Choudhari, A. S.; Chakraborty, S.; Sarkar, D.; Khedkar, V. M.; Shingate, B. B. Triazole-diindolylmethane conjugates as new antitubercular agents: synthesis, bioevaluation, and molecular docking. *MedChemComm* **2018**, *9*, 1114–1130.

(202) Cho, H. J.; Seon, M. R.; Lee, Y. M.; Kim, J.; Kim, J.; Kim, S. G.; Han, J.; Park, Y. 3,3'-Diindolylmethane suppresses theinflammatory response to lipopolysaccharide in murine macrophages 1 – 3. *J. Nutr.* **2008**, *138*, 17–23.

(203) Xue, L.; Pestka, J.; Li, M.; Firestone, G.; Bjeldanes, L. 3,3′-Diindolylmethane stimulates murine immune function in vitro and in vivo. *J. Nutr. Biochem.* **2008**, *19*, 336–344.

(204) Yin, H.; Chu, A.; Li, W.; Wang, B.; Shelton, F.; Otero, F.; Nguyen, D. G.; Caldwell, J. S.; Chen, Y. A. Lipid G protein-coupled receptor ligand identification using β-arrestin PathHunter™ assay. *J. Biol. Chem.* **2009**, *284*, 12328–12338.

(205) Lynch, J.; Wang, J. G protein-coupled receptor signaling in stem cells and cancer. *Int. J. Mol. Sci.* **2016**, *17*, 707.

(206) Kenakin, T.; Watson, C.; Muniz-Medina, V.; Christopoulos, A.; Novick, S. A simple method for quantifying functional selectivity and agonist bias. *ACS Chem. Neurosci.* **2012**, *3*, 193–203.

(207) Thompson, G. L.; Lane, J. R.; Coudrat, T.; Sexton, P. M.; Christopoulos, A.; Canals, M. Biased agonism of endogenous opioid peptides at the μ-opioid receptor. *Mol. Pharmacol.* **2015**, *88*, 335–346.

(208) Winpenny, D.; Clark, M.; Cawkill, D. Biased ligand quantification in drug discovery: from theory to high throughput screening to identify new biased μ opioid receptor agonists. *British Journal of Pharmacology*. **2016**, *173*, 1393–1403.

(209) Pillaiyar, T.; Köse, M.; Namasivayam, V.; Sylvester, K.; Borges, G.; Thimm, D.; Von Kügelgen, I.; Müller, C. E. 6-(Ar)alkylamino-substituted uracil derivatives: lipid mimetics with potent activity at the orphan G protein-coupled receptor 84 (GPR84). *ACS Omega* **2018**, *3*, 3365–3383.

(210) Kenakin, T. The potential for selective pharmacological therapies through biased receptor signaling. *BMC Pharmacol. Toxicol.* **2012**, *13*, 1–8.

(211) Khoury, E.; Clément, S.; Laporte, S. A. Allosteric and biased G protein-coupled receptor signaling regulation: potentials for new therapeutics. *Front. Endocrinol. (Lausanne).* **2014**, *5*, 1–8.

(212) Bologna, Z.; Teoh, J.; Bayoumi, A. S.; Tang, Y.; Kim, I. Biased G protein-coupled receptor signaling: new player in modulating physiology and pathology. *Biomol. Ther. (Seoul).* **2017**, *25*, 12–25.

(213) Violin, J. D.; DeWire, S. M.; Yamashita, D.; Rominger, D. H.; Nguyen, L.; Schiller, K.; Whalen, E. J.; Gowen, M.; Lark, M. W. Selectively engaging β-arrestins at the angiotensin II type 1 receptor reduces blood pressure and increases cardiac performance. *J. Pharmacol. Exp. Ther.* **2010**, *335*, 572–579.

(214) Rosethorne, E. M.; Charlton, S. J. Agonist-biased signaling at the histamine H4 receptor: JNJ7777120 recruits β-arrestin without activating G proteins. *Mol. Pharmacol.* **2011**, *79*, 749–757.

(215) Wisler, J. W.; DeWire, S. M.; Whalen, E. J.; Violin, J. D.; Drake, M. T.; Ahn, S.; Shenoy, S. K.; Lefkowitz, R. J. A unique mechanism of beta-blocker action: carvedilol stimulates beta-arrestin signaling. *Proceedings of the National Academy of Sciences*. 2007, pp 16657–16662.

(216) Maguire, J. J. Evidence for biased agonists and antagonists at the endothelin receptors. *Life Sci.* **2016**, *159*, 30–33.

(217) Hitchinson, B.; Eby, J. M.; Gao, X.; Guite-Vinet, F.; Ziarek, J. J.; Abdelkarim, H.; Lee, Y.; Okamoto, Y.; Shikano, S.; Majetschak, M.; Heveker, N.; Volkman, B. F.; Tarasova, N. I.; Gaponenko, V. Biased antagonism of CXCR4 avoids antagonist tolerance. *Sci. Signal.* **2018**, *11*, 1–12.

(218) Kenakin, T. Is the quest for signaling bias worth the effort? *Mol. Pharmacol.* **2018**, *93*, 266–269.

(219) Wang, L.; Martin, B.; Brenneman, R.; Luttrell, L. M.; Maudsley, S. Allosteric modulators of G protein-coupled receptors: future therapeutics for complex physiological disorders. *J. Pharmacol. Exp. Ther.* **2009**, *331*, 340–348.

(220) Scior, T.; Bender, A.; Tresadern, G.; Medina-Franco, J. L.; Martínez-Mayorga, K.; Langer, T.; Cuanalo-Contreras, K.; Agrafiotis, D. K. Recognizing pitfalls in virtual screening: a

critical review. *J. Chem. Inf. Model.* **2012**, *52*, 867–881.

(221) Strang, B. L.; Asquith, C. R. M.; Moshrif, H. F.; Ho, C. M.-K.; Zuercher, W. J.; Al-Ali, H. Identification of lead anti-human cytomegalovirus compounds targeting MAP4K4 via machine learning analysis of kinase inhibitor screening data. *PLoS One* **2018**, *13*, e0201321.

(222) Wang, Y.; Wang, J.; Shu, M.; Wang, Y.; Hu, Y.; Luo, Y.; Lin, Z. Identification of potential CCR5 inhibitors through pharmacophore-based virtual screening, molecular dynamics simulation and binding free energy analysis. *Mol. Biosyst.* **2016**, *12*, 3396–3406.

(223) Lionta, E.; Spyrou, G.; Vassilatis, D.; Cournia, Z. Structure-based virtual screening for drug discovery: principles, applications and recent advances. *Curr. Top. Med. Chem.* **2014**, *14*, 1923–1938.

(224) Geromichalos, G. D. Virtual screening strategies and application in drug designing. *Drug Des. Open Access* **2012**, *02*, 1–3.

(225) Cheng, T.; Li, Q.; Zhou, Z.; Wang, Y.; Bryant, S. H. Structure-based virtual screening for drug discovery: a problem-centric review. *AAPS J.* **2012**, *14*, 133–141.

(226) Evers, A.; Klebe, G. Successful virtual screening for a submicromolar antagonist of the neurokinin-1 receptor based on a ligand-supported homology model. *J. Med. Chem.* **2004**, *47*, 5381–5392.

(227) Ananthan, S.; Zhang, W.; Hobrath, J. V. Recent advances in structure-based virtual screening of G-protein coupled receptors. *AAPS J.* **2009**, *11*, 178–185.

(228) Irwin, J. J.; Shoichet, B. K. ZINC - a free database of commercially available compounds for virtual screening. *J. Chem. Inf. Model.* **2005**, *45*, 177–182.

(229) Rafehi, M.; Burbiel, J. C.; Attah, I. Y.; Abdelrahman, A.; Müller, C. E. Synthesis, characterization, and in vitro evaluation of the selective $P2Y_2$ receptor antagonist AR-C118925. *Purinergic Signal.* **2016**, *13*, 89–103.

(230) Chao, H.; Turdi, H.; Herpin, T. F.; Roberge, J. Y.; Liu, Y.; Schnur, D. M.; Poss, M. A.; Rehfuss, R.; Hua, J.; Wu, Q.; Price, L. A.; Abell, L. M.; Schumacher, W. A.; Bostwick, J. S.; Steinbacher, T. E.; Stewart, A. B.; Ogletree, M. L.; Huang, C. S.; Chang, M.; Cacace, A.

M.; Arcuri, M. J.; Celani, D.; Wexler, R. R.; Lawrence, R. M. Discovery of 2-(phenoxypyridine)-3-phenylureas as small molecule $P2Y_1$ antagonists. *J. Med. Chem*. **2013**, *56*, 1704–1714.

(231) Stumpfe, D.; Bajorath, J. Exploring activity cliffs in medicinal chemistry. *J. Med. Chem.* **2012**, *55*, 2932–2942.

(232) Stumpfe, D.; Ahmed, H. E. A.; Vogt, I.; Bajorath, J. Methods for computer-aided chemical biology. Part 1: design of a benchmark system for the evaluation of compound selectivity. *Chem. Biol. Drug Des.* **2007**, *70*, 182–194.

(233) Vogt, I.; Stumpfe, D.; Ahmed, H. E. A.; Bajorath, J. Erratum: methods for computer-aided chemical biology. Part 2: evaluation of compound selectivity using 2D molecular fingerprints. *Chem. Biol. Drug Des.* **2007**, *70*, 370.

(234) Stumpfe, D.; Geppert, H.; Bajorath, J. Methods for computer-aided chemical biology. Part 3: analysis of structure-selectivity relationships through single- or dual-step selectivity searching and Bayesian classification. *Chem. Biol. Drug Des.* **2008**, *71*, 518–528.

(235) Morphy, R.; Rankovic, Z. Design of multitarget ligands. In *Lead Generation Approaches in Drug Discovery*; John Wiley & Sons, Inc.: Hoboken, NJ, USA, 2010; pp 141–164.

(236) Morphy, R.; Kay, C.; Rankovic, Z. From magic bullets to designed multiple ligands. *Drug Discov. Today* **2004**, *9*, 641–651.

(237) Millan, M. J. Multi-target strategies for the improved treatment of depressive states: conceptual foundations and neuronal substrates, drug discovery and therapeutic application. *Pharmacol. Ther.* **2006**, *110*, 135–370.

(238) Murugesan, N.; Tellew, J. E.; Gu, Z.; Kunst, B. L.; Fadnis, L.; Cornelius, L. A.; Baska, R. A. F.; Yang, Y.; Beyer, S. M.; Monshizadegan, H.; Dickinson, K. E.; Panchal, B.; Valentine, M. T.; Chong, S.; Morrison, R. A.; Carlson, K. E.; Powell, J. R.; Moreland, S.; Barrish, J. C.; Kowala, M. C.; Macor, J. E. Discovery of N-isoxazolyl biphenylsulfonamides as potent dual angiotensin II and endothelin A receptor antagonists. *J. Med. Chem*. **2002**, *45*, 3829–3835.

(239) Seeger, T. F.; Seymour, P. A.; Schmidt, A. W.; Zorn, S. H.; Schulz, D. W.; Lebel, L. A.; McLean, S.; Guanowsky, V.; Howard, H. R.; Lowe, J. A. Ziprasidone (CP-88,059): a new antipsychotic with combined dopamine and serotonin receptor antagonist activity. *J.Pharmacol Exp Ther.* **1995**, *275*, 101–113.

(240) Slabinski, L.; Jaroszewski, L.; Rodrigues, A. P. C.; Rychlewski, L.; Wilson, I. A.; Lesley,

S. A.; Godzik, A. The challenge of protein structure determination-lessons from structural genomics. *Protein Sci.* **2007**, *16*, 2472–2482.

(241) Smyth, M. S.; Martin, J. H. X ray crystallography. *Mol. Pathol.* **2000**, *53*, 8–14.

(242) Zhang, K.; Zhang, J.; Gao, Z.-G.; Zhang, D.; Zhu, L.; Han, G. W.; Moss, S. M.; Paoletta, S.; Kiselev, E.; Lu, W.; Fenalti, G.; Zhang, W.; Müller, C. E.; Yang, H.; Jiang, H.; Cherezov, V.; Katritch, V.; Jacobson, K. A.; Stevens, R. C.; Wu, B.; Zhao, Q. Structure of the human $P2Y_{12}$ receptor in complex with an antithrombotic drug. *Nature* **2014**, *509*, 115–118.

(243) Brunschweiger, A.; Müller, C. E. P2 receptors activated by uracil nucleotides-an update. *Curr. Med. Chem.* **2006**, *13*, 289–312.

(244) Webb, B.; Sali, A. Protein structure modeling with modeller; Humana Press, New York, NY, 2017; pp 39–54.

(245) Yuan, S.; Chan, H. C. S.; Vogel, H.; Filipek, S.; Stevens, R. C.; Palczewski, K. The molecular mechanism of $P2Y_1$ receptor activation. *Angew. Chemie Int. Ed.* **2016**, *55*, 10331–10335.

(246) Hoffmann, C.; Moro, S.; Nicholas, R. a; Harden, T. K.; Jacobson, K. a; Hill, C.; Carolina, N. The role of amino acids in extracellular loops of the human $P2Y_1$ receptor in surface expression and activation processes. *J. Biol. Chem.* **1999**, *274*, 14639–14647.

(247) Erb, L.; Garrad, R.; Wang, Y.; Quinn, T.; Turner, J. T.; Weisman, G. a. Site-directed mutagenesis of P2U purinoceptors: positively charged amino acids in transmembrane helices 6 and 7 affect agonist potency and specificity. *Journal of Biological Chemistry*. 1995, pp 4185–4188.

(248) Brinson, A. E.; Harden, T. K. Differential regulation of the uridine nucleotide-activated $P2Y_4$ and $P2Y_6$ receptors. Ser-333 and Ser-334 in the carboxyl terminus are involved in agonist-dependent phosphorylation desensitization and internalization of the $P2Y_4$ receptor. *J. Biol. Chem.* **2001**, *276*, 11939–11948.

(249) Herold, C. L.; Qi, A. D.; Harden, T. K.; Nicholas, R. A. Agonist versus antagonist action of ATP at the $P2Y_4$ receptor is determined by the second extracellular loop. *J. Biol. Chem.* **2004**, *279*, 11456–11464.

(250) Kenakin, T. Differences between natural and recombinant G-protein-coupled receptor systems with varying receptor G-protein stoichiometry. *Trends Pharmacol. Sci.* **1997**, *18*, 456–464.

(251) Kinzer-Ursem, T. L.; Linderman, J. J. Both ligand- and cell-specific parameters control

ligand agonism in a kinetic model of G protein-coupled receptor signaling. *PLoS Comput. Biol.* **2007**, *3*, 0084–0094.

(252) Trzaskowski, B.; Latek, D.; Yuan, S.; Ghoshdastider, U.; Debinski, a; Filipek, S. Action of molecular switches in GPCRs - theoretical and experimental studies. *Curr. Med. Chem.* **2012**, *19*, 1090–1109.

(253) Bläker, M.; Ren, Y.; Gordon, M. C.; Hsu, J. E.; Beinborn, M.; Kopin, A. S. Mutations within the cholecystokinin-B/gastrin receptor ligand "pocket" interconvert the functions of nonpeptide agonists and antagonists. *Mol. Pharmacol.* **1998**, *54*, 857–863.

(254) Thor, D.; Schulz, A.; Hermsdorf, T.; Schöneberg, T. Generation of an agonistic binding site for blockers of the m(3) muscarinic acetylcholine receptor. *Biochem. J.* **2008**, *412*, 103–112.

(255) Ahuja, S.; Smith, S. O. Multiple switches in G protein-coupled receptor activation. *Trends Pharmacol. Sci.* **2009**, *30*, 494–502.

(256) Xie, X. Q.; Chowdhury, A. *Advances in methods to characterize ligand-induced ionic lock and rotamer toggle molecular switch in G protein-coupled receptors*, 1st ed.; Elsevier Inc., 2013; Vol. 520.

(257) Urizar, E.; Claeysen, S.; Deupí, X.; Govaerts, C.; Costagliola, S.; Vassart, G.; Pardo, L. An activation switch in the rhodopsin family of G protein-coupled receptors: the thyrotropin receptor. *J. Biol. Chem.* **2005**, *280*, 17135–17141.

(258) Martí-Solano, M.; Sanz, F.; Pastor, M.; Selent, J. A dynamic view of molecular switch behavior at serotonin receptors: implications for functional selectivity. *PLoS One* **2014**, *9*, 1–8.

(259) Wootten, D.; Christopoulos, A.; Sexton, P. M. Emerging paradigms in GPCR allostery: implications for drug discovery. *Nat. Rev. Drug Discov.* **2013**, *12*, 630–644.

(260) Sievers, F.; Wilm, A.; Dineen, D.; Gibson, T. J.; Karplus, K.; Li, W.; Lopez, R.; McWilliam, H.; Remmert, M.; Söding, J.; Thompson, J. D.; Higgins, D. G. Fast, scalable generation of high-quality protein multiple sequence alignments using clustal omega. *Mol. Syst. Biol.* **2011**, *7*, 1-6.

(261) Friesner, R. A.; Banks, J. L.; Murphy, R. B.; Halgren, T. A.; Klicic, J. J.; Mainz, D. T.; Repasky, M. P.; Knoll, E. H.; Shelley, M.; Perry, J. K.; Shaw, D. E.; Francis, P.; Shenkin, P. S. Glide: a new approach for rapid, accurate docking and scoring. 1. Method and assessment of docking accuracy. *J. Med. Chem.* **2004**, *47*, 1739–1749.

(262) Halgren, T. A.; Murphy, R. B.; Friesner, R. A.; Beard, H. S.; Frye, L. L.; Pollard, W. T.;

Banks, J. L. Glide: a new approach for rapid, accurate docking and scoring. 2. Enrichment factors in database screening. *J. Med. Chem*. **2004**, *47*, 1750–1759.

(263) Sherman, W.; Day, T.; Jacobson, M. P.; Friesner, R. A.; Farid, R. Novel procedure for modeling ligand/receptor induced fit effects. *J. Med. Chem*. **2006**, *49*, 534–553.

(264) Bateman, A.; Martin, M. J.; O'Donovan, C.; Magrane, M.; Alpi, E.; Antunes, R.; Bely, B.; Bingley, M.; Bonilla, C.; Britto, R.; Bursteinas, B.; Bye-AJee, H.; Cowley, A.; Da Silva, A.; De Giorgi, M.; Dogan, T.; Fazzini, F.; Castro, L. G.; Figueira, L.; Garmiri, P.; Georghiou, G.; Gonzalez, D.; Hatton-Ellis, E.; Li, W.; Liu, W.; Lopez, R.; Luo, J.; Lussi, Y.; MacDougall, A.; Nightingale, A.; Palka, B.; Pichler, K.; Poggioli, D.; Pundir, S.; Pureza, L.; Qi, G.; Rosanoff, S.; Saidi, R.; Sawford, T.; Shypitsyna, A.; Speretta, E.; Turner, E.; Tyagi, N.; Volynkin, V.; Wardell, T.; Warner, K.; Watkins, X.; Zaru, R.; Zellner, H.; Xenarios, I.; Bougueleret, L.; Bridge, A.; Poux, S.; Redaschi, N.; Aimo, L.; ArgoudPuy, G.; Auchincloss, A.; Axelsen, K.; Bansal, P.; Baratin, D.; Blatter, M. C.; Boeckmann, B.; Bolleman, J.; Boutet, E.; Breuza, L.; Casal-Casas, C.; De Castro, E.; Coudert, E.; Cuche, B.; Doche, M.; Dornevil, D.; Duvaud, S.; Estreicher, A.; Famiglietti, L.; Feuermann, M.; Gasteiger, E.; Gehant, S.; Gerritsen, V.; Gos, A.; Gruaz-Gumowski, N.; Hinz, U.; Hulo, C.; Jungo, F.; Keller, G.; Lara, V.; Lemercier, P.; Lieberherr, D.; Lombardot, T.; Martin, X.; Masson, P.; Morgat, A.; Neto, T.; Nouspikel, N.; Paesano, S.; Pedruzzi, I.; Pilbout, S.; Pozzato, M.; Pruess, M.; Rivoire, C.; Roechert, B.; Schneider, M.; Sigrist, C.; Sonesson, K.; Staehli, S.; Stutz, A.; Sundaram, S.; Tognolli, M.; Verbregue, L.; Veuthey, A. L.; Wu, C. H.; Arighi, C. N.; Arminski, L.; Chen, C.; Chen, Y.; Garavelli, J. S.; Huang, H.; Laiho, K.; McGarvey, P.; Natale, D. A.; Ross, K.; Vinayaka, C. R.; Wang, Q.; Wang, Y.; Yeh, L. S.; Zhang, J. UniProt: the universal protein knowledgebase. *Nucleic Acids Res.* **2017**, *45*, D158–D169.

(265) Behrenswerth, A.; Volz, N.; Toräng, J.; Hinz, S.; Bräse, S.; Müller, C. E. Synthesis and pharmacological evaluation of coumarin derivatives as cannabinoid receptor antagonists and inverse agonists. *Bioorg. Med. Chem*. **2009**, *17*, 2842–2851.

9 Appendices

9.1 Supplementary information

Supplementary Table S1: Cell surface expression of $P2Y_2$ and $P2Y_4$ receptors [a]

Cell-line	% expression ± SEM [b]	n
$P2Y_2$		
wt	100 ± 4	3
R110A	74 ± 4 **	3
F113A	125 ± 10 **	3
F113Y	16 ± 1 ****	3
D185A	105 ± 9 ns	3
F195Y	95 ± 8 ns	3
$P2Y_4$		
wt	100 ± 3	3
N170V	73 ± 13 **	3
R190A	65 ± 6 ***	4
E193A	86 ± 7 ns	4
D195A	132 ± 14 **	4
D195S	90 ± 15 ns	3
Y197A	56 ± 2 ****	4
Y197F	65 ± 5 ***	4
F200A	84 ± 7 ns	3
F200Y	144 ± 6 ****	3

[a] Data represent means ± SEM of 3-4 independent experiments. Cell surface receptor expression rates were determined by ELISA involving antibodies interacting with receptor N-terminus-HA tag. Expression of the respective wildtype (wt) receptor for the mutants was normalized to 100 %. [b] One-way ANOVA with Dunnett's post-hoc test: ns not significant; * $p \leq 0.05$; ** $p \leq 0.01$; *** $p \leq 0.001$; **** $p \leq 0.0001$.

Supplementary Table S9: Potencies of agonists at the human $P2Y_2$ receptor mutants as determined in intracellular calcium mobilization assays.[a]

Cell-line	EC_{50} (nM) ± SEM [b]	n	% Efficacy (± SEM) [b]	EC_{50} mutant/ EC_{50} wt
UTP				
$P2Y_2$-wt	82.2 ± 5.9	5	100 ± 2	1
R110A	>100000	6	n.d [c]	>1200
F113A	25000 ± 2700 ****	3	170 ± 12 ****	304
F113Y	52.6 ± 18.3 [ns]	5	33 ± 2****	0.6
D185A	606 ± 76 ***	4	116 ± 7 [ns]	7
F195Y	23.3 ± 6.4 **	4	104 ± 3 [ns]	0.3
ATP				
$P2Y_2$-wt	102 ± 10	6	100 ± 2	1
R110A	>100000	6	n.d [c]	>980
F113A	20500 ± 4200 ****	3	185 ± 16****	201
F113Y	219 ± 44 [ns]	5	31 ± 7****	2
D185A	2160 ± 454 ****	5	100 ± 9 [ns]	21
F195Y	203 ± 57 [ns]	4	92 ± 7 [ns]	2
Ap_4A				
$P2Y_2$-wt	69.5 ± 6.5	4	88 ± 3	1
R110A	>100000	6	n.d [c]	>1400
F113A	>100000	5	n.d [c]	>1400
F113Y	>100000	5	16 ± 4****	>1400
D185A	>100000	5	9 ±7****	>1400
F195Y	194 ± 43 ***	5	67 ± 8 *	3

MRS4062				
$P2Y_2$-wt	535 ± 44	4	88± 4	1
R110A	>100000	6	n.d [c]	>187
F113A	>100000	5	n.d [c]	>187
F113Y	54.6 ± 14.5 ****	4	20 ± 2 ****	0.1
D185A	>100000	5	7 ± 3 ****	>187
F195Y	178 ± 27 ***	5	71 ± 3 ***	0.3

[a] Data represent means ± SEM of 3-6 independent experiments each in duplicates. [b] Results of One-way ANOVA with Dunnett's post-hoc test: [ns] not significant; * $p \leq 0.05$; ** $p \leq 0.01$; *** $p \leq 0.001$; **** $p \leq 0.0001$. [c] no concentration-dependent activation up to 100 µM; n.d. = not determined.

Supplementary Table S3: Potencies of agonists at the human $P2Y_4$ receptor mutants as determined in intracellular calcium mobilization assays.[a]

Cell-line	EC_{50} (nM) ± SEM [b]	n	% Efficacy (± SEM) [b]	EC_{50} mutant/ EC_{50} wt
UTP				
$P2Y_4$- wt	135 ± 25	3	100 ± 4	1
N170V	259 ± 75 [ns]	5	72 ± 8 *	2
R190A	1980 ± 196 ****	3	53 ± 6 ***	15
E193A	61.6 ± 5.2 [ns]	3	100 ± 8 [ns]	0.5
D195A	47.5 ± 6.6 [ns]	3	83 ± 5 [ns]	0.4
D195S	68.6 ± 12.0 [ns]	4	80 ± 6 [ns]	0.5
Y197A	411 ± 56 [ns]	4	56 ± 6 ***	3
Y197F	84.4 ± 12.0 [ns]	3	75 ± 1 [ns]	0.6
F200A	284 ± 18 [ns]	3	24 ± 5 ****	2
F200Y	47.1 ± 6.4 [ns]	3	106 ± 9 [ns]	0.3

ATP				
$P2Y_4$- wt	>100000	3	n.d [c]	n.d [c]
N170V	>100000	5	4 ± 2 [ns]	n.d [c]
R190A	>100000	4	n.d [c]	n.d [c]
E193A	>100000	4	n.d [c]	n.d [c]
D195A	>100000	4	n.d [c]	n.d [c]
D195S	>100000	5	5 ± 3 [ns]	n.d [c]
Y197A	11900 ± 1560 ****	4	32 ± 3 ****	n.d [c]
Y197F	>100000	4	n.d [c]	n.d [c]
F200A	>100000	5	n.d [c]	n.d [c]
F200Y	>100000	4	5 ± 1 [ns]	n.d [c]
Ap_4A				
$P2Y_4$- wt	>100000	5	n.d [c]	n.d [c]
N170V	>100000	4	n.d [c]	n.d [c]
R190A	>100000	5	n.d [c]	n.d [c]
E193A	>100000	4	n.d [c]	n.d [c]
D195A	>100000	4	n.d [c]	n.d [c]
D195S	>100000	4	n.d [c]	n.d [c]
Y197A	>100000	5	n.d [c]	n.d [c]
Y197F	>100000	6	n.d [c]	n.d [c]
F200A	>100000	4	n.d [c]	n.d [c]
F200Y	>100000	5	n.d [c]	n.d [c]
MRS4062				
$P2Y_4$- wt	76.1 ± 10	3	100 ± 2	1
N170V	77.6 ± 9.6 [ns]	5	56 ± 7 ****	1
R190A	1240 ± 279 ****	3	57 ± 3***	16

E193A	83.1 ± 9.1 ^{ns}	3	94 ± 5 ^{ns}	1
D195A	82.5 ± 10.7 ^{ns}	3	88 ± 5 ^{ns}	1
D195S	154 ± 14 ^{ns}	5	84 ± 6 ^{ns}	2
Y197A	757 ± 68 ***	4	57 ± 5***	10
Y197F	86.6 ± 12.2 ^{ns}	3	75 ± 2 ^{ns}	1
F200A	694 ± 69 **	3	21 ± 5****	9
F200Y	35.9 ± 1.7 ^{ns}	3	89 ± 8 ^{ns}	0.5

[a] Data represents means ± SEM of 3-6 independent experiments each in duplicates. [b] Results of One-way ANOVA with Dunnett's post-hoc test: ^{ns} not significant; * $p \leq 0.05$; ** $p \leq 0.01$; *** $p \leq 0.001$; **** $p \leq 0.0001$. [c] no concentration-dependent activation up to 100 µM; n.d. = not determined.

Supplementary Table S4: Potencies of antagonists versus UTP (EC_{80} values) at the human $P2Y_2$ receptor mutants as determined in intracellular calcium mobilization assays.[a]

Cell-line	**IC_{50} (nM) ± SEM [b]**	**n**
RB-2 purified		
$P2Y_2$-wt	5990 ± 563	4
F113A	4130 ± 714 ^{ns}	4
F113Y	23500 ± 4560 ***	4
D185A	1730 ± 322 ***	4
F195Y	18000 ± 1540 **	5
AR-C118925		
$P2Y_2$-wt	21.2 ± 4.2	5
F113A	34.0 ± 7.1 ^{ns}	4
F113Y	32.4 ± 7.5 ^{ns}	5
D185A	20.4 ± 8.2 ^{ns}	3
F195Y	41.6 ± 8.1 ^{ns}	5

PSB-09114		
$P2Y_2$-wt	1537 ± 61	4
F113A	710 ± 20 ^{ns}	4
F113Y	550 ± 134 *	4
D185A	170 ± 25 **	3
F195Y	2020 ± 513 ^{ns}	4
PSB-16133		
$P2Y_2$-wt	2310 ± 336	4
F113A	4740 ± 522 ^{ns}	3
F113Y	351 ± 87 ****	3
D185A	467 ± 39 ****	4
F195Y	2660 ± 683 ^{ns}	3
PSB-16135		
$P2Y_2$-wt	2010 ± 308	4
F113A	4780 ± 736 ^{ns}	3
F113Y	1380 ± 260 **	5
D185A	1200 ± 63 **	4
F195Y	4890 ± 708 ^{ns}	5
PSB-1699		
$P2Y_2$-wt	3190 ± 971	5
F113A	>100000 ****	3
F113Y	2770 ± 654 ^{ns}	4
D185A	1620 ± 221 ^{ns}	4
F195Y	>100000 ****	4

[a] Data represents means ± SEM of 3-5 independent experiments each in duplicates. [b] Results of One-way ANOVA with Dunnett's post-hoc test: ^{ns} not significant; * $p \leq 0.05$; ** $p \leq 0.01$; *** $p \leq 0.001$; **** $p \leq 0.0001$.

Supplementary Table S5: Potencies of antagonists versus UTP (EC_{80} values) at the human $P2Y_4$ receptor mutants as determined in intracellular calcium mobilization assays.[a]

Cell-line	IC_{50} (nM) ± SEM [b]	n
RB-2 purified		
$P2Y_4$- wt	1050 ± 43	3
N170V	477 ± 83 *	3
R190A	1560 ± 202 ns	3
E193A	1510 ± 179 ns	3
D195A	1780 ± 352 ns	3
D195S	2260 ± 401 *	4
Y197A	566 ± 35 ns	4
Y197F	3300 ± 652 ***	3
F200A	1390 ± 237 ns	3
F200Y	4170 ± 221 ****	3
AR-C118925		
$P2Y_4$- wt	5730 ± 821	3
N170V	>100000 ****	5
R190A	10900 ± 1050 **	4
E193A	12700 ± 1180 ***	4
D195A	1470 ± 224 ****	3
D195S	>100000 ****	5
Y197A	1960 ± 378 ****	3
Y197F	9790 ± 884 **	5
F200A	6280 ± 773 ns	4
F200Y	>100000 ****	4

PSB-09114		
$P2Y_4$- wt	403 ± 17	3
N170V	2260 ± 353 ****	4
R190A	736 ±127 ns	3
E193A	1010 ± 160 **	3
D195A	576 ± 17 ns	2
D195S	487 ± 98 ns	3
Y197A	234 ± 7 ns	3
Y197F	913 ± 59 **	3
F200A	331 ± 51 ns	3
F200Y	2090 ± 236 ****	3
PSB-16133		
$P2Y_4$- wt	1620 ± 166	3
N170V	2840 ± 888 ns	4
R190A	339 ± 10 ***	3
E193A	3080 ± 244 ns	3
D195A	2270 ± 372 ns	3
D195S	1850 ± 407 ns	4
Y197A	205 ± 68 ****	3
Y197F	4770 ± 677 *	3
F200A	680 ± 71 ns	3
F200Y	5430 ± 711 **	3
PSB-16135		
$P2Y_4$- wt	1730 ± 105	3
N170V	2990 ± 722 ns	5
R190A	4980 ± 938 **	3
E193A	4330 ± 645 *	3

D195A	3160 ± 460 ^{ns}	3
D195S	2240 ± 256 ^{ns}	5
Y197A	303 ± 60 ****	3
Y197F	3540 ± 49 ^{ns}	3
F200A	1730 ± 175 ^{ns}	3
F200Y	5690 ± 620 **	3
PSB-1699		
$P2Y_4$- wt	1530 ± 273	5
N170V	537 ± 84 ****	3
R190A	>100000 ****	3
E193A	2190 ± 381 ^{ns}	3
D195A	>100000 ****	3
D195S	504 ± 90 ****	4
Y197A	2130 ± 109 ^{ns}	3
Y197F	8850 ± 531****	3
F200A	>100000 ****	3
F200Y	>100000 ****	3

[a] Data represent means ± SEM of 3-5 independent experiments each in duplicates. [b] Results of One-way ANOVA with Dunnett's post-hoc test: ^{ns} not significant; * $p \leq 0.05$; ** $p \leq 0.01$; *** $p \leq 0.001$; **** $p \leq 0.0001$.

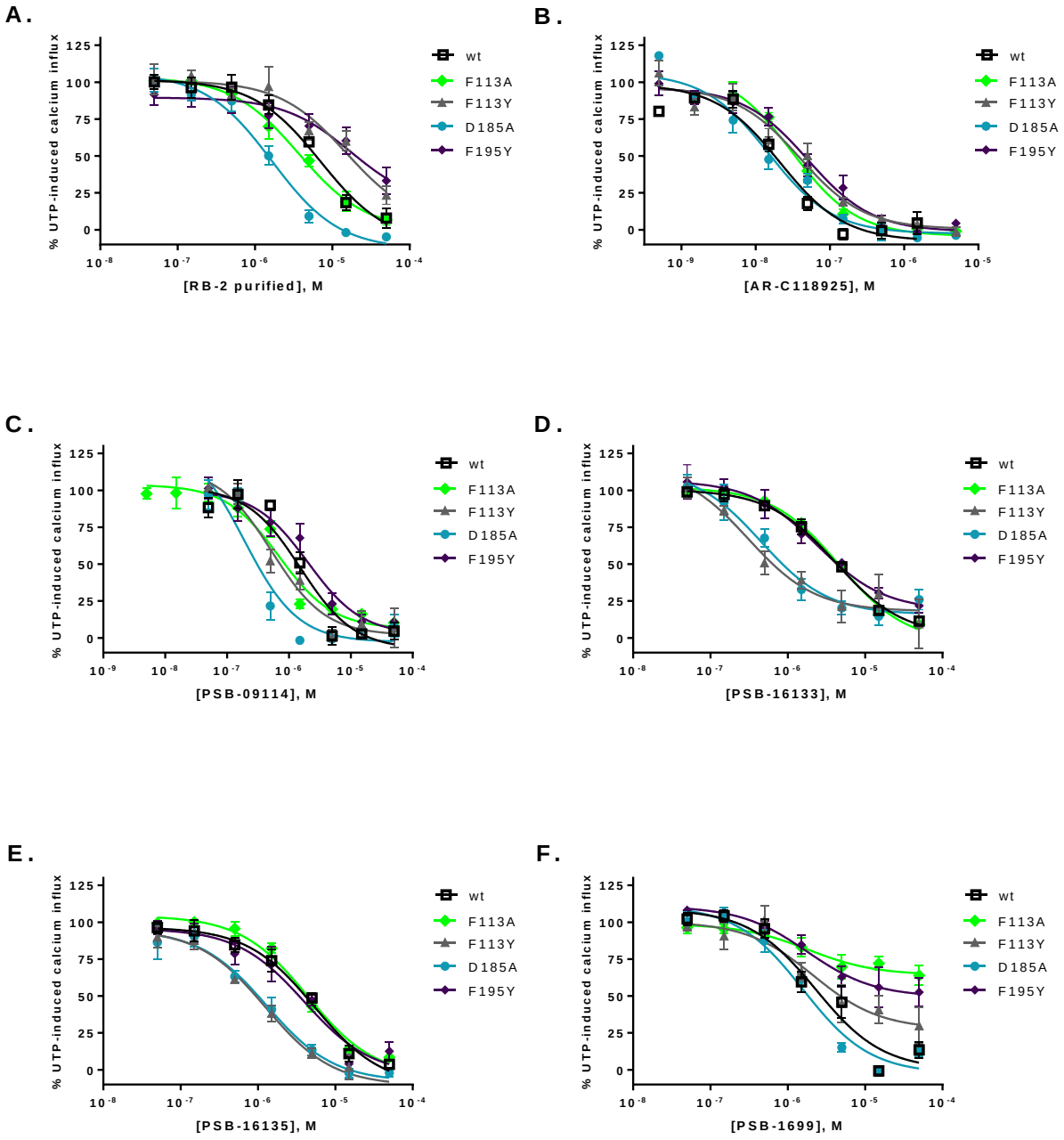

Supplementary Figure S1: UTP-inhibition curves as determined by calcium mobilization assay on the $P2Y_2$ receptors (wt and mutants) expressed in 1321N1 astrocytoma cells by **A)** Reactive blue 2 (RB-2) purified, **B)** AR-C118925, **C)** PSB-09114, **D)** PSB-16133, **E)** PSB-16135 and **F)** YB - 099. Each data point represents mean ± SEM of 3 – 5 independent determinations each in duplicate vs UTP EC_{80} value for the respective cell-line. IC_{50} values are reported in Table S4.

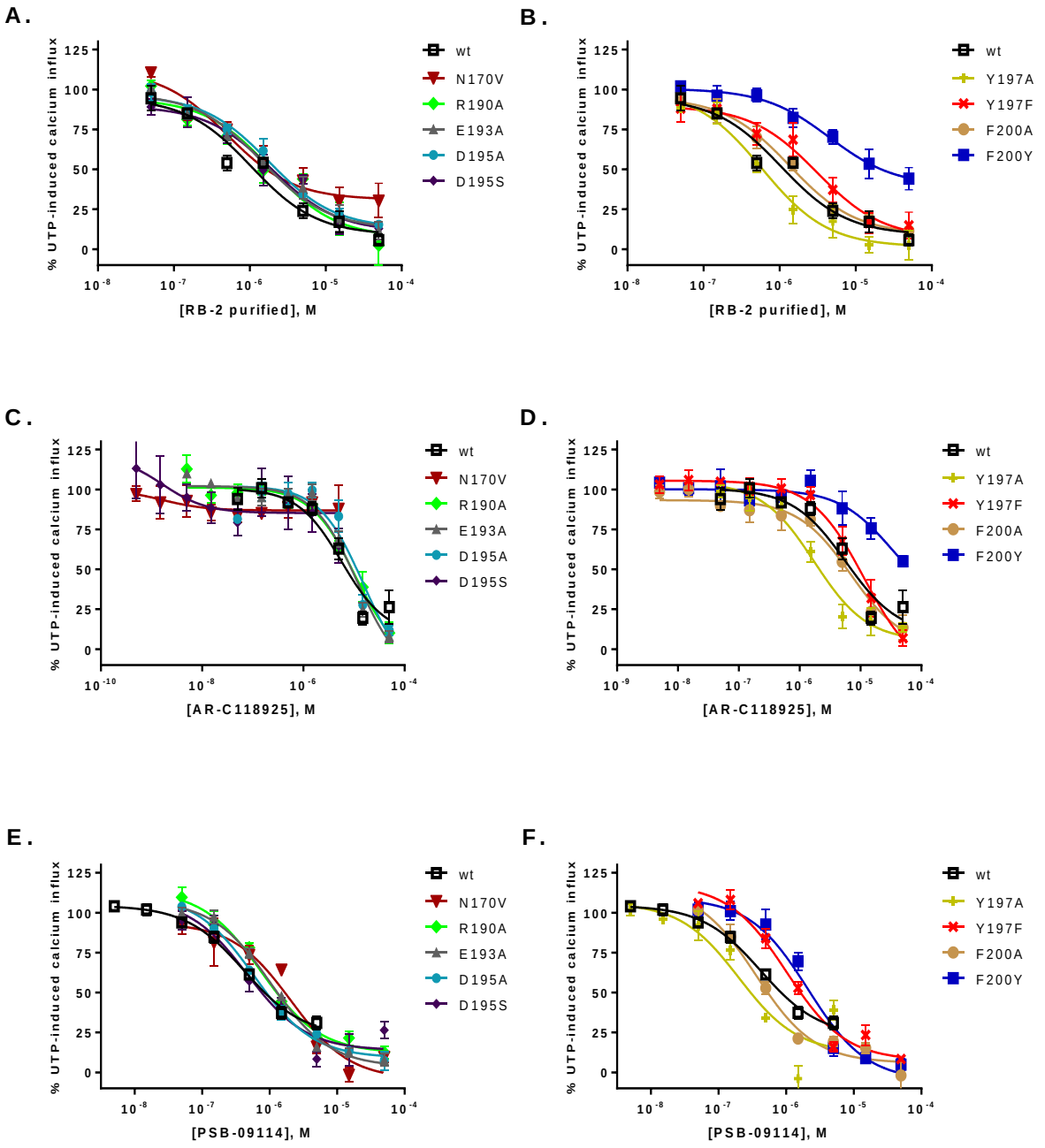

Supplementary Figure S2: UTP-inhibition curves as determined by calcium mobilization assay on the $P2Y_4$ receptors (wt and mutants) expressed in 1321N1 astrocytoma cells by Reactive blue-2 **(A** and **B),** AR-C118925 **(C** and **D),** and PSB-09114 **(E** and **F).** Each data point represents mean ± SEM of 3 – 5 independent determinations each in duplicate vs UTP EC_{80} value for the respective cell-line. IC_{50} values are reported in Table S5.

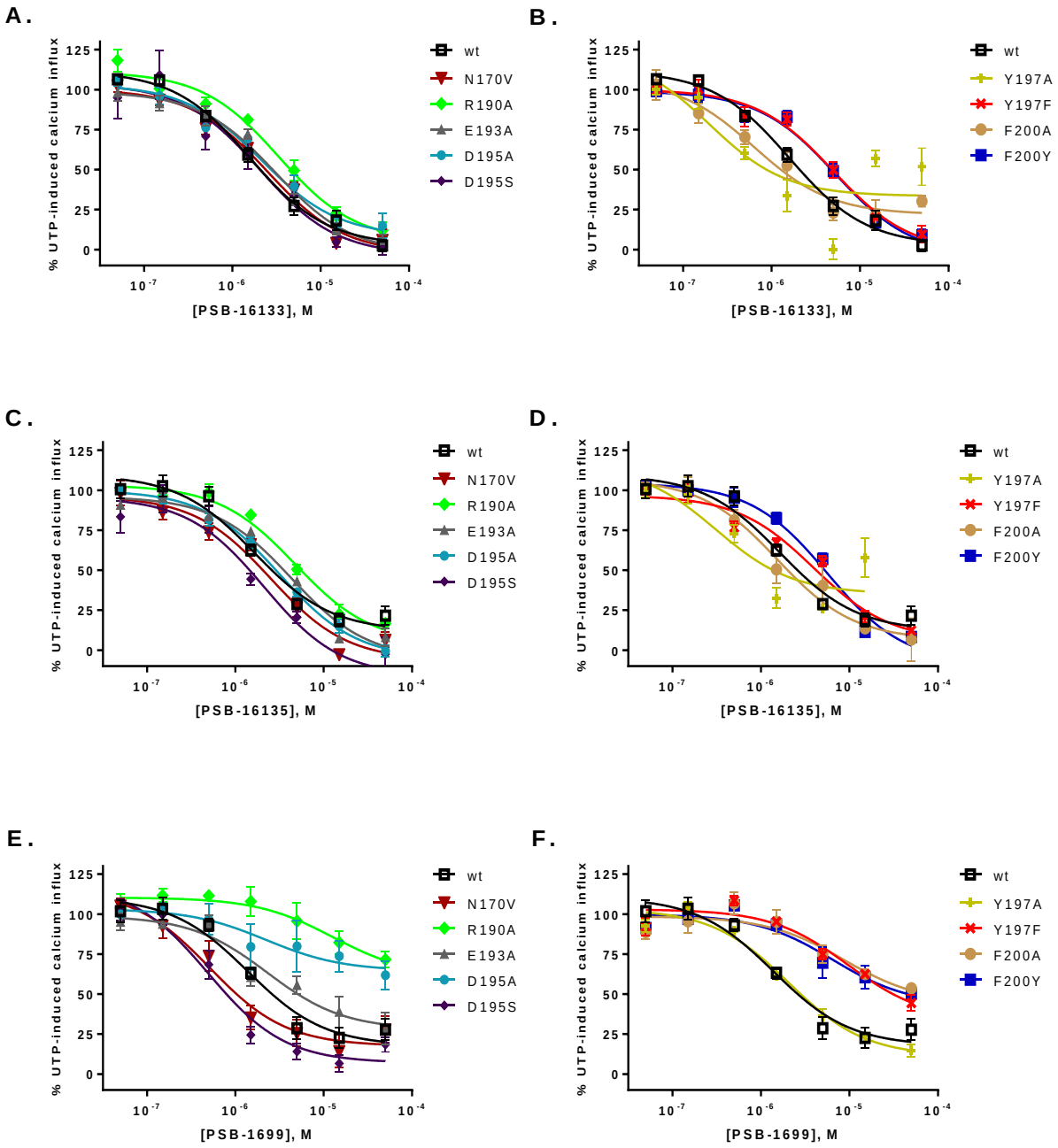

Supplementary Figure S3: UTP-inhibition curves as determined by calcium mobilization assay on the $P2Y_4$ receptors (wt and mutants) expressed in 1321N1 astrocytoma cells by PSB-16133 **(A** and **B),** PSB-16135 **(C** and **D),** and PSB-1699 **(E** and **F).** Each data point represents mean ± SEM of 3 – 5 independent determinations each in duplicate vs UTP EC_{80} value for the respective cell-line. IC_{50} values are reported in Table S5.

9.2 **Abbreviations**

2-MeSATP	2-Methylthioadenosine-5‘-O-triphosphate
5-HT	5-Hydroxytryptamine; Serotonin
ADP	Adenosine 5‘-diphosphate
ATP	Adenosine-5‘-triphosphate
BSA	Bovine serum albumin
cAMP	Cyclic adenosine monophosphate
CB receptor	Cannabinoid receptor
CCR2	C-C chemokine receptor type 2
cDNA	Complementary deoxyribonucleic acid
CHO cells	Chinease hamster ovary cells
CNS	Central nervous system
COX	Cyclooxygenase
Cpd.	Compound
CTX	Cholera toxin
CysLT1 receptor	Cysteinyl leukotriene receptor
DAG	Diacylglycerol
DMEM	Dulbecco’s Modified Eagle’s Medium
DMSO	Dimethyl sulfoxide
DR	Dose ratio
EC_{50}	Concentration of half-maximal receptor activation
ECL	Extracellular loop
EDTA	Ethylenediaminetetraacetic acid
ELISA	Enzyme linked immunosorbent assay
eNOS	Endothelial nitric oxide synthase
ERK	Extracellular singal-regulated kinase
ESI	Electronspray ionization
FAAH	Fatty acid amide hydrolase
FCS	Fetal calf serum
Fluo-4 AM	Fluo-4 acetoxymethyl ester
FRET	Forster-resonance energy transfer
G418	Geneticin

GABA	γ-aminobutyric acid
GDP	Guanosine diphosphate
GI	Gastrointestinal
GIRK	G protein-coupled inwardly-rectifying potassium channels
GP+envAM12	Amphotropic mouse fibroblast packaging cell line
GPCR	G protein-coupled receptor
GRK	G protein-coupled receptor kinase
GTP	Guanosine triphosphate
GTPγS	Guanosine 5'-*O*-[γ-thio]triphosphate
HBSS	Hank's balanced salt solution
HEK293	Human embryonic kidney cell line
HEPES	4-(2-Hydroxyethyl)-1-piperazineethanesulfonic acid
HIV	Human immune-deficiency virus
HPLC	High performance liquid chromatography
HTS	High-throughput screening
IC_{50}	Concentration of half-maximal receptor inhibition
ICL	Intracellular loop
IP3	Inositol triphosphate
K_B	Estimated antagonist affinity constant
K_D	Dissociation constant
K_i	Inhibition constant
LB medium	Lysogeny broth medium
LBD	Ligand binding domain
LGIC	Ligand-gated ion channel
LPS	Lipopolysaccharide
MAP kinase	Mitogen activated protein kinase
max.	Maximal
mRNA	Messenger RNA
MRSA	Methicillin-resistant Staphylococcus aureus
msec	Milliseconds
n. d.	not determined
nACh	Nicotinic acetylcholine receptor

NAM	Negative allosteric modulator
NFκB	Nuclear factor kappa-light-chain-enhancer of activated B-cells
NMDA	N-methyl-D-aspartate
NMDA-receptor	*N*-methyl-D-aspartate receptor, a glutamate receptor
NMR	Nuclear magnetic resonance spectroscopy
NOS	Nitric oxide synthase
NSAID	Non-steroidal anti-inflammatory drug
PAM	Positive allosteric modulator
PAR1	Protease-activated receptor 1
PCR	Polymerase chain reaction
PDB	Protein data bank
pEC_{50}	Negative decadic logarithm of EC_{50} value
PEG	Polyethylene glycol
pIC_{50}	Negative decadic logarithm of IC50 value
PPADS	Pyridoxalphosphate-6-azophenyl-2‘-4‘-disulfonic acid
PPARα	Peroxisome proliferator-activated receptor α
PPARγ receptor	Peroxisome proliferator-activated receptor gamma
PTX	Pertussis toxin
VSV-G	Vesicular stomatitis virus-expressing vector
PZB	Pharma-Zentrum Bonn
QSAR	Quantitative structure-activity relationships
RB-2	Reactive Blue-2
RMSD	root mean square deviation
RNA	Ribonucleic acid
rt	Room temperature
SAR	Structure-activity relationships
SEM	Standard error of the mean
SRE	Serum response element
STAT3	Signal transducer and activator of transcription 3
TAE buffer	Tris-acetate-EDTA buffer
TM	Transmembrane α-helix
TMD	Transmembrane domain

TRIS	Tris(hydroxymethyl)-aminomethane
UDP	Uridine 5‘-diphosphate
UTP	Uridine 5‘-triphosphate
Δ^9-THC	Δ^9-tetrahydrocannabinol

10 Acknowledgements

To God be the glory, great things He has done for me! To Him be my deepest gratitude.

I am deeply grateful to Prof. Dr. Christa E. Müller for the opportunity to pursue my PhD in her group. Dear Christa, thanks for the interesting project and all the insightful scientific discussions. Your patience and mentorship has made my research stay successful. Thanks for training me to become a good scientist.

I would like to thank my co-supervisor, PD Dr. Anke Schiedel, for her support during my PhD especially on issues related to molecular biology. I enjoyed your seminars on molecular biology and medicinal chemistry and learnt a great deal.

Also, I would like to thank Prof. Dr. Ivar von Kügelgen and Prof. Dr. Rainer Manthey for accepting to be co-examiners in my PhD examination committee.

To all my officemates: Sonja, Wenji, Inge, Andhika and Yvonne, thank for the wonderful and relaxing time in the office. I really enjoyed our discussions, both scientific and social, that made the occupational stress more bearable and fun.

My gratitude also goes to Dr Thanigaimalai Pillaiyar for synthesizing the diindolylmethane derivatives that I tested, and Dr. Vigneshwaran Namasivayam and Alexander Neumann for the constructing the homology models. Your insights were very meaningful to this dissertation. You are wonderful team players.

I would to thank Dr. Aliaa Abdelrahman and Steffi Weyer for introducing me to the various techniques and practices in the lab during my early days in the group.

To all the present and past members the AK Müller group: thanks for the cordial and collaborative working atmosphere. Many of the friendships here are sure to last. I am also grateful to all members of Pharmaceutical Institute and BIGS DrugS, University of Bonn who contributed in any way to the success of this PhD.

As the saying goes, “All work and no play, makes Jack a dull boy”. Therefore, to all who enriched my social life in Germany namely the beautiful choir members and families from St. Thomas More

Church, my German friends and "families", the Ghanaian community, my football club, I say "Bedanke Alle."

Furthermore, I am especially grateful to my lovely wife, Imelda, and my family for being a pillar in my life all these years. Thank you.

Finally, I would like to thank the DAAD for the funding and legal support during my PhD; without which my stay would have been impossible. I am also grateful to the University of Cape Coast for the support during my PhD studies. I also thank IPID4all, University of Bonn for the travel grant to attend conferences.